Design Optimisation of Hybrid Photovoltaic and Energy Storage Systems through Smart Grid Technologies to Maximise Economic Benefit

Jeremy Paul Every
BE(Elec)(Hons 1), BMath

Supervisor:
A/Prof. Li Li

Co-supervisors:
A/Prof. Youguang Guo, Prof. David G. Dorrell (External)

Doctor of Philosophy

University of Technology Sydney
School of Electrical and Data Engineering
Faculty of Engineering and Information Technology

February 2020

Certificate of Original Authorship

I, Jeremy Paul Every, declare that this thesis, is submitted in fulfilment of the requirements for the award of Doctor of Philosophy, in the School of Electrical and Data Engineering of the Faculty of Engineering and Information Technology at the University of Technology Sydney.

This thesis is wholly my own work unless otherwise referenced or acknowledged. In addition, I certify that all information sources and literature used are indicated in the thesis.

This document has not been submitted for qualifications at any other academic institution.

This research is supported by the Australian Government Research Training Program.

Production Note:
Signature removed prior to publication.

Jeremy Paul Every
February 8, 2020

Acknowledgements

Firstly, I wish to thank Associate Professor Li Li for his supervision during my candidature. Dr Li's attention to detail has greatly improved the quality of my work and the flexibility he has afforded me to pursue my research areas of interest is greatly appreciated. I wish to thank my external supervisor Professor David Dorrell for first of all taking me on as a PhD student and secondly remaining in the game following his move to Durban, South Africa. Thanks also go to my co-supervisor Associate Professor Youguang Guo for his valued input towards my research publications.

I wish to thank my parents Allan and Libby Every for their support and personal sacrifices enabling me to pursue my chosen career and study interests.

Finally, my deepest appreciation goes to Nancy-Maree Ryan for her patience, understanding and unwavering support over the journey.

Contents

List of Figures

List of Tables

Nomenclature

α	Contraction-expansion coefficient (QPSO)
α	Solar altitude
$\alpha(\cdot), \lambda(\cdot), h(\cdot), \psi(\cdot)$	Penalty function components (PSO)
α_s	Sunset hour solar altitude ($-0.833°$)
β	Solar collector surface tilt angle
β_0,β_1,β_2,β_3,β_4,β_5	BRL parameter coefficients for
χ	Constriction factor (PSO)
Δ	Brightness index
δ	Maximum depth of discharge
δ	Solar declination
$\delta(m)$	Optical thickness
$\delta_R(m)$	Rayleigh atmosphere optical thickness
ϵ	Clearness index
η_e	Balance of plant efficiency
$\eta_{ac,wire}$	AC wiring efficiency
η_{batt}	BESS round-trip efficiency
$\eta_{dc,wire}$	DC wiring efficiency
η_{inv}	Inverter efficiency
η_{mm}	Module mismatch efficiency
$\eta_{mpp,STC}$	Maximum power point efficiency at standard test conditions
η_{mpp}	Maximum power point efficiency at operating conditions
η_{soil}	Soiling efficiency
γ	Solar collector surface azimuth angle
κ_b	Battery cost reduction rate
κ_{inv}	Inverter cost reduction rate
μ_{mpp}	Maximum power point temperature coefficient
μ_{P2P}	Sale margin of P2P participant
μ_T	P2P trader margin
$\omega, \omega_s, \omega_{z,s}$	Solar hour angle, sunset hour angle and sunset zenith angle ($90.833°$)
ω_1, ω_2	Solar hour angle 1 and 2

ϕ	Latitude
ψ	Persistence factor
ψ,ψ^2	Particle characteristic wave function and probability density (QPSO)
ρ_g	Composite ground reflectance factor
θ, θ_z,$\theta_{z,s}$	Direct irradiance angle of incidence, solar zenith angle and zenith angle at sunset
ζ_{batt}	Cycle degradation rate (kWh/cycle)
A_c	PV module area
A_i	Anisotropy index
AST	Apparent solar time
B_T	Direct irradiation on a tilted surface
$B_{BESSsell,qdh}$	BESS sell reservation price of hour h, day d, billing period q
$B_{BUY,qdh}$	Final successful buy reservation price in a P2P bidding hour h, day d, billing period q
$B_{buy,qdh}$	BESS sell reservation price of hour h, day d, billing period q
$B_{pvsell,qdh}$	PV sell reservation price of hour h, day d, billing period q
$B_{sell,qdh}$	P2P sell reservation price (either $B_{pvsell,qdh}$ or $B_{BESSsell,qdh}$)
c_1, c_2	Acceleration coefficients (PSO)
$C_{\max 0}$	Initial maximum capacity
$C_{\max,qdh}$	Maximum capacity at the start of hour h, day d, billing period q
$C_{base,q}$	Electricity cost in period q without PV installed (lowest cost plan)
$C_{c,qdh}$	Total BESS charge cost up to hour h, day d, billing period q
C_{degrad}	Battery degradation cost
C_{EOL}	End-of-life maximum capacity
$C^j_{i,n}$	Mean best position of particle i in dimension j at iteration n (QPSO)
$C_{pv,q}$	Electricity cost in period q with PV installed
C_{qdh}	Available capacity at the start of hour h, day d, billing period q
C_{STC}	Cost of STC certificates
d	Day number of billing period q
D_q	Days in billing period q
D_T	Diffuse irradiation on a tilted surface
D_y	PV module degradation factor in year y
E	Equation of time
E_{bal}	Energy balance after accounting for DER energy flows and losses
$E_{bd,qdh}$	BESS discharge energy at the end of hour h, day d, billing period q
$E_{bdbid,qdh}$	P2P BESS sell energy bid of hour h, day d, billing period q
$E_{bdloss,qdh}$	BESS energy loss during discharge in hour h, day d, billing period q

$E_{bg,qdh}$	BESS grid-charge energy at the end of hour h, day d, billing period q
$E_{bgloss,qdh}$	BESS energy loss during grid-charge in hour h, day d, billing period q
$E_{bloss,qdh}$	Total BESS energy loss in hour h, day d, billing period q
$E_{bpv,qdh}$	BESS PV-charge energy at the end of hour h, day d, billing period q
$E_{bpvloss,qdh}$	BESS energy loss during PV-charge in hour h, day d, billing period q
$E_{buybid,qdh}$	P2P Buy energy bid of hour h, day d, billing period q
E_{EOL}	Total energy throughput of BESS before reaching end-of-life
$E_{load,qdh}$	Load energy in hour h, day d, period q
$E_{P2P,qdh}$	P2P energy cleared of hour h, day d, billing period q
$E_{pv,qdh}$	PV generated energy in hour h, day d, period q
$E_{pvbid,qdh}$	P2P PV sell energy bid of hour h, day d, billing period q
$E_{through,qdh}$	Cumulative BESS energy throughput up to hour h, day d, billing period q
E_{year}	Yearly energy consumption
F	BESS loss factor
f	Horizon brightening modulating factor
F_1, F_2	Circumsolar and horizon brightening coefficients
F_{x-y}	View factors for each irradiation component
$g_k(\boldsymbol{x})$	Optimisation constraint functions (PSO)
G_T	Incident solar irradiance
$G_n^j, P_{i,n}^j$	Global and personal best positions of particle i in dimension j and iteration n (PSO)
G_o, G_{on}	Extra-terrestrial irradiance incident on a horizontal plane projected from Earth's surface and on the plane normal to propagation
G_{sc}	Solar constant (1367 W/m^2)
H	Daily global (total) irradiation on the horizontal plane
h	Hour number of day d
H_b, H_d	Daily direct and diffuse irradiation on the horizontal plane
H_o	Daily extra-terrestrial solar irradiation on a horizontal plane projected from Earth's surface
i	Particle number (PSO)
I, I_T	Hourly global (total) irradiation on the horizontal plane and a tilted plane
I_b, I_d	Hourly direct (beam) and diffuse irradiation on the horizontal plane
I_bn	Direct normal irradiation
I_o, I_{on}	Hourly extra-terrestrial solar irradiation incident on a horizontal plane projected from Earth's surface and on the plane normal to propagation
$I_{d,cs}$	Circumsolar diffuse irradiation
$I_{d,hz}$	Horizon brightening diffuse irradiation
$I_{d,iso}$	Isotropic diffuse irradiation

$I_{d,T}$	Diffuse irradiation on a tilted surface
I_{gc}, I_{dc}, I_{bnc}	Global, diffuse and direct normal clear-sky irradiation
$I_{op,qdh}$	Off-peak BESS charge/discharge control variable for hour h, day d, billing period q
$I_{pk,qdh}$	Peak BESS charge/discharge control variable for hour h, day d, billing period q
$I_{sh,qdh}$	Shoulder BESS charge/discharge control variable for hour h, day d, billing period q
J	Number of unique buy reservation prices in particular bidding hour
j, J	Particle dimension and dimensionality of the problem (PSO)
K	Number of problem constraints (PSO)
K	Number of unique sell reservation prices in particular bidding hour
K_T, k_T	Daily and hourly clearness indexes
$L_{i,n}^{j}$	Delta potential well characteristic length (QPSO)
L_{st}, L_{loc}	Longitudes of the standard meridian and the location in question
M	Particle swarm size (PSO)
m	Air mass
m	Comprehensive learning refreshing gap (CLQPSO)
M_x	BESS operation mode variable
M_{life}, M_{loc}	SRES contribution length and location multipliers
n	Day number of the year
n, N	Iteration number and maximum number of iterations (PSO)
P	Payback period
p, p_0	Mean site elevation and sea level atmospheric pressure
$P_{\max,pvbatt,q}$	Maximum power demand with a PV-BESS system
$P_{\max,q}$	Maximum power demand without a PV-BESS system
$P_{c,i}$	Learning probability of particle i (CLQPSO)
$P_{c,qdh}, P_{d,qdh}$	BESS charge and discharge permission control parameters of hour h, day d, billing period q
$p_{i,n}^{j}$	Local attractor of particle i in dimension j at iteration n (QPSO)
$P_{pv,rat}$	PV module rated power
P_{pv}	PV module output power
Q	Number of billing periods q in system lifetime
q	Billing period of year y
R^2	Coefficient of determination
R_b	Ratio of direct irradiance on a tilted plane versus the horizontal plane
r_e	Effective real electricity price growth
R_T	Ground-reflected irradiation on a tilted surface

$R_{\max}$	Maximum BESS charge/discharge rate
$R_{BUY,qdh}$	Supply and demand ratio at the final successful buy reservation price of hour h, day d, billing period q
$R_{buy,qdh}$	Supply and demand ratio for a particular P2P participant buying energy of hour h, day d, billing period q
r_{deg}	Degradation rate
r_d	Effective real discount rate per billing period
r_e	Effective real electricity price growth rate per billing period
$r_{i,n}^j, R_{i,n}^j$	Sequence of uniformly distributed random numbers (PSO)
r_{inf}	Rate of inflation
r_{nom}	Annual nominal discount rate
r_{real}	Annual real discount rate
$R_{SELL,qdh}$	Demand and supply ratio at the final successful sell reservation price of hour h, day d, billing period q
$R_{sell,qdh}$	Demand and supply ratio for a particular P2P participant selling energy of hour h, day d, billing period q
S_b	Total BESS cost
S_{pv}	PV system cost
t	Number of discounting (billing) periods per year
T_a	Ambient temperature
T_c	PV module temperature
$T_L(m)$	Linke Turbidity
$T_{\max,der,qd}$	Maximum power demand with DERs
$T_{\max}$,$T_{\min}$	Maximum and minimum daily temperatures
$T_{c,qdh}$	Moving average electricity tariff for BESS charging up to hour h, day d, billing period q
$T_{DC0,qd}, T_{DC,qd}$	Network demand charge under lowest cost and alternative plans
$T_{fit,qdh}$	PV feed-in tariff
$T_{luos,qdh}$	LUoS energy charge of hour h, day d, billing period q
T_{NOCT}	Nominal operating cell temperature
$T_{P2P,qdh}$	P2P clearing price of hour h, day d, billing period q
$T_{pv,qdh}$	PV feed-in tariff or power purchase agreement supply rate
$T_{ret0,qdh}, T_{ret,qdh}$	Retailer tariff under lowest cost and alternative plan
$T_{sc0,qd}, T_{sc,qd}$	Daily supply charge under lowest cost and alternative plans
$T_{tuos,qdh}$	TUoS energy charge of hour h, day d, billing period q
U_b	Per unit battery cost
U_{inv}	Unit inverter replacement cost (\$/W)
U_{pv}	Unit cost of PV system replacement(\$/W_p)

$v_{i,n}^{j}, x_{i,n}^{j}$	Velocity and position of particle i in dimension j & iteration n (PSO)
W_q	Maintenance cost
X	Number of batteries
$x_{\rho,j}, y_{\rho,k}$	Unique buy and sell reservation prices in a particular bidding hour
$x_{\xi,j}, y_{\xi,k}$	Cumulative energy bids up to a unique buy and sell reservation price in a particular bidding hour
y	Year number
Y_{EOL}	Cycle life
Y_{qdh}	Operational cycles at the end of hour h, day d, billing period q
$Z, Z_{\max}$	Number of PV modules and maximum number of modules permitted
AEMC	Australian Energy Market Commission
AER	Australian Energy Regulator
AMI	Advanced metering infrastructure
AREMI	Australian Renewable Energy Mapping Infrastructure
ARENA	Australian Renewable Energy Agency
BAU	Business-as-Usual
BESS	Battery energy storage system
BoM	Australian Bureau of Meteorology
BRL	Boland–Ridley–Lauret diffuse fraction model
BSRN	Baseline Surface Radiation Network+
CDF	Cumulative distribution function
CDO	Climate Data On-line
CdTe	Cadmium telluride
CER	Australian Government Clean Energy Regulator
CIGS	Copper indium gallium selenide
CPI	Combined Performance Index
CPP	Critical peak pricing
CSV	Comma-separated variable
DAP	Day-ahead pricing
DER	Distributed energy resource
DG	Distributed generation
DHI	Diffuse horizontal irradiation
DLC	Direct load control
DLT	Distributed ledger technology
DNI	Direct normal irradiation
DNSP	Distribution Network Service Provider
DR	Demand response

DS	Distributed storage
DSM	Demand-side management
DUoS	Distribution use-of-system
ESRA	European Solar Radiation Atlas
ET	Extra-terrestrial
FiT	Feed-in tariff
GEBA	Global Energy Balance Archive
GHI	Global horizontal irradiation
GW	Gigawatt
GWh	Gigawatt hour
HDKR	Hay-Davies-Klucher-Reindl
HSI	Hourly Solar Irradiance Data
ICT	Information and communications technology
IWEC2	International Weather files for Energy Calculations (Second Generation)
KSI	Kolmogorov-Smirnov Integral
kW	Gigawatt
kWh	Kilowatt hour
LCOE	Levelised cost of energy
LGC	Large-scale generation certificate
LGNC	Local general network credit
LNC	Local network charge
LRET	Large-scale Renewable Energy Target
LRMC	Long-run marginal cost
LUoS	Local use-of-service
MBE	Mean bias error
MeAPE	Median absolute percentage error
MINLP	Mixed-Integer Non-Linear Programming
MIRR	Modified internal rate of return
MMR	Mid-market rate
MW	Megawatt
MWh	Megawatt hour
NASA	National Aeronautical and Space Administration
NEM	National Electricity Market
NOCT	Nominal operating cell temperature
NPV	Net Present Value
NREL	National Renewable Energy Laboratory
NSRDB	National Solar Resource Database

NUoS	Network use-of-system
OMS	One Minute Solar Data
OVER	Relative frequency of exceedence from KSI
P2P	Peer-to-peer
PPA	Power purchase agreement
PSO	Particle swarm optimisation
PTR	Peak-time rebates
PV	Photovoltaic
QDPSO	Quantum delta potential well-based particle swarm optimisation
QPSO	Quantum-behaved particle swarm optimisation
RET	Renewable Energy Target
rMBE	Relative mean bias error
RMSE	Root mean square error
rRMSE	Relative root mean square error
RTP	Real-time pricing
SAM	System Advisor Model
SBS	Solar Bonus Scheme
SDR	Supply and demand ratio
SGSC	Smart Grid, Smart City
SoDa	Solar Radiation Data
SRES	Small-scale Renewable Energy Scheme
SSE	Surface Meteorology and Solar Energy
STC	Small-scale technology certificate
STC	Standard test conditions
TMY	Typical Meteorological Year
TOU	Time-of-use
TSS	Tariff structure statement
TUoS	Transmission use-of-system
UTC	Coordinated Universal Time
W	Watt
WMO	World Meteorological Organisation
WRDC	World Radiation Data Centre

Abstract

Advances in photovoltaic and battery energy storage system (BESS) technologies have made hybrid PV-BESS systems an attractive prospect for residential energy consumers. However, the process to select an appropriate system is non-trivial due to the relatively high cost of batteries, a multitude of available retail electricity plans, the removal of incentive schemes and the impending introduction of disruptive technologies such as peer-to-peer energy trading.

The introduction of Smart Grid technologies, particularly smart meters, enables consumers to leverage high temporal resolution energy consumption data to optimise system design based on an individual customer's circumstance. In this research, real-world energy consumption data for a large sample of homes are applied to an optimisation strategy developed to the select system size, tilt, azimuth and retail electricity plan for a residential PV-BESS based on a customer's temporal load profile. A case study examining a real world hybrid PV-BESS is presented to demonstrate the potential benefit of applying the optimisation process established in this research.

Particle swarm optimisation (PSO) is utilised as the underlying optimisation algorithm given its suitability to mixed integer non-linear programming problems, characteristic of the energy models developed in this research. To improve global search performance with minimal parameter adjustments, various forms of PSO are applied including quantum-behaved PSO and a modified version with a comprehensive learning component.

To facilitate energy yield modelling, accurate hourly solar irradiation and photovoltaic array generation models are critical to the optimisation process. Numerous models have been developed to estimate diffuse and direct irradiance components based on global irradiation measurements. The Boland–Ridley–Lauret (BRL) model consists of a single set of parameters for all global locations. There is scope to improve the BRL model to better match local climatic conditions. In this research, the Köppen-Geiger climate classification system is considered to develop a set of adjusted BRL models for Australian conditions, which are subsequently applied to the energy models developed in this research.

With the future application of peer-to-peer energy trading markets, prospective investors would benefit from prior consideration of market conditions and the penetration rates of participant PV-BESS systems when designing such systems. In this research, a lifetime assessment of PV-BESS systems is undertaken for a hypothetical peer-to-peer market of over 2,000 participants. Trader margin, participant margin, network tariff structures and PV-BESS penetration rate scenarios are considered to examine the impacts on the optimal PV-BESS design maximising the economic return.

Chapter 1

Introduction

The photovoltaic (PV) industry has undergone rapid growth over the last decade attributable to a number of factors including increased PV module efficiencies, reduced manufacturing costs, reduced installation costs and the introduction of government subsidies, rebates and other incentive schemes. Photovoltaics as a standalone system, while providing an avenue for consumers to reduce overall energy costs, introduce difficulties from network operator's perspective due to the non-scheduled generation profile exhibited by PV modules – they only produce electricity during daylight hours and energy generated is highly dependent on weather and season. To manage the fluctuating output of renewable energy sources, network and market operators are required to invest extensively to maintain grid stability and provide spinning reserve generation during periods of low solar irradiation [1]. Consequently, the magnitude of network wide photovoltaic capacity is inherently limited before cost-prohibitive network upgrades are required, potentially effecting the economic viability of PV systems.

The introduction of energy storage technologies has the potential to dramatically change the feasibility of solar and other renewable energy source contributions. Energy storage systems enable multiple objectives to be achieved. Coupled with advanced power electronics and communications, energy storage systems can provide power quality improvement roles such as voltage and frequency regulation [2] in addition to load or generation shifting functions normalising demand profiles, collectively reducing costs for both networks and consumers.

The integration of energy storage has historically been cost prohibitive. Electrical energy is difficult to store efficiently and cheaply. Large-scale energy storage in the form of pumped hydro has been utilised for many decades however the technology does not scale well and cannot be used in smaller installations or at the distribution network level. Other technologies such as flywheels, compressed air and superconducting magnetic energy storage have also been introduced, however the complexities of integration, scalability and cost limit their viability [3].

A battery energy storage system (BESS), in principle, presents a viable option at all levels of the electricity network. The technology is scalable, ranging from small residential installations to large transmission network services. Recent progress in battery research through the development of more efficient chemistries, improved manufacturing techniques

and economies of scale, is forecast to continue to reduce the cost of BESSs [4,5]. However, to operate at its maximum potential, battery storage requires a more flexible, smarter electricity network.

The Smart Grid is an evolving paradigm in electrical energy delivery, gaining significant traction in recent years. The concept involves the marriage of the electricity network with state-of-the-art information and communications technology to provide increased controllability and flexibility. One of the key enabling technologies are advanced electricity meters, referrred to as smart meters – devices that enable energy data to be captured over short time intervals in near real-time and transmitted via advanced communication networks to interested parties [6]. Additionally, smart meters facilitate the introduction of variable electricity price signals, better reflecting the true cost of electricity generation and encouraging economical energy usage.

The integration of the Smart Grid, particularly smart metering, has the potential to significantly influence the penetration of small-scale energy storage systems into the distribution network. Flexible pricing plans may allow customers to take advantage of low-cost electricity during off-peak periods to charge storage systems and discharge during peak hours when electricity cost is high. Combined with renewable energy sources such as solar to form a hybrid energy source, BESSs enable the formation of what are effectively small-scale grid-connected microgrids, providing a consumer with the flexibility to utilise on-site generation, stored energy or import energy from the grid in order to maximise electricity cost savings.

The research presented in this thesis focuses on small-scale hybrid PV-BESS systems at the residential level, investigating the numerous factors effecting photovoltaic sources coupled with energy storage to determine optimal system design and operation methodologies to maximise electricity cost savings.

The removal of government incentive schemes and the introduction of dynamic tariffs increases the complexity of the installation business case for small-scale hybrid PV-BESS systems. The findings of the 'Smart Grid, Smart City' (SGSC) project and the Grattan Institute detailed in Section 2.4 highlight the need for a comprehensive assessment tool to inform prospective investors and establish the economic efficacy of new hybrid energy systems.

A design optimisation strategy for hybrid PV-BESS systems is developed in this research. The maximisation of the net benefit achieved through reduced imported energy costs is set as the underlying objective. Within a competitive retail electricity market with various tariff structures including flat and time-of-use (TOU) tariffs, as well as the impending introduction of peer-to-peer energy trading, the most appropriate retail electricity and peer-traded energy agreements are not self-evident. The research presented in this thesis is principally focused towards leveraging high temporal resolution energy consumption data facilitated by smart meters to develop a specific consumer-centred evaluation based on influential factors such as subject location, prevailing solar irradiation and available retail electricity plans. The traditional PV installation objective aiming to maximise gross energy generation is challenged as the most cost-effective approach. Fur-

thermore, the trending popularity of residential energy storage devices has highlighted the necessity for a detailed economic assessment to establish the viability of such a system for a specific customer's applications. The ultimate objective of this research is to remove the uncertainty in system specification and retail electricity plan selection in a competitive retail market and dynamic regulatory environment.

The desire for flexibility and empowerment to choose renewable electricity sources at the consumer level has driven the introduction of collaborative economy concepts in electricity markets [7]. Electricity markets are transitioning from traditional centralised generation to decentralised structures, facilitated by the widespread introduction of distributed energy resources (DERs) such as PV and BESSs, and the introduction of other disruptive 'sharing economy' concepts popularised by companies such as Uber and AirBnB. The concept that energy can be traded between self-organised peers and groups [8], either as independent producers or community-based structures [7], is expected to be facilitated by the introduction of physical microgrids or blockchain technologies.

Peer-to-peer (P2P) trading, as a concept whereby bilateral agreements are established between two electricity peers for the exchange of electricity, is not restricted to large traditional generators and industrial consumers. The concept, through enabling soft technologies, can be applied to all levels of the network including single household consumers or prosumers, leveraging DERs such as solar PV and BESSs.

P2P research is still in its infancy with no agreement on the most efficient data sharing and processing structures or fair market designs that facilitate local energy trading. In this research, a hypothetical P2P market structure is investigated based on an auction scheme reflecting the mechanisms adopted in the Australian wholesale electricity market. The final contributions of this thesis aim to provide commentary on key factors influencing optimal DER system design associated with a potential P2P market structure to provide investment context to prospective DER investors.

1.1 Contributions of the Thesis and Claims to Originality

The research presented in this thesis spans a range of concepts including solar irradiation modelling enabling PV energy yield model development and assessment, economic analysis, BESS energy flow models and finally P2P market structures and trade settlement. The key contributions of this research and duly noted claims to originality are as follows:

- A comprehensive review of solar irradiation databases for energy yield assessment is presented for the purposes of small-scale PV system energy assessment in the context of Australia. The Climate Data On-line (CDO) database for daily data and the Australian Renewable Energy Mapping Infrastructure (AREMI) database for hourly data processed by the Australian Bureau of Meteorology (BoM) are identified as suitable references for a low-cost energy resource assessment.

- The diffuse irradiation model referred to as the Boland–Ridley–Lauret (BRL) model is improved through specific consideration of locational climatology and a rigorous

data quality control methodology, which to the author's knowledge has not been previously applied in the context of Australia. The Köppen-Geiger climate classification system is used to define Australian climate zones. New Köppen-Geiger zone BRL models are developed for each climate zone and shown to improve diffuse irradiation assessment across Australian climatologies for ground-based global irradiation measurement. For satellite-based global irradiation estimates, a new National BRL model is developed for the Australian continent and shown to out-perform the existing models used to develop the irradiation components of the AREMI database.

- While PV system design optimisation may be undertaken using many existing software platforms, widespread application of optimisation techniques at the residential consumer level using real-world high temporal resolution smart meter consumption data has not previously been investigated. The novelty of this research lies in the large sample size application of design optimisation techniques to establish market trends in different geographical and electricity network areas. The research presented in this thesis is intended to establish viability trends for PV systems in the Australian electricity market including drawing comparisons against recently installed PV systems and highlighting the economic efficacy of such systems.

- In response to the increasing penetration of residential BESSs in the Australian consumer market, the design optimisation methodology established in this research is extended to hybrid PV-BESS systems to provide an assessment of BESS viability based on a large sample of high resolution real-world consumption data.

- Given the infancy of P2P trading in an Australian context, a comprehensive and timely review of P2P energy trading projects and schemes is presented to establish key issues and concepts associated with residential PV-BESS systems participating in P2P markets.

- Finally, an expansive P2P market assessment based on real-world electricity consumption data from over 2,200 residential premises is conducted, an assessment which to the author's knowledge has not yet been undertaken at such as scale with actual smart meter data in the context of the Australian National Electricity Market (NEM). A novel assessment of PV-BESS lifetime economic performance is presented in the context of a P2P market structure with unique consideration given to system design optimisation. Recently proposed cost-reflective network tariffs developed in response to updated regulator requirements are considered for the first time under P2P trading scenarios to assess the impacts on DER design optimisation. An auction-based market structure previously considered in literature, is expanded to enable battery degradation and charge costs to be considered prior to market participation. A comprehensive sensitivity analysis is undertaken to investigate the impact on DER investment decisions and the physical characteristics of optimally designed PV-BESS systems intended for operation in a P2P trading market.

1.2 Thesis Structure

Given the wide range of concepts considered in this research, including solar irradiation modelling, battery energy flow models, optimisation strategies and algorithms and peer-to-peer energy trading concepts, with the exception of an initial background chapter and Chapter 3, relevant literature reviews are introduced at the beginning of each chapter. The remainder of this thesis is structured as follows.

Chapter 2 presents a brief review of the principles and defining aspects associated with Smart Grids with a specific focus towards smart metering. A review of the recently conducted SGSC project in Australia is presented. Motivating factors behind the research presented in this thesis are drawn from the SGSC project outcomes and observations.

Chapter 3 presents a literature review of solar irradiation modelling aspects including a summary of solar irradiation databases. Key solar irradiation modelling equations are described and a plane-of-array transposition model selected as a key component of PV energy yield modelling. The BRL model estimating diffuse irradiation components is introduced and an area for further improvement through specific consideration of climatological zones is identified. The Köppen-Geiger climate classification system is introduced, establishing the basis for the original research presented in Chapter 4.

In Chapter 4, modified versions of the BRL diffuse model used by BoM are developed based on Köppen-Geiger climate classifications to improve the accuracy of the current single national-level model. Specific models for each Köppen-Geiger climate classification zone are developed for use on ground-based global irradiation measurements. A rigorous data quality control regime is applied, with the filtered data used to develop improved BRL models proposed for use in Australian locations. For satellite-based global irradiation estimates, a new National BRL diffuse model is developed leveraging the data filtered through the extensive quality control tests considered in this research.

Chapter 5 describes the PV energy yield and economic models and other financial metrics assumed in this research. The central optimisation problem to maximise the economic benefit to a prospective investor is defined. A particle swarm optimisation algorithm using a penalty function and a hypercube nearest vertex approach to handle constraints is defined and applied to solve the optimisation problem. The efficacy of the optimisation methodology is demonstrated on a small selection of real-world consumer data from the SGSC project before a wider extension to a large number of customers in different geographic regions of Australia.

Chapter 6 describes the battery energy flow and lifetime operation models developed for this research. The optimisation problem previously defined for a standalone PV system is modified for a hybrid PV-BESS system. The methodology is applied to two commercially available residential energy storage systems investigated for 100 real customers to demonstrate the viability of the PV-BESS systems against a particular customer's energy circumstances.

Chapter 7 presents a case study for the application of the optimisation methodology against a real-world hybrid PV-BESS system. The output of the PV energy yield model is compared against measured PV energy to establish the model accuracy. A hypothetical

system is modelled to establish the potential investment opportunities had an optimised system been considered prior to installation.

Chapter 8 investigates the influence on PV-BESS system design optimisation in the context of a P2P energy trading market. A hypothetical market structure is established based on mechanisms presented in literature and a large pool of over 2,200 residential participants leveraging smart meter data from the SGSC project. Revised energy flow, energy bidding and reservation price models are developed and simulated over a 20-year market horizon under various market cases based on PV-BESS market penetration rate scenarios, expected profit margins and network tariff structures among other considerations. Design optimisation is undertaken for a sample of 100 customers under numerous scenarios to investigate the viability and design characteristics of PV-BESS systems intending to engage in a P2P trading market.

Finally, Chapter 9 presents a summary of research conclusions and potential areas for future work are identified.

1.3 Associated Publications

Principal Author

J. Every, L. Li, D. G. Dorrell, "Leveraging smart meter data for economic optimization of residential photovoltaics under existing tariff structures and incentive schemes," *Applied Energy*, vol. 201, pp. 158–173, 2017

J. P. Every, L. Li, D. G. Dorrell, "Köppen-Geiger Climate Classification Adjustment of the BRL Diffuse Irradiation Model for Australian Locations," *Renewable Energy*, vol. 147, pp. 2453–2469, 2020

J. P. Every, L. Li, D. G. Dorrell, "Distributed Energy Resource Design Optimisation for Peer-to-Peer Energy Trading," *Manuscript submitted to Renewable and Sustainable Energy Reviews*, 2020

J. Every, L. Li, Y. G. Guo, D. G. Dorrell, "Maximizing investment value of small-scale PV in a smart grid environment," in *2016 IEEE International Conference on Renewable Energy Research and Applications (ICRERA)*, Birmingham, United Kingdom, Conference Proceedings, pp. 385–390

J. Every, L. Li, D. G. Dorrell, "Optimal selection of small-scale hybrid PV-battery systems to maximize economic benefit based on temporal load data," in *2017 12th IEEE Conference on Industrial Electronics and Applications (ICIEA)*, Conference Proceedings, pp. 471–476

J. Every, L. Li, D. G. Dorrell, "Economic optimization of hybrid PV-battery systems using hourly satellite insolation and daily temperature data: A case study," in *2017 20th International Conference on Electrical Machines and Systems (ICEMS)*, Conference Proceedings, pp. 1–6

Contributing Author

A. Khademlahashy, L. Li, J. Every, J. Zhu, "A review on protection issues in micro-grids embedded with distribution generations," in *2017 12th IEEE Conference on Industrial Electronics and Applications (ICIEA)*, Conference Proceedings, pp. 913–918.

Chapter 2

Background

Smart Grid technologies provide a wide range of services designed to achieve the primary objectives of improving electrical network stability, reliability and energy delivery efficiency. To provide context towards the research presented in this thesis, general aspects and introductory terms associated with Smart Grid technologies and DERs are presented in this chapter as a prelude to the deeper literature reviews and original research undertaken in subsequent chapters. A review of the SGSC project as a wide-scale Smart Grid technology assessment within the Australian NEM is presented. The chapter concludes with a summary of the motivating factors behind the research presented in this thesis.

2.1 The Smart Grid

The Smart Grid is an evolving paradigm associated with the integration of innovative control, monitoring and communication technologies into the electricity network. The primary objectives of Smart Grids are to improve energy efficiency, security and reliability while increasing the integration of renewable energy [9]. Smart Grids rely on advanced programs and algorithms installed in smart devices at all levels of the electricity network; from generation and transmission, through to the distribution network and end consumers; combined with an extensive communications network to achieve the following core applications [9]:

1. Volt and Var control
2. Fault detection, isolation and restoration
3. Wide area monitoring, protection and control
4. Demand response (DR)
5. Distributed generation (DG)

Advanced control devices have long been employed by utilities to dispatch and control large-scale generators based on fluctuating electricity spot market prices and manage power flow through the transmission network. However, the penetration of Smart Grid

technologies into the distribution network and ultimately the end user is, as described by Feng et al., the "last frontier of power system modernisation" [9].

Residential customers, in contrast to industrial and commercial customers, generally have more flexibility regarding their energy usage behaviours [1]. Therefore residential customers form a user group with significant potential to influence grid-wide energy usage to create a more efficient and reliable Smart Grid.

DR and DG are the two Smart Grid applications most directly applicable to the distribution network and ultimately present the greatest potential for end-customer engagement and influence. Participation in DR and integration of DG at the residential level are the key Smart Grid focus areas for this research.

2.1.1 Demand Response

Electricity utilities must constantly balance load with available dispatchable generation in order to maintain grid stability. DR programs provide an extra degree of freedom to achieve this balance as they allow the utility and/or customer to time shift or curtail load without the need for additional generation capacity. DR is a mid-point solution between manipulating energy demand through the electricity price spot market and instigating emergency load shedding [9].

DR programs fall into two broad categories – incentive-based DR and price responsive DR [9]. Incentive-based DR programs have been leveraged by utilities for decades [9]. Programs such as direct load control (DLC), aim to shift operation of energy demanding appliances such as hot water systems to off-peak hours. In these applications, customer inconvenience is compensated through credits on energy bills or reduced energy tariffs.

Another incentive-based DR program relates to interruptible/curtailable load and emergency demand reduction where customers act as a virtual spinning reserve [10]. Under these programs, requests to reduce demand are sent to customers. In contrast to DLC, these requests are not compulsory but the customer may incur penalties for non-conformances.

Price responsive DR is gaining increased attention through the opportunities presented by the transition to the Smart Grid [9]. As advanced metering infrastructure (AMI) becomes increasingly integrated into the electricity network, the cost of transmitting price signals reduces, enabling price responsive DR to become one of the most effective DR programs [6].

Customers are not restricted by the contractual obligations that are a feature of incentive-based DR. Therefore price responsive DR is also referred to as voluntary DR [9]. Under these programs, utilities provide dynamic pricing signals to customers, encouraging them to reduce demand during peak hours and shift load to off-peak hours. In situations where loads cannot be shifted without a certain degree of inconvenience, such as entertainment systems or cooking appliances, price signalling motivates the customer to purchase energy efficient appliances.

The potential collective economic benefits to both the utility and the customer through price responsive DR and advanced forms of DLC enabled by home automation networks

are key drivers for the Smart Grid [9]. However, the implementation of price responsive DR is only possible through AMI and the introduction of intelligent metering devices known as smart meters.

Demand Response in the form of price responsive PV and BESS systems is investigated in Chapters 5 to 8 to assess the influence on optimal PV and BESS system design. Smart meters, as a key enabling DR technology, are leveraged. A description of smart meters and their market penetration is provided in Section 2.1.2.

2.1.2 Smart Meters

Traditional electro-mechanical energy meters measure cumulative energy consumption and are usually read by technicians periodically, typically on a quarterly basis for residential or small business consumers. Consequently, traditional meters can only provide information on total energy usage, not the time during which the energy was consumed.

Smart meters are advanced electronic energy meters capable of measuring electricity consumption in real-time and providing bi-directional communication between the utility and the customer [11–13]. Smart meters are an integral component of the future Smart Grid paradigm and electricity utilities are progressively integrating them into their networks [14, 15].

High temporal resolution energy consumption data available through smart meters are leveraged in Chapters 5 to 8 to facilitate design optimisation of PV and BESS systems as a core input to the original research presented in this thesis. The subsequent subsections provide additional background and context around smart meter integration and common energy pricing mechanisms available through smart meter deployment.

2.1.2.1 Smart Meter Deployment

Smart meters have been rapidly adopted by numerous countries in the last 5 to 10 years with many undertaking aggressive rollout plans. The single largest smart meter integrator is China which, by the end of 2013, had installed 250 million smart meters, accounting for 62% of households [16]. The bullish adoption of smart meters in China was projected to continue, with a penetration target of 95% by the end of 2018 [16].

In 2013, the Council of European Energy Regulators published a report detailing the current rollout status of smart meters in European member countries [15]. The report determined that two countries had completed their rollout (Sweden 100% and Italy 95%), Finland would reach its 80% target by the end of 2013 and thirteen others were currently rolling out or intending to rollout smart meters with penetration rates of at least 80% [15]. In the UK, a program to roll-out 50 million smart meters by 2020 was adopted with the majority of customers beginning to receive smart meters from 2016 [17].

In North America, the United States has invested in numerous Smart Grid AMI projects under funding provided by the American Recovery and Reinvestment Act 2009. As of March 2013, a total of 14.2 million smart meters had been installed through the various AMI projects [18] to give a total installation base of 46 million (accounting for

40% of households) [16]. By the end of 2015, 65 million smart meters were projected to be installed in the United States [18].

In Australia, the widest deployment of smart meters was instigated by the Victorian State Government through its 2006 mandate to install smart meters in every Victorian residence and small business [19]. By early 2014, 2.8 million smart meters had been installed in Victorian premises [14].

2.1.2.2 Pricing Strategies

Traditional pricing strategies structured for traditional electromechanical meters involve a single fixed, or 'all-in', rate for all energy consumption [20]. Traditional flat or 'incremental block' rates do not reflect the true cost of energy, but are a reflection of the expected average cost of electricity generation [6] and the proportion of the network long-run marginal cost (LRMC) [21] over a billing period. As a result, the fluctuating demand that is a defining feature of the electricity network is not transparent to the consumer and the quarterly bill provides little feedback and incentive to change energy usage patterns [1].

Smart meters allow the introduction of alternate energy pricing strategies involving cost reflective dynamic tariffs [1, 6]. The primary objective of dynamic pricing is to encourage customers to shift a percentage of load from peak to off-peak hours to produce a levelised demand profile throughout the day. As detailed in Section 2.1, dynamic pricing strategies are therefore a form of voluntary DR. Examples of various pricing strategies are provided in Figure 2.1 and subsequently discussed in the remainder of this section.

2.1.2.3 Time-of-Use Pricing

TOU pricing involves dividing the day into two or more time periods and setting prices for each period [20]. Rudimentary TOU pricing has been used by utilities for many years in the form of separate metering circuits for off-peak hot water systems and other limited applications. However, generally the term TOU pricing refers to a more flexible strategy whereby all appliances are subject to the time-based rates and therefore able to participate in price responsive DR.

TOU strategies include different rates for peak, off-peak and shoulder periods. Typically, peak periods are in the morning and evening, off-peak are late at night and early morning, while shoulder periods may be any period in between. Figure 2.1 presents a simple example of a TOU strategy with three price levels. A TOU strategy may also include different pricing periods for weekdays and weekends, as well as seasonal pricing, to allow for the different demand profiles over these days.

The influence on optimal DER design characteristics of TOU pricing mechanisms is investigated in Chapters 5 to 8.

2.1.2.4 Critical Peak Pricing

Critical peak pricing (CPP) is a pricing strategy that aims to better reflect the true cost of power generation under extreme operating scenarios [20]. CPP is a variation on TOU,

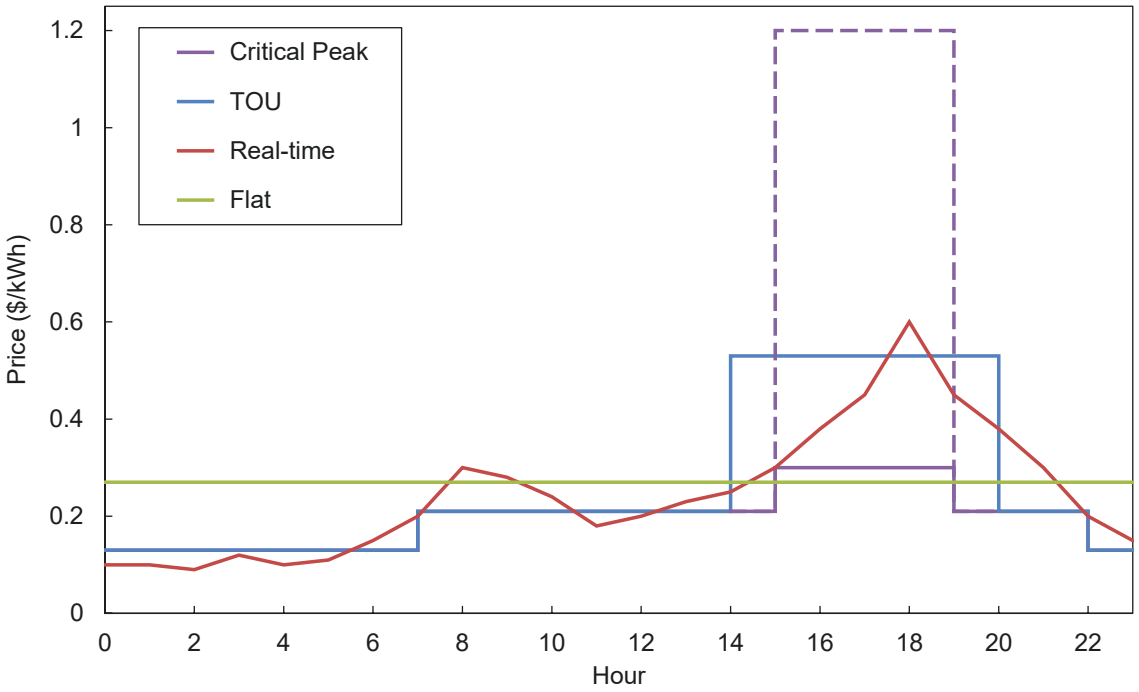

Figure 2.1: Electricity dynamic pricing strategies

as shown in Figure 2.1 where customers are subjected to energy prices that may be 5 to 10 times higher [6] than the base peak rate. CPP periods occur on the few days per year where network demand is at its highest [20]. Customers are notified a day in advance before a critical day will take place.

Another concept closely related to CPP is known as a peak-time rebate (PTR) [20]. In the United States, particularly in California, utilities offer PTR in the form of Demand Bidding Programs [22]. Under these programs, the customer receives a rebate for reducing consumption by the bid amount during critical peaks.

However, in an Australian context CPP is not typically applied, particularly at the residential consumer level.

2.1.2.5 Real-Time Pricing

Real-time pricing (RTP) reflects the temporal variation of electricity prices throughout the day as energy demand fluctuates. While it is a more accurate reflection of the wholesale electricity market prices [20,23,24], RTP cannot be easily predicted or understood by small-scale customers [6]. Under RTP, price signals are released an hour or day ahead [20, 24] (whereby it is also known as Day-ahead Pricing (DAP)) to customers, enabling them to identify periods of increased prices and adjust their consumption patterns accordingly.

Similar to CPP, RTP has not yet been adopted in Australia at the residential consumer level. However, RTP in the form of real-time energy bids and settlement is investigated in Chapter 8 as part of a design optimisation strategy in the presence of hypothetical P2P energy markets.

2.2 Distributed Generation

DG, also referred to as embedded generation, typically involves small-scale generation installed within a customer's private network or embedded in the distribution network, rather than the transmission network [9]. DG challenges the traditional network architecture where electricity is produced by large centralised generators and flows in a single direction to load centres [6]. Instead, DG forces the electricity network to become 'bi-directional' as the network must allow power flow both to and from load centres [6]. Integrating DG seamlessly and reliably is one of the key challenges and drivers for the Smart Grid.

DG has significant potential to reduce network congestion, particularly at the transmission level, by enabling generation self-sufficiency within localised networks zones [6, 9]. Numerous experts have studied the economic implications of adopting a less centralised network architecture with many concluding that substantial cost savings can be achieved through reduced transmission infrastructure capital expenditure [6].

However the advantages of DG must first overcome significant hurdles before viability can be achieved. Not only does DG rely on system wide technology upgrades, extensive regulatory reform must also be undertaken to increase the liberalisation of the energy market, enabling small-scale generators to participate effectively [6, 9].

DG consists of a variety of technologies and energy sources [9, 25] including:

- PV
- Small wind turbines
- Fuel Cells
- Microturbines
- Combined Cooling, Heat and Power

For the purposes of this research, DG in the form PV is investigated, establishing design and operating philosophies and relationships to enable optimal PV participation in a Smart Grid environment.

The fundamental principles and modelling techniques for PV panels are presented in Chapter 5 along with the contextual background and the intended scope of this research from a DG perspective. However, preliminary motivating factors for this research stemming from recent Smart Grid trials and studies are first presented in Section 2.4.

2.3 Distributed Storage

Distributed storage (DS) in many ways fulfils a similar role to DG in a Smart Grid environment [6]. During particular periods of the day or for certain seasons of the year, DS can supplement the main grid or other DG sources to meet demand while providing other ancillary services associated with improving power quality. However, unlike DG, the net

energy contribution to the network through DS is zero (or more precisely, slightly negative due to charge/discharge inefficiencies). Therefore, DS primarily performs an energy arbitrage or load shifting role [3] in addition to other ancillary services such as voltage regulation and frequency support.

DS, and to a lesser extent DG and DR, are considered disruptive technologies, as the need to maintain an immediate balance with traditional large-scale generators is reduced or removed entirely [6]. DS, DG and DR programs can be dispatched to perform a load following application, enabling central generators to maintain relatively continuous operation.

With extensive DS penetration levels, the need to maintain the electricity network to cater for pronounced peak periods is greatly reduced. At the greatest extreme, the network need only be constructed and maintained to provide sufficient energy to ensure the energy storage devices can be charged [6].

There are numerous energy storage system technologies available, with varying degrees of efficiency, practicality and fields of application. Some technologies are more suited to larger scale applications while others may be implemented at all levels of the grid. The following energy storage systems may be applied in a DS context:

- Pumped Hydro
- Flywheels
- Superconducting Magnetic Energy Storage
- Compressed Air Energy Storage
- Fuel Cells
- Electrochemical Energy Storage

At the small-scale customer level of the electricity network, fuel cells and electrochemical energy storage in the form of batteries present the greatest opportunity for DS deployment. In this research, electrochemical energy storage in the form of a BESS is investigated.

DG and DS are often collectively referred to as DERs [26], as introduced in Chapter 1. The term DER hereafter refers to either DG, DS or a combination of both. Design optimisation of DS is first investigated in Chapter 6 and expanded to a real-world case study in Chapter 7. Finally, design optimisation of DS for utilisation in P2P energy trading markets is investigated in Chapter 8.

2.4 Smart Grid Trials

Smart Grid trials have been implemented by numerous electrical utilities and research organisations in many countries around the world [13]. The United States, France, UK European Union, Japan and South Korea collectively invested US$3.2 billion in Smart Grid development programs between 2013 and 2015 [13]. China's nation building 'Strong

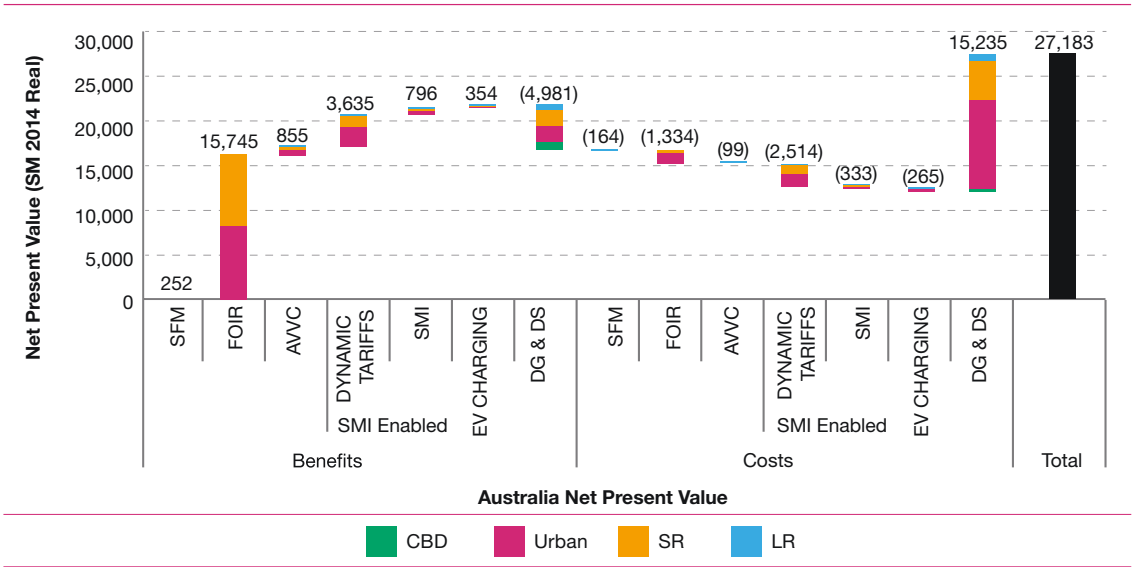

Figure 2.2: NPV analysis for national application of Smart Grid technologies in Australia under a medium macro-economic scenario until 2034. Source: Arup [1]

and Smart Grid Program' greatly out-scales other world programs with investment funding totalling $100 billion through to 2020 [13]. However the 'Strong and Smart Grid Program' is more aligned with the development of new traditional network infrastructure as opposed to a pure Smart Grid architecture.

The Australian Government initiated SGSC project was one of the largest and widest ranging Smart Grid technology trials to have been conducted in the world to date [1]. Ausgrid, owner and operator of one of the largest distribution networks in Australia on a customer basis, was selected to facilitate the trial and provided with $100 million in funding from the Australian Government. Through Ausgrid and its consortium of consultant, research and technology partners, a total of $490 million was invested to complete the program [1].

Beginning in 2010 and ending in 2013, the trial was divided into numerous work-streams including common platforms (focusing on communication technology and data management), grid applications, customer applications, DG/DS and Electric Vehicles. Of particular interest to this research are the key findings and recommendations associated with the customer applications, DG and DS workstreams.

For all Smart Grid technologies implemented as part of the trial, a net present value (NPV) assessment was conducted by extrapolating the results from the trial base to forecast the potential benefits and costs at a national level. Ultimately, the trial results indicated that implementing the full range of Smart Grid technologies at all levels of the electricity network would result in a net benefit of between $9.5 billion and $28.5 billion over 20 years depending on the macro-economic scenario considered [1, 13]. The NPV analysis under the medium macro-economic scenario is shown in Figure 2.2.

The SGSC trial data are leveraged as a key input to the analysis and original research presented in this thesis. The DER design optimisation investigations presented in Chapters 5, 6 and 8 utilise the data gathered from thousands of real Australian residences.

2.4.1 Customer Applications Findings

The customer applications workstream tested different methods of interacting with customers to determine if behavioural practices could be influenced through the introduction of empowering feedback technologies. To implement the workstream, just over 17,000 smart meters were installed in individual homes in rural and urban networks within New South Wales [1]. To test the effectiveness of Smart Grid technologies, a number of different electricity plans and products were made available to the participating customers. In some instances, customers kept their existing fixed rate electricity plans commonly associated with the traditional grid, while other customers were switched to alternative plans with dynamic tariffs. Under these plans, customers were offered a number of different products including in-home displays, online appliance control, sub-circuit metering devices, interruptible air-conditioning rebates and a dynamic peak rebate [1].

As part of the trial, a survey of the participating customers was conducted to gauge their personal level of engagement. As Figure 2.3 shows, most customers reported changes to their daily routine with 50% reporting they continued to maintain all their behavioural changes six to eight months after the trial [1]. Of the potential behavioural changes to be achieved through the development of the Smart Grid, participation in peak events is considered to be of primary importance to justify Smart Grid development. Based on the post-trial survey results, 87% of customers reported participating while 66% reported lasting behavioural changes [1]. The results of the survey results clearly indicate a willingness to engage with dynamic peak pricing and peak rebates in an effort to reduce their electricity bills.

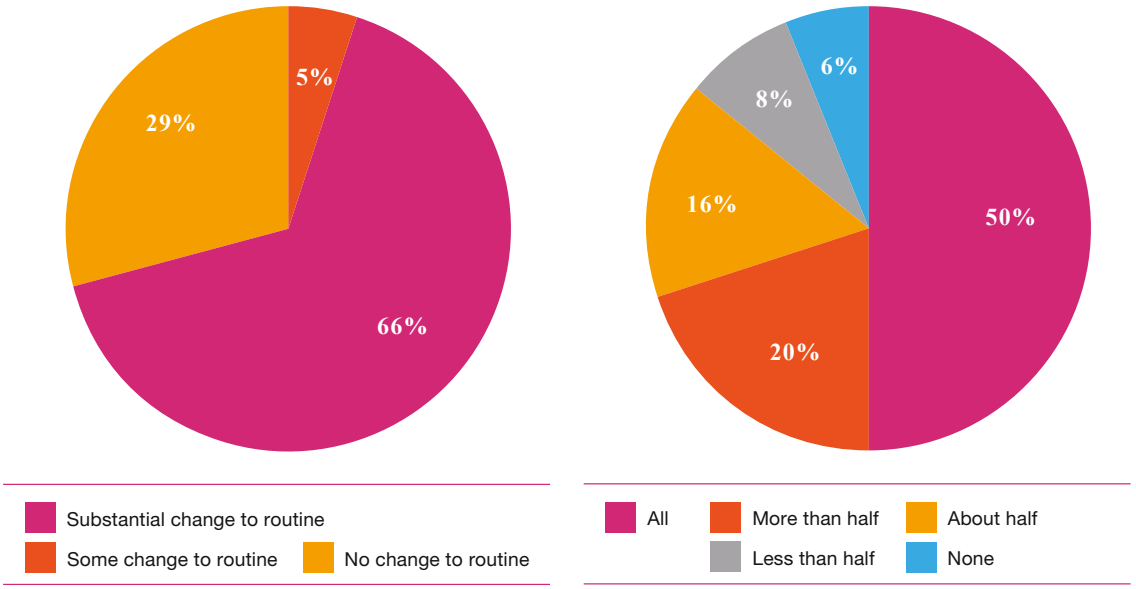

Figure 2.3: Proportion of customers reporting behavioural changes during the trial (left). Proportion of customers reporting maintained behavioural changes 6-8 months after the trial (right). Source: Arup [1]

2.4.2 Smart Meter Infrastructure Findings

The national benefits of smart metering infrastructure rollout were assessed as part of the trial. Two scenarios were considered for the rollout of smart meters. The first considered deployment of smart meters as a stand-alone technology group. The second considered the rollout of smart meters and AMI in a Smart Grid environment with features such as dynamic pricing plans and remote control of appliances. Within the stand-alone scenario, two different deployment strategies were modelled – mandated full deployment and customer-led voluntary deployment. The results of the cost-benefit analysis suggested that a mandated full deployment of smart meters without other Smart Grid features was not economically efficient in 2014 [1, 13]. This conclusion is supported by a cost-benefit analysis conducted for the mandated separate rollout of smart meters in Victoria [19].

In contrast to the stand-alone deployment, the SGSC cost-benefit analysis concluded that there was a strong business case to immediately deploy dynamic tariffs, feedback technologies and AMI [1]. An analysis of the potential smart meter integration dynamics, presented in Figure 2.4, suggested that by 2024, organic customer-led smart meter growth would reach a saturating penetration level to justify full-deployment beyond 2024 [1].

2.4.3 Distributed Generation and Storage Findings

Under the SGSC trial, almost 500 homes with existing PV systems were selected to participate in the program to determine the impact of DG on the future electricity network. In addition, other DG technologies including ten 2.4 kW wind turbines and 25 1.5 kW solid oxide fuel cells were also installed at a number of residences [13]. To provide data for a cost-benefit assessment of DS, 60 Redflow 10 kWh zinc-bromide flow batteries were also installed [13].

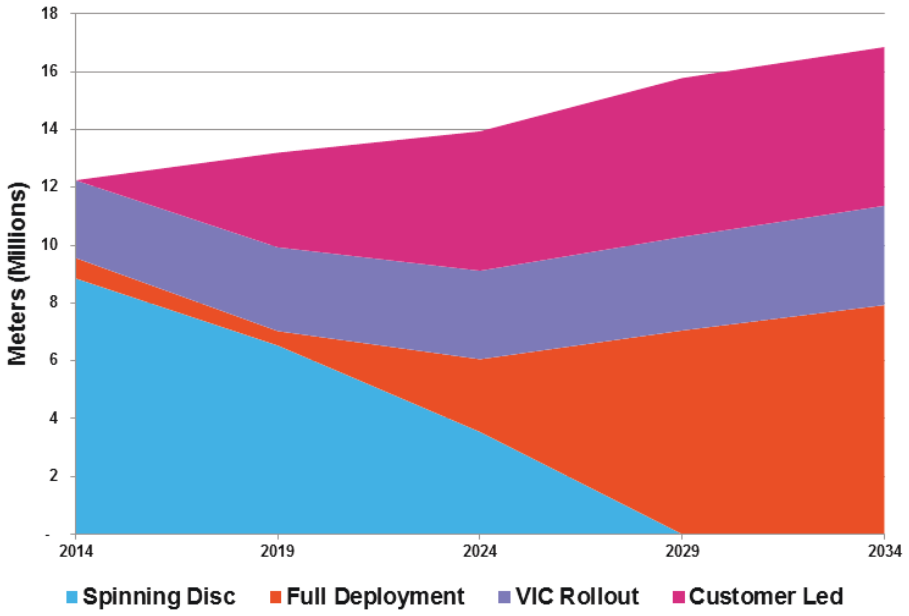

Figure 2.4: Expected change in smart meter penetration over time as a stand-alone technology. Source: Arup [1]

The results of the national cost-benefit assessment found that the primary benefit of introducing the Smart Grid in relation to DG and DS is a reduction in capital expenditure by limiting unnecessary deployment and over-sizing of DG systems. The net benefit of introduced Smart Grid technologies when applied to DG and DS is shown in Figure 2.5; where the reduction is capital expenditure can be seen to be clearly significant. The study found that under the business-as-usual (BAU) case with fixed electricity tariffs, customers are incentivised to install larger systems, with the other customers effectively providing a cross-subsidy for the PV owners' electricity costs. Under the BAU case, the degree of cross-subsidisation was predicted to continue to increase through to 2034.

In a Smart Grid environment, it was found that PV would still continue to grow in Australia, however the average system size would immediately reduce for new systems. The reduction in system size is primarily due to the application of cost-reflective dynamic tariffs that effectively remove the cross-subsidies from other customers. However, it was noted that if PV efficiencies increased and installation costs decreased at greater rates than assumed, then PV systems sizes and uptake rates would still increase in the future.

Limited useful data could be obtained for DS due to technical issues encountered, stemming from a lack of technology maturity, installation limitations and delayed deployment [13]. Consequently, analysis of DS integration in a future Smart Grid scenario reverted to the well-established lead-acid technology. The cost-benefit analysis of DS found that DS was unlikely to be deployed through to 2034 if the BAU fixed tariff structures were retained. However, if the Smart Grid topology was adopted and dynamic tariffs employed, DS was likely to see justifiable deployment beyond 2024 [1].

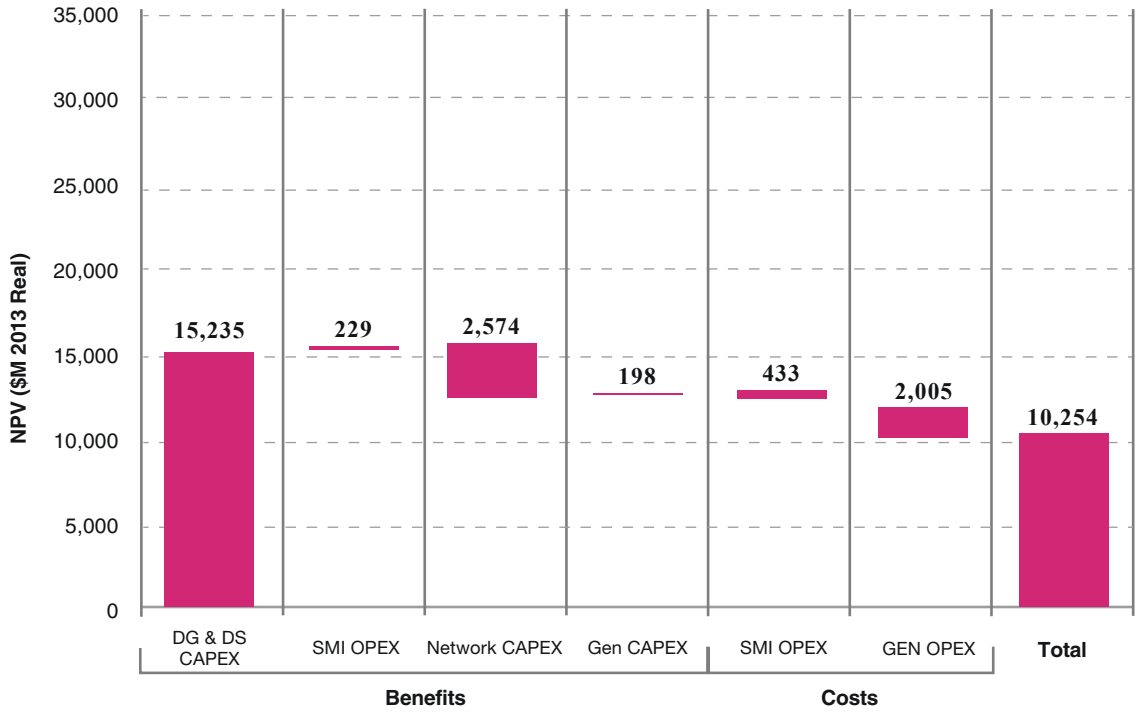

Figure 2.5: NPV assessment of DG and DS in a Smart Grid environment under a medium macro-economic scenario. Source: Arup [1]

2.4.4 Comparison of SGSC Findings to Other Literature

The results of the SGSC trial are largely supported by statements made in other literature. The merits of dynamic tariffs have been reviewed for many years and are largely seen as a step in the right direction for energy reform [6, 20, 27]. Additionally, the difficulties in integrating DG, particularly PV, at large penetration levels without burdening the existing network are well known [6, 28, 29].

A report published by the Grattan Institute investigated the policy and regulatory changes required to ensure PV DERs is adopted efficiently, providing a net positive benefit to the Australian economy [29]. The report found that under existing tariff structures, PV ownership is still a good investment, even after the closure of the small-scale renewable energy scheme (SRES) introduced in Australia between 2008 and 2011, and the removal of the generous feed-in tariff structures that at their peak, offered up to 60 cents/kWh. A the time of the report, the feed-in tariffs in Australia between 6–8 cents/kWh were deemed to represent a more realistic figure of energy production costs when compared with other large-scale sources [29]. However, a reduction in excessive feed-in tariffs was found to be only part of the necessary changes to ensure a fair electricity policy.

The Grattan Institute found that existing tariffs are poorly structured as they are currently based around total energy consumption rather than peak demand [27]. The electricity network must be designed and operated for peak load and whle average energy consumption may be declining [29], without a coincident reduction in peak demand, cost savings from reduced network infrastructure capital expenditure cannot materialise. Due to the general misalignment between peak generation and peak load, PV ownership does little to reduce peak demand on the electricity grid. Traditional network tariffs, at the time designed to reflect the average cost to deliver electricity to customers, are designed to cover the costs of network infrastructure. As PV owners contribute very little to the reduction in peak demand but reduce potential utility revenue, the current tariff structures were found to unfairly disadvantage non-PV owners [29]. Therefore the findings of the Grattan Institute in relation to energy tariff reform strongly correlate with the observations of the 'Smart Grid, Smart City' cost-benefit analysis, indicating that a cross-subsidy exists from non-PV owners to PV owners.

The Grattan Institute found that dynamic tariffs will make solar ownership less attractive at the scale currently implemented on average in Australia. Figure 2.6 and Figure 2.7 show cost-benefit assessments of PV ownership for residential houses in major Australian cities; firstly under existing tariff structures (Figure 2.6) and secondly under a Smart Grid environment with dynamic demand tariffs (Figure 2.7). The analysis clearly shows PV ownership would not be economically viable with the dynamic tariffs assumed in the study. However, the Gratten Institute also noted that a relative small reduction in system costs would again swing PV ownership into a net benefit situation for a number of Australian cities [29]. The analysis presented by the Grattan Institute again generally reflects the SGSC findings that inefficient DG capital expenditure will reduce in a Smart Grid environment, providing a net positive benefit to the national economy.

However, the Grattan Institute also observed that the situation would change with

the introduction of DS [29]. Under a Smart Grid scenario with dynamic tariffs, it was determined that energy storage systems would find economically viable deployment far sooner than under existing fixed tariff structures as shown in Figure 2.8.

Remark 2.1 *It should be noted that the system cost reductions identified in [29] as required to move PV ownership into a net benefit position have since eventuated with PV system costs continuing to falling below historical projections consistently over the last five years.*

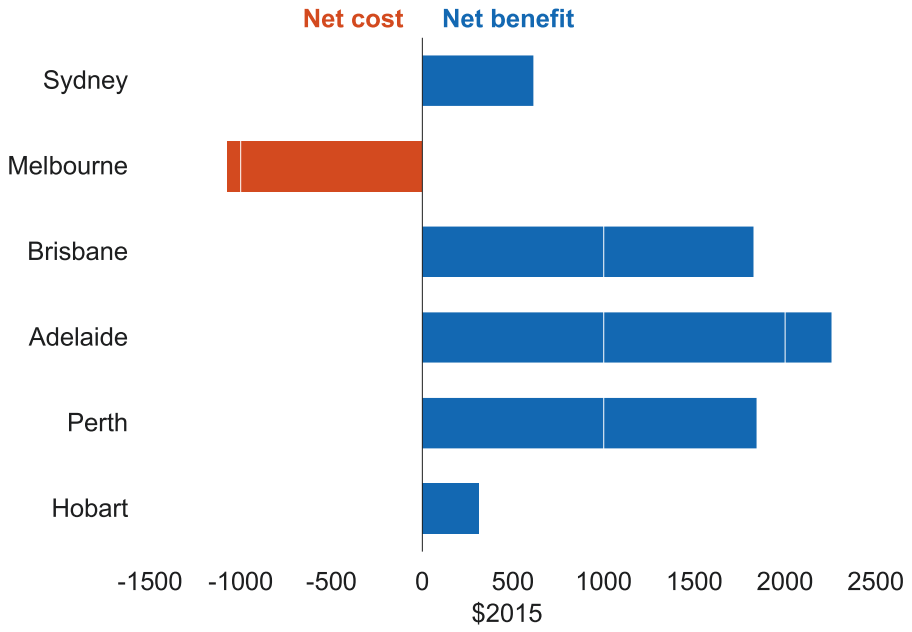

Figure 2.6: Cost-benefit assessment of a 3 kW PV system under existing tariff structures. Source: Wood et al. [29]

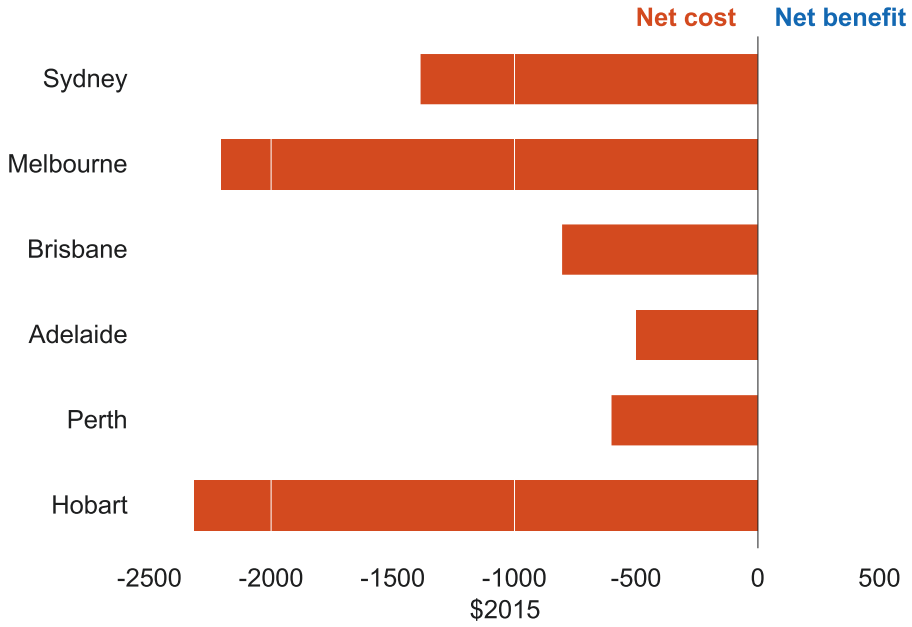

Figure 2.7: Cost-benefit assessment of a 3 kW PV system under under a demand tariff. Source: Wood et al. [29]

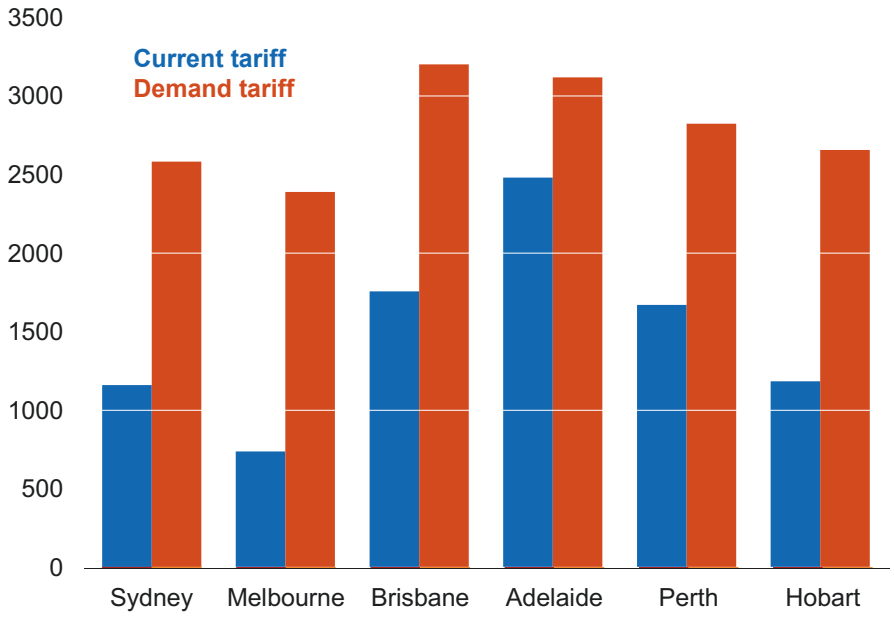

Figure 2.8: Break-even installed price of a 7 kWh battery for a house with 3 kW of PV installed. Source: Wood et al. [29]

2.5 Motivation for Research

On face value, the reports published by the Grattan Institute and the cost-benefit analyses conducted for the Victorian smart meter roll-out and the Ausgrid facilitated SGSC trial, suggest that DERs are likely to face significant challenges in a Smart Grid environment from an Australian perspective. The results highlight aspects associated with the paradigm shift towards adopting the Smart Grid and the difficulties in determining economically efficient energy policies.

However, the results of the SGSC trial and the recommendations published in current literature indicate there will be an ongoing need for comprehensive and reasoned decision making tools to ensure DERs are integrated to their maximum potential. From a system owner's perspective, the merits of DERs are not intuitive in a complex dynamic operating scenario that is highly dependent on installation location, electricity tariff policies and future technology options available.

Furthermore, analyses presented in Section 2.4 are broad brush and exclude the potential for certain installations to benefit from a detailed and accurate assessment of an optimal DER installation. In principle, DG and DS both have justifiable deployment in a Smart Grid context. The fundamental question is, when is the tipping point reached and what are the contributing factors that drive the decision process?

This research aims to present a clear picture of the interdependencies between the technological constraints of DERs and future proposed regulatory frameworks and electricity tariffs in a Smart Grid environment.

Chapter 3

Solar Irradiation Literature Review

KNOWLEDGE of site-specific solar irradiation is essential when determining the energy yield capability of a photovoltaic system. Numerous solar irradiation databases are available providing access to monthly, daily, hourly and in some cases, sub-hourly irradiation data. However, most databases are geographically limited, with coverage in South-east Asia and the Pacific Region (including Australia) unavailable in many databases. In this chapter, a literature review is undertaken of solar irradiation databases with a particular focus on Australian applications. The AREMI spatial mapping platform, providing access to hourly data captured by BoM is identified as a suitable, low cost source of hourly solar irradiation for solar PV modelling purposes.

To determine the solar irradiation received on a given plane on the Earth's surface, knowledge of the Earth's orbit around the Sun is required. As planetary motion is predictable, the Sun's apparent position in the sky at any arbitrary time throughout the year can be accurately established. Knowledge of solar geometry when coupled with knowledge of the incident solar irradiation from either ground-based measurement or satellite-derived estimates enables the estimation of solar irradiation on inclined surfaces.

Solar irradiation incident on horizontal surfaces, may be classified at the fundamental level as either direct or diffuse. Accurate knowledge of the proportion each component contributes to global (total) incident irradiation is critical for an accurate resource assessment. Numerous models have been developed to describe diffuse components, a summary of which is presented in this chapter. One such model, referred to as the BRL model has been shown to be one of the more accurate models for Australian based applications. An adjusted version of the BRL model has been implemented by BoM for use as part of its hourly satellite irradiation service specific to Australian locations. However, the adjusted model, similar to the original BRL model, does not take into account the large climatic diversity of the Australian continent.

A description of the BRL model is provided and an area for further improvement through specific consideration of climatological zones is identified. The Köppen-Geiger climate classification system is introduced along with a review of data quality methodologies, establishing the basis for the original research presented in Chapter 4.

Finally, to enable the estimation of solar PV energy generation, as a central component of the research presented in this thesis, models for the transposition of solar irradiation on a horizontal plane to irradiation on a tilted surface are reviewed. A single model is identified for the research applications presented in subsequent chapters.

3.1 Solar Irradiation Databases

A number of solar irradiation databases are available using either ground-based measurement or satellite-based estimates or a combination of both. While ground-based observations are considered to be the most accurate form of measurement at a specific location, geographic coverage of ground-based measurements is limited due to high installation and operation costs of high accuracy solar irradiation monitoring stations.

For locations further than 30 km from ground-based stations, satellite-based estimates have been shown to be more accurate [30]. Current generation geostationary meteorological satellites offer temporal resolutions up to 15 minutes and spatial resolutions down to 1 km grid cells [31]. In addition, solar irradiation models for satellite-based observations are becoming increasingly sophisticated, taking into account aerosol properties, water vapour content and ozone local to the satellite observation. Consequently, satellite solar irradiation databases form an integral component of the methodology to establish the solar energy resource at arbitrary locations.

A summary of a number of available databases consisting of ground-based and satellite-based estimates are further discussed in Section 3.1.1 and Section 3.1.2 respectively.

3.1.1 Ground-Based Solar Irradiation Databases

The Global Energy Balance Archive (GEBA) maintained by ETH Zurich [32] and the World Radiation Data Centre (WRDC) of the World Meteorological Organisation (WMO) [33] manage solar irradiation data from two of the largest networks of ground-based solar irradiation measurement sites. GEBA consists of a network of approximately 2,500 contributing stations [34] (although multi-year records enabling representative climatologies to be established have only been gathererd for around 760 stations [34, 35]) while the WRDC includes over 1,000 contributing stations [31, 36]. Daily sums and monthly sums and means are available in the WRDC from 1964 until the present [33], while only monthly means are stored in GEBA from 1950 (only a few stations) until 1990 for most locations [37].

Meteonorm is a software platform enabling the generation of representative climatology data for any location on Earth [35,38]. The software utilises a database of ground station derived average monthly data from sources including GEBA, WMO and the National Climatic Data Center (USA), as well as satellite data where spatial coverage is deemed insufficient. The satellite component of Meteonorm is further discussed in Section 3.1.2. The software uses a three dimensional inverse distance model to interpolate irradiation and weather data for any location [38]. As the database stores only monthly means for nodal points, the software synthetically generates hourly and daily data using stochas-

tic algorithms. Daily profiles are synthetically generated through the method of Aguiar et al. [39] which uses markov transition matrices to synthetically generate daily clear-sky clearness indexes from monthly clearness indexes. Hourly data are synthetically generated using the Aguiar and Collares-Pereira TAG model [40]. Data from 8,352 weather stations are accessible in Meteonorm, 1,336 of which include solar irradiation measurements.

The National Renewable Energy Laboratory (NREL) maintains the National Solar Resource Database (NSRDB) for the United States [41]. The database includes hourly time series data as well as representative weather years, referred to as typical meteorological year (TMY) data sets for the United States' network of around 1,500 ground stations. Numerous updates have been made to the database resulting in TMY, TMY2 and TMY3 data sets. All TMY files have been converted to the latest System Advisor Model (SAM) comma-separated-variable (CSV) format developed for use with NREL's SAM renewable energy performance and financial modelling software.

The EnergyPlus project, managed by NREL, maintains a database of weather data from 20 external sources with more than 2,100 locations worldwide across all WMO regions [42]. The data are available in a variety of formats developed by various contributing organisations. All data files consist of a single representative year of weather data, synonymous with TMY, compiled from multiple years of measured data. Approximately 78 Australian locations are made available through EnergyPlus.

In comparison to the previous databases, a smaller database known as the Baseline Surface Radiation Network (BSRN) [43] maintains high quality, high temporal resolution (one minute) data for approximately 50 stations around the world [36]. The database is a project of the Global Energy and Water Experiment forming part of the World Climate Research Program (WCRP) [31, 43]. Data access is provided free of charge for research purposes only.

The Australian BoM operates a network of ground-based solar monitoring stations capturing one minute irradiation data. The data for 21 weather stations distributed throughout the major climate zones of Australia are available online via the 'One Minute Solar Data' (OMS) website [44].

A summary of available ground-based solar irradiation databases is provided Table 3.1.

3.1.2 Satellite-Based Solar Irradiation Databases

Meteonorm enables satellite images to be leveraged to establish representative solar irradiation climatologies for any location on Earth. The satellite images are processed using an approximation of the Heliosat-2 method by Lefevre et al. [38] which are processed to daily means and summed to monthly averages [35].

For locations outside of Europe, when the proposed site is located within 10 km of three ground-based stations (30 km for rest of the world), ground-based data only are used. For greater distances, supplementary satellite data are used due to the reduced correlation between the ground-based data and the actual conditions at the proposed location. For distances greater than 50 km in Europe (200 km for the rest of the world), ground-based measurements are no longer considered to be sufficiently accuracte for climatology corre-

Table 3.1: Ground-based solar irradiation databases

Database	Provider	URL	Access	Time Resolution	Stations	Area	Period	Reference
EnergyPlus	NREL	energyplus.net	Free	Hourly	2,100	Global	Various	[42]
NSRDB	NREL	nsrdb.nrel.gov	Free	Hourly	1,454	United States	1961-2010	[41]
WRDC	WMO, NREL	wrdc.mgo.rssi.ru	Free	Daily / Monthly	1000+	Global	1964-Present	[31, 33, 36]
GEBA	ETH Zurich	www.geba.ethz.ch	Free	Monthly	2,500+ (760)	Global	1950-1990	[32, 34, 35, 37]
BSRN	WCRP	bsrn.awi.de	Free	Minutely	50	Global	1992-Present	[31, 36, 43]
Meteonorm 7.2	Meteotest	www.meteonorm.com	Paid	Hourly	8,352 (1,336)	Global	1991-2010	[35, 38]
One Minute Solar	BoM	www.bom.gov.au/climate/data/oneminsolar/	Free	Minutely	21	Australia	1993-Present	[44]

lations and satellite-only data are used [35]. The resolution of the contributing satellite images vary region to region ranging from 2 km to 8 km [35].

Solargis and Vaisala 3TIER provide high-resolution satellite derived irradiation data services with complete world coverage. Solargis has a temporal resolution of 15 or 30 minutes depending on the region, a spatial resolution of 3-6 km and a 250 m resolution based on altitude [45]. Vaisala 3TIER has a spatial resolution of 3 km for hourly irradiation data [46]. An assessment by Ineichen [47] for the University of Geneva and the International Energy Agency determined Solargis be to one of the two most accurate compared to four other products including Vaisala 3TIER when assessed against ground-based measured data for western European locations. However, Ineichen also noted that it was difficult to draw general conclusions due to a lack of aerosol ground-data measurements, exact calibration data and interannual variability of irradiance conditions [47].

SoDa is a broker of numerous consolidated databases made accessible via a web interface [31,48]. Coverage for Europe and Africa is provided through the HelioClim-3 database derived from Meteosat Second Generation images using the Heliosat-2 method proposed by Rigollier et al. [49, 50]. World coverage is provided through access to the NASA SSE database [48]. Two versions (Versions 4 and 5) are currently available, principally differentiated by the atmospheric models considered. Under Version 5, atmospheric properties are updated every three hours providing estimates of surface solar irradiance under cloudless skies for any global site since 2004 [50].

The National Aeronautical and Space Administration (NASA) maintains the Surface Meteorology and Solar Energy (NASA SSE) database for satellite-derived data. The database enables irradiation data to be accessed for locations covering the entire globe. However, the spatial resolution is coarse, with latitude and longitude resolutions of 1° (approximately 111 km) [51].

The most recent version of the NREL NSRDB includes satellite-derived solar irradiation estimates, enabling the development of TMY data sets for any location in North America, Central America and India. Satellite images are processed using the latest Physical Solar Model (PSM) [41] for the United States and Central America and the SUNY (State University of New York) model [52, 53] for India [41]. Temporal and spatial resolutions currently available are 30 minutes/4 km respectively (America) (1998-2015) and 1 hour/10 km for India (2000-2014). Data from the NSRDB are also used in the Photovoltaic Geographical Information System (PVGIS) developed by the European Commission Joint Research Centre [54], referred to as PVGIS-NSRDB [54].

The Australian BoM maintains two satellite-based solar irradiation databases. The CDO database [55] stores satellite-derived daily irradiation data for the BoM's national network of weather stations, providing access to irradiation data for hundreds of Australian locations. To facilitate the daily totals of the CDO database, the BoM also maintains a database of Australian Hourly Solar Irradiance Gridded Data (HSI). The data are derived from satellite images obtained from the GMS-4 satellite through to the current generation Himawari-8 satellite [56]. The images are converted to irradiation estimates through the methodology established by Weymouth and Le Marshall [57] and Ridley et al. [58]. Im-

provements to the BoM package have been investigated in independent research [59–61] as well as by BoM itself [56, 59]. HSI data have a spatial resolution of approximately 5 km [56,62], enabling estimates of solar irradiation to be established for for any Australian location. However, unlike CDO, access to HSI data requires payment, primarily to cover data handling costs [62]. The data have been calibrated through data from the BoM OMS database, enabling the removal of estimate bias [56] and to develop irradiation component models [58].

Alternatively, the AREMI spatial data platform developed by the Australian Renewable Energy Agency (ARENA) provides free access to HSI data for the period between 1990–2015 [63].

EnMetSOL is a database managed by the University of Oldenburg providing irradiation data for Europe and Africa. Coverage is provided for Europe, India, Middle East and the USA [64] with between two and four observations per hour [64]. Comparison of data generated using the the EnMetSOL models against four other databases found EnMetSOL, along with Solargis, produced the best correlations with ground data.

The Satellite Applications Facility on Climate Monitoring (CM SAF) of the European Organisation for the Exploitation of Meteorology Satellites (EUMETSAT), maintains a database for Europe, Africa and parts of Asia derived from the Meteosat Second Generation (MSG) satellites. CM SAF data were also used to develop the PVGIS databases, PVGIS-CMSAF (Europe and Africa) and PVGIS-SARAH (Europe, Africa, Asia) [54,65].

Numerous other irradiation databases exist, however coverage is limited to certain geographic regions. Examples include Satel-light (Europe/North Africa) [66] and SOLEMI (Europe/Africa/Western Asia) [67, 68], both developed through joint European research efforts; and SolarAnywhere, a proprietary product developed by Clean Power Research [69] using the methodology developed by Perez et al. [52, 53] at the State Univeristy of New York [69], providing coverage for North America only.

A summary of satellite-based solar irradiation databases is presented in Table 3.2 and Table 3.3, showing the temporal and spatial resolution, geographical coverage and period of coverage.

3.1.3 Irradiation Data for Australian Applications

To determine the most appropriate data service for a particular application, priority must be placed on, in no particular order, data coverage, model accuracy (satellite-derived data), data resolution (temporal/spatial) and finally, cost of access. The accuracy of individual satellite data services for Australian locations, similar to the assessment conducted for Western Europe by Ineichen [47], had not been established in literature at the time of writing[a]. Consequently, the accuracy criteria is disregarded for the purposes of selecting a data resource for Australia. The following acceptance criteria were considered for this research:

(i) Free access

[a] Refer to Remark 3.1

(ii) Hourly data

(iii) 5 km resolution (approximate)

(iv) Minimum 10 years of measurements

(v) Observed data (not synthetic or re-analysis)

(vi) Full Australian coverage

Amongst the products summarised in Section 3.1, Meteonorm, Solargis, 3TIER, NASA SSE, BoM HSI and AREMI represent the only available satellite-based irradiance data services for Australian locations. The NASA SSE database is a free database, however the spatial resolution of the data is very coarse (111 km) and data are only available in monthly averages. In contrast, Meteonorm, Solargis, 3TIER and BoM HSI provide access to data of a high temporal and spatial resolution, however accessibility is only available through paid access. As the analysis to be presented in the subsequent chapters utilises solar irradiation at multiple locations, paid access services were deemed untenable for the purposes and objectives of this research.

Consequently, the AREMI spatial mapping platform represents the only freely available option for complete coverage of hourly irradiance data for all Australian locations. Given the relatively high temporal and spatial resolutions of AREMI, which are in-line with those available through the alternative paid access services for the Pacific region, AREMI represents an adequate package for a comprehensive analysis of solar irradiation across Australia.

Remark 3.1 *Recently published research by Copper and Bruce [112] presented a comparative assessment of various irradiation maps for Australian locations. The assessment considered Solargis, Vaisala 3TIER, BoM HSI, NASA SSE and Meteonorm among others. A high level of variance was observed across the databases considered with the authors noting the potential for using multiple data sources through weighted averages to form a more robust dataset. No specific conclusion was drawn towards the database yielding the highest accuracy against ground-measured data. However, Solargis and BoM HSI showed the lowest average absolute MBE.*

Part of the research presented in this thesis considered solar irradiance models based on daily solar irradiation data, including the research presented in Chapter 5 and Chapter 6 Section 6.4.1. To facilitate this, data from the BoM CDO database, as a freely available daily irradiation database, were also utilised. Models based on AREMI data were considered for the more recent research components conducted for this thesis including those presented in Chapter 4, Chapter 6 Section 6.4.2, Chapter 7 and Chapter 8.

Table 3.2: Satellite-based irradiation databases

Database	Provider	URL	Access	Area	Australia Coverage	References
3TIER	Vaisala	www.3tier.com	Paid	Global	Complete	[46]
AREMI	ARENA	nationalmap.gov.au/renewables/	Free	Australia	Complete	[56, 63, 70]
Climate Data On-line	BoM	www.bom.gov.au/climate/data/	Free	Australia	Partial	[55]
Hourly Gridded Data	BoM	www.bom.gov.au/climate/data-services/solar-information.shtml	Paid	Australia	Complete	[56, 62, 70]
Meteonorm 7.2	Meteotest	www.meteonorm.com	Paid	Global	Complete	[35, 38]
NASA SSE	NASA	eosweb.larc.nasa.gov/sse/	Free	Global	Complete	[71]
NSRDB	NREL	nsrdb.nrel.gov	Free	Nth/Ctrl America India	N/A	[41]
HelioClim-3	SoDA	www.soda-pro.com	Paid	Euro/Africa	N/A	[31, 48, 50]
Satel-light	ENTPE	www.satellight.com	Free	Euro/Nth Africa	N/A	[66]
Solargis	Solargis	solargis.com	Paid	Global	Complete	[45]
SolarAnywhere	Clean Power Research	www.solaranywhere.com	Paid	North America	N/A	[69]
EnMetSOL	University of Oldenburg	www.uni-oldenburg.de/en/	-	Euro/Africa	N/A	[64, 72]
SOLEMI	DLR	dlr.de/tt/solemi	-	Euro/Africa/Asia (except East Asia)	N/A	[67, 68]
CM SAF	DWD	www.cmsaf.eu	Free	Eur/Africa	N/A	[54, 73, 74]

Table 3.3: Temporal and spatial resolution of satellite-based irradiation databases

Database	Time Resolution	Spatial Resolution	Period	References
3TIER	Hourly	3 km	1998-Present	[46]
AREMI	Hourly	5 km	1990-2015	[56, 63, 70]
Climate Data On-line	Daily	Individual Stations	1990-Present	[55]
Hourly Gridded Data	Hourly	5 km	1990-Present	[56, 62, 70]
		5 km	1993-2012 (Africa)	
Meteonorm 7.2	Hourly	2-3 km	2004-2010 (Europe)	[35, 38]
		8 km	2010-2016 (Global)	
NASA SSE	Monthly	111 km	1983-2005	[71]
NSRDB	30 mins	4 km	1998-2014 (North/Central America)	[41]
	Hourly	10 km	2000-2014 (India)	
HelioClim-3	15 minutes	3-5 km	2004-Present	[31, 48, 50]
Satel-light	30 minutes	5 km (lon) 6 km (lat)	1996-2000	[66]
Solargis	Hourly	3-6 km	1994-Present (Europe/Africa) 1999-Present (Asia/Americas) 2006-Present (Pacific)	[45]
SolarAnywhere	Hourly	10 km	1998-Present	[69]
EnMetSOL	15/30 minutes	1 km	1995-2005/2005-Present	[64, 72]
SOLEMI	Hourly	3-5 km	1991-Present	[67, 68]
CM SAF	Hourly	3-5 km	2005-Present	[54, 73, 74]

Table 3.4: Global irradiation calculation methodology and atmospheric data sources for satellite-based irradiation databases

Database	Global Methodology	Atmospheric Properties	References
3TIER	Vaisala cloud algorithm	MODIS [75], MACC-II [76], MERRA2 [77]	[46]
AREMI	Weymouth and Le Marshall [57]	-	[56, 63, 70]
Climate Data On-line	Weymouth and Le Marshall [57]	-	[55]
Hourly Gridded Data	Weymouth and Le Marshall [57]	-	[56, 62, 70]
Meteonorm 7.2	Heliosat-2 approx. [49, 78] Synthetic daily/hourly irradiation [39, 40]	Solar Consulting Services [79]	[35, 38]
NASA SSE	NASA GEWEX SRB	-	[71]
NSRDB	Physical Solar Model (PSM) (Americas) [80]	MODIS [75], MISR [81], AERONET [82], MERRA [77]	[41]
	SUNY (India) [52, 53]	Solar Consulting Services [79]	
HelioClim-3	Heliosat-2 [49]	MACC-II [76] Linke Turbidity [83]	[31, 48, 50]
Satel-light	Modified Heliosat [84]	Linke Turbidity (ESRA) [85]	[66]
Solargis	Solargis method	MACC-II [76], NOAA GFS [86]	[45]
SolarAnywhere	SUNY [52, 53]	-	[69]
EnMetSOL	Modified Heliosat [84, 87]	MACC [76]	[64, 72]
SOLEMI	Heliosat-2 [49]	MACC [76]	[67, 68]
CM SAF	MAGICSOL (Modified Heliosat [88, 89])	MACC [76] ERA-interim reanalysis of ECMWF [90]	[54, 73, 74]

Table 3.5: Clear-sky, diffuse and direct irradiation models used by satellite-based irradiation databases

Database	Clear-Sky	Diffuse	Direct	References
3TIER	Modified Kasten (SUNY) [52] REST2 [92]	- -	DIRINT [91] REST2 (with modulation function) [92]	[46]
AREMI	-	Modified BRL [58, 70]	-	[56, 63, 70]
Climate Data On-line	-	-	-	[55]
Hourly Gridded Data	-	Modified BRL [58, 70]	-	[56, 62, 70]
Meteonorm 7.2	Modifed ESRA clear-sky [38, 93]	BRL [58], Perez (1991) [94]	-	[35, 38]
NASA SSE	-	-	-	[71]
NSRDB	REST2 (Americas) [92]	REST2 [92]	REST2 [92], DISC [95]	[41]
	SOLIS clear-sky (India) [96]	-	DIRINT [91]	
HelioClim-3	McClear clear-sky v5 [97, 98] ESRA clear-sky v4 [93, 99]	-	-	[31, 48, 50]
Satel-light	Page (1996) [100], Dumortier (1995) [101]	Skartveit (1998) [102]		[66]
Solargis	Simplified SOLIS clear-sky [103]	-	Modified DIRINDEX [45, 52, 104]	[45]
SolarAnywhere	-	-	-	[69]
EnMetSOL	SOLIS clear-sky [96] Dumortier clear-sky [106]	- Diffuse fraction [107]	Kemper (2007) [72, 105] -	[64, 72]
SOLEMI	Bird clear-sky [108] (modified Iqbal [109])	-	-	[67, 68]
CM SAF	SPECMAGIC [102, 110, 111]	-	SPECMAGIC [102, 110, 111]	[54, 73, 74]

3.2 Solar Irradiation on the Horizontal Plane

3.2.1 Solar Time

When utilising minutely or hourly solar irradiation data, it is necessary to establish the relationship between standard (clock) time and solar time. Irradiation data is predominantly time-stamped in standard clock time. However, the geometric relationships describing Earth's solar orbit, and therefore the relationships describing the angle of incidence of solar irradiance on the Earth's surface, are referenced to solar time.

The Earth's tilt (in relation to the Earth's plane of orbit) and the slightly elliptical nature of Earth's orbit, lead to variations in the Sun's position relative to the same clock time each day [113]. The Equation of Time, E, accounts for the apparent time difference between clock time and solar time for any given day of the year. According to Spencer [114] as cited by Iqbal [109] and referenced in Duffie and Beckman [115][b], E is defined as:

$$E = 229.2(0.0000075 + 0.001868\cos B - 0.032077\sin B - 0.014615\cos B - 0.04089\sin B) \tag{3.1}$$

where B is given by

$$B = (n-1)\frac{360}{365} \tag{3.2}$$

and n is the day number of the year.

Taking into account the longitude of the subject location and the corresponding time zone standard meridian, solar time is defined as follows:

$$\text{Solar Time} = \text{Standard Time} + 4\,(L_{st} - L_{loc}) + E \tag{3.3}$$

where L_{st} and L_{loc} are the longitudes of the standard meridian and the location respectively. In (3.3), the longitudes are defined in degrees west with respect to the prime meridian such that:

$$0^\circ \leq (L_{st},\ L_{loc}) \leq 360^\circ \tag{3.4}$$

3.2.2 Components of Horizontal Irradiation

Irradiance is defined as the solar power received per unit area commonly referenced in the unit W/m^2. Irradiation is the integrated irradiance over a certain period of time and therefore quantifies the solar energy received, referenced in units of either Wh/m^2 or MJ/m^2. The total irradiance incident on a horizontal plane, referred to as global horizontal irradiance (GHI) can be broken into two components – direct (also referred as as beam) and diffuse irradiance (referred to a diffuse horizontal irradiance DHI). Direct refers to irradiance received directly from the solar disc whereas diffuse irradiance is received from atmospheric scattering across the entire sky dome. Consequently, daily (H) and hourly

[b] It should be noted, based on advice provided by Spencer [116], the term 0.0000075 in (3.1) was corrected from 0.000075 as quoted by Iqbal [109] and Duffie and Beckman [115] from Spencer [114]

(I) global irradiation quantities can be expressed as:

$$H = H_b + H_d \tag{3.5}$$

$$I = I_b + I_d \tag{3.6}$$

where subscripts b and d refer to the direct and diffuse components respectively.

Direct normal irradiation (DNI), as opposed to direct horizontal irradiation, is most frequently considered in irradiation decomposition models. DNI is defined as the irradiation incident on a plane perpendicular to the direction of radiation propagation. DNI irradiation, I_{bn}, is related to I_b through a sinusoidal function of solar altitude α, the angle between the horizontal and the direct irradiation direction propagation to an observed position, as shown in (3.7)

$$I_{bn} = \frac{I_b}{\sin(\alpha)} \tag{3.7}$$

3.2.3 Geometric Relationships for Solar Irradiation

The calculation of irradiance received from the sun incident on a particular surface is dependent on solar geometry on both an intra-day and an annual basis. Descriptions of key geometric relationships and parameters critical to the estimation of solar irradiance are provided in this section.

The angle of incidence of direct irradiance θ on a surface is described as a function of latitude ϕ, solar declination δ, tilt of the irradiated surface β, azimuth of the irradiated surface γ and solar hour angle ω as shown in (3.8):

$$\begin{aligned}\cos\theta = {} & \sin\delta\sin\phi\cos\beta + \sin\delta\cos\phi\sin\beta\cos\gamma + \cos\delta\cos\phi\cos\beta\cos\omega \\ & - \cos\delta\sin\phi\sin\beta\cos\gamma\cos\omega + \cos\delta\sin\beta\sin\gamma\sin\omega\end{aligned} \tag{3.8}$$

In (3.8), the solar hour angle ω describes the angular displacement of the Sun assuming the Earth rotates 15° per hour. With respect to solar noon (the local meridian), ω is negative during morning hours and positive in afternoon hours. The remaining parameters in (3.8) are subject to the following constraints:

$$-90^\circ \leq \phi \leq 90^\circ \tag{3.9a}$$

$$-\delta_{\max} \leq \delta \leq \delta_{\max} \tag{3.9b}$$

$$0^\circ \leq \beta \leq 180^\circ \tag{3.9c}$$

$$-180^\circ \leq \gamma \leq 180^\circ \tag{3.9d}$$

where a negative γ corresponds to a surface facing east of north and a positive γ, an azimuth that is west of north.

In (3.9b), $\delta_{\max}$, equal to the axial tilt of the earth, varies slowly over time following an approximately 40,000 year cycle [51]. To be consistent with the literature upon which

this thesis is based, $\delta_{\max}$ is assumed to be 23.45°, as defined by Duffie and Beckman [115]. Spencer [114] as cited by Iqbal [109], defines the solar declination angle δ as follows:

$$\begin{aligned}\delta = 0.006918 - 0.399912\cos(B) + 0.070257\sin(B) - 0.006758\cos(2B) \\ + 0.000907\sin(2B) - 0.002697\cos(3B) + 0.00148\sin(3B)\end{aligned} \tag{3.10}$$

Solar zenith angle θ_z, the angle between the sun and vertical, is a further parameter key to the calculation of solar irradiation. Zenith angle is the complement of solar altitude such that $\theta_z = 90 - \alpha$ and can be further expressed as follows:

$$\cos\theta_z = \cos\phi\cos\delta\cos\omega + \sin\phi\sin\delta \tag{3.11}$$

The sunset hour angle ω_s and the sunrise hour angle (which is simply $-\omega_s$) defines the boundaries of a solar day. Without the presence of an atmosphere, sunset would occur when the solar zenith angle is 90°. Substituting ω_s into (3.11) and rearranging gives the following expression for sunset hour angle:

$$\cos\omega_s = -\frac{\sin\phi\sin\delta}{\cos\phi\cos\delta} = -\tan\phi\tan\delta \tag{3.12}$$

However, due to atmospheric refraction, at sunset the solar disc appears lifted above the horizon for a brief period after the true geocentric position of the sun has travelled beneath the horizon. The effect of atmospheric refraction yields an approximate sunset zenith angle of $\omega_{z,s} = 90.833°$ [117]. Rearranging (3.11) and noting that sunset solar altitude α_s is the compliment of sunset zenith angle $\theta_{z,s}$, the following expression for sunset hour angle is derived:

$$\cos\omega_s = \frac{\sin\alpha_s - \sin\phi\sin\delta}{\cos\phi\cos\delta} \tag{3.13}$$

where $\alpha_s = 90 - \theta_{z,s} = -0.833°$.

With expressions for angle of incidence and zenith angle developed, the ratio of direct irradiance incident on an inclined surface to that of a horizontal surface (R_b) is defined as:

$$R_b = \frac{\cos\theta}{\cos\theta_z} \tag{3.14}$$

3.2.4 Extra-Terrestrial Irradiance

Extra-terrestrial (ET) irradiance is the irradiance that would be received on the Earth's surface without the presence of an atmosphere. ET irradiance varies over the course of the year, primarily due to variations in the Earth-Sun distance created by Earth's elliptical orbit leading to irradiance fluctuations in the order of ±3.3% [115]. Other variabilities created by fluctuating solar activity conincident with sunspots also effect estimates of ET irradiance. However, the fluctuating activity can be largely ignored due to the un-

certainty and variability in atmospheric transmittance due to climatic conditions [115]. Consequently, the radiation emitted by the Sun at the minimum Earth-Sun distance may be considered uniform, leading rise to the solar constant G_{sc}, considered to be 1367 W/m^2 in this research [115]. The extra-terrestrial irradiance incident on the plane normal to the radiation G_{on} and on a horizontal plane projected from the Earth's surface G_o are defined in accordance with (3.15) and (3.16) respectively.

$$G_{on} = G_{sc}\left(1 + 0.033\cos\frac{360n}{365}\right) \tag{3.15}$$

$$G_o = G_{sc}\left(1 + 0.033\cos\frac{360n}{365}\right)\cos\theta_z \tag{3.16}$$

Integrating the ET irradiance over a particular hour or a full day enables the hourly and daily extra-terrestrial solar irradiation to be calculated as in (3.17) and (3.18) where I_o and H_o are hourly and daily irradiation respectively.

$$\begin{aligned} I_o = {} & \frac{12 \times 3600 G_{sc}}{\pi}\left(1 + 0.033\cos\frac{360n}{365}\right) \\ & \times \left[\cos\phi\cos\delta\left(\sin\omega_2 - \sin\omega_1\right) + \frac{\pi\left(\omega_2 - \omega_1\right)}{180}\sin\phi\sin\delta\right] \end{aligned} \tag{3.17}$$

$$\begin{aligned} H_o = {} & \frac{24 \times 3600 G_{sc}}{\pi}\left(1 + 0.033\cos\frac{360n}{365}\right) \\ & \times \left(\cos\phi\cos\delta\sin\omega_s + \frac{\pi\omega_s}{180}\sin\phi\sin\delta\right) \end{aligned} \tag{3.18}$$

3.2.5 Clearness Index

The clearness index gives a relative measure of the percentage of time the sun is obscured by cloud for a particular location. The daily clearness index K_T is defined as the ratio of daily global (total) irradiation H, to the daily extra-terrestrial irradiation defined in (3.18). The daily clearness index may be written as:

$$K_T = \frac{H}{H_o} \tag{3.19}$$

The hourly clearness index k_T may also be defined in a similar fashion such that

$$k_T = \frac{I}{I_o} \tag{3.20}$$

where I is the global hourly irradiation on the horizontal plane.

3.2.6 Clear-Sky Irradiation

Clear-sky irradiation is an important parameter in solar energy system assessment as it corresponds to the maximum solar energy available [92]. Clear-sky models are used as the basis for many cloudy-sky (all-sky) irradiance models and the estimation of irradiation characteristics from satellite imagery [118, 119]. Clear-sky models vary significantly in complexity from single parameter models relying on solar zenith angle only such as the Kasten model [120], to complex, multi-paramter, multi-band models covering both direct and global irradiation parameters [118], for example the REST2 model [92]. Complex models rely on an extensive list of detailed atmospheric measurements such as water vapour, Angstrom Beta, ozone, aerosols, dew point temperature and Rayleigh Scattering among others [118, 121].

Numerous assessments of clear-sky global irradiation models have been conducted to establish the most accurate models for different geographic regions. However, no single model has been shown to perform better than all others across all regions.

Ineichen [119] compared eight clear-sky broadband models against 20 years of data at differing climates and altitudes for 16 ground measurement stations across different states in the United States as well as stations in Portugal and Germany. Ineichen found the Solis model gave the most accurate results. However, overall clear-sky estimate accuracy was not deemed to be highly dependent on the model selected in the first instance but rather the accuracy of the input turbidity data. Consequently, Ineichen indicated consideration should be given towards implementation simplicity where the European Solar Radiation Atlas (ESRA) and Molineaux models have an advantage (as they were found to perform well) and the availability of input parameters such as aerosol optical depth and Linke Turbidity.

Gueymard [122] assessed 18 broadband radiative models for clear-sky irradiance with an improved validation methodology. The performance of the models were validated with key statistics including MBE, RMSE, uncertainty confidence intervals and a proposed Combined Performance Index (CPI) with the Kolmogorov-Smirnov Integral as an input. The true performance of each model was established through tightly controlling measurement uncertainty and propagation uncertainty. Measurement uncertainty was controlled by using data derived from high quality measurement devices while propagation uncertainty associated with imperfect description of atmospherics was reduced by applying a strict selection criteria, using only real time data. Data selected from five measurement locations were used to test the models – four United States locations (including Hawaii) and Saudi Arabia. Gueymard found that the REST2 and Ineichen models were amongst the best performing models, however it was noted they contain a complex combination of atmospheric inputs.

Badescu et al. [123] assessed 54 clear-sky radiation models against measured global irradiance at two ground-based stations in Romania. A unique testing procedure was applied involving 26 testing stages for each ground station, with each stage testing the model performance under non-ideal conditions and low input data quality associated with the model parameters. Badescu et al. found that no single model performed the best for

all input data. Rather, some models were noted to rank amongst the best for the majority of the testing steps, including the ESRA3, Ineichen, REST2 clear-sky models. ESRA3 is similar to ESRA but with Linke Turbidity obtained from an empirical formula which is a function of precipitable water and Angstrom β. The ESRA3 model was found to have a relatively good performance.

Engerer and Mills [118] conducted an assessment of nine clear-sky models for Australia conditions. The models tested including Kasten, Ineichen, Bird, ESRA, REST2, Molineaux and the Simplified Solis models among others. Using high frequency (one-minute) data from BoM for 14 chosen locations, the analysis applied the quality control methodology of Long and Shi [124]. Atmospheric data were taken from the SoDa data services for ozone, turbidity and aerosols. A polynomial function was fitted to the data to avoid discontinuities similar to [119]. Engerer and Mills found the ESRA to be the clear "best" choice for clear-sky direct irradiation and performed well for global irradiance. Ultimately, it was concluded that the ESRA model is best for Australian conditions with the REST2 model coming second [118].

Based on the assessment of Engerer and Mills [118], the ESRA clear-sky model is used in this thesis as the basis for quality control assessments presented in Section 3.4. The ESRA clear-sky model is described in further detail in Section 3.2.6.2.

3.2.6.1 Linke Turbidity

The attenuation of solar irradiation, in particular direct irradiation [125], due to atmospheric absorption and scattering is conveniently approximated by the Linke Turbidity factor T_L. Atmospheric turbidity is commonly modelled as a descriptor of atmospheric composition and considered in many irradiance models including the ESRA and other clear-sky models as well as other models for global, direct and diffuse irradiance.

Linke Turbidity describes the optical thickness $\delta(m)$ of a wet and turbid atmosphere in units of the Rayleigh optical thickness $\delta_R(m)$, the spectrally integrated optical thickness of a clean and dry 'Rayleigh' atmosphere under standard conditions [125]. Optical thickness and therefore Linke Turbidity are functions of relative optical air mass m (the spectral distribution of incident solar direct irradiation which varies with solar altitude) [125]. Linke Turbidity is defined as:

$$T_L(m) = \frac{\delta(m)}{\delta_R(m)} \tag{3.21}$$

A number of the clear-sky irradiation models assessed in [119] included the application of Linke Turbidity data, data for which were derived from the SoDa database at a relative optical air mass of 2 ($AM2$). However, as only monthly data are available through the SoDa service, a polynomial function was fitted to the data to avoid discontinuities. A similar polynomial fit was used by Engerer and Mills [118, 126] as part of an assessment of clear-sky irradiation models for Australian locations. Monthly mean values for T_L were derived from the SoDa database for input into the ESRA and other clear-sky models.

For this research, a similar methodology to [118,119,126] is adopted for the application of the ESRA clear-sky irradiance model defined in Section 3.2.6.2. Figures 3.1 and 3.2

show the polynomial fit for Linke Turbidity data from the SoDa data bank associated with Wagga Wagga and Rockhampton stations within the BoM OMS network.

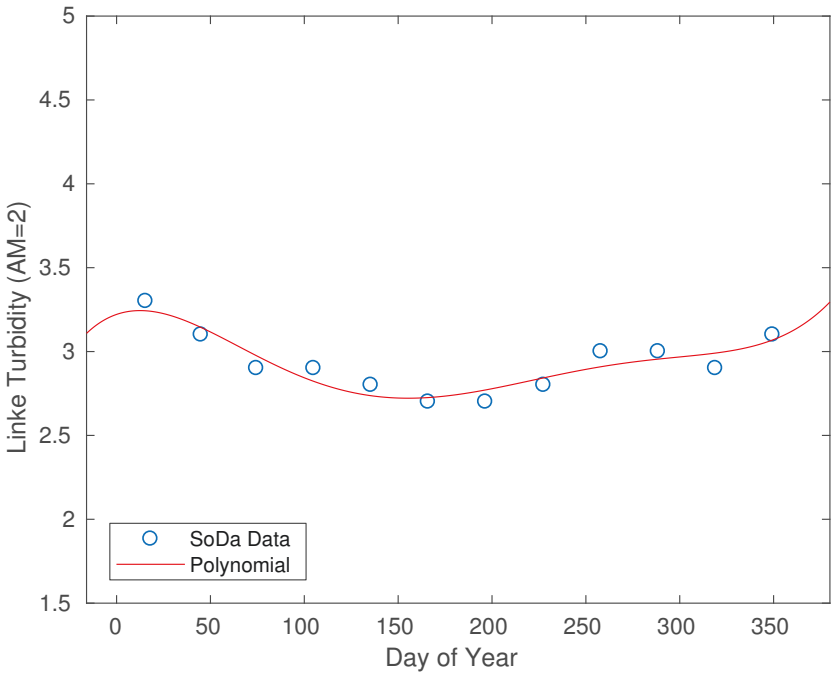

Figure 3.1: Polynomial fit of Linke Turbidity based on SoDa data for Wagga Wagga

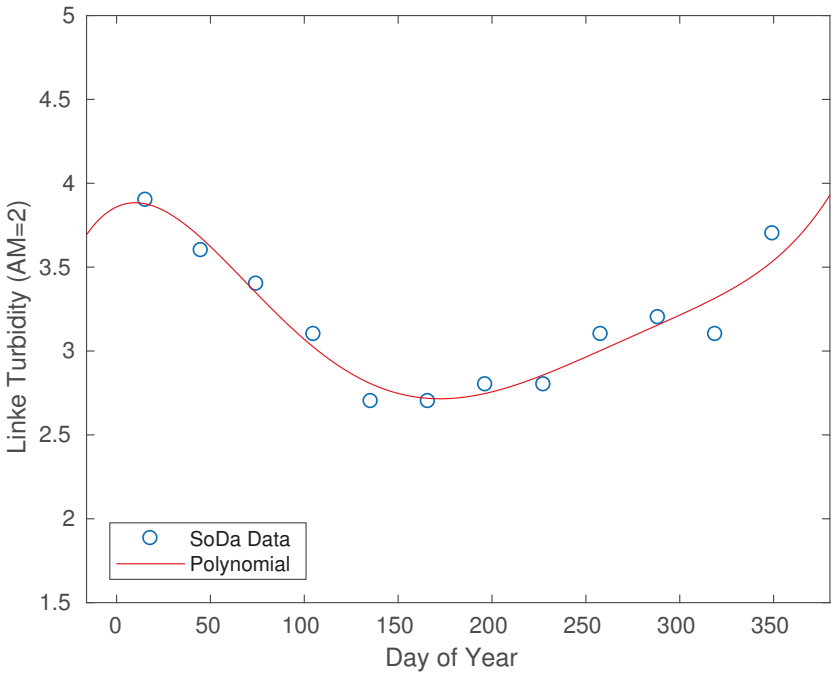

Figure 3.2: Polynomial fit of Linke Turbidity based on SoDa data for Rockhampton

3.2.6.2 ESRA Clear-Sky Model

As discussed in Section 3.2.6, the ESRA clear-sky model has been observed to perform well [118,123], particularly in Australian locations [118]. A description of the ESRA model

as provided by Rigollier et al. [93] and summarised in this section. Clear-sky irradiance can be broken into a direct and diffuse component. The direct normal clear-sky irradiance component of the ESRA clear-sky model is defined as follows:

$$I_{bnc} = I_{on} e^{-0.8662 T_L(AM2) m \delta_R(m)} \tag{3.22}$$

where $T_L(AM2)$ is the Linke Turbidity factor at an air mass of 2 and m is the relative optical air mass.

The relative optical air mass is unitless and can be expressed as a function of solar altitude α. However, due to to atmospheric refraction a correction was introduced by Rigollier et al. [93] such that α^{true} can be calculated as:

$$\alpha^{\text{true}} = \alpha + 0.061359 \left(\frac{180}{\pi}\right) \left[\frac{0.1594 + 1.1230(\pi/180)\alpha + 0.065656(\pi/180)^2\alpha^2}{1 + 28.9344(\pi/180)\alpha + 277.3971(\pi/180)^2\alpha^2}\right] \tag{3.23}$$

With the refraction correction for solar altitude, the relative optical air mass is defined as:

$$m\left(\alpha^{\text{true}}\right) = \frac{p/p_0}{\sin \alpha^{\text{true}} + 0.50572 \left(\alpha^{\text{true}} + 6.07995\right)^{-1.6364}} \tag{3.24}$$

where p and p_0 are the mean atmospheric pressure at the site elevation and at sea level respectively. The ratio of p/p_0 can be expressed as:

$$\frac{p}{p_o} = e^{-z/z_h} \tag{3.25}$$

where z is the site elevation and z_h is the scale height of the Rayleigh atmosphere, equal to 8434.5 m [93].

The Rayleigh optical thickness $\delta_R(m)$, as an input to (3.22), is calculated as follows based on Rigollier et al. [93]:

$$\frac{1}{\delta_R(m)} = \begin{cases} 6.62960 + 1.75130m - 0.12020m^2 + 0.00650m^3 - 0.00013m^4 & \text{if } m \leq 20 \\ 10.4 + 0.718m & \text{if } m > 20 \end{cases} \tag{3.26}$$

Remark 3.2 *Geiger et al. [99] and Remund et al. [83] introduced a pressure correction to the Rayleigh optical thickness $\delta_R(m)$ formulation as the model of (3.26) performs incorrectly for high elevations. The corrections are not introduced in this paper due to inconsistencies in the equations reported in [83] and [99]. In the original model of [93], the pressure errors were not immediately evident as the elevations of the assessed locations were less than 500 m. The vast majority of Australian locations are less than 500 m while the network of BoM OMS stations are universally less than 500 m, with the exception of Alice Springs (546 m). Consequently, the formulation error in (3.26) as detailed in [93] is not expected to appreciably effect the results presented in this research.*

The diffuse component of the ESRA clear-sky model, I_{dc}, is defined in [93] and repeated

as (3.27), noting the Remund et al. [83] pressure correction observation for site elevation as discussed in Remark 3.2. While the exact influence on the model output is unclear, the pressure corrected Linke Turbidity $T_L^*(AM2) = p/p_0 \times T_L(AM2)$ is considered in this research. The diffuse component of the ESRA clear-sky model with atmospheric pressure corrections is defined as follows:

$$I_{dc} = I_o T_{Rd}\left[T_L^*(AM2)\right] F_d\left[\alpha, T_L^*(AM2)\right] \tag{3.27}$$

where T_{Rd} and F_d are diffuse transmission and angular functions defined according to (3.28) and (3.29) below.

$$\begin{aligned} T_{Rd}\left[T_L^*(AM2)\right] = &-1.5843 \times 10^{-2} + 3.0543 \times 10^{-2} T_L^*(AM2) \\ &+3.797 \times 10^{-4}\left[T_L^*(AM2)\right]^2 \end{aligned} \tag{3.28}$$

$$F_d\left[\alpha, T_L^*(AM2)\right] = A_0 + A_1 \sin(\alpha) + A_2 \sin^2(\alpha) \tag{3.29}$$

The coefficients A_0, A_1 and A_2 are dependent only on Linke Turbidity and expressed as:

$$A_0 = 0.26463 - 0.061581 T_L^*(AM2) + 0.0031408\left[T_L^*(AM2)\right]^2 \tag{3.30a}$$

$$A_1 = 2.04020 + 0.018945 T_L^*(AM2) - 0.011161\left[T_L^*(AM2)\right]^2 \tag{3.30b}$$

$$A_2 = -1.33025 + 0.03231 T_L^*(AM2) - 0.0085079\left[T_L^*(AM2)\right]^2 \tag{3.30c}$$

With the direct and diffuse components of clear irradiation, the global clear-sky irradiation is calculated as:

$$I_{gc} = \frac{I_{bnc}}{\sin(\alpha)} + I_{dc} \tag{3.31}$$

3.2.7 Models for Global Irradiation

Global irradiation models typically combine clear-sky models with models for estimating cloud index [127]. The complexity of the models vary. Some simple models take into account cloud cover, humidity, temperature and wind speed only, such as the Zhang and Huang model [128] defined as follows:

$$\begin{aligned} I_g = \Big\{ G_{sc} \sin(\alpha_s) \Big[&c_o + c_1 (CC_{10}) + c_2 (CC_{10})^2 \\ &+ c_3 \left(T_n - T_{n-3}\right) + c_4 \phi + c_5 V_w \Big] + d \Big\} / k \end{aligned} \tag{3.32}$$

where CC_{10} is the level of cloud cover, ϕ is relative humidity, T_n and T_{n-3} are dry bulb temperature at hours n and $n-3$ respectively, V_w is wind speed and c_0–c_5, d and k are the regression coefficients.

Other models such as the REST2 model [92] are based on complex combinations of

aerosols. Consequently, many are heavily reliant on detailed atmospheric data, which are not always freely available, especially for Australian locations.

Seo and Huang [129] investigated modified versions of the Zhang and Huang model to test the dependence on the input variables in order simplify the model. It was found that 7 out of the 23 locations tested, the models could be simplified by removing the wind speed and humidity terms, thereby becoming a 2 variable model, with 4 regression coefficient terms instead of 6 [121]. One such location was Darwin, Australia. Furthermore, it was found that that two variables were sufficient for non-tropical sites, with the additional variables necessary for tropical locations.

Noting the model dependence on climatology, Seo and Krarti [130] expanded the Zhang and Huang model of (3.32) to develop a set of coefficients for different climatological zones based on the Köppen-Geiger climate classification system for which a further description is presented in Section 3.3. It was noted that the root mean square error (RMSE) and mean bias error (MBE) was remarkably improved from the Zhang and Huang model, however no data from Australian locations were used to develop the coefficients while the performance of the model in Australia was also untested.

Copper [127] aimed to test the accuracy of various widely adopted global irradiation models for Australian locations. When separately assessing the global models, Copper found that the six variable model of Seo and Huang outperformed the other global irradiation models [127]. However, it was noted that the Köppen-Geiger variation of the Zhang and Huang model, used to develop the second generation International Weather files for Energy Calculations (IWEC2) TMY files, showed improved or matched performance for three out of four locations.

Numerous other models exist such as Thevenard and Brunger, Kasten and Cesplak (simple) as translated to english by Davis and McKay, and Moriarty [121]. A review of each model is beyond the scope of this research.

In this research, the unique application of the Köppen-Geiger climate classification in the Seo and Huang global irradiance model is the motivator for an extension to diffuse decomposition irradiation models. Diffuse irradiance models are discussed in Section 3.2.8 and a particular model known for its good performance across many climatological zones is investigated to determine if accuracy improvements are possible through consideration of Köppen-Geiger climate classification.

3.2.8 Diffuse Decomposition Models

Due to the high variability of cloud cover and changes in atmospheric gases, accurate estimation of the diffuse fraction of irradiation is difficult. A multitude of models have been developed to estimate diffuse irradiation with many reviews aiming to identify the most accurate model [103, 127, 131, 132] with recent studies including [133–135]. However, all assessments are limited in scope and typically assess the models against a limited network of ground-based weather stations.

Diffuse fraction is defined as the ratio of diffuse horizontal irradiation over global horizontal irradiation and is often the primary reference when referring to diffuse to enable

ease of comparison with clearness index, previously defined in Section 3.2.5, which is also defined as a fraction.

Orgill and Hollands developed one of the earliest models diffuse fraction models expressed as a function of clearness index, consisting of sub-intervals for the hourly clearness index k_T. Orgill and Holland noted that diffuse fraction $d = I_d/I$ varies little around the ends clearness index range, but varies substatially in the middle range. Consequently, the models of Orgill and Holland and other early models such as Erbs et al. [136] and Reindl et al. [137] break the clearness index index in sub-intervals, with piecewise correlations developed for each sub-interval [138]. At the simplest level, the piecewise diffuse fraction model is a function of clearness index only with a linear relationship in each sub-interval, as is the case with the Orgill and Hollands model detailed in (3.33):

$$\frac{I_d}{I} = \begin{cases} 1 - 0.249k_T & \text{for } 0 \leq k_T \leq 0.35 \\ 1.557 - 1.84k_T & \text{for } 0.35 < k_T < 0.75 \\ 0.165 & \text{for } k_T \geq 0.75 \end{cases} \tag{3.33}$$

The Erbs hourly correlation is an extension of sorts on the Orgill and Hollands, introducing a higher order polynomial as a function of clearness index. The model was developed from data gathered from the stations in the US and one Australian station [115,136]. The model is noted by Duffie and Beckman to be, for practical purposes, very similar to the Erbs model [115] defined in (3.34) as:

$$\frac{I_d}{I} = \begin{cases} 1 - 0.09k_T - 2.5557k_T^2 + 0.8448k_T^3 & \text{for } k_T \leq <= 0.22 \\ 0.9511 - 0.1604k_T + 4.388k_T^2 - 16.638k_T^3 + 12.336k_T^4 & \text{for } 0.22 < k_T \leq 0.80 \\ 0.165 & \text{for } k_T \geq 0.80 \end{cases} \tag{3.34}$$

The Dirint model of Perez et al. [91] is a modified version of the Direct Insolation Simulation Code (DISC) model by Maxwell [95]. Rather than modelling DHI, the Dirint model estimates DNI which can then be used to estimate the diffuse irradiation through the relationships of (3.6) and (3.7). DNI is first calculated through the DISC model and the resultant output I_{DISC} is then scaled by $X(K_t', \theta_z, W, \Delta K_t')$, a coefficient function of the solar irradiation condition parameters of clearness index (K_t' – modified to be independent of the sun's position), solar zenith (θ_z), atmospheric precipitable water (W – derived from dew point temperature measurements) and a stability index ($\Delta K_t'$) [91,132,138]. The last parameter $\Delta K_t'$ reflects the dynamics of the time series [91]. The coefficent function is taken from a four-dimensional lookup table consisting of a $6 \times 6 \times 5 \times 7$ matrix [91]. The Dirint model is therefore expressed simply as:

$$I_{bn} = I_{DISC} X(K_t', \theta_z, W, \Delta K_t') \tag{3.35}$$

where the DISC model is itself a function of global irradiation and solar zenith angle [91], a detailed description for which is provided in [95].

A further evolution of Dirint is DirIndex [52], developed through an alternative consideration of atmospheric turbidity [132]. The DirIndex model is considered in the Solargis satellite-based solar irradiation database [45]. The Dirint model is used by the Vaisala 3TIER and NSRDB (India) databases, while the DISC model is used in the NSRDB (Americas) database.

The model developed by Skartveit et al. [102] is a modified version of the original model developed by the authors to include an hourly variability index [132], similar to the modifications of Perez et al. in the development of the Dirint model [104]. The model also included additional corrections for surface albedo to differentiate between snowy and non-snowy conditions [132]. The Skartveit model consists of an extensive array of analytical functions to estimate diffuse irradiation from global irradiance, solar elevation and clearness index [121] [132]. The model is essentially a piecewise polynomial model that separates clearness index into numerous regions [121]. The primary disadvantage of the model is the high number of parameters requiring estimation, with over 20 parameters depending on the surface albedo circumstances [121].

Boland et al. [138] noted a number of shortfalls associated with piecewise polynomial diffuse fraction models such as those of Orgill and Hollands, Reindl, Erbs and Skartveit. Various authors use different clearness index sub-interval end points in their models while the models assume only two significant predictors – clearness index and solar altitude. Boland et al. identified that additional predictors can be introduced to account for the highly variable spread in the middle sub-interval whilst also accounting for spread featured around the end sub-intervals. Finally, Boland et al. reasoned that a model accounting for clearness index in a single uniform manner enables easy alteration, allowing adjustments for future climate change to be made more easily than fixed sub-intervals.

The early work by Boland et al. [139] presented a simple logistic function model for diffuse fraction developed for Australian locations involving clearness index only. The model was the first step in the development of a generic model of diffuse fraction that could address the transportability issues associated with others models developed for other climates [58]. The ultimate aim was to develop a single model from global irradiance and other predictors [58] to cover the whole range of clearness indices rather than splitting the range into sections as was the case for the models of [102, 136, 140].

The theoretical framework for the use of the logistic model was further expanded and the model modified again by Boland et al. [141]. The version of the logistic function model with the addition of a persistence factor, as updated by Ridley et al. [58] and known as the BRL model, is widely referenced in literature. In developing the new model, Ridley et al. [58] aimed to use as few predictors that rely on measured data as possible to enable the prediction of diffuse irradiation from global irradiation or inferred from satellite data only.

The BRL model considers five key parameters:

- An hourly clearness index k_T;

- Solar altitude α in units of degrees;
- Apparent solar time (AST) in units of hour number, which is asymmetric about solar noon and may explain differences between morning and afternoon;
- A daily clearness index K_T as Ridley et al. noted that the whole day may have common characteristics; and
- A clearness variability predictor, similar to the models of Skartveit [102] and Dirint [91], referred to as a persistence factor ψ, to capture the values of lagged clearness index due to atmospheric inertia [58].

The BRL model is defined as:

$$d = \frac{1}{1 + e^{\beta_0+\beta_1 k_T+\beta_2 AST+\beta_3\alpha+\beta_4 K_T+\beta_5\psi}} \tag{3.36}$$

where β_0, β_1, β_2, β_3, β_4 and β_5 are fitted coefficients with the values of -5.38, 6.63, 0.006, -0.007, 1.75 and 1.31 respectively [58]. Data from seven world locations were amalgamated and the residual sum of squares minimised to estimate each parameter coefficient. The persistence term ψ is defined as:

$$\psi = \begin{cases} \frac{k_{t-1}+k_{t+1}}{2} & \text{sunrise} < t < \text{sunset} \\ k_{t+1} & t = \text{sunrise} \\ k_{t-1} & t = \text{sunset} \end{cases} \tag{3.37}$$

Ridley et al. compared the BRL model against the Skartveit [102], Reindl [137] and Perez Dirint [91] models, providing graphical comparisons between the models for the city of Adelaide, reproduced as Figure 3.3. The common theme between the Skartveit, BRL and Perez Dirint models is the introduction of the persistence term to account for the high variability in the diffuse fraction and clearness index as clearly seen in Figure 3.3. Based on absolute percentage error and MBE statistical indicators, the BRL model performed equally as well as the other models for the northern hemisphere, while the Bayesian Information Criterion suggested that the BRL model outperformed all other models in both hemispheres. Ridley postulated that given its strong performance in both hemispheres and its relatively simple formulation, the BRL model could be used a universal model for all locations and climates.

Boland et al. [138] undertook further research to determine if the BRL diffuse fraction predictor can be used to give delineations for both diffuse and direct irradiance accurately. While energy predictions for PV installations are reliant on global and diffuse irradiation estimates only, accurate DNI estimates are critical for concentrated solar thermal systems. The performance of the BRL model using (3.6) and (3.7) to predict DNI was tested against a new logistic model developed specifically for DNI and the Dirint model. It was shown that the new logistic model performed better than the Dirint model in all four error analyses conducted for all locations examined with the exception of MBE in Lisbon, Portugal.

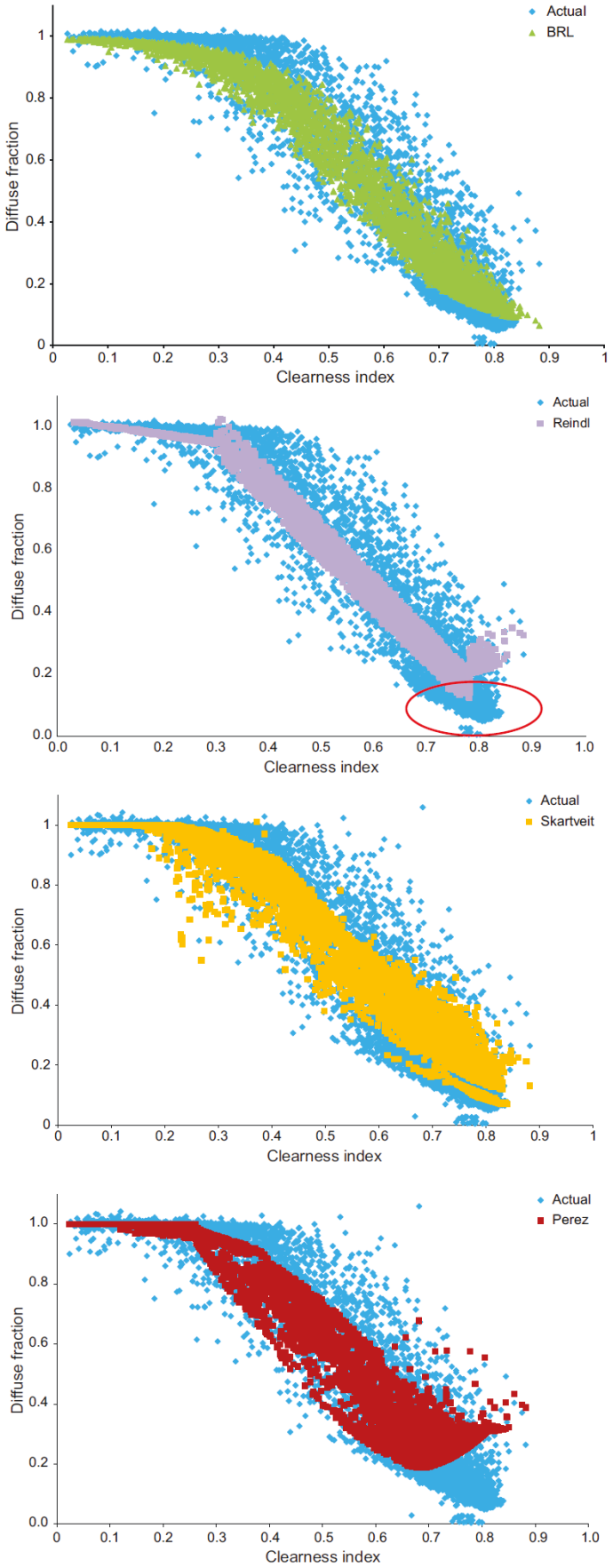

Figure 3.3: Comparison of diffuse fraction models for Adelaide irradiation data. Source: Ridley et al. [58]

The BRL model was then shown to perform as well as the new logistic model, with the BRL model giving better results in the middle clearness index range. It was ultimately concluded that the BRL model is suitable to model both diffuse and direct irradiation.

Torres et al. [132] reviewed 17 diffuse fraction models of three primary types: twelve piecewise polynomial models (from 1st to 4th order polynomals), two logistic models and three dynamic process models. It was found that the higher order polynomials do not appreciably improve the estimation over lower order models, an observation supported by Duffie and Beckman [115] when comparing the 4th order correlation of Erbs et al. [136] against the earlier piecewise linear correlation of Orgill and Hollands [140]. Torres et al. found that the relative RMSE (rRMSE) and coefficient of correlation were significantly improved with the use of the dynamic models of Skartveit, Dirint and BRL, which demonstrated a far better fit to the measured data. Torres et al. [132] also noted that the results confirmed the previously published findings of Ineichen [103], which established that the dynamic models of Skartveit and DirIndex (a modified version of Dirint) performed better than the piecewise polynomial model of Erbs et al. [136]. Of the three dynamic process models, Torres et al. [132] found the Dirint and BRL models to show the highest level of precision, as virtually all statistical indicators were better than the other models tested. Ultimately, the BRL model was recommended due to its advantages in calculation simplicity compared to the more complicated Dirint model [132].

Abal et al. [135] considered the BRL model of Ridley et al. [58] in a comparison of ten diffuse models for applications in Uruguay. It was found that when the BRL model is adjusted based on local irradiation data, the model outperformed all others.

Copper [127] aimed to test the accuracy of diffuse irradiation models for Australian locations either in the absence of measured data or with global irradiation measurements only. A particular focus was placed on the coupling of global and diffuse/direct models and examining error propagation through both. When separately assessing the diffuse models, Copper found no clear superior model under all-sky conditions, using ground measured global irradiation data as an input. However, it was noted that the BRL and Skartveit models outperformed the others in estimating direct irradiation under clear-sky conditions [127].

When coupling the global and diffuse models, Copper found diffuse model uncertainty doubled when using global models as an input [127]. Ultimately, Copper recommended the use of either the BRL or Skartveit models for diffuse/direct irradiation, coupled with BoM HSI satellite data for global irradiation in the absence of ground measured data [121].

3.2.8.1 BoM BRL Model

The Australian BoM uses a modified version of the BRL model for its HSI database derived from satellite-based estimates. The BoM model replaces the persistence term with a variability term based on the RMSE between the irradiance at a particular hour and the irradiance for the previous and subsequent hours as shown in (3.38) [70]. The variability term was adopted because it gave a lower mean absolute percentage error when fitted against the BoM network of surface stations.

$$\upsilon = \begin{cases} \sqrt{\frac{(k_{t-1}-k_t)^2+(k_{t+1}-k_t)^2}{2}} & \text{sunrise} < t < \text{sunset} \\ 0 \quad t = \text{sunrise},\ t = \text{sunset} \end{cases} \tag{3.38}$$

The BRL model is applied to the BoM HSI database of satellite observations acquired by numerous satellites and instruments since 1990, from the original GMS-4 satellite to the latest Himawari-8 satellite.

3.2.9 Hourly Irradiation from Daily Data

The time resolution of available solar radiation data vary significantly for each site. While some installations and weather stations have pyranometers (measuring global irradiance) or pyrheliometers (measuring direct irradiance normal to the direction of propagation) which gather data over minutely or hourly intervals, for the vast majority of locations, solar irradiation data are based on satellite observations, which are saved as cumulative daily global irradiation in databases such as BoM CDO. Consequently, in order to investigate the hourly PV generation potential at a particular location, it is necessary to establish an estimate of hourly solar irradiation when only daily data are available.

Determining hourly solar irradiation from daily data is an inexact process. The most obvious shortfall is the lack of transparency regarding the clearness of the sky. The presence of intermittent or continuous cloud cover cannot be determined through investigating the daily irradiation data alone [115]. However, available estimation methods "tend to produce conservative estimates of the long-time process performance" [115], working best for clear days, which correspond to the days of highest energy harvesting.

Studies of the daily irradiation components have resulted in the development of an expression for the fraction of daily diffuse irradiation in terms of the daily clearness index K_T. An expression for the set of correlations was developed by Erbs et al. [136], defined in (3.39) and (3.40) as follows:

For $\omega_s \leq 81.4°$

$$\frac{H_d}{H} = \begin{cases} 1 - 0.2727K_T + 2.4495K_T^2 - 11.9514K_T^3 + 9.3879K_T^4 & \text{for } K_T < 0.715 \\ 0.143 & \text{for } K_T \geq 0.715 \end{cases} \tag{3.39}$$

For $\omega_s > 81.4°$

$$\frac{H_d}{H} = \begin{cases} 1 + 0.2832K_T - 2.5557K_T^2 + 0.8448K_T^3 & \text{for } K_T < 0.722 \\ 0.143 & \text{for } K_T \geq 0.722 \end{cases} \tag{3.40}$$

Through knowledge of the total daily irradiation and the application of equations (3.39) and (3.40), the daily diffuse irradiation can be determined and subsequently daily direct irradiation through (3.5).

Equation (3.41), developed by Collares-Pereira and Rabl [142], provides an estimate

of the ratio of hourly total and daily total radiation defined as

$$\frac{I}{H} = \frac{\pi}{24}(a + b\cos\omega)\frac{\cos\omega - \cos\omega_s}{\sin\omega_s - \frac{\pi\omega_s}{180}\cos\omega_s} \tag{3.41}$$

where the coefficients a and b are established to be

$$a = 0.409 + 0.5016\sin(\omega_s - 60) \tag{3.42a}$$

$$b = 0.6609 - 0.4767\sin(\omega_s - 60) \tag{3.42b}$$

The same principle may be applied to the diffuse component of the irradiation. Liu and Jordan [143] described a relationship for the ratio of hourly and daily diffuse irradiation expressed as follows:

$$\frac{I_d}{H_d} = \frac{\pi}{24}\frac{\cos\omega - \cos\omega_s}{\sin\omega_s - \frac{\pi\omega_s}{180}\cos\omega_s} \tag{3.43}$$

Remark 3.3 *It is important to note that when the midpoint of the solar hour occurs after sunset or before sunrise, (3.41) and (3.43) yield a negative value which is not practically possible. Consequently, solar hours that straddle sunrise or sunset should be ignored when utilising (3.41) and (3.43) to estimate the hourly solar irradiation.*

3.3 Köppen-Geiger Climate Classification

The Köppen-Geiger climate classification, originally developed by Wladimir Köppen in 1900, for which the most notable version is presented in [144], as stated in [145], was one of the first quantitative classifications of world climates [146]. The classification system is based on the notion that native vegetation is one of the best ways to define climate zone boundaries [147]. A significant revision was undertaken by Rudolf Geiger in 1961 [146], resulting in the development of the most recent hand drawn map [145]. Since the work of Geiger, enhanced versions have been progressively developed in part due to the availability of updated meteorological data and the introduction of modified analysis methodologies. Recent notable revisions include the work by Kottek et al. [146], Peel et al. [148] and Rubel et al. [145]. However, Geiger's revision is still the most frequently referenced [146].

The classification system groups world geography into five key climate categories (variations on the naming conventions are given in literature [145, 147, 148], however the categorisations are largely equivalent). The categories as documented in [146] are:

- Equatorial (Tropical/Tropical Rainy)
- Arid (Dry)
- Warm temperate
- Snow (Cold/Boreal/Cold Snowy Forest/Continental)
- Polar (Alpine)

Within the key climate categories are sub-classes, delineated by criterions for average precipitation and air temperature [146,148]. In particular, monthly average, minimum and maximum temperatures, annual average temperatures, threshold limits on monthly and annual average precipitation and average precipitation for summer and winter months are considered [146]. Tthe climate classification sub-classes, as defined in [146], are detailed in Table 3.6.

Table 3.6: Köppen-Geiger sub-classes based as defined by Kottek et al. [146]

Main Climates	Sub-Classes	
	Precipitation	Temperature
(A) Equatorial	(W) Desert	(h) Hot Arid
(B) Arid	(S) Steppe	(k) Cold Arid
(C) Warm Temperate	(f) Fully Humid	(a) Hot Summer
(D) Snow	(w) Dry Winter	(b) Warm Summer
(E) Polar	(m) Monsoonal	(c) Cool Summer
		(d) Extremely Continental
		(F) Polar Frost
		(T) Polar Tundra

The Köppen-Geiger system has a number of shortfalls. Criticism has been placed on the rigid boundary criteria which can lead to large discrepancies between adjacent sub-classes. Some sub-classes have been defined based on natural landscape features, for example 'Rainforest', while others are based on the human experience, for example 'monsoon' [147]. Trewartha, as referenced by Stern et al. [147], noted that even though boundaries are precisely defined, they are limited by human judgement and are consequently open to debate and modification. However, the wide acceptance of the classification system as noted by [146, 147, 149] indicates the merits outweigh the deficiencies.

Applications for the climate classification systems include micrometeorological flux measurements, global river discharge, vegetation coverage assessments, soil erosion, human thermal comfort, particulate air pollution and composition of European disease vectors [145]. In an Australian context, the classification system has been used to reflect current vegetation distribution to enable the the prediction of distributions in future climates and the resultant hydrological implications under climate change scenarios [149]. Crosbie et al. [149] note that vegetation coverage is inextricably linked to climate and therefore investigated changes in climate types as a surrogate for changes in vegetation under climate change scenarios.

Stern et al. [147] of BoM, in an effort to improve the Köppen-Geiger climate classification to better reflect the human experience, made slight departures from the original classification through additional division of some climates and recombination of other groups. The research was developed with a particular focus on Australia and Australian climes. Using data gathered from 6000 rainfall and 600 temperature measurement locations between the years of 1961-1990, a revised digital map was generated using the Hutchinson's interpolation method of thin plate smoothing splines with a resolution of 0.025°, incorporating elevation to facilitate a three-dimensional classification. Following interpolation, the data were then smoothed using a filter resulting in a digital climate

classification map for Australia. The major classification groups and climate sub-classes considered in the methodology of [147] are presented in Figure 3.4 and Figure 3.5.

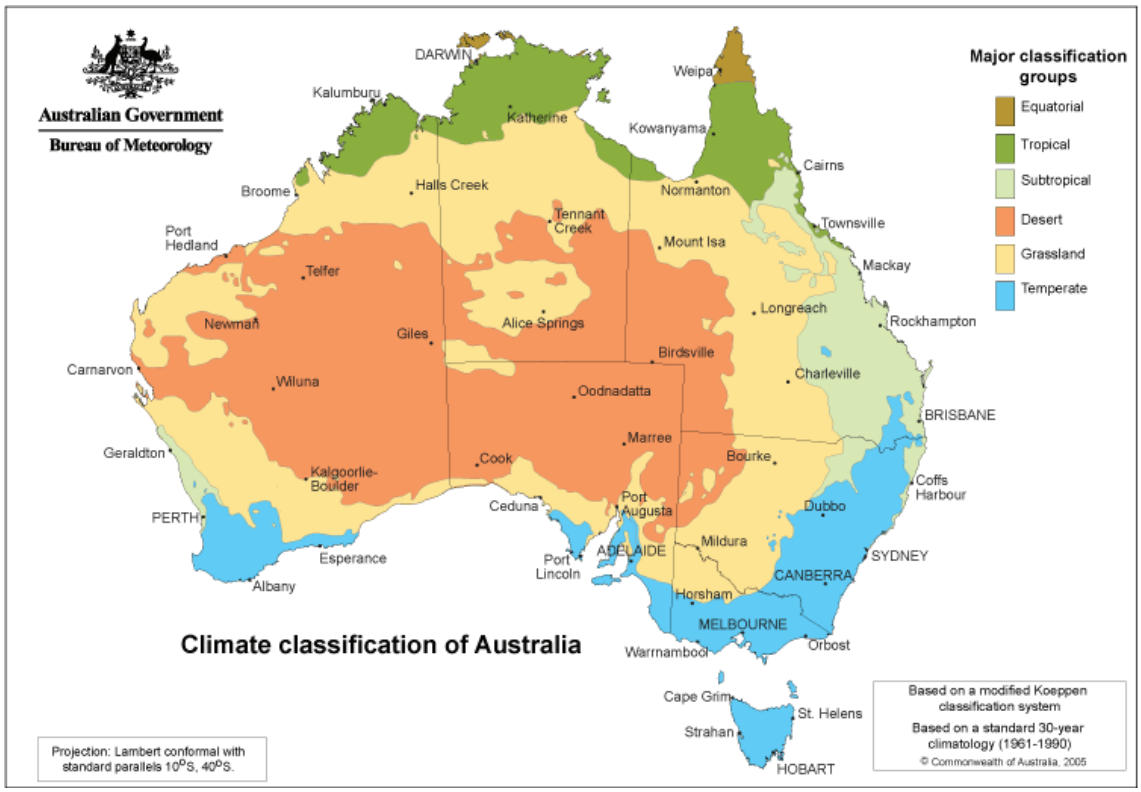

Figure 3.4: BoM major climate classification groups for Australia. Source: Australian Bureau of Meteorology [150]

The revised version of the Köppen-Geiger classification by Kottek et al. in 2006 was the first revision aiming to develop a digital version of the global map [145,146]. The revision was developed through a process of extensive data checks to remove inhomogeneities associated with temperature data and a multi-stage quality control check for precipitation data [146] for the period 1951-2000. The resultant digital map, allowing for 31 discrete climate types, as shown in Figure 3.6, provided a Köppen-Geiger climate classification at a latitude and longitude resolution of 0.5° [146].

Most recently, Rubel et al. expanded upon the work of the Kottek et al. and developed a re-analysed map of the European Alps using downscaling algorithms with a resolutions of 30 arc-seconds over the 1800-2010 for the purposes of climate zone change forecasting out to 2100. The methodology of Rubel et al. was applied to a revised global map, available as Google Earth .kmz files with resolutions of 30, 10 and 5 arc-minutes for data over the period 1986–2010 [151]. For Pacific and South-east Asian locations, including Australia, a map up to a resolution of 10 arc-minutes is available. The Köppen-Geiger climate classification map based on the reanalysis methodology of [151], reproduced in Figure 3.7, indicates 15 different climate divisions are present in Australia, noting that some divisions, for example 'As' and 'Csc', only appear as a few pixels.

Despite the Australia continent specific climate research by [147] and [148] among others, which show improvements to the original Köppen-Geiger classification, the recent

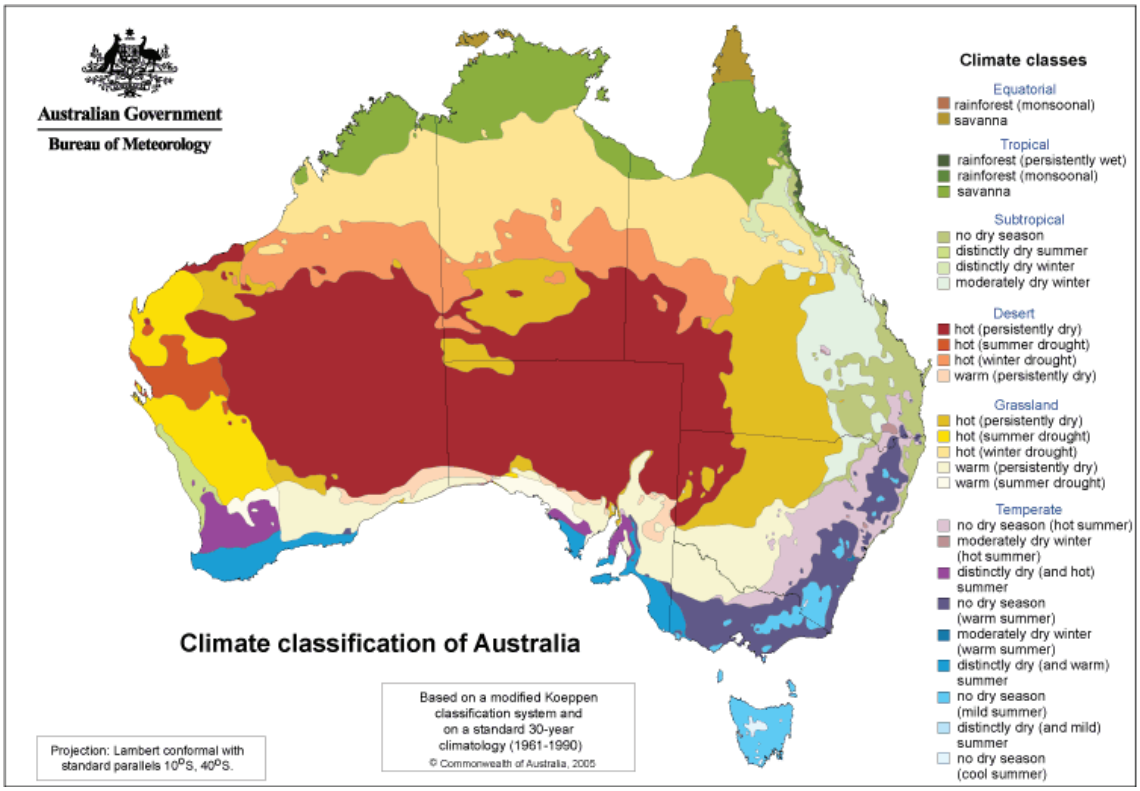

Figure 3.5: BoM climate classification of Australia (climate classes). Source: Australian Bureau of Meteorology [150]

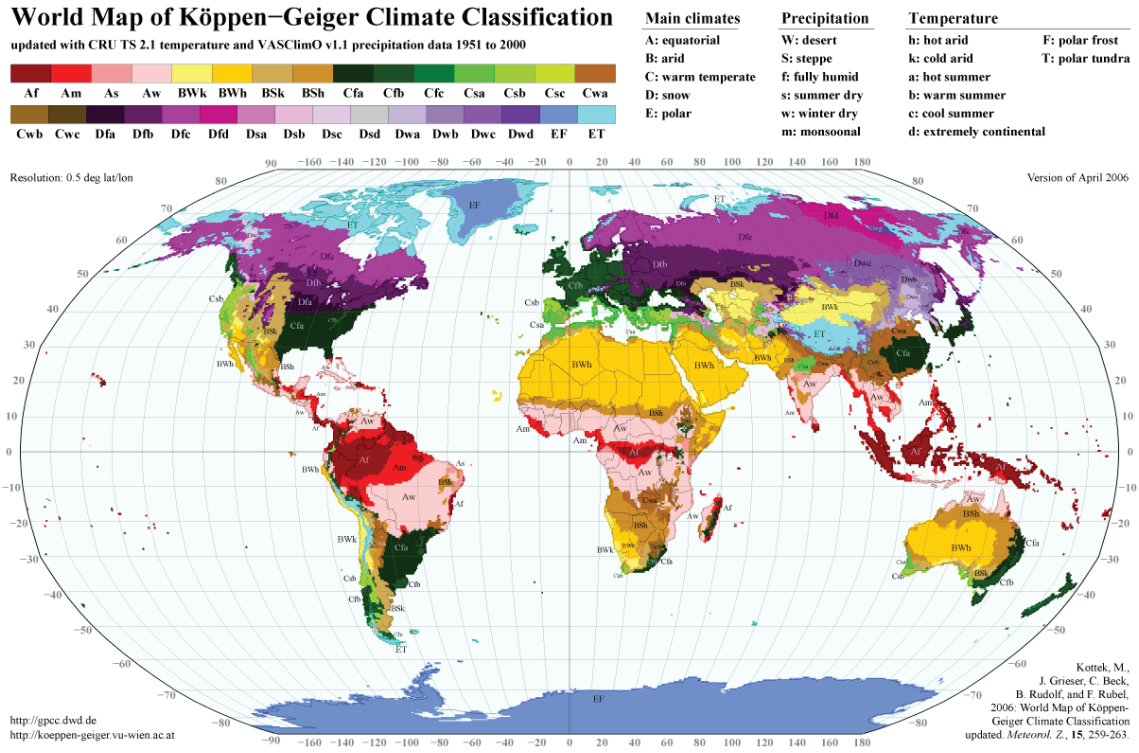

Figure 3.6: Köppen-Geiger climate classification world map. Source: Climate Change & Infectious Diseases Group [151]

methodology of Rubel et al. [145] undertaken in 2017 is considered in this research. The resultant reanalysis yielding the 10 arc-minute map reproduced as Figure 3.7 is used as the defining climate classification map of Australia.

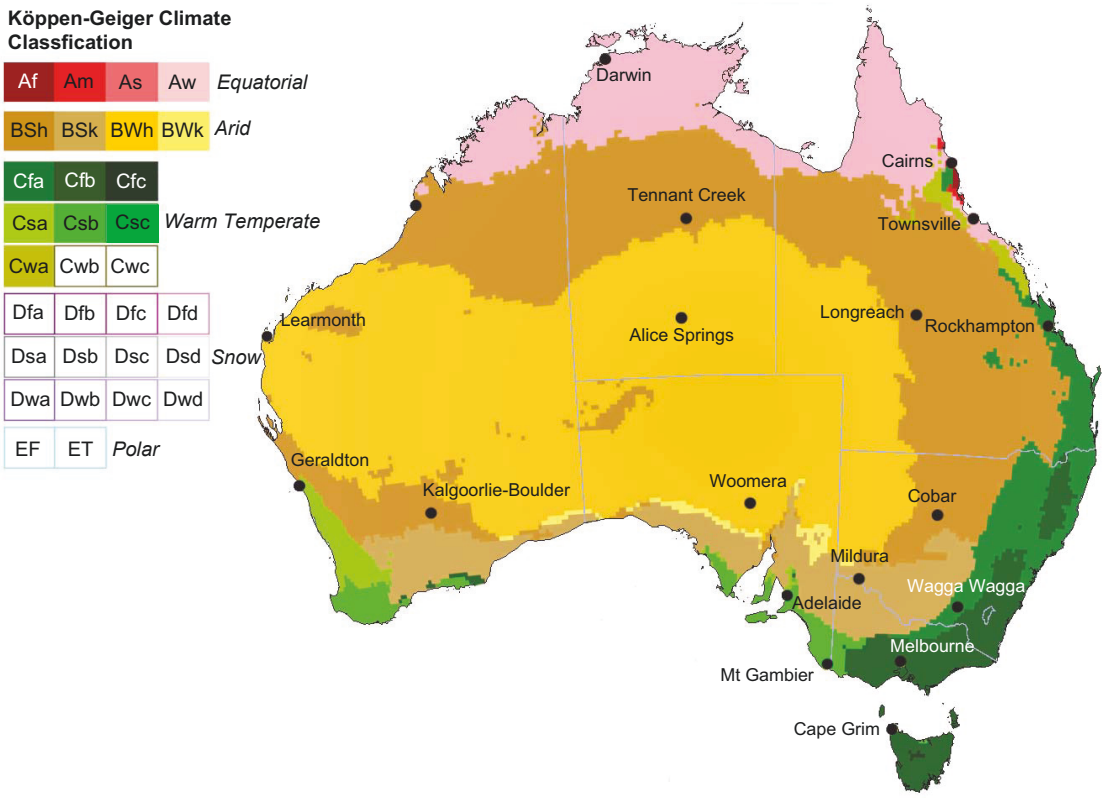

Figure 3.7: Köppen-Geiger climate classification for Australia based on re-analysis of Rubel et al. [145] adapted from [151]

Table 3.7: Köppen-Geiger climate classification divisions of Australia based on methodology of Rubel et al. [145] and location of One Minute Solar Stations

Köppen-Geiger Classification Divisions	BoM One Minute Solar Stations
Af	-
Am	Cairns
As	-
Aw	Darwin, Townsville
BSh	Broome, Cobar, Longreach, Kalgoorlie-Boulder, Tennant Creek
BSk	Mildura
BWh	Alice Springs, Learmonth, Woomera
BWk	-
Cfa	Rockhampton, Wagga Wagga
Cfb	Cape Grim, Melbourne
Cfc	-
Csa	Adelaide, Geraldton
Csb	Mt Gambier
Csc	-
Cwa	-

In the research presented in Chapter 4, the unique application of the Köppen-Geiger climate classification in the Seo and Krarti global irradiance model is the motivator for an extension to diffuse decomposition irradiation models, specifically the BRL diffuse model.

The diverse range of climate classifications within Australia highlights there is some scope to develop climate classification based diffuse irradiation models, as opposed to a single internationally tuned model. Furthermore, the low spatial density of ground-based diffuse and direct irradiation measurements within Australia places increased reliance on the accuracy of satellite-based estimates for solar energy system performance assessments. Improvements to diffuse estimates from satellite global irradiation using modified versions of the BRL model are investigated in Chapter 4.

3.4 Data Quality Control

To enable solar irradiation models to be developed, the accuracy of the irradiation data is critical. The measurement quality control procedures undertaken by meteorological organisations provide a first level of data quality assurance, however for numerous research applications, particularly the investigation of solar irradiation models, additional precise and fine control tests are necessary to remove questionable and erroneous data [152]. Lemos et al. [153] undertook a series of quality control tests on data gathered from the seventeen station network of the Environmental Data Organization System (SONDA) in Brazil. Similarly, Engerer and Mills relied on the QCRad process developed by Long and Shi [124] to remove erroneous measurements and improve the overall quality of data in order to investigate the accuracy of clear-sky irradiation models.

Younes et al. [154] undertook a review of existing quality control methodologies undertaken for solar irradiation related research and analysis. The methods of Page, Helioclim, Molineaux/Ineichen, NREL SERI QC, CIE and Muneer/Fairooz were reviewed with a view to propose a new procedure, taking learnings from existing methods.

The Page model developed for the ESRA and the Meteorological Office of the United Kingdom, sets upper and lower boundaries for diffuse irradiation and an upper boundary for global irradiation measurements.

The Helioclim quality control algorithm, developed as part of the SoDa project based on the Geiger et al. [99] web-based quality control service, is performed through comparing data against simulated clear-sky results and estimated extra-terrestrial irradiation. Consequently, the Helioclim method is based on likelihood control rather than a means for precise and fine control [152]. The procedure of Molineaux and Ineichen is also web-based and is used to output a series of coherence tests along plots for comparison between modelled and measured data.

The SERI QC programme of NREL establishes boundaries and limits within which acceptable data are expected to lie, similar to the Page and Helioclim methods. However, the SERI QC programme is far more sophisticated, enabling boundaries to be set for ranges of air masses, applied monthly to each station. The programme also provides a means to fill in data gaps following removal of erroneous values through an averaging technique using acceptable measurements of other irradiation components or if not available, irradiation models based on synoptic data.

The CIE automatic quality control procedure proposed that testing should not be conducted when global irradiance is less than 20 W/m^2 and when the solar altitude is

less than 4°. The procedure consists of five test levels including absolute limit checks on irradiation components, consistency checks based on redundancy between irradiation component measurements, tests related to irradiation/illuminance measured in the four cardinal directions, inter-comparison of irradiance/illuminance and a comparison of the zenith illuminance against diffuse illuminance.

The Muneer and Fairooz procedure is a combination of the page and CIE procedures with additional filters, consisting of five test levels. The first test applies the CIE procedure, while the remaining tests consist of consistency checks of measured components, expected diffuse ratio and clearness index envelopes for the removal of outliers, checks against the Page clear and overcast sky limits and finally calculation of Linke Turbidity and checking for its limits.

Based on the methodologies observed in existing literature, Younes et al. proposed a new semi-automatic quality control process [154]. First, preliminary filters are applied, including physical constraints on hourly clearness index k_T ($0 < k_T < 1$) and a more conservative approach to the removal of low solar altitude hours ($\alpha < 7°$ instead of 4° in the CIE procedure). The Page upper and lower boundaries for diffuse and global irradiation are then applied. Finally, a quality control envelope is established to remove outliers. A description of the envelope methodology is discussed in Section 4.2.1. The process, while largely automatic, requires human intervention to select the cut-off point of the envelopes at the extremes ends of the clearness index range to ensure envelope cross-over has not occurred. The envelope method of [154] was adopted in [152, 155] and also referenced by Lemos et al. [153] in the creation of an alternative envelope based on the logistic function.

In addition to the method proposed in [154] and the other methods outlined therein, Journée and Bertrand [152] developed a method for the Royal Meteorological Institute of Belgium (RMIB), intended for sub-hourly data such as 10 or 30 minute averages. The methodology applies tests for physical reasoning and statistical variability while spatial and temporal dependencies are also accounted for. The threshold values considered in the test are specific to the RMIB network and are therefore only applicable to low altitude European regions. The quality control envelope procedure of [154] is also applied but modified to set an upper limit on the clearness index. While most of the tests are automatic, the overall procedure is semi-automatic as some tests, such as impacts of snow and shadow and misleading calibrations, require a human identification.

The QCRad product by Long and Shi [124] follows the quality procedures of the BSRN, part of the WMO WCRP program. Long and Shi propose additional modifications by developing comparison tests for irradiation components and configurable climatological limits [155]. The procedures of the QCRad product are extensively referenced in [118, 153, 155]. The QCRad methodology was used by Engerer and Mills [118] to validate clear-sky irradiation models in Australia.

Lemos et al. [153] undertook a recent investigation of solar irradiation in Brazil with the objective of developing a country specific BRL diffuse model for hourly and sub-hourly data. The QCRad quality control tests developed by Long and Shi [124] were

applied. Additional checks following the methods of Younes et al. [154] and Journée and Bertrand [152] and the World Meteorological Organization were also applied.

The method of [153] first applied the same solar altitude limit proposed in [154], due to the high measurement uncertainty at sunrise and sunset and the low contribution to the overall daily irradiation. A set of physical tests were then applied, rejecting data outside the physical ranges of clearness index and diffuse fraction. Additionally, a range limit was placed on the persistence factor considered in the BRL irradiation model.

The QCRad quality control procedures of Long and Shi [124], testing for irradiation component consistency and plausibility, along with tracking system malfunctions were then applied. Based on guidelines by the WMO [156], a variability test was introduced to check for excessive irradiation fluctuations between successive observations.

A check for heavily overcast conditions was made by applying a lower limit on the global irradiation measurements and the daily average in accordance with the methodology of [152]. Conversely, cloud enhancement irradiation events were removed by checking against the Solis clear-sky model [96]. A lower bound was placed on diffuse irradiation in clear-sky conditions by considering the Rayleigh limit, defining the lowest amount of diffuse irradiation that can reach the Earth's surface in ideal clear-sky conditions. The Rayleigh limit test was based on the QCRad method [124].

Based on the arguably superior performance of a logistic function when fitting a single-curve against the diffuse fraction vs clearness index relationship [141, 153], Lemos et al. created outlier quality control envelopes by fitting a logistic function on the previously filtered data. However, the process was semi-automatic, requiring a human operator to translate the mean logistic function to upper and lower envelope boundaries based on visual inspection.

As a final filter, Lemos et al. discarded hours with less than 45 minutes of contributory observations prior to hourly averaging of the filtered irradiation data.

The quality control methodologies reviewed in this section are applied in the research presented in Chapter 4 aiming to develop a Köppen-Geiger BRL diffuse model adjustment for Australian locations. The specific quality control methodologies used are defined in the next chapter.

3.5 Solar Irradiation on a Tilted Surface

After establishing hourly irradiation models on a horizontal plane as presented in Section 3.2, to enable the assessment of solar PV energy yield, models for transposing horizontal irradiation onto a tilted plane are required. This section provides a general review of various transposition models and model comparisons presented in literature.

Tilted plane irradiation models are divided into two categories – isotropic and anisotropic [115, 131]. In isotropic models, diffuse irradiation is considered to be uniform across the entire sky dome. Consequently, the total irradiation on the tilted plane may be expressed as:

$$I_T = B_T + D_T + R_T \tag{3.44}$$

where B_T, D_T and R_T are the total direct (beam) irradiation, diffuse irradiation and ground reflected irradiation on the tilted plane respectively [157].

Anisotropic models consider the diffuse irradiation to be non-uniform and attempt to incorporate additional irradiation components such as circumsolar diffuse (the forward scattering of solar irradiation around the solar disc) and horizon brightening (concentrated diffuse irradiation near the horizon most prominent on clear days) [115]. Consequently, the diffuse term in (3.44) may be broken into several components to give a more complete expression for irradiation on a tilted surface defined as:

$$I_T = I_b R_b + I_{d,iso} F_{c-s} + I_{d,cs} R_b + I_{d,hz} F_{c-hz} + I \rho_g F_{c-g} \tag{3.45}$$

where I_b is the direct irradiation, R_b is as defined in (3.14), $I_{d,iso}$ is the isotropic component of diffuse irradiation, $I_{d,cs}$ is circumsolar diffuse, $I_{d,hz}$ is horizon brightening diffuse, ρ_g is the composite ground reflectance and the F_{x-y} terms are the corresponding view factors for each irradiation component [115].

Remark 3.4 *When utilising observed horizontal solar irradiation data to determine the irradiation on a tilted surface, care must be taken during the solar hours containing sunrise or sunset. As the solar zenith angle approaches sunset hour angle, the term* $\cos\theta_z$ *becomes small and consequently* R_b *becomes large. If any direct irradiation is observed during the period, multiplying it by the large* R_b *may yield values that exceed the solar constant [115]. A solution is to either ignore the solar hours containing sunrise or sunset, or alternatively redefine the expression of (3.14) from an instantaneous one to one integrated over time [115]. According to Duffie and Beckman, the average* R_b *during the sunrise and sunset hours may be expressed according to (3.46)–(3.49) where* ω_1 *and* ω_2 *are the sunrise and sunset hour angles respectively. During sunrise and sunset hours, (3.46) provides a far more reasonable magnitude for* R_b *than (3.14).*

$$R_{b,avg} = \frac{a}{b} \tag{3.46}$$

$$\begin{aligned} a = {} & (\sin\delta \sin\phi \cos\beta - \sin\delta \cos\phi \sin\beta \cos\gamma)(\omega_2 - \omega_1) \\ & + (\cos\delta \cos\phi \cos\beta + \cos\delta \sin\phi \sin\beta \cos\gamma)(\sin\omega_2 - \sin\omega_1) \qquad (3.47) \\ & - (\cos\delta \sin\beta \sin\gamma)(\cos\omega_2 - \cos\omega_1) \qquad (3.48) \end{aligned}$$

$$b = (\cos\phi \cos\delta)(\cos\omega_2 - \cos\omega_1) + (\sin\phi \sin\delta)(\omega_2 - \omega_1) \tag{3.49}$$

3.5.1 Transposition Model Comparisons in Literature

Numerous models have been developed to define incident irradiation on a tilted surface based on measured horizontal irradiation. Three models particularly prominent in literature include the Liu and Jordan model (isotropic) [158], Hay-Davies-Klucher-Reindl (HDKR) model (anisotropic) [137] and Perez (1990) model (anisotropic) [159].

According to Duffie and Beckman [115], the Perez model is the least conservative of the three models and has been shown to be the most accurate, particularly for west

facing solar surfaces [131,160,161] or in general, surfaces with azimuths far from zero. For surfaces facing the equator, Duffie and Beckman recommend the use of the HDKR model due to its relative simplicity compared to the Perez (1990) model.

Comparative evaluations for irradiation transposition models have been performed by numerous authors for the Liu and Jordan, HDKR and Perez models among others. Khoo et al. [162] compared the Liu and Jordan, HDKR and Perez (1990) models against measured data in Singapore, finding the Perez model to be the most accurate. Noorian et al. [131] and Khalil and Shaffie [160] evaluated the performance of numerous models against measured irradiation data for south and west facing surfaces in Iran and Egypt respectively and found the Perez (1990) model to be the most accurate for both surface orientations.

Wattan and Janjai [161] assessed the performance of fourteen models against measured data in Thailand for various inclined surface orientations. While the HDKR and Perez (1987) models performed comparatively well, it was found that two other models by Gueymard [163] and Muneer [164] were slightly more accurate across the entire orientation range. However, it should be noted that for tilt angles of 60 degrees or less, the Perez (1987) model out-performed all other models.

Gueymard [165] reviewed the effect of direct and indirect irradiation uncertainties for tilted surface irradiation estimates. Ten models were assessed including Liu and Joran (isotropic) [158], HDKR [165], Perez (1990) [159], Gueymard [163], Muneer [164], Hay [166] and Skartveit and Olseth [167] among others. The Perez and Gueymard models were shown to perform the best when considering clear-sky conditions only. However, when considering all-sky conditions and in situations where only global irradiation was known, the HDKR model demonstrated the best performance.

David et al. [168] assessed four tilt models for application in a southern hemisphere location. The Hay [166], Skartveit and Olseth [167], Gueymard [167] and Perez (1987) [169] models were assessed. The Perez model was shown to perform the best with both hourly and minutely data.

Copper presented a summary of comparative studies for irradiation tilt models in a PhD thesis [127], surmising that no single tilt model has been shown to perform the best for all locations and at all ranges of tilt and azimuth. However, Copper noted that generally the Perez model were shown to have the best average performance [127].

A review conducted by Freeman et al. [170] for NREL compared the HDKR and Perez models against measured data from an existing PV array. Although the models yielded similar results, Freeman et al. found the Perez model provided slightly better correlations.

In addition to the comparative evaluations in literature, the Liu and Jordan, HDKR and Perez models have found extensive applications in proprietary solar irradiation and PV array performance modelling software. PVsyst, as the industry leading software program for large-scale solar PV system modelling, uses the Hay [166] and Perez [159] transposition models. The developers noted that the Perez model is sensitive to the accurracy of diffuse irradation data [171], an observation supporting the research of [165], and stated previously that the use of the model was not justified unless hourly irradiance data are available.

However, it was also noted that recent research by Ineichen [172] concluded that the Perez model is slightly better. When applied using PVsyst, the estimates tend to be less conservative than the Hay model, with estimates up to 2% higher depending on location [171]. Helioscope, a cloud based platform by Folsom Labs, also allows users to choose between the Hay and Perez models [173].

Other platforms such as the HOMER microgrid optimisation software utilise the HDKR model [174] while the NREL System Advisor Model enables users to choose between the Liu and Jordan (isotropic), HDKR and Perez models [170]. The Sandia National Laboratory PVLIB toolbox for Matlab allows either the Liu and Jordan, HDKR, Perez or a fourth model known as the Simple Sandia Model developed for the Sandia National Laboratory to be selected [175].

Given the prevalence of the Liu and Jordan, HDKR and Perez (1990) models in energy yield assessment software platforms and the demonstrated performance of the HDKR and Perez models in comparative studies, the mathematical formulation for each model is summarised in Section 3.5.2 to Section 3.5.4 for reference. The final model selected for use in this research is established in Section 3.5.5.

3.5.2 Liu and Jordan Model

The Liu and Jordan model [158] was one of the earliest established models. The model is the most conservative as it consistently underestimates incident solar irradiation but has nonetheless been utilised by numerous authors in literature pertaining to PV panel tilt optimisation [176, 177].

The Liu and Jordan model, defined in (3.50) is an isotropic model and is therefore relatively simple as the circumsolar and horizon brightening components of (3.45) are ignored. The diffuse irradiation view factor F_{c-s} between the solar collector and the sky and the reflected irradiation view factor F_{c-g} between the solar collector and the ground are expressed as a function of collector tilt β.

$$I_T = I_b R_b + I_d \left(\frac{1 + \cos\beta}{2} \right) + I\rho_g \left(\frac{1 - \cos\beta}{2} \right) \tag{3.50}$$

3.5.3 HDKR Model

The HDKR model was iteratively updated [115] by expanding upon the anisotropic model originally developed by Hay and Davies [166, 178]. Reindl et al. [137] amended the Hay and Davies model to incorporate a modified version of the Temps and Coulson horizon brightening factor [179] as proposed by Klucher [180].

The HDKR model is effectively an extension of the original Liu and Jordan model to include additional diffuse components for circumsolar and horizon brightening irradiation.

The HDKR model is expressed as:

$$I_T = (I_b + I_d A_i) R_b + I_d (1 - A_i) \left(\frac{1 + \cos\beta}{2}\right) \left[1 + f \sin^3\left(\frac{\beta}{2}\right)\right] + I\rho_g \left(\frac{1 - \cos\beta}{2}\right) \tag{3.51}$$

where A_i is the anisotropy index accounting for forward scattering of circumsolar irradiation defined as:

$$A_i = \frac{I_b}{I_o} \tag{3.52}$$

and f is a modulating factor of the horizon brightening term $\left[1 + f \sin^3\left(\frac{\beta}{2}\right)\right]$ to account for cloudiness defined as:

$$f = \sqrt{\frac{I_b}{I}} \tag{3.53}$$

3.5.4 Perez Model

The Perez (1990) model [159] (hereafter referred to as the Perez model) is the latest model in a series of progressive improvements undertaken by Perez et al. [169, 181]. The Perez model is based on a far more detailed analysis of the diffuse components of the anisotropic model and features statistically derived brightness coefficients based on hourly diffuse irradiation observations.

According to the Perez model, the diffuse irradiation incident on a tilted plane can be described by the following:

$$I_{d,T} = I_d \left[(1 - F_1)\left(\frac{1 + \cos\beta}{2}\right) + F_1 \frac{a}{b} + F_2 \sin\beta\right] \tag{3.54}$$

where F_1 and F_2 are the circumsolar and horizon brightening coefficients respectively and a and b are terms accounting for the angles of incidence of the cone of circumsolar irradiation [115]. The a and b terms are described as:

$$a = \max(0, \cos\theta) \tag{3.55}$$

$$b = \max(\cos 85, \cos\theta_z) \tag{3.56}$$

The brightness coefficients F_1 and F_2, are functions of the zenith angle θ_z, a clearness index ϵ and a brightness index Δ. The clearness and brightness indexes are described as:

$$\epsilon = \frac{\frac{I_d + I_{bn}}{I_d} + 5.535\mathrm{e}^{-6}\theta_z^3}{1 + 5.535\mathrm{e}^{-6}\theta_z^3} \tag{3.57}$$

$$\Delta = m\frac{I_d}{I_{on}} \tag{3.58}$$

where m is air mass, I_{bn} is the direct normal incident irradiation and I_{on} is the extra-terrestrial normal incident irradiation.

The brightness coefficients F_1 and F_2 are functions of statistically derived coefficients for ranges of the clearness index ϵ [115] as shown in (3.59) and (3.60). Details of the recommended set of coefficients, as prescribed by Perez et al. [159], are provided in Table 3.8.

$$F_1 = \max\left(0, f_{11} + f_{12}\Delta + \frac{\pi\theta_z}{180} f_{13}\right) \tag{3.59}$$

$$F_2 = f_{21} + f_{22}\Delta + \frac{\pi\theta_z}{180} f_{23} \tag{3.60}$$

Table 3.8: Brightness coefficients for Perez anisotropic sky. Source: Perez et al. [159]

Range of ϵ	f_{11}	f_{12}	f_{13}	f_{21}	f_{22}	f_{23}
1.000-1.065	-0.008	0.588	-0.062	-0.06	0.072	-0.022
1.065-1.230	0.13	0.683	-0.151	-0.019	0.066	-0.029
1.230-1.500	0.33	0.487	-0.221	0.055	-0.064	-0.026
1.500-1.950	0.568	0.187	-0.295	0.109	-0.152	0.014
1.950-2.800	0.873	-0.392	-0.362	0.226	-0.462	0.001
2.800-4.500	1.132	-1.237	-0.412	0.288	-0.823	0.056
4.500-6.200	1.06	-1.6	-0.359	0.264	-1.127	0.131
6.200-inf	0.678	-0.327	-0.25	0.156	-1.377	0.251

With reference to (3.55)–(3.60) defined above, the total irradiation on the tilted plane according the Perez model, including direct, isotropic diffuse, circumsolar diffuse, diffuse from the horizon and ground reflected irradiation [115] is defined as:

$$I_T = I_b R_b + I_d\left(1 - F_1\right)\left(\frac{1+\cos\beta}{2}\right) + I_d F_1 \frac{a}{b} + I_d F_2 \sin\beta + I\rho_g\left(\frac{1-\cos\beta}{2}\right) \tag{3.61}$$

3.5.5 Selected Transposition Model

Although the Perez model has been shown to generally outperform other transposition models [131, 160, 162], the HDKR model has also been shown to perform well across a variety of locations and climates [161,165]. The complexity of the Perez model places it at a distinct disadvantage when applied to the design optimisation analyses presented in the subsequent chapters of this research. The increased complexity of the Perez model requires additional computation time, a penalty which cannot be discounted. For system design optimisation involving thousands of calculations to reach a solution for a multitude of test installations, the Perez model is at a distinct disadvantage. Consequently, for the purposes of this research and the optimisation problems presented in the remaining chapters, the HDKR model, as defined in (3.51), is assumed.

3.6 Summary

An introduction to solar irradiation modelling was presented in this chapter. Available solar irradiation databases, including both ground-based and satellite-based observations, were summarised with specific consideration given towards Australian applications.

Concepts associated with solar geometry were explored as the basis for the establishment of models associated with irradiation on the horizontal plane. Clear-sky irradiation models were reviewed with the ESRA clear-sky model described in detail based on its established performance in literature under Australian conditions, intended for application in the quality control tests conducted for the research detailed in Chapter 4.

Models for global irradiation were briefly discussed. A particular variant by Seo and Huang [130], based on the Köppen-Geiger climate classification system and since used to develop the IWEC2 weather files, was established as a motivator for the original research undertaken in this thesis, presented in Chapter 4.

Diffuse and direct irradiation components were introduced. A summary of numerous reviews conducted in literature assessing the multitude of diffuse models developed was presented. The BRL model by Ridley et al. [58] was found to perform well in both global and Australian conditions and selected for further improvement in Chapter 4, through application of the Köppen-Geiger climate classification system.

Finally, transposition models to calculate irradiation on the horizontal plane were reviewed. Based on widely accepted applications in literature and energy yield modelling software, the Perez and HDKR model were considered to be superior. The HDKR model's simplicity and efficiency of calculation were considered to be the justification for application to the PV design optimisation methodologies presented in subsequent chapters of this thesis.

Chapter 4

Köppen-Geiger BRL Diffuse Irradiation Models

Improvements to solar irradiation resource assessments enable solar PV system energy yield uncertainty to be reduced. Site-specific irradiation assessments are facilitated by existing networks of irradiation component measurement stations which are particularly sparse in an Australian context. The Australian BoM, which operates the ground-based network of OMS measurement stations, has only commissioned 21 stations (eight of which have since closed) for the entire country.

Measurement of global irradiation is less cost restrictive, compared to the measurement of direct and diffuse components, as only a single pyranometer sensor is required. Satellite-based global irradiation estimates are also available, such as the HSI database maintained by BoM, providing hourly and in some cases, sub-hourly irradiation data with complete global coverage.

Numerous models have been developed to describe either the diffuse or direct components based on global irradiation and other meteorological parameter measurements. One such model, commonly referred to as the BRL diffuse model has been shown to be amongst the most accurate models [58, 132, 138], performing well in Australian climates [121]. The model consists of a single set of parameters defining an empirical logistic function to describe diffuse irradiation based on global irradiation measurements or estimates only. As the model includes a universal set of parameters, no allowance is provided for different climatic areas.

The simple form, accuracy and low computational demand of the BRL model makes the model an attractive option amongst the multitude of other models, many of which have considerable complexity. BoM applies a slightly adjusted version of the BRL model for use as part of its HSI service specific to Australian locations. However, the BoM adjusted BRL model, similar to the original BRL model, does not take into account the large climatic diversity of the Australian continent.

Research on global irradiation models has found merits in developing model variants for specific climates. The Seo and Krati variation on the Zhang and Huang global irradiation model applies the widely adopted Köppen-Geiger climate classification system to develop models for various climate types [130].

In this research, the concept of climate zone based irradiation models is extended for the application to the BRL model specifically for Australian locations and climates. Using data from the BoM network of OMS stations, techniques for irradiation data quality control are applied to create high quality data sets from which the BRL model is adjusted. A new national-level model is developed for the Australian mainland while climate zone models using the Köppen-Geiger climate classification system are developed for Australian climate zones. The estimates of the new adjusted BRL models are compared against the original BRL model.

Given the high reliance on satellite-based irradiation estimates for Australian applications, this research extends the Köppen-Geiger zone adjusted BRL model methodology to satellite data. A subset of the BoM HSI database made available via the AREMI spatial mapping infrastructure platform is analysed and compared against ground-based data to determine the accuracy improvements that may be gained. In parallel to the Köppen-Geiger models developed for satellite data, a new Australian national-level model, tuned using a quality controlled data set is also developed and compared against the BoM adjusted BRL model estimates within the AREMI database.

4.1 Improved BRL Model

In this research, the application of the Köppen-Geiger climate classification system to Australian irradiation data is investigated to establish potential improvements over the original BRL and BoM modified BRL models through climatological classification considerations.

Two main model categories are developed, each with two sub-categories as follows:

(i) New national-level Australian BRL models

  (a) Original BRL method (persistence factor)

  (b) BRL with BoM variability term (3.38) replacing persistence

(ii) BRL models for each Köppen-Geiger zone in Australia

  (a) Original BRL method (persistence factor)

  (b) BRL with BoM variability term replacing persistence

A third level is also developed for each BoM OMS station for initial comparison purposes only – comparing the original BRL model against models tuned for a specific location.

During earlier work, Boland et al. [141] did not perform any rigorous quality control procedures aside from the application of an author-developed quadratic programming process to identify values with a high probability of infeasibility, as opposed to direct testing against physical and statistical constraints. In this research, extensive quality control tests are applied to raw minutely data to improve the accuracy of the input data used to calibrate the BRL models. The methodologies adopted to first filter the data and then develop new BRL models and undertake statistical analyses of the resultant irradiation estimates are presented in Section 4.2.

Following irradiation data filtering, local BRL models for each station are fitted, representing the closest possible BRL model fit for a specific location. Plots to visually demonstrate the potential improvement over the original BRL model are provided in Section 4.3.

However, the practical application of BRL models specific to a single location is limited given the limited availability of sites measuring diffuse irradiance. The new National BRL models are developed from an amalgamated set of filtered data based on observations from all BoM OMS stations. To facilitate a compromise between the large quantity of data at the national-level and specific locational tuning, the climatological coverage of the BoM OMS network is leveraged to develop a limited number of BRL models for the Australian continent. Consequently, the establishment of BRL models based on Köppen-Geiger zones is investigated in Section 4.3 as a potential improvement over a single national model.

The low spatial coverage of ground-based measurement locations with a minimum data output consisting of GHI is a materially limiting factor for energy yield prospecting analysis. Although significantly higher than the density of high frequency tracking stations operating within the BoM OMS network, GHI-only measurements locations in Australia are sparse.

Satellite-based observations from the BoM HSI and AREMI databases present an opportunity for complete GHI spatial coverage. The BoM HSI database retains hourly solar irradiation values estimated from satellite observations. As detailed in Section 3.1.2, the outputs from the BoM HSI database up to 2015 are included in the AREMI database. As AREMI is a publicly accessible tool providing universal spatial coverage for the continent of Australia at zero cost, AREMI data were considered for this research. As detailed in Section 3.2.8.1, BoM applies a modified version of the BRL correlation to estimate DNI irradiation. In Section 4.4, a new adjusted BRL model at the national-level and models based on Köppen-Geiger zone classifications are tested on the AREMI data. The objective is to determine if the irradiation component estimates of DHI and DNI can be improved through climatologically specific considerations.

4.2 Research Methodology

4.2.1 Quality Control Methodology

Given the similarity of objectives presented in this research to the investigations by Lemos et al. [153], the quality control process adopted in [153] was applied to this research with some minor modifications:

(i) The ESRA clear-sky model was applied to the cloud enhancement and "tracker-off" tests as opposed to the Solis clear-sky model due to its demonstrated performance in Australian locations (refer Section 3.2.6 and [118]).

(ii) A modified quality control envelope based on the methodology of [152] and [154] is applied to the average hourly data.

(iii) Hourly and daily parameters for clearness index and persistence factor are recalculated following the application of the final data filters.

The quality control process used in this research is detailed Table 4.1. With the exception of the adoption of the ESRA clear-sky model, the Lemos et al. methodology was adopted up to the construction of hourly data outlier envelopes.

Remark 4.1 *In this research, the outlier envelope method of Lemos et al. was not used due to its semi-automatic nature rather than a statistical approach based on standard deviations within a sub-set of the clearness index range. Consequently, the original envelope methodologies of [152] and [154] are applied in this research, as they largely follow a more automated process.*

The Younes et al. [154] quality control envelope is applied in this research. The method is based on dividing the clearness indices into bins (ten bins are nominated) and calculating means for diffuse fraction d and clearness index k_T and the standard deviation of diffuse fraction (σ_d) within each bin. The upper and lower outlier envelope is then formed by $d \pm 2\sigma_d$ for each bin mean $\overline{k_T}$ and fitting a second-order polynomial through the points.

The method of [154] is also semi-automatic as it requires visual inspection of the shoulder effects at the extreme ends of the clearness index range whereby the upper and lower boundaries may cross each other. In this research, the need to visually inspect each plot is removed through an automated procedure to introduce a piece-wise adjustment of the lower envelope boundary. At low clearness indexes, data dispersion for d–k_T plots reduces and the resultant curve connecting each clearness index bin mean $\overline{k_T}$ flattens out. A limit is set on the polynomial curve for the lower boundary whereby for lower clearness values, the ordinate (diffuse fraction) of the envelope remains constant, i.e. the lower boundary is limited to be less than $-2.5\sigma_d$.

For high clearness indexes, the method of Journée and Bertrand [152] is adopted to identify obvious outliers. The outlier envelope boundary is made vertical at a maximum clearness index $k_{T,max}$ whereby all clearness indexes higher than $k_{T,max}$ are at least 0.02 higher. Therefore for all data points with the associated $k_{T,i}$ values arranged in ascending order of magnitude, where $i \in \{1, \ldots, n-1\}$ and n is the number of hourly data points, the upper clearness index limit boundary is defined as follows:

$$k_{T,max} = \max\left(k_{T,i}\right), \text{ where } \left|k_{T,i} - k_{T,i+1}\right| > 0.02 \tag{4.1}$$

Furthermore, in [152] the overall envelope was defined to be $\pm 5\sigma_d$ rather than $\pm 2\sigma_d$ as proposed in [154], giving an approximately 25% wider envelope with the intention of avoiding unnecessary rejection of valid data. Based on visual inspection of the data for Australian locations, an envelope based on $\pm 5d$ appeared to be too wide. Instead, an envelope of $\pm 2.5\sigma_d$ is applied in this research.

A summary of the modifications to the Younes et al. [154] envelope process applied in this research is as follows:

(i) Increase number of clearness index bins to 15 (from ten) to improve efficacy of polynomial fitting.

(ii) Restrict lower envelope boundary to less than $-2.5\sigma_d$ at low clearness indexes.

(iii) Adopt the maximum clearness index boundary $k_{T,max}$ of [152].

(iv) Define the envelope to be $\pm 2.5\sigma_d$ rather than $\pm 2\sigma_d$.

The complete historical ground-based solar irradiation data records of the BoM OMS database for 19 weather stations in mainland Australia and Tasmania were subjected to the rigorous quality control tests detailed in Table 4.1. The procedure is further outlined in the flow chart of Figure 4.1. Linke Turbidity data, as an input to the ESRA clear-sky model, was derived from the SoDa database [48]. SoDa was also used for air pressure data at each location assessed as inputs into the Rayleigh limit test.

Following the application of the quality control tests in Step 1 of Figure 4.1, many of the minutely irradiation data are rejected. To ensure excessive data rejection does not misrepresent the hourly irradiation used in the BRL model development, hours with less than 45 minutes of data are not considered as outlined in Step 2 of Figure 4.1, similar to the methodology of [153].

Examples of the minutely data filtering process for the Melbourne, Wagga Wagga and Townsville BoM weather stations are presented in Figure 4.2 to Figure 4.10. The data quality control process of [153] in Step 1 of Figure 4.1 is first applied to the OMS data as shown in Figures 4.2 to 4.4. The results of Step 2 are shown in Figures 4.5 to 4.7. The removal of outliers in hourly data calculated from cumulative minutes within the hour in Step 3 is shown in Figures 4.8 to 4.10.

A percentage breakdown of the data retained in each quality control step is provided in Table 4.2 for each BoM OMS station. In Step 1, on average 55% of minutely data are retained for each station. In Step 2, 21% of the previously accepted hourly data are rejected following the application of the minute threshold filter process. Finally, following the removal of outliers in Step 3, 98% of the remaining data are retained. Overall, on average 43% of data are retained across all 19 OMS stations to be used for the development of the adjusted BRL models proposed in this research.

4.2.2 Statistical Indicators

Numerous statistical indicators have been used in literature as part of the error analysis process to establish the accuracy of solar irradiation models. These include:

- Median absolute percentage error (MeAPE)
- Root mean square error (RMSE)
- Mean bias error (MBE)
- Coefficient of determination (R^2)
- Kolmogorov-Smirnov Integral (KSI)

Table 4.1: Quality control tests for raw solar irradiation data

Step	Test	Description	Reference	Criteria
(i)	Physical Tests	Solar altitude limit.	[154]	$\alpha < 7^\circ$
		Persistence factor plausibility.		$0 < \psi < 1$
		Clearness index limits (minute, hour, day).		$0 < k_t, k_T, K_T < 1$
	Consistency	Diffuse fraction limit.		$0 < d < 1$
		Check if irradiation component measurements are consistent.	[124]	$\lvert\frac{I-(I_d+I_{bn}\sin\alpha)}{I}\rvert < 0.08$, if $\alpha > 15^\circ$ and $I_d + I_{bn}\sin\alpha > 50$ $\lvert\frac{I-(I_d+I_{bn}\sin\alpha)}{I}\rvert < 0.15$, if $\alpha < 15^\circ$ and $I_d + I_{bn}\sin\alpha > 50$ If $I_d + I_{bn}\sin\alpha < 50$, test not possible
	Plausibility	Plausible limits for irradiation (W/m^2) based on the solar constant adjusted for the earth-sun distance, i.e. $G = G_{sc}(1-\epsilon^2)/(1+\epsilon\cos(360n/365))$ where ϵ is orbit eccentricity.	[124]	$0 < I < 1.5G(\sin\alpha)^{1.2} + 100$ $0 < I_d < 0.95G(\sin\alpha)^{1.2} + 50$ $0 < I_{bn} < G$
	"Tracker-off" Test	Check for tracking system malfunctions.	[124]	If $\frac{I}{I_c} > 0.85$ and $\frac{I_d}{I} > 0.85$, reject
	Data variability Test	Check irradiation values between successive time stamps (W/m^2).	[156]	$\lvert I_i - I_{i-1}\rvert < 800$ and $\lvert I_{i+1} - I_i < 800$
	Heavily Overcast Conditions	Lower bound on global irradiation (W/m^2).	[152]	$\frac{I}{I_o} \geq 10^{-4}(\alpha - 10)$, if $\alpha > 10$ $\mu\left(\frac{I}{I_o}\right) \geq 0.03$, day average
	Cloud Enhancement	Remove high irradiation values attributable to cloud enhancement by checking against clear-sky conditions.	[153]	$\frac{I}{I_c} < 1.1$
	Rayleigh Limits	Compare Rayleigh lower limit to diffuse irradiation.	[124]	For $R_L = 209.3\sin\alpha - 708.3(\sin\alpha)^2 + 1128.7(\sin\alpha)^3$ $-911.2(\sin\alpha)^4 + 287.87(\sin\alpha)^5 + 0.046725(\sin\alpha)P$ If $I > 50$ and $d < 0.8$ and $I_d < R_L - 1$, reject
(ii)	Sub-hourly Data Limits	Check quantity of minutely data (m) in each hour after all other filters.	[153]	If $m < 45$, reject hour
		Statistical assessment of clearness index bins to establish upper and lower measurement boundaries.	[154]	If outside outlier envelope, reject
(iii)	Quality Envelope	Define upper limit of clearness index $k_{t,max}$ by removing sparse outliers amongst n data points clearness indexes are ordered by magnitude.	[152]	$k_{t,max} = max(k_{T,i})$ where $\lvert k_{T,i} - k_{T,i+1}\rvert > 0.02$

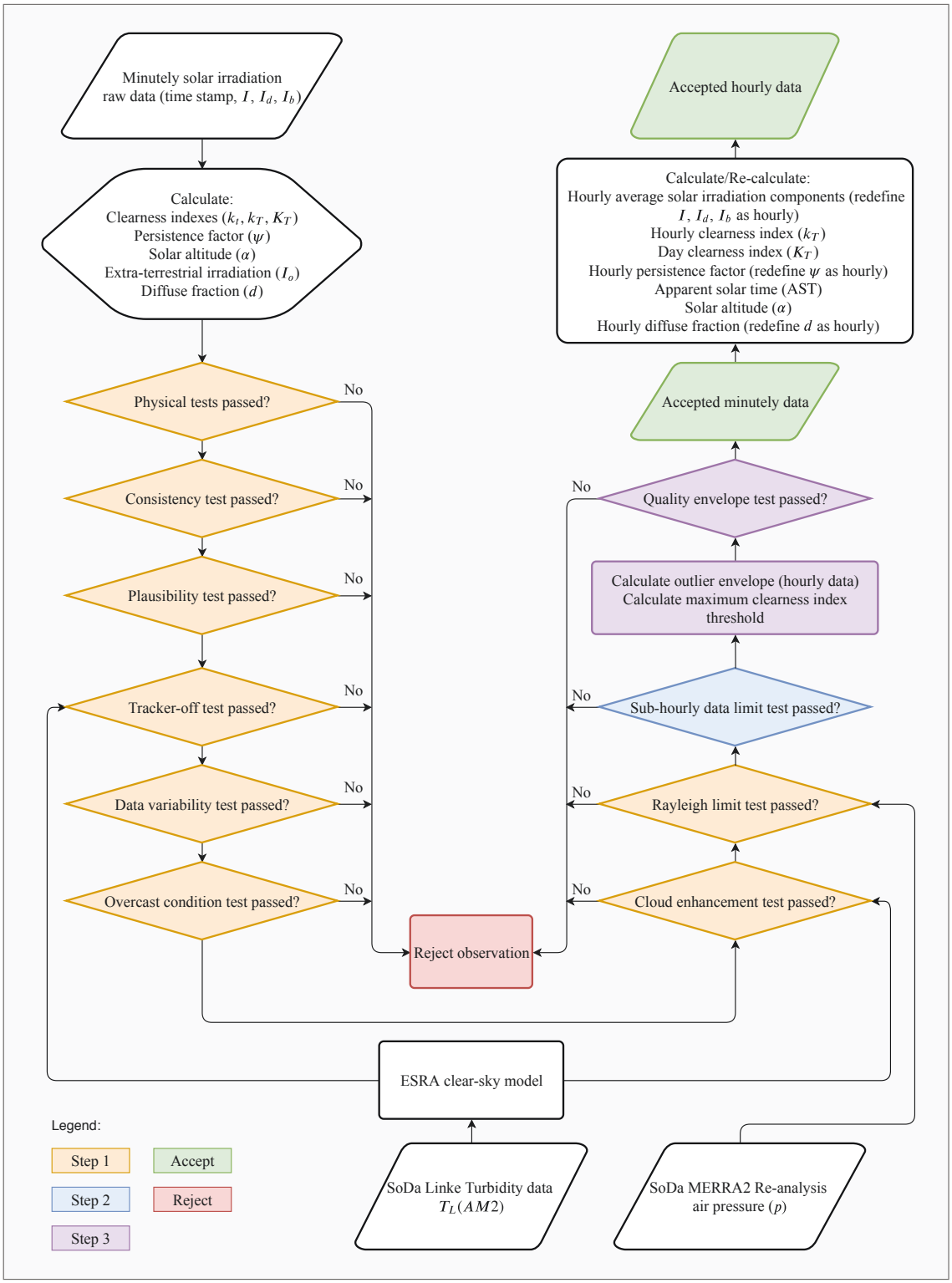

Figure 4.1: Solar irradiation data quality control process flow chart

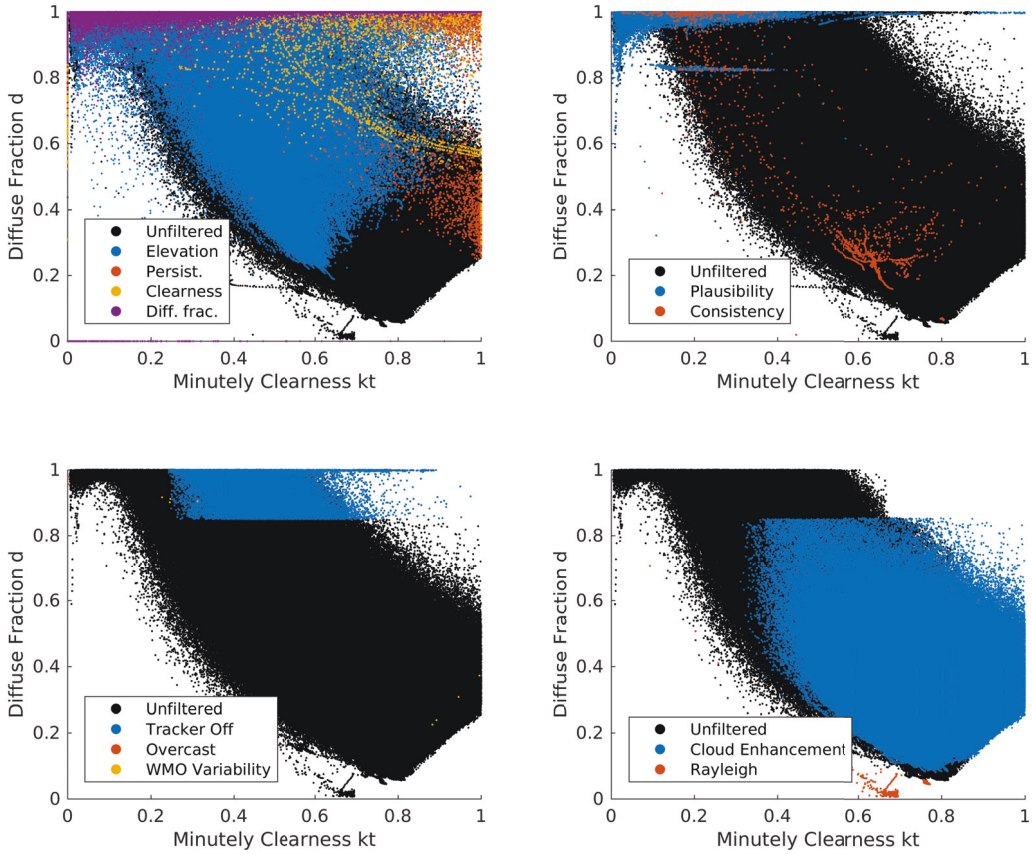

Figure 4.2: Quality control tests and filtering process for the BoM Melbourne station

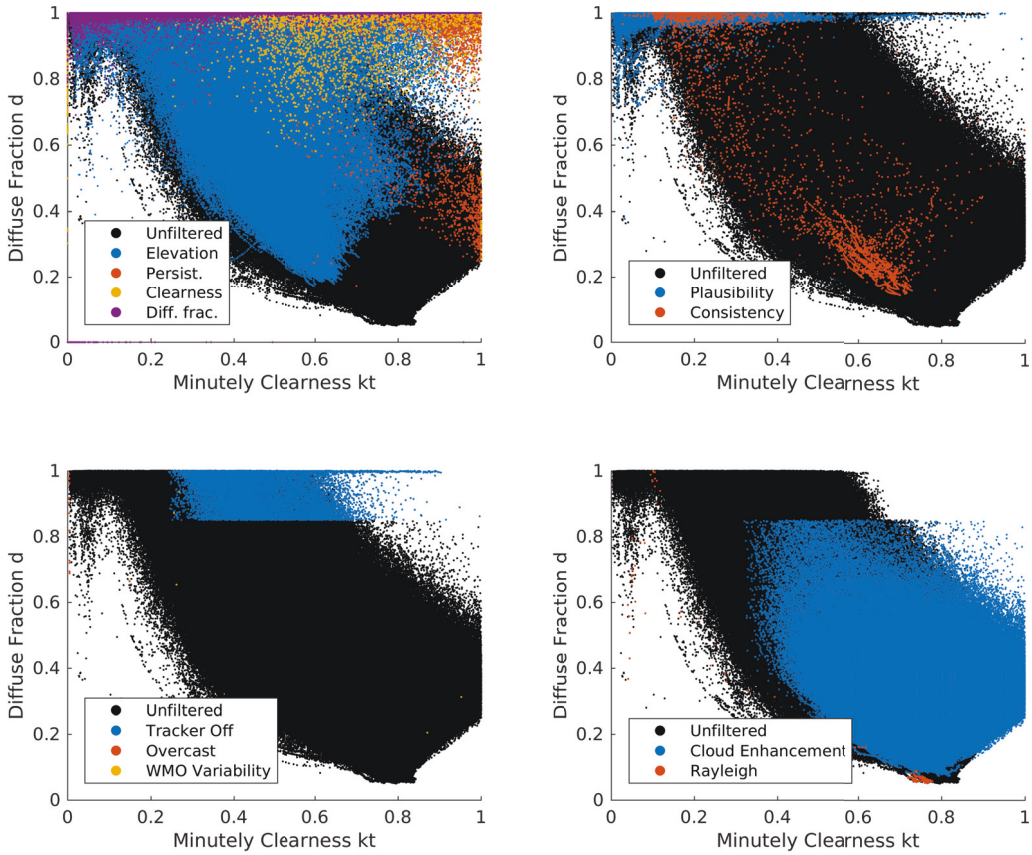

Figure 4.3: Quality control tests and filtering process for the BoM Wagga Wagga station

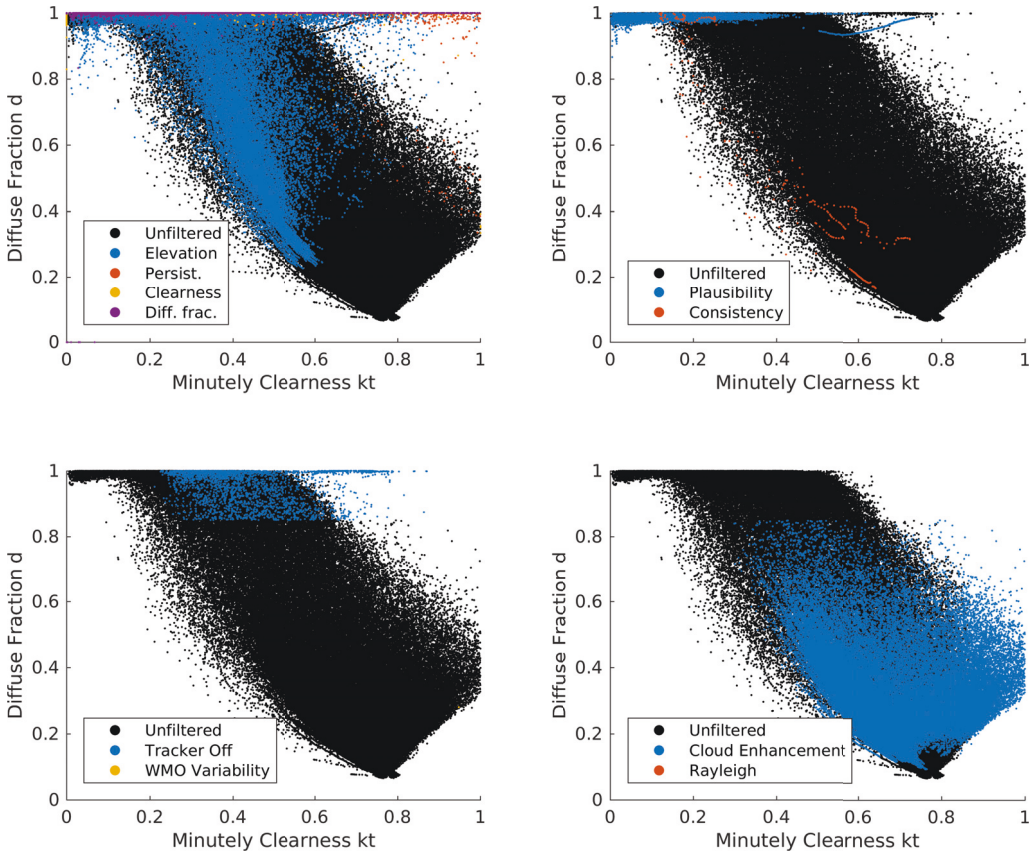

Figure 4.4: Quality control tests and filtering process for the BoM Townsville station

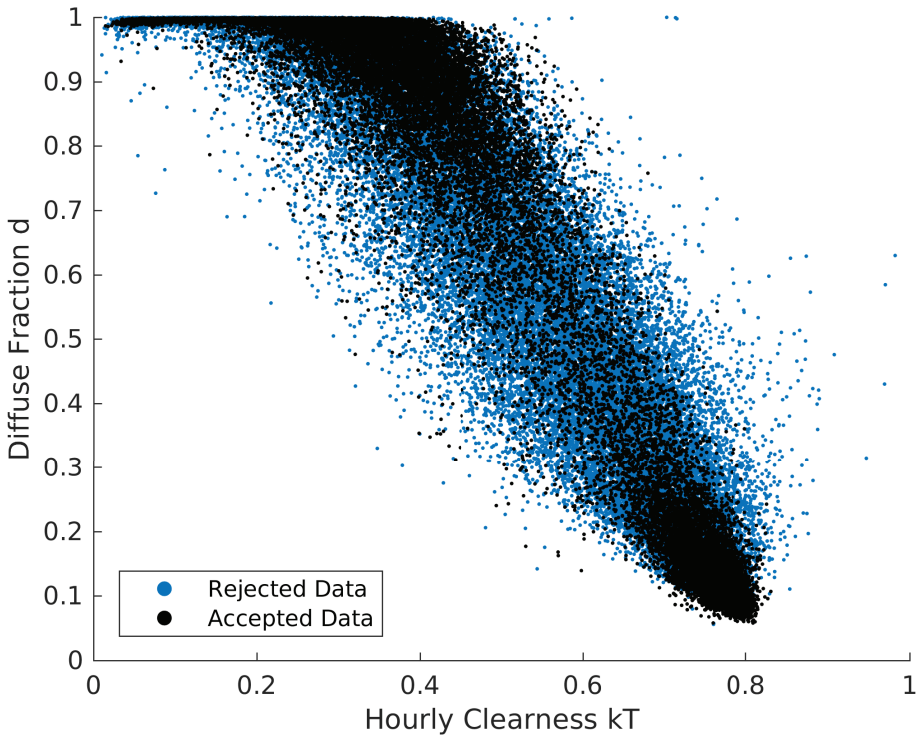

Figure 4.5: Removal of hourly data below minute count threshold (45 mins) for Melbourne

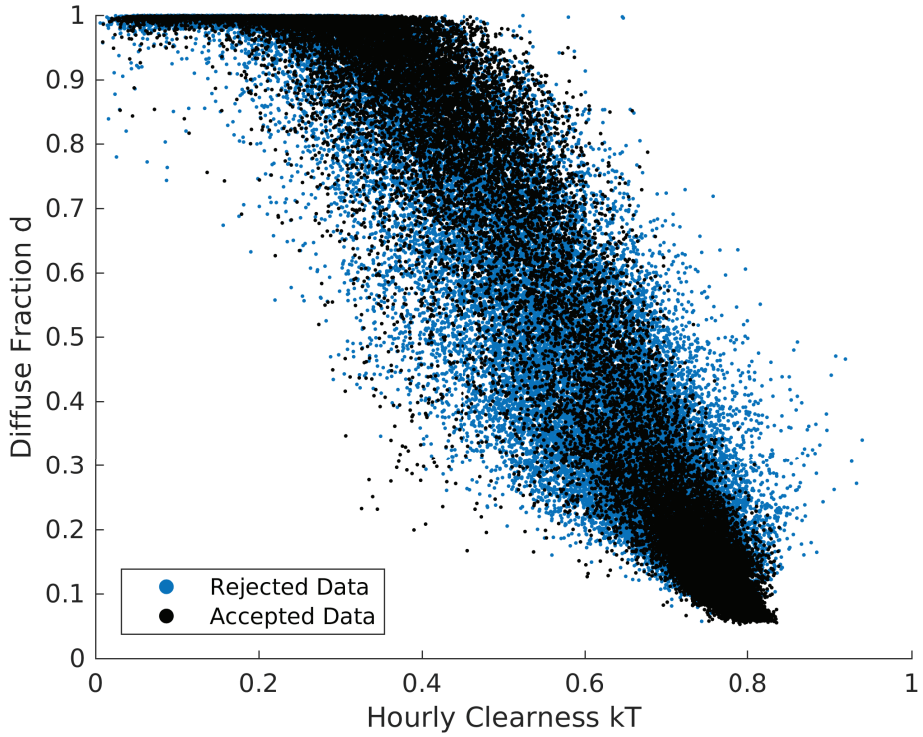

Figure 4.6: Removal of hourly data below minute count threshold (45 mins) for Wagga Wagga

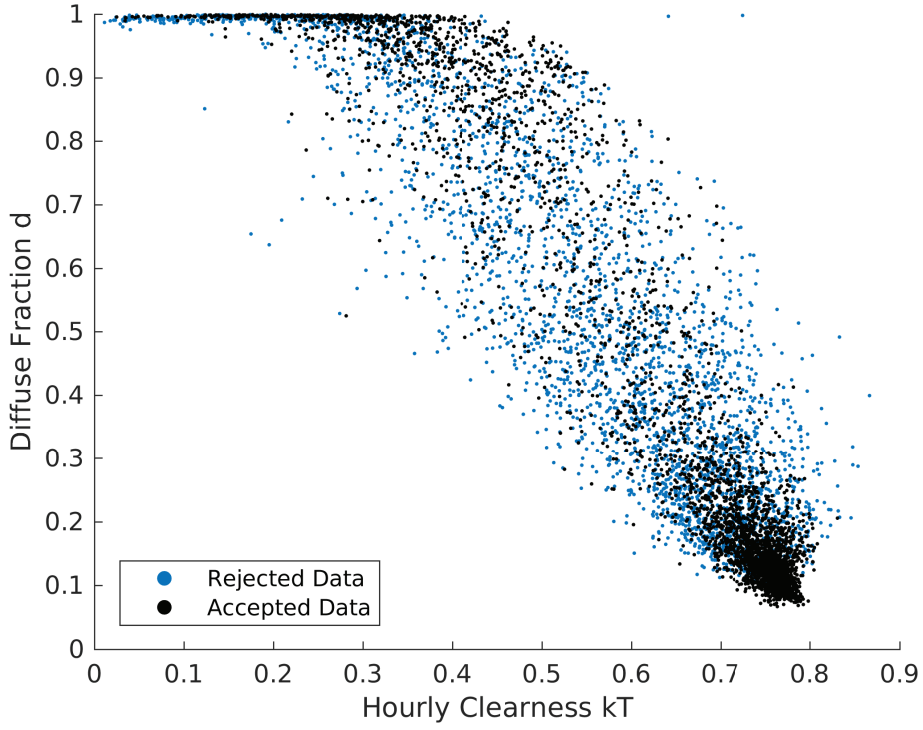

Figure 4.7: Removal of hourly data below minute count threshold (45 mins) for Townsville

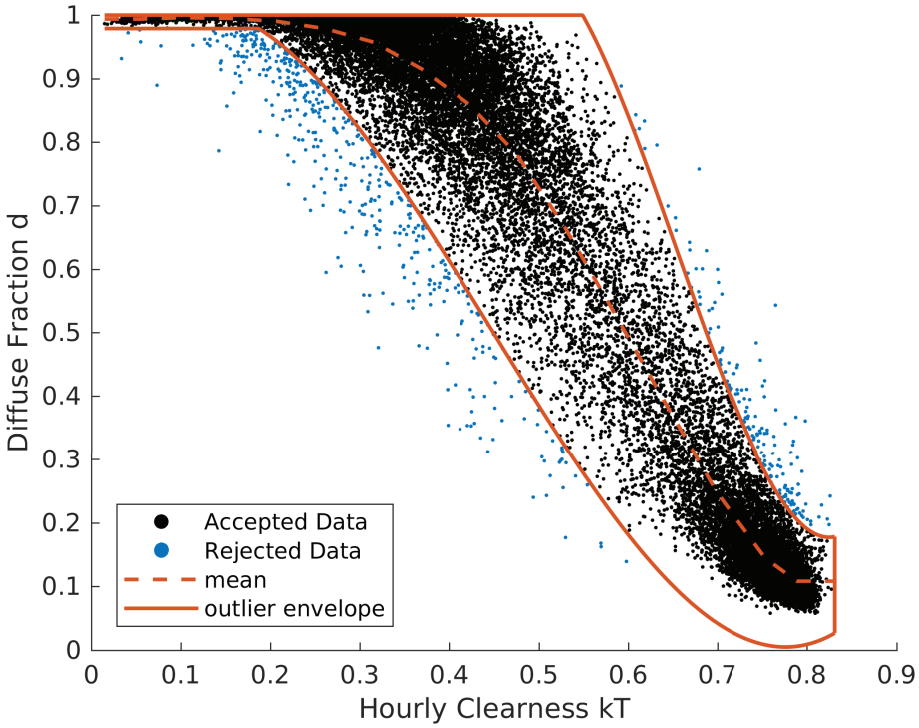

Figure 4.8: Outlier envelope of filtered Melbourne data

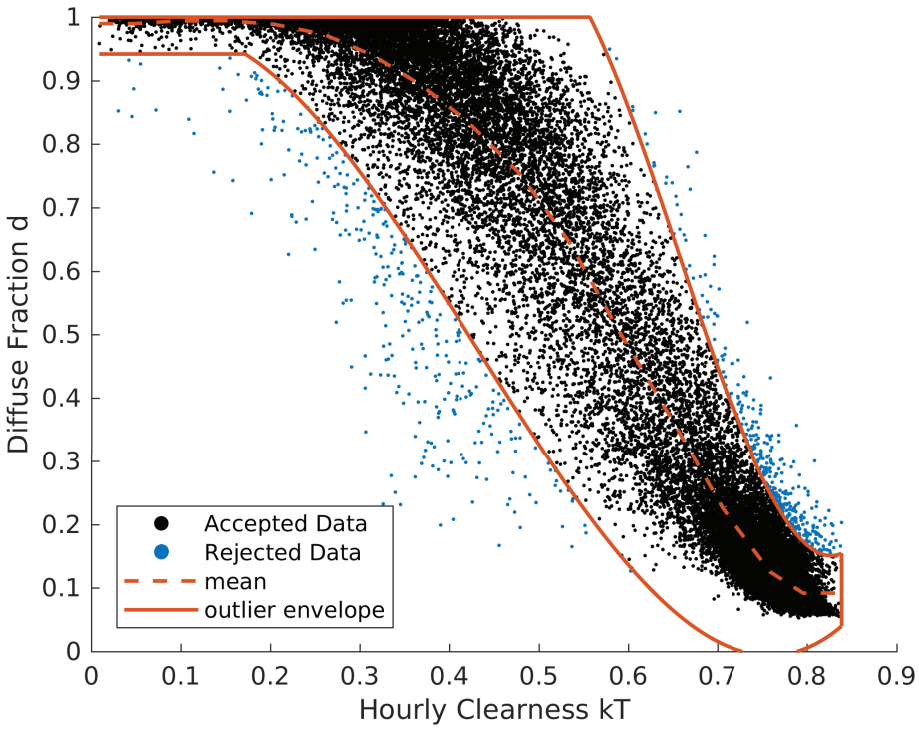

Figure 4.9: Outlier envelope of filtered Wagga Wagga data

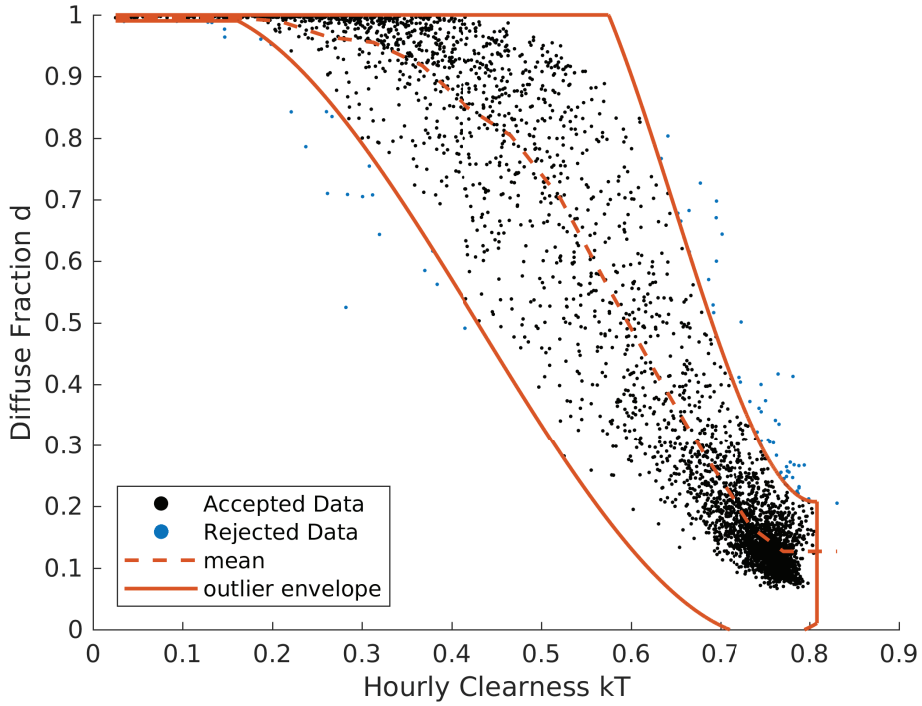

Figure 4.10: Outlier envelope of filtered Townsville data

Table 4.2: Percentage breakdown of retained data following each quality control step

Station	Quality Control Step			
	Step 1 (%)	Step 2 (%)	Step 3 (%)	Overall (%)
Cairns	61	78	98	46
Darwin	60	82	98	48
Townsville	64	83	98	52
Broome	60	86	98	51
Cobar	45	78	98	34
Kalgoorlie-Boulder	55	78	98	42
Longreach	55	82	97	44
Tennant Creek	61	87	98	52
Mildura	48	74	98	35
Alice Springs	57	85	98	48
Learmonth	52	84	98	43
Woomera	38	69	98	26
Rockhampton	61	81	98	49
Wagga Wagga	56	78	98	43
Cape Grim	56	76	98	42
Melbourne	55	73	98	39
Adelaide	52	76	98	39
Geraldton	53	79	98	41
Mt Gambier	53	72	98	37
Average	55	79	98	43

- Relative frequency of exceedence from KSI (OVER)
- Combined Performance Index (CPI)

MeAPE (indicating the size of the errors) and RMSE (capturing overall goodness of fit) were used in [58, 138] to validate the accuracy of the original BRL model. In [138], MBE (capturing average model bias) and KSI (described further below) were also used, while an additional method known as the Bayesian Information Criterion (BIC) was used in [58]. Lemos et al. [153] used MeAPE, RMSE and KSI as part of the formal error analysis for a new BRL model adjusted for Brazil. Copper and Sproul [127] used RMSE, R^2 (indicating level of variance in the dependent variable that is predictable from the independent variable) and MBE as part of a comparative study for solar irradiance models for Australia. Badescu et al. [123] used MBE and RMSE in the testing of 54 models for global and diffuse clear-sky irradiance, while [161] and [131] also used the same indicators as the primary error analysis tools for the assessment for diffuse irradiation models on inclined surfaces. Engerer and Mills [118] used relative versions of MBE (rMBE) and RMSE (rRMSE) along with the coefficient of determination R as the performance metrics for clear-sky irradiation models under Australian conditions.

Mathematical definitions of MeAPE, rMBE, rRMSE and R^2 are defined as follows:

$$\text{MeAPE}(\%) = \text{median}\left(\left|\frac{\hat{d}_i - d_i}{d_i}\right| \times 100\right) \tag{4.2}$$

$$\text{rMBE}(\%) = \frac{\sum_{i=1}^{n}\left(\hat{d}_i - d_i\right)}{n\overline{d}} \times 100 \tag{4.3}$$

$$\text{rRMSE}(\%) = \frac{1}{\overline{d}}\sqrt{\frac{\sum_{i=1}^{n}\left(\hat{d}_i - d_i\right)^2}{n}} \times 100 \tag{4.4}$$

$$R^2 = 1 - \frac{\sum_{i=1}^{n}\left(d_i - \hat{d}_i\right)^2}{\sum_{i=1}^{n}\left(d_i - \overline{d}\right)^2} \tag{4.5}$$

where $\hat{d}_i$ is the predicted values for diffuse irradiation fraction, d_i is the measured data, $\overline{d}$ is the mean of the measured data and n is the number of data.

KSI, provides a measure of the distribution similitude between the cumulative distribution function (CDF) of different data sets [138, 182]. KSI has been used in numerous studies and assessments of solar irradiation modelling [122, 138, 153, 182] and is defined as follows:

$$\text{KSI}(\%) = 100 \times \frac{\int_{x_{min}}^{x_{max}} D_n dx}{\alpha_{critical}} \tag{4.6}$$

where D_n is the difference between the CDFs of the measured and the model predicated values while x_{max} and x_{min} are the extreme values of the independent variable [138, 153]. The variable $\alpha_{critical}$, calculated as $\alpha_{critical} = V_c \times (x_{max} - x_{min})$, depends on the population size N and the critical value V_c calculated for the 99% confidence level so that for $N \geq 35$,

$V_c = 1.63/\sqrt{N}$.

An additional statistic referred to as OVER, originally defined in [182] and updated in [122], is derived during the KSI calculation process, providing a measure of the frequency of exceedence of the CDF error against a critical value V_c and is defined as follows:

$$\text{OVER}(\%) = 100 \times \frac{\int_{x_{min}}^{x_{max}} \max\left(D_n - V_c, 0\right) dx}{\alpha_{critical}} \tag{4.7}$$

Gueymard [183] developed the CPI statistic taking percentage measures of distribution similitude (KSI and OVER) and dispersion (rRMSE) to provide an overall measure of model performance defined as:

$$\text{CPI}(\%) = \frac{\text{KSI} + \text{OVER} + 2\text{rRMSE}}{4} \tag{4.8}$$

For the formal error analysis conducted in this research, MeAPE, rMBE, rRMSE, R^2, KSI, OVER and CPI, representative of the common approach in solar irradiation model assessments, are selected to test the accuracy of the modified BRL models developed in this research.

4.2.3 Satellite Data Time Stamps

The AREMI database includes data from 1990 to 2015. Over this 35 year measurement period, numerous satellites have been commissioned and decommissioned. Satellite observations for the entire continent are not synchronous. Rather, satellite sensors undertake progressive latitude scans with observation times fixed for each hour of the day. For each satellite generation, the observation time within each hour differs while in some satellite cases, the times differ for different hours in the day. Consequently, the fluctuating observation times over the data set history must be accounted for when comparing against ground-based observations. Table 4.3 reproduces the documented observation times by BoM [70] for each satellite generation.

Each satellite observation constitutes a near-instantaneous irradiation estimate and is considered to be representative of the entire hour. Consequently, the hourly integration of ground-based minutely observations undertaken for the results presented in Section 4.3 is not applicable. To correctly correlate satellite observations with ground-based data, the ground-based minutely data closest to the satellite observation time stamps are required for comparison. Consequently, the quality control procedure previously established in Section 4.2.1 requires the following modification:

- Sub-hourly sub-limits removed (i.e. no longer require at least 45 mins of data)
- The closest minutely ground-based observations to the satellite time stamps are assumed to be representative of the entire hour

In this research, specific consideration was given to satellite observation time stamps as published by BoM. Corrections were meticulously applied to identify the closest minute approximation from ground-based data measurements. Furthermore, careful consideration

Table 4.3: Minute time stamps associated with each satellite observation for BoM HSI and AREMI data sets. Source: BoM [70]

Start Date	1990-01-01		1993-01-01		1994-07-01		1995-06-11		2003-05-21		2005-11-01	2010-07-01	2016-06-22
End Date	1992-12-31		1994-06-30		1995-06-10		2003-05-20		2005-10-31		2010-06-30	2016-03-21	Ongoing
Satellite	GMS-4 A	GMS-4 B	GMS-4 A	GMS-4 B	GMS-4 A	GMS-4 B	GMS-5 A	GMS-5 B	GOES-9 A	GOES-9 B	MTSAT-1R	MTSAT-2	Himawari-8
Latitude													
-10	45.7	38.7	47.2	40.7	46.7	40.5	46.7	39.7	39.9	27.9	46.2	44.7	36
-15	46.7	39.7	48.2	41.7	47.7	41.5	47.7	40.7	41	29	47.2	45.7	36.9
-20	47.7	40.7	49.3	42.8	48.8	42.6	48.8	41.8	42	30	48.3	46.8	37
-25	48.7	41.7	50.2	43.7	49.7	43.5	49.7	42.7	43	31	49.2	47.7	37.9
-30	49.6	42.6	51.1	44.6	50.6	44.4	50.6	43.6	43.9	31.9	50.1	48.6	38.4
-35	50.5	43.5	52	45.5	51.5	45.3	51.5	44.5	44.7	32.7	51	49.5	38.6
-40	51.2	44.2	52.7	46.2	52.2	46	52.2	45.2	45.5	33.5	51.7	50.2	38.9
-44	51.8	44.8	53.3	46.8	52.8	46.6	52.8	45.8	46	34	52.3	50.8	39.1

A columns: UT hours 18 19 20 21 23 00 01 02 03 05 06 07 08 09 11
B columns: UT hours 22 04 10

was also given to central Australia local standard time L_{st} which is not a full hour multiple ahead of the Co-ordinated Universal Time (UTC). Consequently, for satellite observations in the central Australia time zone, the hour component of the satellite observation L_{st} UTC time equivalent actually corresponds to the ground-measured data in the following hour as demonstrated by the example in Table 4.4.

Table 4.4: Satellite and ground measurement time stamps for Adelaide enabling synchronous irradiation data comparison (nearest minute)

AREMI Time stamp (UTC)	AREMI Time stamp (L_{st})	Nearest Latitude	Observation Minute	L_{st} of ground data equivalent
20/05/2003 00:00	20/05/2003 09:30	-35	52	10:22

4.2.4 BRL Modelling Procedure

Following the removal of erroneous data through the quality control tests established in Section 4.2.1, the accepted irradiation data set can be used for the development of revised BRL models.

To enable the creation of a National BRL and Köppen-Geiger zone BRL models, data from the contributing irradiation measurement stations require amalgamation. Some weather stations have significantly longer operational lifespans that others resulting in a larger database of irradiation measurements. Lemos et al. [153] sampled data from the entire measurement history of each station, with the number of points sampled for each station limited to the site with the smallest quantity of measured data (post-filtering) to remove locational bias. However, due to the relatively short measurement history of many Australian based weather stations, limiting the analysis to the shortest data set would result in a poor representation of Australian irradiation characteristics.

Consequently, to maintain a sufficiently large data set from which correlations are fitted and tested whilst avoiding locational bias, each site was limited to a maximum of 17,520 data points or two years of hourly data. The hourly data were not sequentially selected but rather randomly sampled across the entire measurement history of the station. For stations with less than an equivalent of two years' data, all data (post-filtering) were sampled. The sampled data were then amalgamated into a single data set, representative of Australia nationally or a specific Köppen-Geiger zone within Australia.

Two-thirds of the amalgamated data were randomly sampled and used to fit BRL diffuse irradiation correlations. The remaining one-third were used as part of the model validation and statistical assessment process.

The problem of determining a BRL correlation to the diffuse irradiation fraction data with parameter β_0, β_1, β_2, β_3, β_4, β_5, was solved using the *fminunc* function of Matlab to find the minimum of an unconstrained multi-variable function $f(\beta_0, \beta_1, \beta_2, \beta_3, \beta_4, \beta_5)$ where

$$f(\beta_0, \beta_1, \beta_2, \beta_3, \beta_4, \beta_5) = d - \frac{1}{1 + e^{\beta_0 + \beta_1 k_T + \beta_2 AST + \beta_3 \alpha + \beta_4 K_T + \beta_5 \psi}} \tag{4.9}$$

The rigorous quality control methodology considered in this research resulted in a large number of rejected data as previously shown in Figures 4.5 to 4.10 of Section 4.2.1.

Consequently, many data time stamps associated with sunrise and sunset have the potential to be rejected. To ensure the persistence and variability terms remain consistent with the intended scope, the terms as defined in (3.37) and (3.38) must be slightly modified. Where a sunset or sunrise hour has been rejected through the filtering process, the persistence and variability terms are assumed to be $\psi = k_t$ and $\upsilon = 0$ respectively for the first or last remaining hour of the day within the data set.

The diffuse fraction BRL model of (3.36) also enables estimates for DNI to be established through the relationships of (3.6) and (3.7) which give:

$$I_{bn} = \frac{I(1-d)}{\sin(\alpha)} \tag{4.10}$$

The overall data merger and BRL modelling procedure is summarised in the flow chart of Figure 4.11.

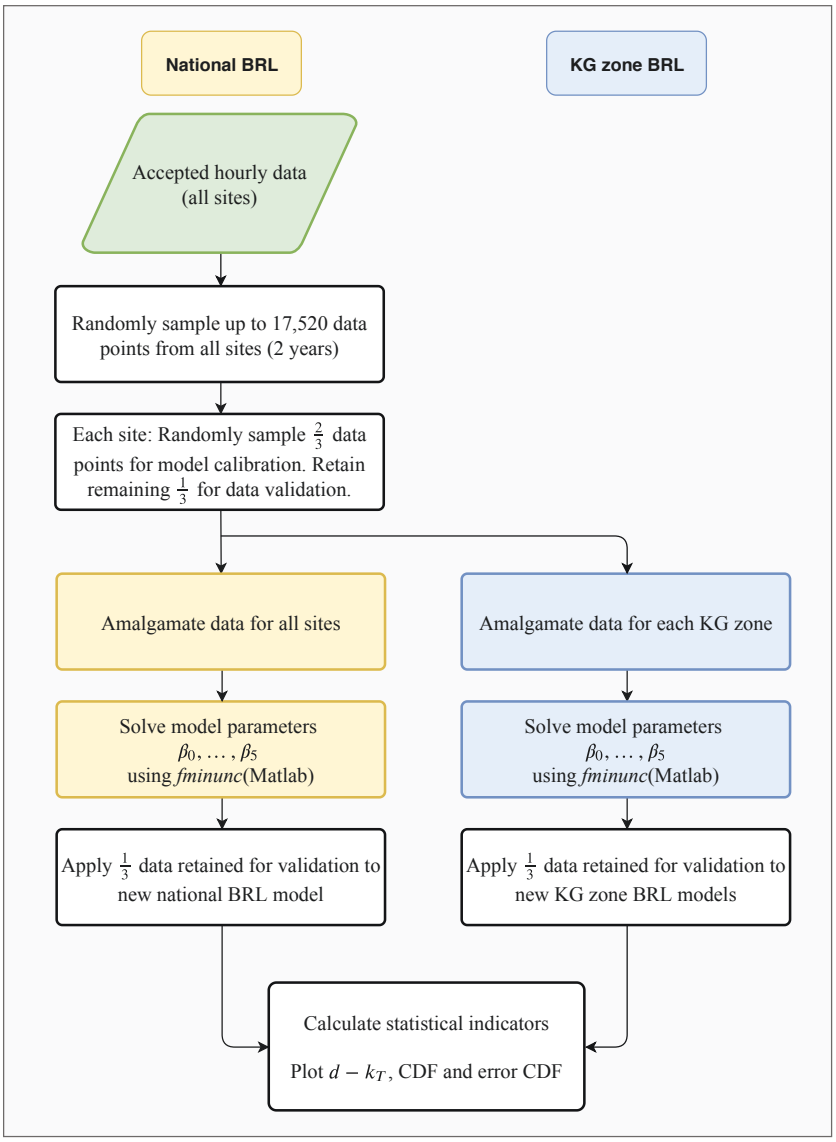

Figure 4.11: BRL model adjustment and validation procedure

4.3 Ground-Based Data Results

Following the application of the quality control and BRL model fitting procedure summarised in Figure 4.1 and Figure 4.11, new adjusted BRL models for individual stations were established for comparison purposes. Additionally, new models based on the BoM modification to the BRL methodology replacing persistence ψ with variability υ were also determined. The resultant plots of diffuse fraction and direct normal irradiation against hourly clearness index for Adelaide, Cape Grim, Alice Springs and Townsville stations are presented in Figures 4.12 to 4.19. It can be clearly seen that both the adjusted BRL and adjusted BoM models demonstrate a closer approximation to the underlying measured data than the original BRL correlation parameters of Ridley et al. [58].

Amalgamating the filtered data for an Australian national irradiation data set and fitting an adjusted BRL model results in the clearness index versus diffuse fraction plots of Figure 4.20 and Figure 4.21. Again a preliminary visual assessment of the the data plotted against clearness index shows a clear improvement. Detailed statistical assessments based on the methodology in Section 4.2.2 are presented in Sections 4.3.1 and 4.3.2 for diffuse and direct irradiation respectively.

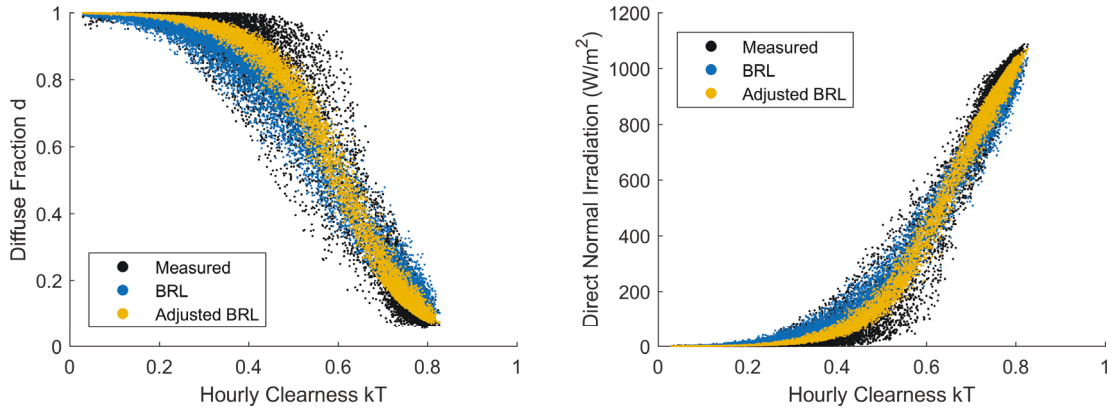

Figure 4.12: BRL model results for diffuse fraction (left) and DNI (right) for Adelaide

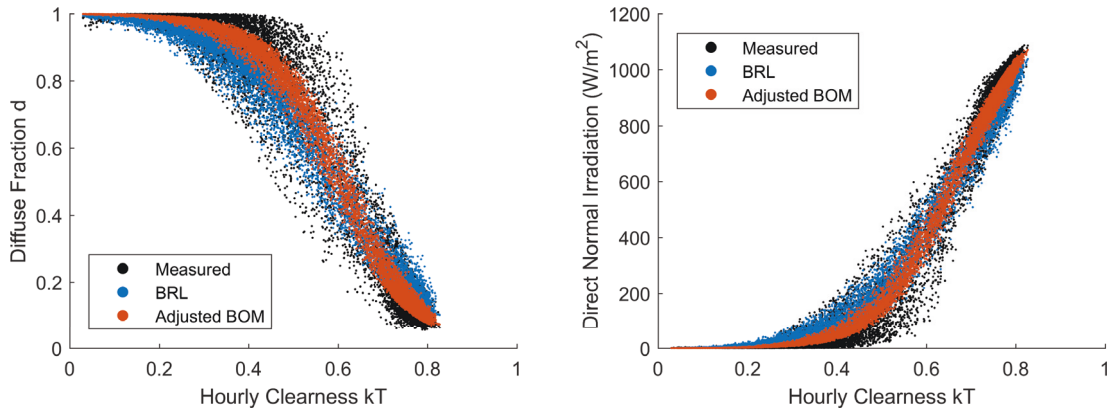

Figure 4.13: BRL model (with BoM variability parameter) results for Diffuse fraction (left) and DNI (right) for Adelaide

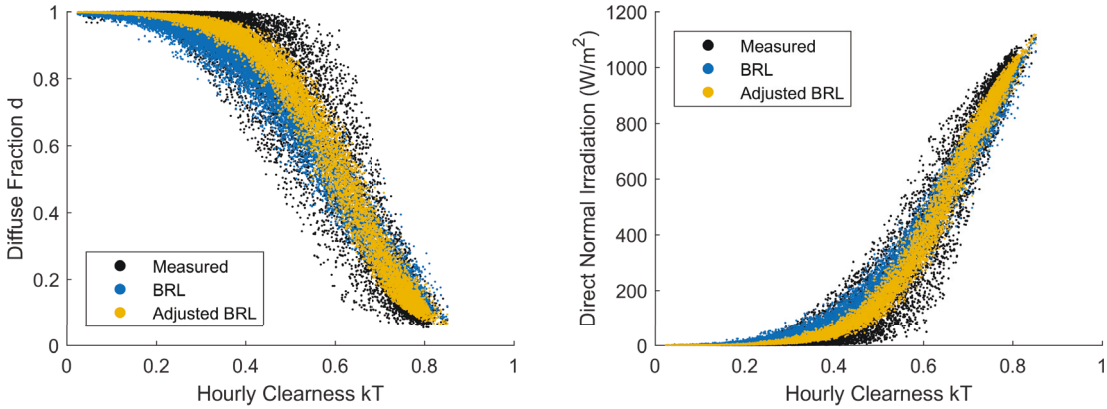

Figure 4.14: BRL model results for diffuse fraction (left) and DNI (right) for Cape Grim

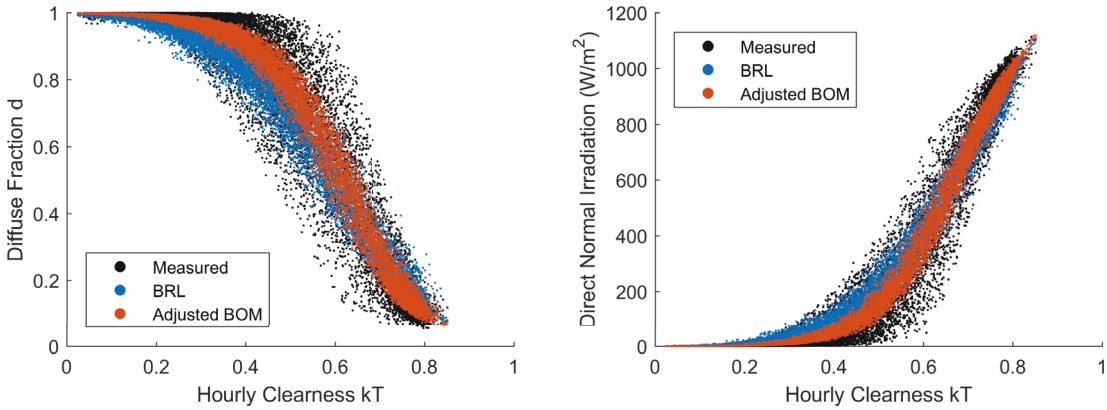

Figure 4.15: BRL model (with BoM variability parameter) results for diffuse fraction (left) and DNI (right) for Cape Grim

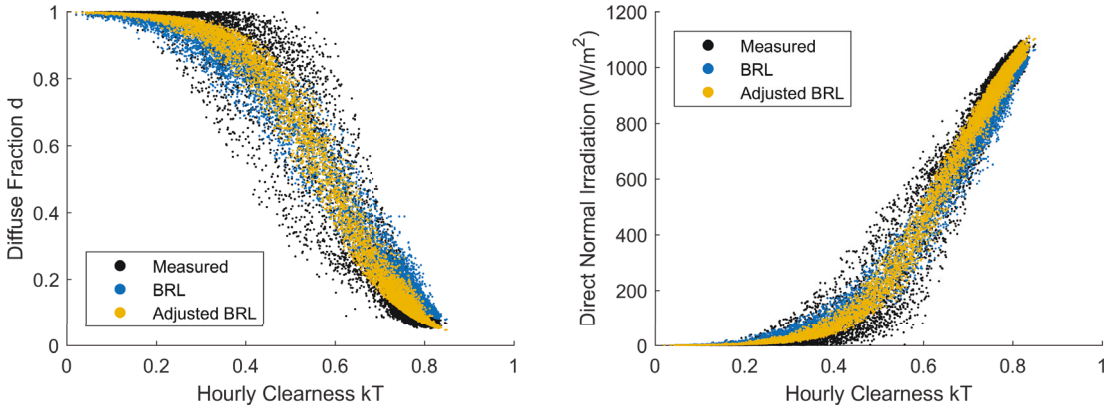

Figure 4.16: BRL model (with BoM variability parameter) results for diffuse fraction (left) and DNI (right) for Alice Springs

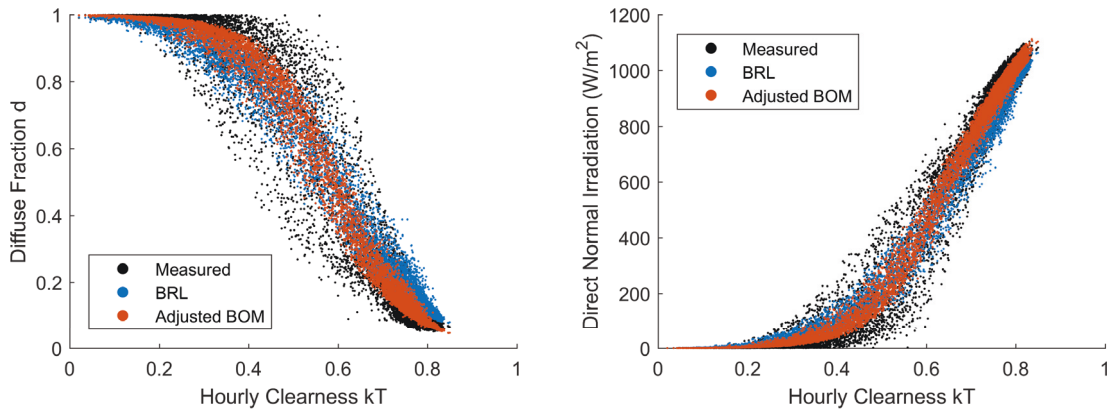

Figure 4.17: BRL model results for diffuse fraction (left) and DNI (right) for Alice Springs

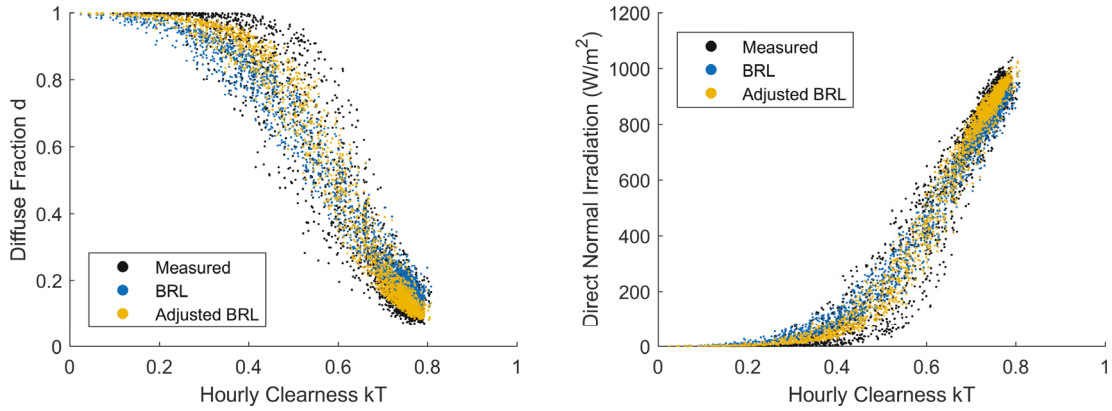

Figure 4.18: BRL model results for diffuse fraction (left) and DNI (right) for Townsville

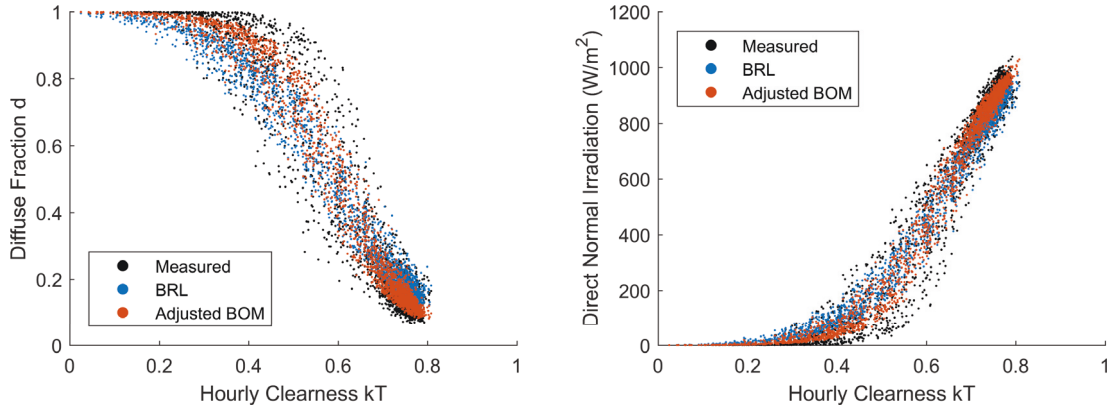

Figure 4.19: BRL model (with BoM variability parameter) results for diffuse fraction (left) and DNI (right) for Townsville

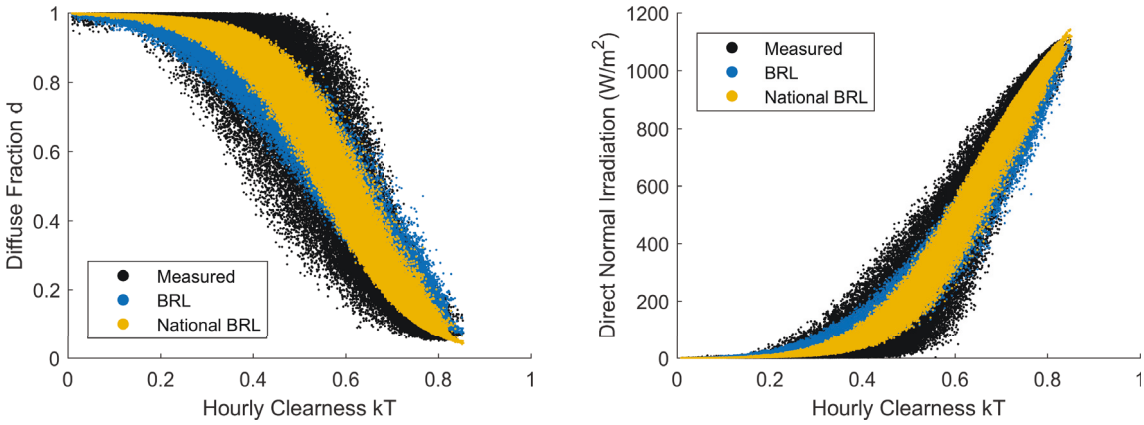

Figure 4.20: National BRL model results for diffuse fraction (left) and DNI (right) for all Australian measurement locations

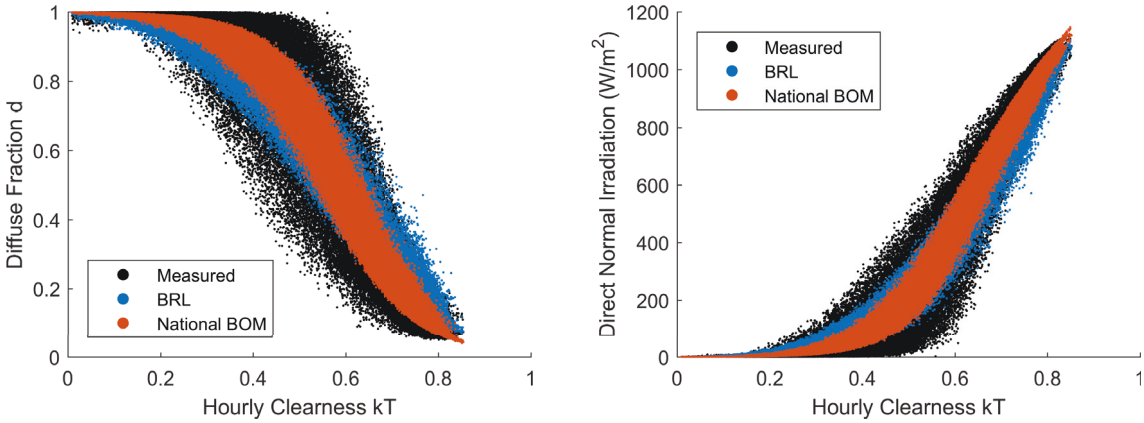

Figure 4.21: National BRL model (with BoM variability parameter) results for diffuse fraction (left) and DNI (right) for all Australian measurement locations

4.3.1 Diffuse Horizontal Irradiation

The CDF of diffuse horizontal irradiation fraction d generated for the measured data, the original BRL model and modified BRL models for the location of Adelaide is presented in Figure 4.22. The CDF for the original BRL model (purple) can be seen to markedly deviate from the CDF of the measured data (dotted black). It is also apparent in Figure 4.22 that the nationally and Köppen-Geiger zone adjusted BRL models present a closer approximation to the CDF of the measured data. However, precisely which model performs better is not easily identifiable.

CDF errors for Adelaide are shown in Figure 4.23. Based on the left plot of Figure 4.23, the original BRL model clearly performs worse than the new adjusted models of this research. A comparison of CDF error for each of the adjusted models is shown on the right of Figure 4.23. The magnitude of the error for the Köppen-Geiger zone BRL correlation is evidently lower than the adjusted National BRL and BOM models for the majority of the diffuse fraction range. Differentiation between the BRL models with a persistence term (designated as BRL) or a variability term (designated as BoM) is difficult to discern and it is not immediately clear which model performs best. Similar observations can be made for Cape Grim as shown in Figure 4.24 and Figure 4.25.

The CDF and CDF errors for Alice Springs shown in Figure 4.26 and Figure 4.27 do not present strong evidence for either the Köppen-Geiger or national models. In Townsville's case, the national models appear to provide a closer correlation to the measured data CDF than the Köppen-Geiger models as shown in Figure 4.28 and Figure 4.29. Despite the inability to clearly differentiate between the BRL and BoM variants of the Köppen-Geiger and national models, and the fluctuating performance of the Köppen-Geiger and national models, at least one of the new adjusted BRL models out-performs the original BRL model for each of the sites represented in Figures 4.22 to 4.29.

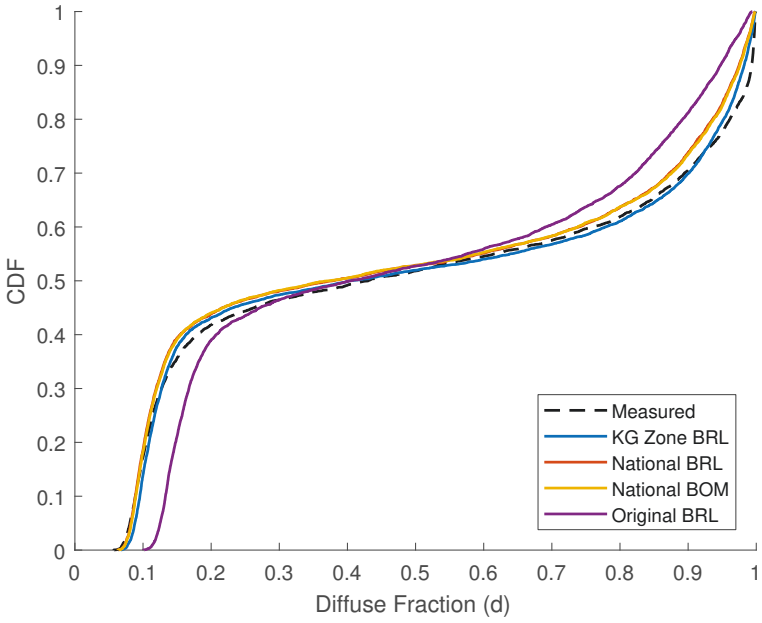

Figure 4.22: CDFs of diffuse fraction for different BRL models for Adelaide

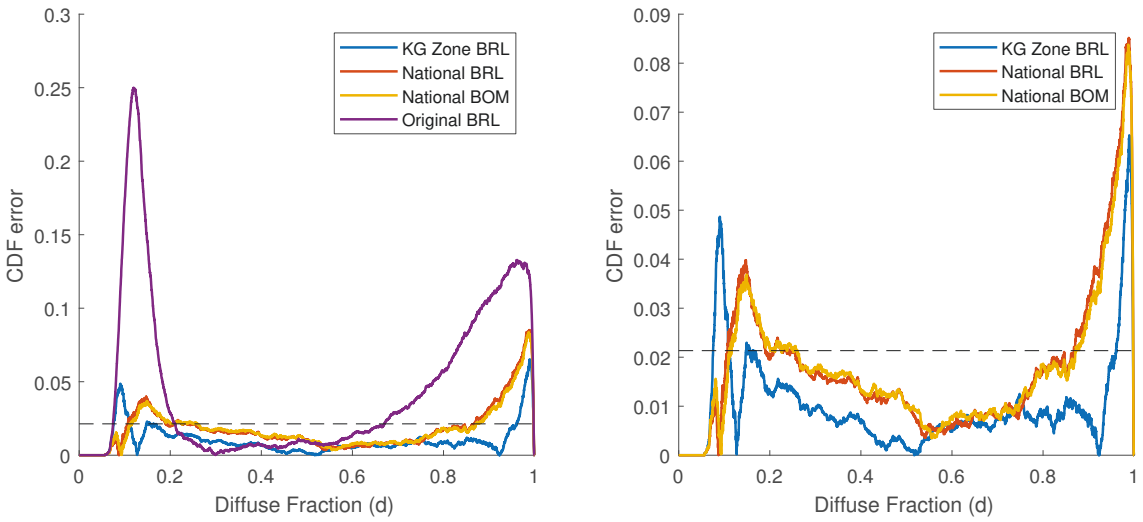

Figure 4.23: CDF error of diffuse fraction for different BRL models for Adelaide. Critical value V_c shown as dotted line

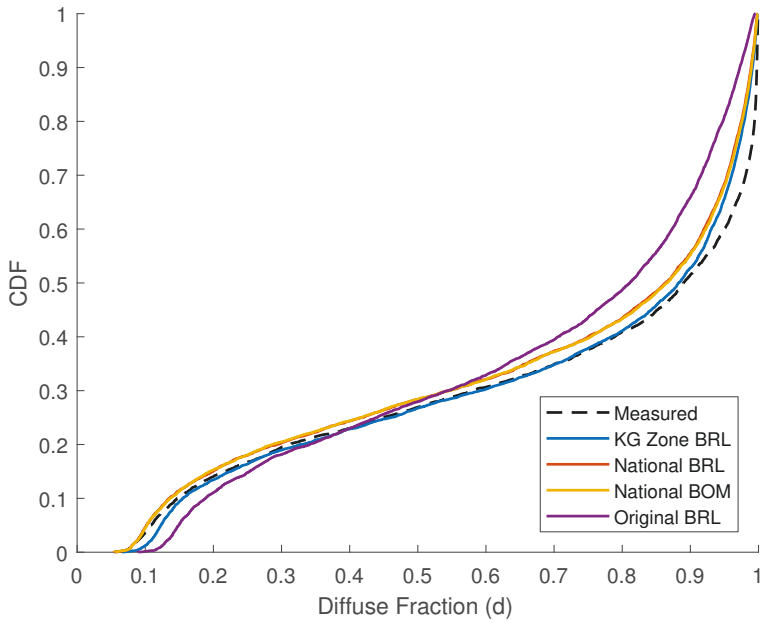

Figure 4.24: CDFs of diffuse fraction for different BRL models for Cape Grim

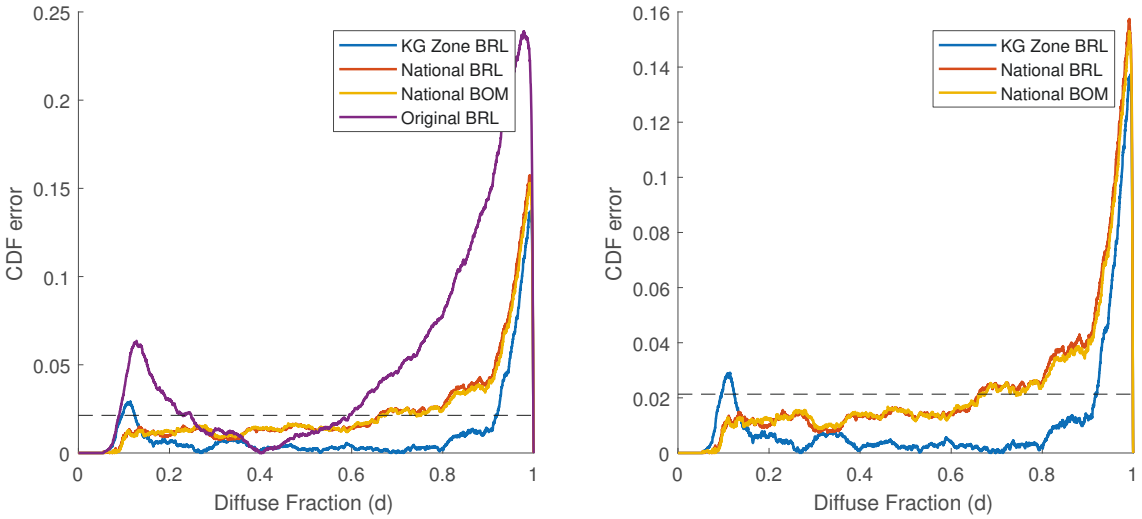

Figure 4.25: CDF error of diffuse fraction for different BRL models for Cape Grim. Critical value V_c shown as dotted line

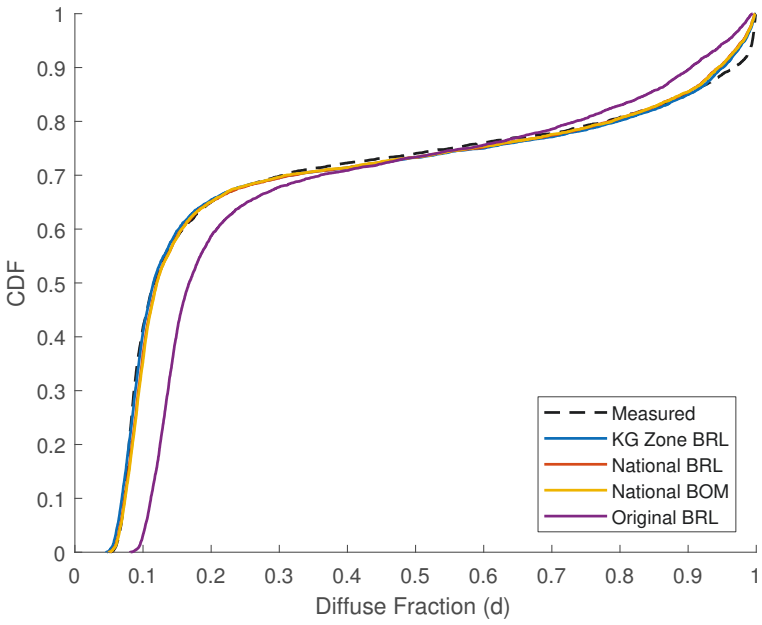

Figure 4.26: CDFs of diffuse fraction for different BRL models for Alice Springs

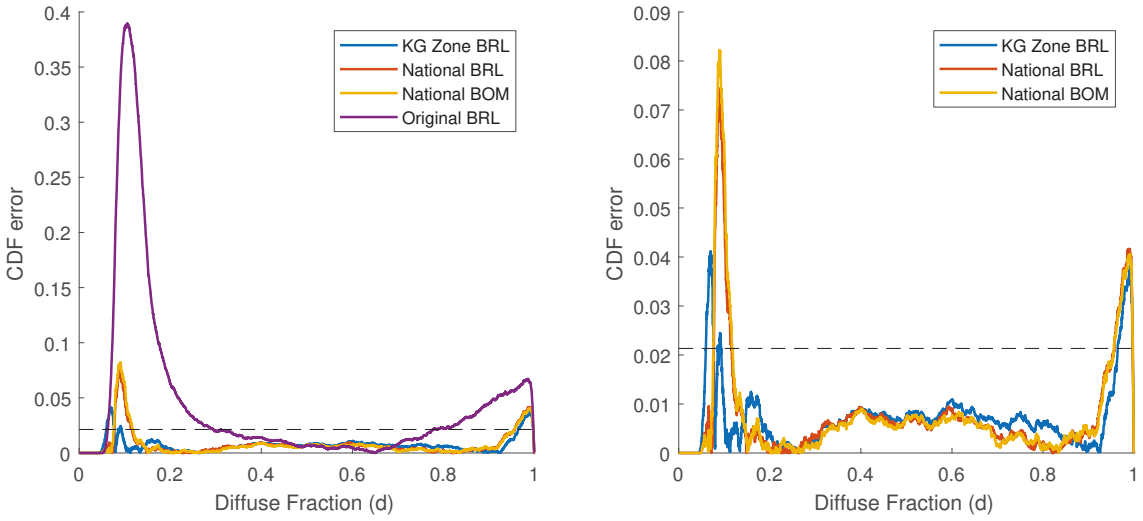

Figure 4.27: CDF error of diffuse fraction for different BRL models for Alice Springs. Critical value V_c shown as dotted line

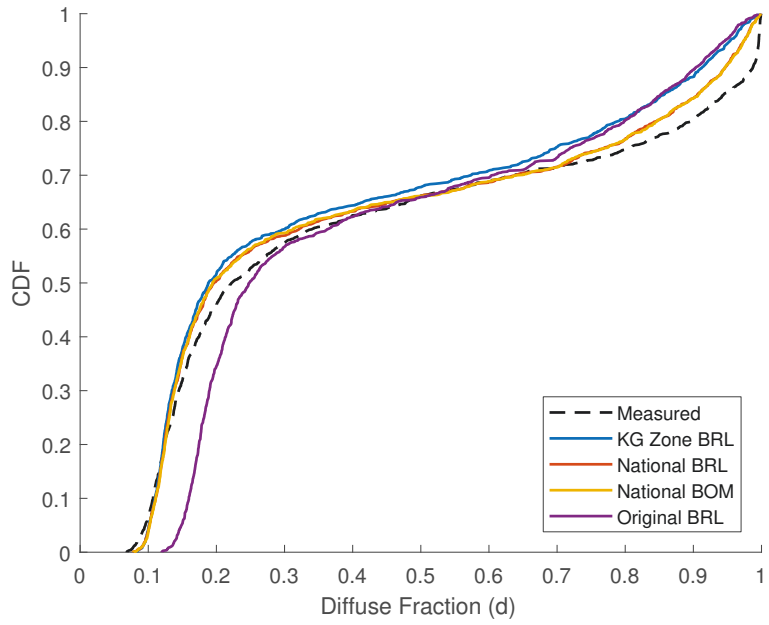

Figure 4.28: CDFs of diffuse fraction for different BRL models for Townsville

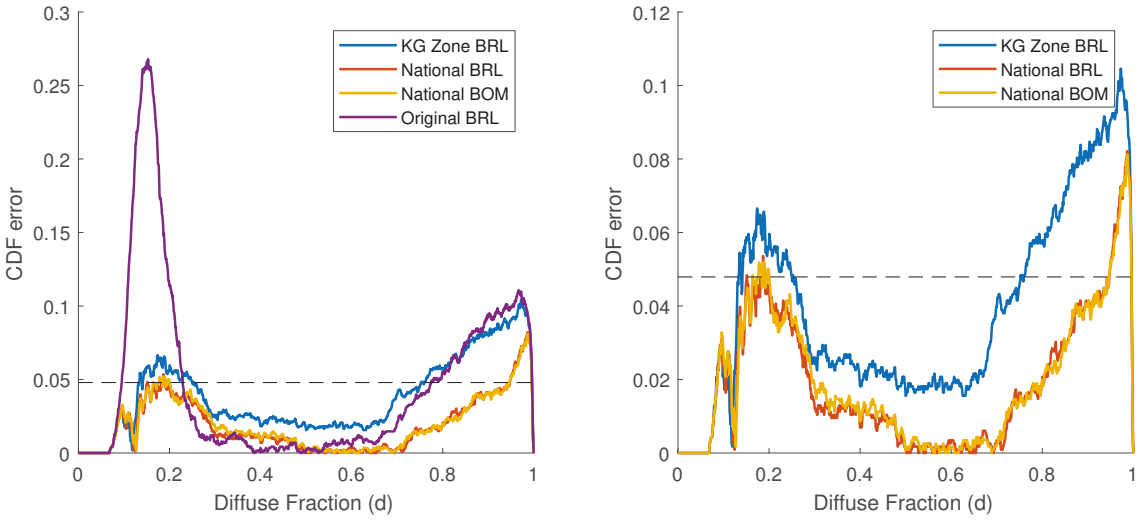

Figure 4.29: CDF error of diffuse fraction for different BRL models for Townsville. Critical value V_c shown as dotted line

CDF plots provide an early assessment of model improvement or lack thereof. To firmly establish model performance with an aim to identify the best performing model, the rigorous statistical assessment defined in Section 4.2.2 is applied. For each of the BoM OMS weather station locations, statistical indicators were calculated.

A tiered approach was adopted for comparisons between model statistical indicators. Direct comparisons were drawn as follows:

(i) Original BRL model and new National BRL model (Table 4.6)

(ii) New National BRL model and new National BoM model (Table 4.7)

(iii) New Köppen-Geiger zone BRL or BoM model against either the new National BRL model or the new National BoM model, depending on the performance established in the previous comparisons tables (Table 4.8)

To facilitate the comparison, colour codes are applied with green designating model improvement, orange a clear worse performance and gold a marginally worse performance. The marginal performance thresholds for each of the statistical indicators are designated as follows:

- MeAPE within 2%
- rMBE within ±1%
- rRMSE within 2%
- R^2 within 0.02
- KSI within 2%
- OVER within 1%
- CPI within 2%

With reference to the measured data, the statistical indicators of the diffuse fraction estimates determined by the original BRL model, as defined in [58], are presented in Table 4.5, including the relative scaling term for rMBE and rRMSE, $\overline{d}$. Significant positive bias (over 10%) can be seen in a number of locations which provides immediate confirmation of the inadequacy of the original BRL model when tuned against data that have not been thoroughly quality controlled. A comparison of the new National BRL model against the original BRL shows a clear model improvement in Table 4.6. For 96% of the statistical results, the application of the new National BRL model shows an improvement in diffuse fraction estimates. The exceptions are associated with rMBE with Townsville, Mildura and Adelaide showing rMBEs of -3.96%, -1.68% and -3.43% respectively, approximately 3.5%, 1.2% and 1.3% greater than the original BRL model. Two other locations show only a marginal deterioration in rMBE. Overall, the rMBE demonstrates a roughly even split between over-estimation and under-estimation, with the absolute magnitude greatly improved compared to the original BRL model in Table 4.5.

The application of the the BoM variability adjustment to the BRL model for nationally aggregated data generally shows a slightly worse performance than the persistence based BRL model. Table 4.7 demonstrates an improvement in 37% of the statistical indicators while 58% demonstrate a marginally worse performance. Consequently, it can be concluded that the new National BRL model out-performs the variability based National model.

Table 4.5: Statistical indicators for diffuse fraction under original BRL model

Location	KG Zone	Statistical Indicators (%)							$\overline{d}$
		MeAPE	rMBE	rRMSE	R^2	KSI	OVER	CPI	
Cairns	Am	13.71	1.46	16.41	94.50	142.90	74.52	62.56	0.52
Darwin	Aw	23.36	10.32	21.06	92.23	255.83	171.46	117.35	0.43
Townsville	Aw	18.44	0.52	20.08	94.02	98.03	47.73	46.48	0.42
Broome	BSh	40.93	15.32	28.08	91.71	285.60	213.11	138.72	0.32
Cobar	BSh	28.72	5.68	18.21	96.03	83.66	43.56	40.91	0.43
Kalgoorlie-Boulder	BSh	23.69	2.41	18.80	96.04	218.03	156.57	103.05	0.40
Longreach	BSh	45.31	14.67	29.32	93.18	103.33	59.68	55.41	0.26
Tennant Creek	BSh	36.20	10.37	26.15	92.95	236.26	162.78	112.84	0.34
Mildura	BSk	19.05	0.51	16.61	96.16	211.80	148.89	98.48	0.46
Alice Springs	BWh	33.65	7.98	24.88	94.63	216.81	149.38	103.99	0.32
Learmonth	BWh	48.04	13.94	30.45	93.27	264.15	202.65	131.92	0.25
Woomera	BWh	20.14	1.54	15.98	96.32	66.98	25.97	31.23	0.48
Rockhampton	Cfa	16.64	5.03	17.93	94.24	237.44	152.99	106.57	0.49
Wagga Wagga	Cfa	17.28	0.77	16.30	96.20	178.71	121.84	83.29	0.45
Cape Grim	Cfb	8.40	-4.80	13.78	90.67	235.86	161.91	106.33	0.72
Melbourne	Cfb	8.35	-2.33	11.57	95.91	189.20	136.44	87.19	0.65
Adelaide	Csa	14.42	-2.08	16.44	95.26	214.72	148.88	99.12	0.51
Geraldton	Csa	26.85	2.67	23.99	94.01	237.28	164.85	112.53	0.36
Mt Gambier	Csb	12.01	-4.49	14.87	95.01	174.35	107.74	77.96	0.58

Table 4.6: Statistical indicators for diffuse fraction under National BRL model (compared to original BRL model)

Location	KG Zone	Statistical Indicators (%)						
		MeAPE	rMBE	rRMSE	R^2	KSI	OVER	CPI
Cairns	Am	9.43	-0.05	14.46	95.74	42.83	4.65	19.10
Darwin	Aw	12.43	6.85	19.70	93.20	146.29	61.27	61.74
Townsville	Aw	10.89	-3.96	17.39	95.52	39.74	1.92	19.11
Broome	BSh	15.31	7.47	23.05	94.41	122.76	49.14	54.50
Cobar	BSh	11.12	2.16	14.75	97.40	22.88	3.07	13.87
Kalgoorlie-Boulder	BSh	10.09	-1.20	14.56	97.62	37.58	12.28	19.74
Longreach	BSh	12.30	2.77	19.77	96.90	27.63	6.02	18.30
Tennant Creek	BSh	13.21	4.25	23.23	94.43	81.23	12.02	34.93
Mildura	BSk	9.21	-1.68	12.72	97.75	55.45	18.50	24.85
Alice Springs	BWh	12.53	0.87	20.83	96.23	36.19	7.18	21.26
Learmonth	BWh	14.97	1.24	21.04	96.79	70.41	33.62	36.53
Woomera	BWh	8.07	-0.34	12.07	97.90	14.54	0.78	9.86
Rockhampton	Cfa	10.14	3.34	16.45	95.15	108.15	30.61	42.91
Wagga Wagga	Cfa	8.74	-1.70	14.33	97.06	44.80	9.56	20.75
Cape Grim	Cfb	5.64	-3.23	12.54	92.28	109.11	41.19	43.85
Melbourne	Cfb	5.07	-1.57	9.55	97.21	66.27	25.56	27.73
Adelaide	Csa	8.78	-3.43	14.06	96.53	82.99	19.34	32.61
Geraldton	Csa	12.42	-2.91	19.43	96.07	63.58	11.25	28.42
Mt Gambier	Csb	7.48	-4.39	12.45	96.51	88.24	23.69	34.21
Improved	96%	19	14	19	19	19	19	19
Marginal	2%	0	2	0	0	0	0	0
Worse	2%	0	3	0	0	0	0	0

Table 4.7: Statistical indicators for diffuse fraction under National BRL model (with BoM variability parameter) (compared to National BRL model)

Location	KG Zone	Statistical Indicators (%)						
		MeAPE	rMBE	rRMSE	R^2	KSI	OVER	CPI
Cairns	Am	9.65	-0.19	14.34	95.80	40.65	4.25	18.40
Darwin	Aw	12.92	6.88	19.79	93.14	146.13	61.67	61.85
Townsville	Aw	11.09	-4.04	17.62	95.40	41.02	1.85	19.53
Broome	BSh	15.90	7.66	23.05	94.41	125.13	52.57	55.95
Cobar	BSh	11.33	2.18	14.77	97.39	22.56	3.43	13.88
Kalgoorlie-Boulder	BSh	10.17	-1.09	14.67	97.59	39.03	12.67	20.26
Longreach	BSh	12.80	3.08	19.90	96.86	28.94	7.43	19.04
Tennant Creek	BSh	13.42	4.30	23.13	94.48	81.59	14.00	35.46
Mildura	BSk	9.26	-1.52	12.69	97.76	55.69	18.05	24.78
Alice Springs	BWh	12.74	0.92	20.86	96.22	36.55	8.44	21.68
Learmonth	BWh	15.59	1.61	21.16	96.75	74.34	37.17	38.46
Woomera	BWh	8.04	-0.25	12.00	97.92	14.22	0.76	9.75
Rockhampton	Cfa	10.18	3.32	16.53	95.10	105.50	28.69	41.81
Wagga Wagga	Cfa	8.93	-1.53	14.39	97.03	42.32	8.15	19.81
Cape Grim	Cfb	5.71	-3.14	12.55	92.26	105.89	37.03	42.01
Melbourne	Cfb	5.04	-1.46	9.64	97.16	62.67	23.34	26.32
Adelaide	Csa	8.93	-3.35	14.19	96.47	81.82	16.92	31.78
Geraldton	Csa	12.64	-2.77	19.65	95.98	65.53	11.94	29.19
Mt Gambier	Csb	7.64	-4.29	12.46	96.50	86.68	21.64	33.31
Improved	37%	2	10	4	4	10	10	9
Marginal	58%	17	9	15	15	7	4	10
Worse	5%	0	0	0	0	2	5	0

Table 4.8: Statistical indicators for diffuse fraction under Köppen-Geiger zone BRL model (compared to National BRL model)

Location	KG Zone	Statistical Indicators (%)						
		MeAPE	rMBE	rRMSE	R^2	KSI	OVER	CPI
Cairns	Am	9.72	-0.05	14.39	95.77	45.85	7.46	20.52
Darwin	Aw	11.09	1.46	17.31	94.76	72.79	16.55	30.99
Townsville	Aw	12.17	-8.85	20.13	94.00	80.73	15.50	34.12
Broome	BSh	12.77	2.97	21.52	95.13	63.22	14.37	30.16
Cobar	BSh	10.18	-0.40	14.75	97.40	11.71	0.41	10.41
Kalgoorlie-Boulder	BSh	10.47	-4.04	15.40	97.34	74.95	23.08	32.20
Longreach	BSh	11.08	-2.04	20.18	96.77	19.83	0.14	15.08
Tennant Creek	BSh	12.24	0.50	22.42	94.82	39.52	3.21	21.89
Mildura	BSk	9.17	0.58	12.34	97.88	42.71	13.24	20.16
Alice Springs	BWh	12.97	0.49	20.98	96.18	33.73	2.39	19.52
Learmonth	BWh	13.82	0.27	20.65	96.91	50.68	19.68	27.92
Woomera	BWh	7.27	-0.22	11.98	97.93	11.74	0.47	9.04
Rockhampton	Cfa	10.10	1.53	15.67	95.60	94.22	25.85	37.85
Wagga Wagga	Cfa	9.14	-2.97	14.74	96.89	73.56	18.24	30.32
Cape Grim	Cfb	5.05	-0.58	11.58	93.41	51.03	20.64	23.71
Melbourne	Cfb	4.98	1.03	9.57	97.20	75.59	25.25	29.99
Adelaide	Csa	8.69	-0.25	13.20	96.95	46.71	6.21	19.83
Geraldton	Csa	12.90	1.45	18.80	96.32	49.14	19.85	26.64
Mt Gambier	Csb	7.30	0.05	10.85	97.35	44.30	10.82	19.21
Improved	72%	13	15	13	13	14	14	14
Marginal	14%	6	1	5	6	0	0	1
Worse	14%	0	3	1	0	5	5	4

The results of the Köppen-Geiger zone diffuse fraction BRL model for Australian based locations investigated in this research are presented in Table 4.8. With reference to the results of the new National BRL, which were shown to clearly out-perform the original BRL and BoM variability adjusted model, the Köppen-Geiger formulation can be seen to provide an improvement for the majority of the locational statistical indicators. Generally, rMBE shows a marked improvement with only three locations exhibiting a worse performance (Townsville, Kalgoorlie-Boulder and Wagga Wagga). rRMSE and R^2 also show strong support for the Köppen-Geiger improvement with under-performing metrics mostly within the marginal range. KSI, OVER and CPI show clear under-performance for the five locations, while close to 50% of the MeAPE results are marginally worse. Overall, 72% of the statistics indicators show improvement and 14% show a clearly worse performance. Referring to the CPI statistics, 14 (74%) of locations demonstrate an improvement. With reference to the methodology in [183], if a single statistic is used to confirm model improvement as suggested, the CPI statistic supports the adoption of the Köppen-Geiger adjustment to the original BRL model for ground-based data measurement.

Consequently, for ground-measured irradiation, separate Köppen-Geiger zone BRL correlations using the original BRL formulation of (3.36) clearly demonstrate an improvement over a National BRL model and by extension the orignal BRL correlation of [58]. The results of the error analysis show strong support for the application of the Köppen-Geiger climate classification to a new set of BRL models for the Australian continent. The BRL parameters proposed for ground-based GHI measurements within Australia determined through this research are detailed in Table 4.9.

Table 4.9: BRL model parameters for ground-based measurements

Model	β_0 (constant)	β_1 (k_T)	β_2 (AST)	β_3 (α)	β_4 (K_T)	β_5 (ψ)
National BRL	-6.862	9.068	0.01468	-0.00472	1.703	1.084
Köppen-Geiger (Am)	-6.433	8.774	-0.00044	-0.00578	2.096	0.684
Köppen-Geiger (Aw)	-6.047	7.540	0.00624	-0.00299	2.077	1.208
Köppen-Geiger (BSh)	-6.734	8.853	0.02454	-0.00495	1.874	0.939
Köppen-Geiger (BSk)	-7.310	10.089	0.01852	-0.00693	1.296	1.114
Köppen-Geiger (BWh)	-7.097	9.416	0.01254	-0.00416	1.661	1.130
Köppen-Geiger (Cfa)	-6.484	8.301	0.01577	-0.00338	1.607	1.307
Köppen-Geiger (Cfb)	-6.764	9.958	0.01271	-0.01249	0.928	1.142
Köppen-Geiger (Csa)	-7.099	10.152	-0.00026	-0.00744	1.147	1.184
Köppen-Geiger (Csb)	-7.080	10.460	0.00964	-0.01420	1.134	1.017

4.3.2 Direct Normal Irradiation

The statistical error analysis for diffuse fraction models suggest the Köppen-Geiger model gives an improvement to DHI estimation. Diffuse irradiation is just one of the two primary components of global horizontal irradiation. The performance the BRL model used for the estimation of direct irradiation is assessed in this section. Following the fitting of a BRL correlation for diffuse fraction d, a BRL model for DNI is determined through substitution of d into (4.10).

Plots of the CDFs and CDF errors for the original BRL model and new adjusted

Köppen-Geiger zone BRL and National BRL models against measured data are shown in Figures 4.30 to 4.37. Similar to the diffuse fraction case in Section 4.3.1, the new Köppen-Geiger zone BRL models for DNI associated with Adelaide and Cape Grim can be seen to present a closer approximation to the CDF of the measured data as shown in the CDF error plots of Figure 4.31 and Figure 4.33. For Adelaide in Figure 4.31, the Köppen-Geiger approximation is out-performed by the National BRL model at higher levels of DNI (in the vicinity of 1000 W/m^2), consistent with the converse results observed in Figure 4.23 at low values of diffuse fraction. Köppen-Geiger DNI estimates for Cape Grim show near universal improvement across the entire range of DNI from a CDF perspective as evident in Figure 4.33.

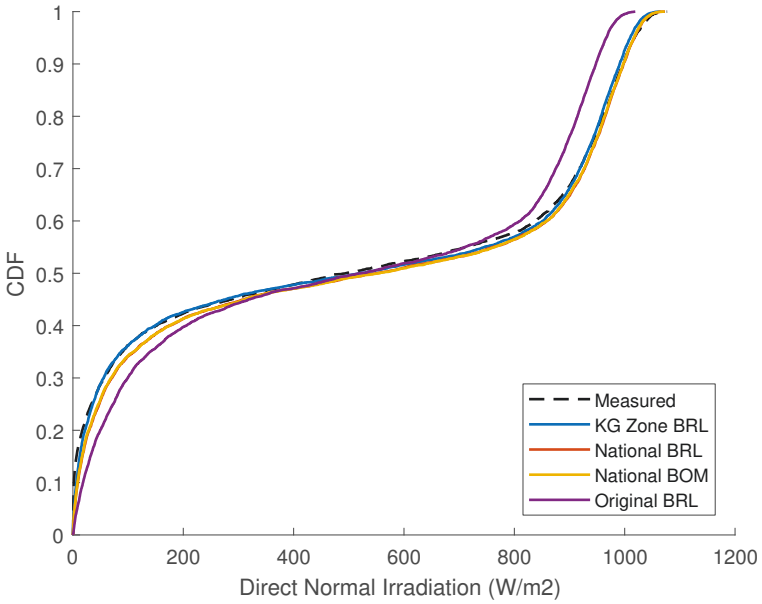

Figure 4.30: CDFs of DNI for different BRL models for Adelaide

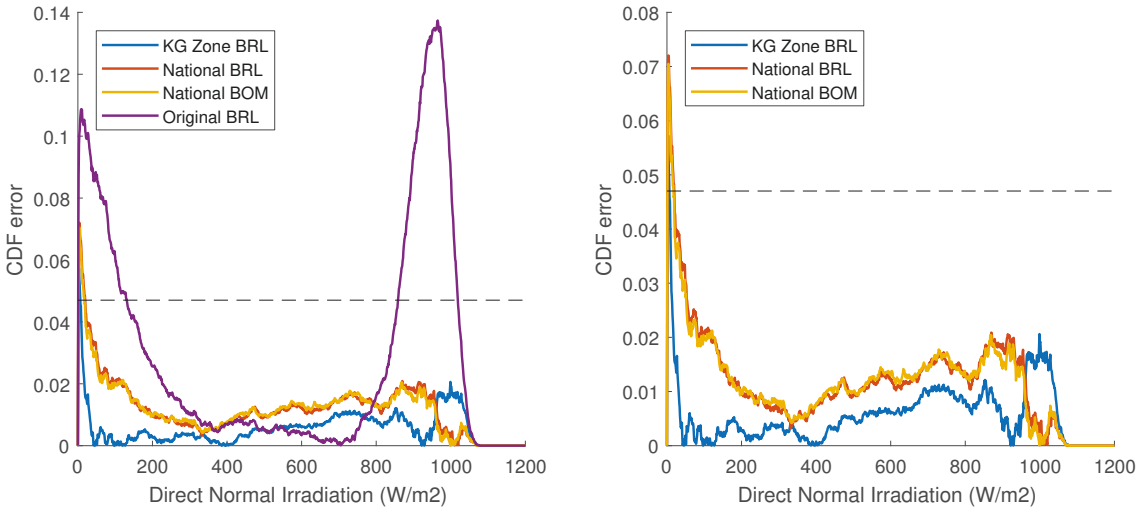

Figure 4.31: CDF error of DNI for different BRL models for Adelaide. Critical value V_c shown as dotted line

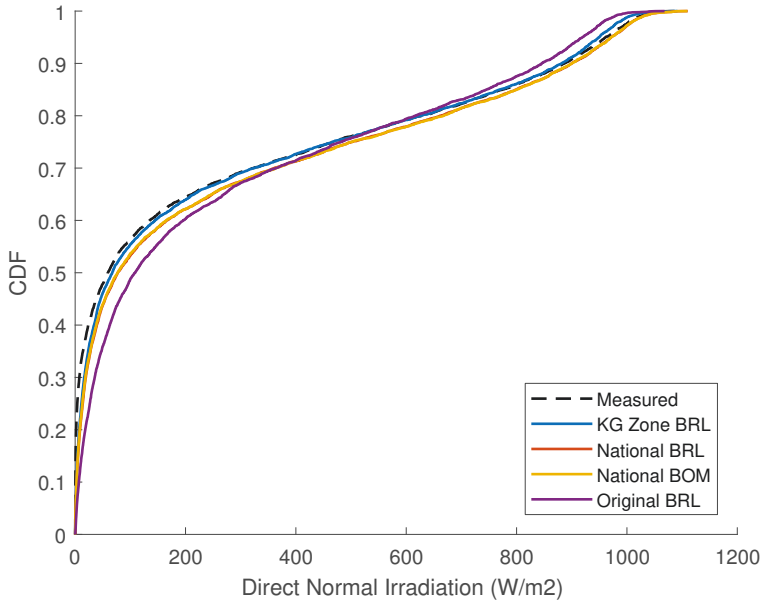

Figure 4.32: CDFs of DNI for different BRL models for Cape Grim

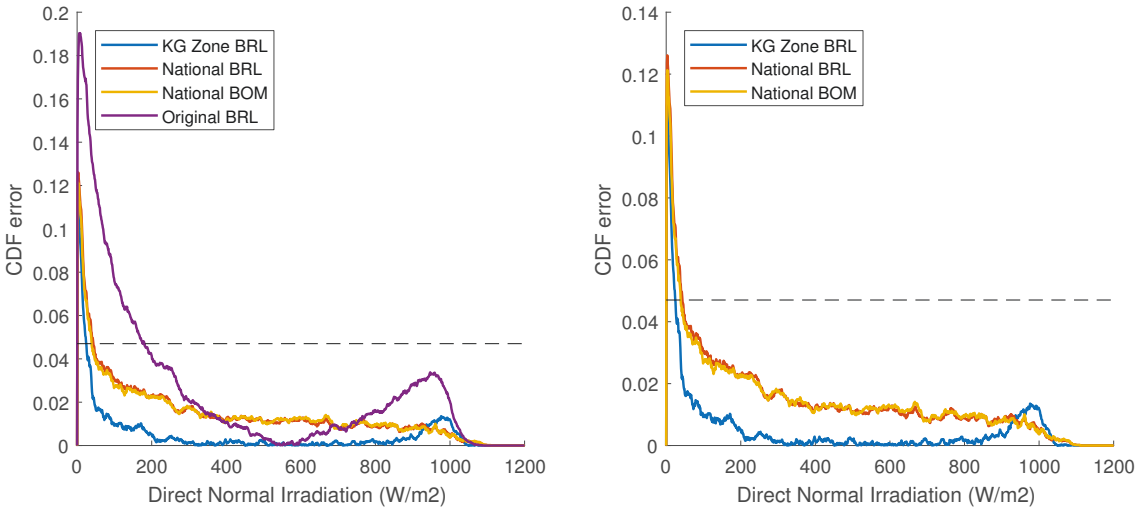

Figure 4.33: CDF error of DNI for different BRL models for Cape Grim. Critical value V_c shown as dotted line

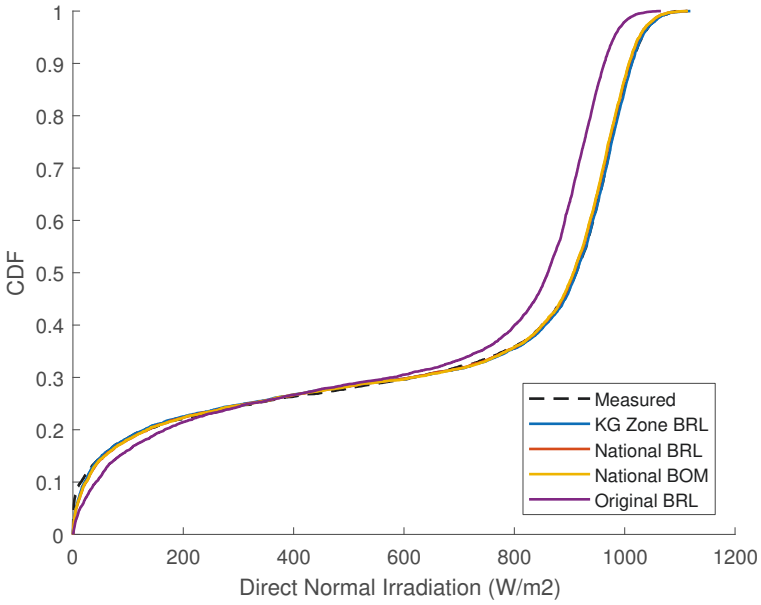

Figure 4.34: CDFs of DNI for different BRL models for Alice Springs

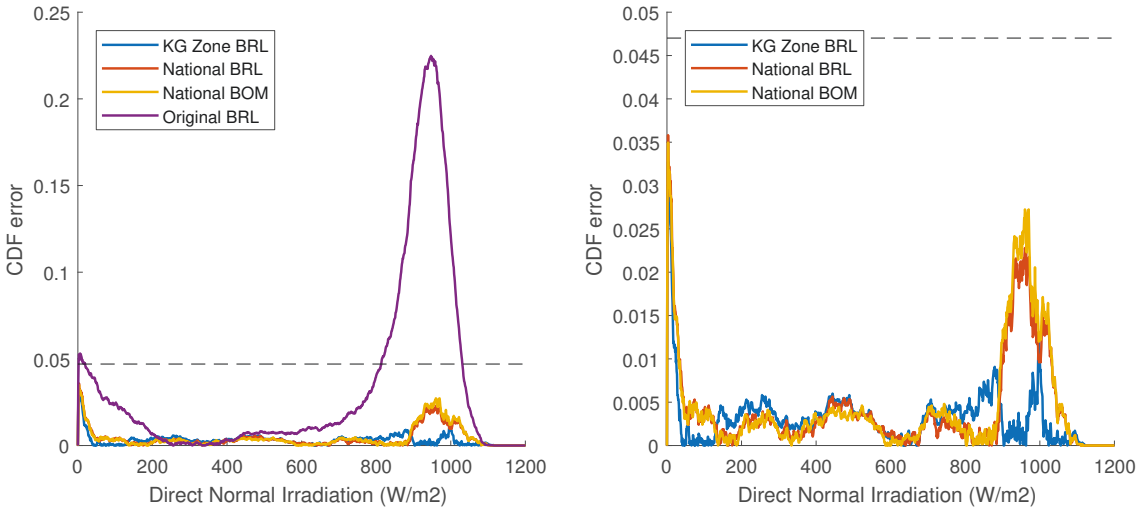

Figure 4.35: CDF error of DNI for different BRL models for Alice Springs. Critical value V_c shown as dotted line

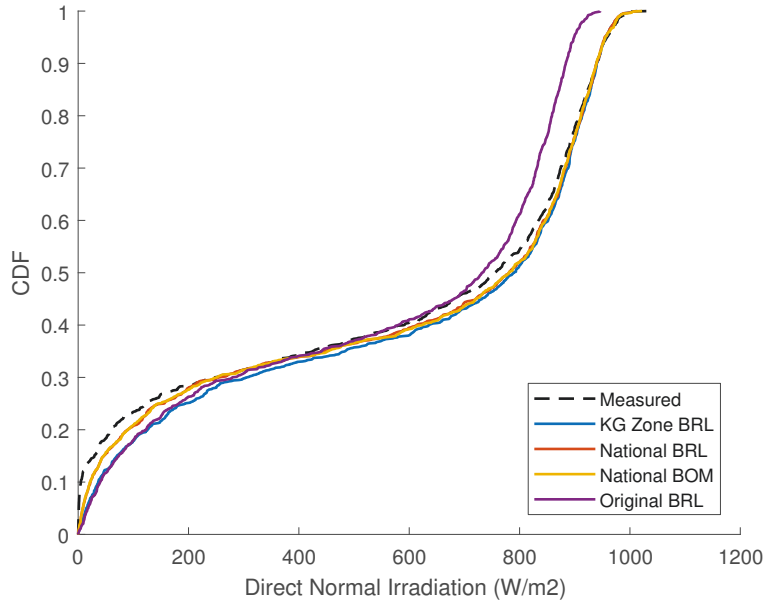

Figure 4.36: CDFs of DNI for different BRL models for Townsville

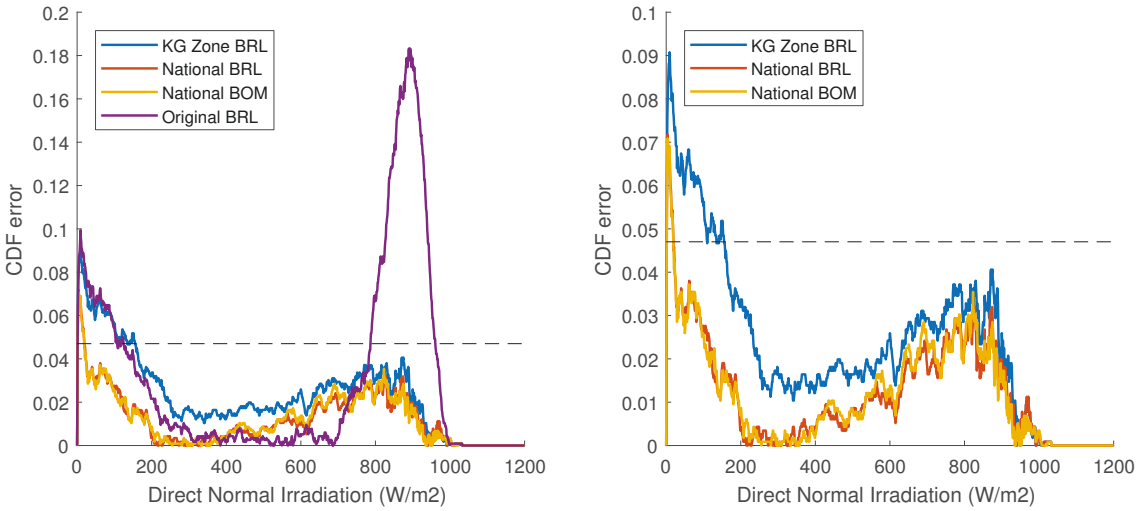

Figure 4.37: CDF error of DNI for different BRL models for Townsville. Critical value V_c shown as dotted line

However, consistent with the observations for diffuse fraction in Section 4.3.1, the CDF error plots for Alice Springs and Townsville in Figure 4.35 and Figure 4.37 respectively show the Köppen-Geiger model does not lead to invariably improved performance for all locations.

A complete statistical analysis of MeAPE, rMBE, rRMSE, R^2 and KSI was conducted for the DNI components estimated from the new BRL models. Following the same tiered approach as adopted for diffuse fraction in Section 4.3.1, Table 4.11 shows the new National BRL model for DNI, including the relative scaling term for rMBE and rRMSE, $\overline{I_{bn}}$. Worse performance compared to the original BRL model statistics shown in Table 4.10 is seen only in the rMBE statistic for Townsville, Cape Grim, Melbourne, Adelaide and Mt Gambier. Similar to the diffuse fraction case, 96% of the statistics show a clear improvement over the original BRL model.

A comparison of the persistence (BRL) and variability (BoM) variants of the new nationally adjusted models in Table 4.12 suggests the inclusion of a persistence term provides a better estimate. For the variability variant, a marginally worse performance is seen for 59% of the statistics across all measurement locations.

Table 4.13 shows the statistical comparison between the the Köppen-Geiger BRL model and the new National BRL model. With reference to the results for diffuse fraction, the Köppen-Geiger BRL estimates for DNI show even stronger support for the adoption of a Köppen-Geiger zone based modelling system. Only 7% show a clearly worse performance while 74% of the indicators show improvement (compared to 72% for diffuse fraction in Table 4.8).

Table 4.10: Statistical indicators for DNI under original BRL model

Location	KG Zone	Statistical Indicators (%)							$\overline{I_{bn}}$
		MeAPE	rMBE	rRMSE	R^2	KSI	OVER	CPI	
Cairns	Am	12.55	-3.39	14.34	97.06	60.97	18.90	27.14	456
Darwin	Aw	10.43	-7.81	13.79	95.54	79.08	25.87	33.13	521
Townsville	Aw	8.48	-2.08	11.81	96.70	66.27	27.38	29.32	571
Broome	BSh	9.08	-7.47	11.75	94.68	96.64	51.99	43.03	658
Cobar	BSh	9.19	-5.29	11.52	97.67	73.74	36.26	33.26	587
Kalgoorlie-Boulder	BSh	7.67	-3.31	10.28	97.81	71.40	31.72	30.92	610
Longreach	BSh	7.26	-5.65	9.19	95.34	95.65	53.47	41.87	750
Tennant Creek	BSh	7.95	-5.71	11.38	96.04	78.54	33.15	33.61	651
Mildura	BSk	8.93	-2.74	11.32	97.97	73.41	31.28	31.83	547
Alice Springs	BWh	6.80	-4.43	9.69	96.94	73.57	34.81	31.94	696
Learmonth	BWh	7.33	-5.33	9.13	95.40	95.30	58.96	43.13	767
Woomera	BWh	9.40	-3.67	11.82	98.05	73.81	31.44	32.22	532
Rockhampton	Cfa	12.33	-5.67	14.02	96.84	70.24	17.15	28.86	486
Wagga Wagga	Cfa	7.79	-2.24	10.72	98.02	55.03	18.44	23.73	549
Cape Grim	Cfb	65.56	6.57	28.59	95.33	55.26	16.08	32.13	257
Melbourne	Cfb	33.71	0.16	15.93	98.15	47.38	13.96	23.30	340
Adelaide	Csa	10.12	-0.49	12.95	97.74	63.00	22.18	27.77	496
Geraldton	Csa	7.53	-3.00	10.86	96.65	82.58	34.94	34.81	654
Mt Gambier	Csb	19.46	2.15	14.89	97.78	64.86	20.21	28.71	423

Table 4.11: Statistical indicators for DNI under National BRL model (compared to original BRL model)

Location	KG Zone	Statistical Indicators (%)						
		MeAPE	rMBE	rRMSE	R^2	KSI	OVER	CPI
Cairns	Am	10.69	0.17	12.08	97.91	13.45	0.24	9.46
Darwin	Aw	6.69	-3.97	11.50	96.90	37.79	0.00	15.20
Townsville	Aw	5.82	2.38	10.08	97.59	25.32	0.43	11.48
Broome	BSh	4.46	-3.05	8.48	97.23	37.14	4.88	14.75
Cobar	BSh	4.55	-1.30	8.08	98.86	16.30	0.49	8.24
Kalgoorlie-Boulder	BSh	3.79	0.38	7.42	98.86	11.78	0.25	6.72
Longreach	BSh	2.69	-1.07	5.68	98.21	24.63	1.56	9.39
Tennant Creek	BSh	3.98	-1.64	9.04	97.50	20.83	0.00	9.73
Mildura	BSk	5.62	0.75	8.19	98.94	17.18	0.49	8.51
Alice Springs	BWh	3.00	-0.29	7.29	98.27	9.01	0.00	5.90
Learmonth	BWh	2.94	-0.63	5.70	98.20	24.61	4.02	10.01
Woomera	BWh	6.26	-0.09	8.02	99.10	14.62	0.57	7.81
Rockhampton	Cfa	9.36	-2.39	11.89	97.73	25.65	0.25	12.42
Wagga Wagga	Cfa	5.80	1.28	9.09	98.57	13.37	0.18	7.93
Cape Grim	Cfb	43.53	6.93	27.30	95.74	31.34	2.56	22.13
Melbourne	Cfb	27.53	2.17	13.39	98.70	15.17	1.95	10.97
Adelaide	Csa	9.61	2.85	11.10	98.34	25.14	0.41	11.94
Geraldton	Csa	3.67	1.06	8.47	97.97	18.95	0.00	8.97
Mt Gambier	Csb	16.84	4.63	13.02	98.30	35.51	2.45	16.00
Improved	96%	19	14	19	19	19	19	19
Marginal	2%	0	2	0	0	0	0	0
Worse	2%	0	3	0	0	0	0	0

Table 4.12: Statistical indicators for DNI under National BRL model (with BoM variability parameter) (compared to National BRL model)

Location	KG Zone	Statistical Indicators (%)						
		MeAPE	rMBE	rRMSE	R^2	KSI	OVER	CPI
Cairns	Am	10.66	0.35	12.00	97.94	12.77	0.20	9.24
Darwin	Aw	6.74	-3.97	11.57	96.87	37.68	0.00	15.20
Townsville	Aw	6.05	2.45	10.29	97.49	25.72	0.41	11.68
Broome	BSh	4.65	-3.15	8.53	97.19	38.22	5.92	15.30
Cobar	BSh	4.70	-1.32	8.12	98.85	16.80	0.55	8.40
Kalgoorlie-Boulder	BSh	3.81	0.33	7.50	98.84	12.38	0.21	6.90
Longreach	BSh	2.81	-1.18	5.75	98.17	25.82	2.56	9.97
Tennant Creek	BSh	4.11	-1.68	9.02	97.51	21.23	0.05	9.83
Mildura	BSk	5.58	0.67	8.18	98.94	17.71	0.38	8.61
Alice Springs	BWh	3.06	-0.32	7.32	98.25	9.54	0.00	6.05
Learmonth	BWh	3.03	-0.75	5.76	98.17	26.10	5.05	10.67
Woomera	BWh	6.24	-0.13	8.01	99.10	13.87	0.53	7.61
Rockhampton	Cfa	9.58	-2.34	11.95	97.70	24.86	0.21	12.24
Wagga Wagga	Cfa	6.00	1.18	9.16	98.55	12.49	0.14	7.74
Cape Grim	Cfb	42.83	6.83	27.39	95.71	30.87	2.26	21.97
Melbourne	Cfb	27.96	2.07	13.57	98.66	14.39	1.75	10.82
Adelaide	Csa	9.94	2.80	11.25	98.29	24.86	0.34	11.92
Geraldton	Csa	3.81	1.00	8.59	97.91	20.05	0.00	9.31
Mt Gambier	Csb	17.13	4.57	13.08	98.28	35.18	2.18	15.88
Improved	40%	4	10	4	4	9	14	8
Marginal	59%	15	9	15	15	10	3	11
Worse	2%	0	0	0	0	0	2	0

Table 4.13: Statistical indicators for DNI under Köppen-Geiger zone BRL model (compared to National BRL model)

Location	KG Zone	Statistical Indicators (%)						
		MeAPE	rMBE	rRMSE	R^2	KSI	OVER	CPI
Cairns	Am	10.90	-0.11	12.03	97.93	14.48	0.49	9.76
Darwin	Aw	6.12	-0.91	10.32	97.50	17.17	0.00	9.45
Townsville	Aw	5.81	4.76	11.37	96.94	48.96	3.74	18.86
Broome	BSh	3.72	-1.17	7.87	97.61	16.53	0.06	8.08
Cobar	BSh	4.69	0.21	8.10	98.85	10.68	0.06	6.74
Kalgoorlie-Boulder	BSh	3.79	1.92	7.81	98.74	21.44	0.52	9.39
Longreach	BSh	2.30	0.41	5.68	98.22	14.75	0.00	6.53
Tennant Creek	BSh	3.59	0.01	8.79	97.64	7.27	0.00	6.21
Mildura	BSk	5.40	-0.53	7.93	99.01	12.60	0.04	7.13
Alice Springs	BWh	2.88	0.02	7.31	98.26	6.61	0.00	5.31
Learmonth	BWh	2.65	-0.23	5.57	98.29	17.48	0.50	7.28
Woomera	BWh	6.11	0.09	7.91	99.12	10.02	0.42	6.56
Rockhampton	Cfa	9.00	-1.34	11.37	97.92	21.46	0.66	11.22
Wagga Wagga	Cfa	5.85	1.79	9.36	98.49	19.62	0.51	9.71
Cape Grim	Cfb	39.00	1.18	25.03	96.42	11.14	1.34	15.63
Melbourne	Cfb	27.20	-1.79	13.31	98.71	18.38	1.13	11.53
Adelaide	Csa	8.73	0.48	10.30	98.57	11.96	0.05	8.15
Geraldton	Csa	4.23	-0.84	8.30	98.05	18.04	0.01	8.66
Mt Gambier	Csb	15.91	-0.11	11.25	98.73	17.73	0.63	10.21
Improved	74%	14	16	14	14	14	13	14
Marginal	19%	5	1	5	5	1	5	3
Worse	7%	0	2	0	0	4	1	2

4.4 Satellite-Based Data Results

The strong performance of the Köppen-Geiger zone BRL model applied to ground-based data presents an improvement opportunity to irradiation component estimation from GHI only data. BRL model improvements for satellite-based observations are investigated in this section.

As ground-based data measurements consist of single minutely observations to be representative of an entire hour to synchronise with the satellite estimate, new National BRL and Köppen-Geiger zone BRL models were fitted. Figures 4.38 and 4.39 show comparisons against the original AREMI data and ground-based measurements for the new National BRL models with persistence (National BRL) and variability parameters (National BoM) respectively. Improvements introduced by the new national models are not markedly apparent, however inspection at the high end of the clearness index range suggests the new national models may present an enhancement.

The statistical comparison between all models follows a similar tiered approach to the one presented in Section 4.3.1. Comparisons are first drawn against the diffuse fraction or DNI estimate of the original AREMI data set before direct model-to-model comparisons. To facilitate the comparison, different colour codes are applied from those used in Section 4.3 to better differentiate between the ground-based and satellite-based data analysis. In this section, blue indicates model improvement, purple a clear worse performance and grey a marginally worse performance.

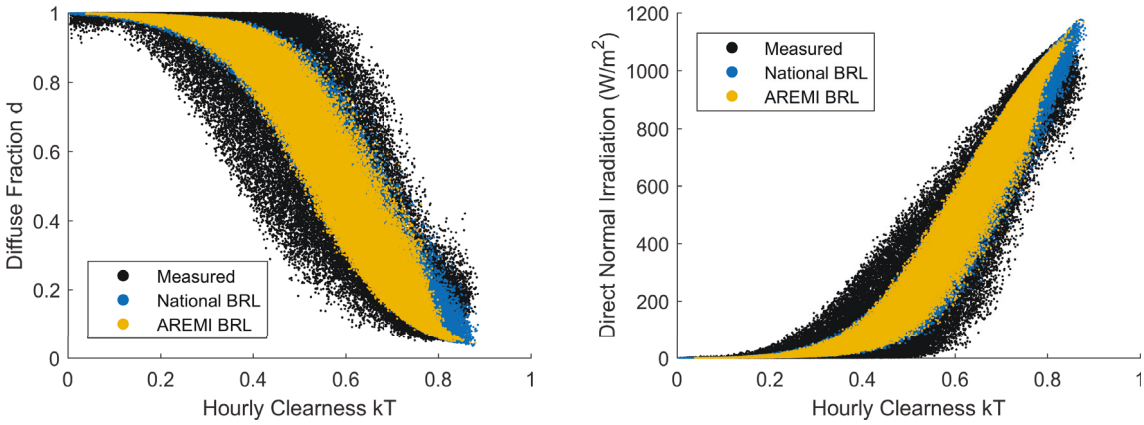

Figure 4.38: National BRL model results applied to satellite-based data for diffuse fraction (left) and DNI (right) for all Australian measurement locations

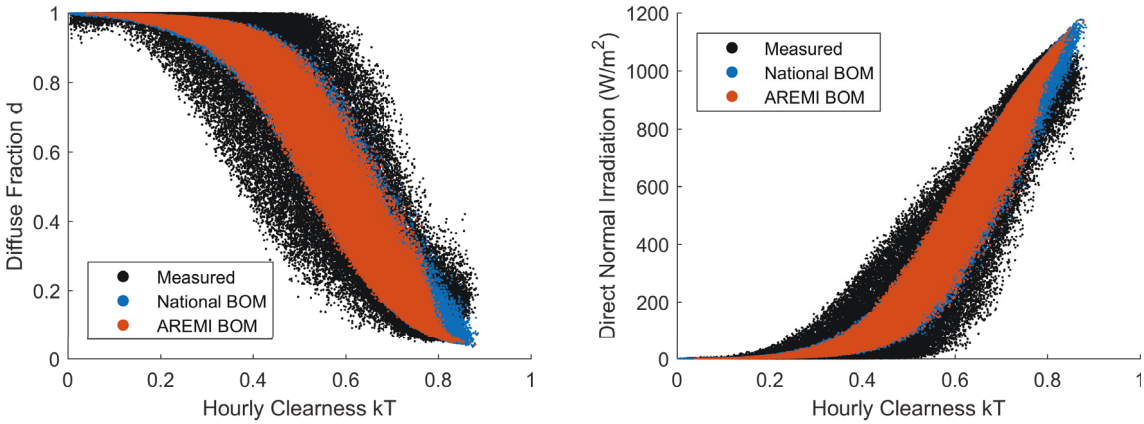

Figure 4.39: National BRL model (with BoM variability parameter) results applied to satellite-based data for diffuse fraction (left) and DNI (right) for all Australian measurement locations

4.4.1 Diffuse Horizontal Irradiation

AREMI diffuse fraction estimates are calculated from the estimated DNI data using a transposed version of (4.10). The statistical results associated with the original AREMI diffuse fraction data set against the measured ground-based data are shown in Table 4.14. The rMBE statistics can all be seen to be negative and consistently very high while the other statistics indicate generally poor correlation with the ground-based data. This suggests that improvements to the overall global irradiation model employed by BoM, which is based on the methodology of Weymouth and Le Marshall [57], is likely required, with consideration given to the quality control tests detailed in this article. Further discussion and context is provided in Section 4.5.

Similar to the ground-based results in Section 4.3, the development of a National BRL model based on high quality filtered data, provides a closer match to ground measurements than the original AREMI diffuse fraction estimate as shown in Table 4.15. Only 6% of the statistics demonstrate a worse result than the original AREMI data set and just one statistic exhibits a marginally worse outcome. The affected locations are all situated in arid areas with Köppen-Geiger zone designations of 'BSh' and 'BWh'. While improvement

in the statistics is clear through the application of a new National BRL model, rMBE continues to show universal under-estimation, further highlighting the requirement for review of the global irradiation satellite model.

Table 4.14: Statistical indicators for original AREMI diffuse fraction data set

Location	KG Zone	Statistical Indicators (%)							$\overline{d}$
		MeAPE	rMBE	rRMSE	R^2	KSI	OVER	CPI	
Cairns	Am	27.40	-17.79	47.24	51.67	355.56	270.57	180.15	0.57
Darwin	Aw	25.49	-16.21	44.78	63.02	424.08	327.17	210.20	0.49
Townsville	Aw	29.00	-26.14	55.45	54.02	284.73	184.95	145.15	0.46
Broome	BSh	27.02	-10.39	47.52	76.08	230.54	139.54	116.28	0.36
Cobar	BSh	23.44	-14.15	41.23	78.77	152.37	60.65	73.87	0.45
Kalgoorlie-Boulder	BSh	22.82	-14.16	42.97	75.83	341.78	245.08	168.20	0.46
Longreach	BSh	29.65	-12.64	51.17	76.64	117.39	29.96	62.42	0.32
Tennant Creek	BSh	31.01	-16.40	54.63	69.39	342.51	242.77	173.64	0.37
Mildura	BSk	23.59	-18.42	42.87	70.36	434.01	334.44	213.55	0.51
Alice Springs	BWh	26.47	-16.13	52.30	74.93	310.33	212.74	156.92	0.36
Learmonth	BWh	35.77	-2.18	58.91	73.26	276.79	185.25	144.97	0.29
Woomera	BWh	24.68	-22.00	43.32	64.82	208.78	115.14	102.64	0.55
Rockhampton	Cfa	22.52	-15.32	42.85	65.44	409.70	311.92	201.83	0.53
Wagga Wagga	Cfa	24.41	-16.25	40.67	73.13	403.03	299.66	196.01	0.50
Cape Grim	Cfb	19.04	-20.51	36.99	35.30	747.88	646.74	367.15	0.74
Melbourne	Cfb	17.32	-16.08	32.28	65.20	543.93	441.12	262.41	0.68
Adelaide	Csa	22.74	-16.95	37.36	72.66	469.45	367.38	227.89	0.56
Geraldton	Csa	28.07	-13.52	52.87	68.48	283.30	189.57	144.65	0.41
Mt Gambier	Csb	18.74	-16.67	34.68	65.83	413.61	310.58	198.39	0.65

Table 4.15: Satellite data statistical indicators for diffuse fraction under National BRL model (compared to original AREMI diffuse fraction data set)

Location	KG Zone	Statistical Indicators (%)						
		MeAPE	rMBE	rRMSE	R^2	KSI	OVER	CPI
Cairns	Am	23.89	-12.95	44.54	57.05	305.07	212.20	151.59
Darwin	Aw	21.24	-13.04	42.11	67.30	346.75	249.44	170.10
Townsville	Aw	20.76	-20.13	51.93	59.68	234.67	137.76	119.07
Broome	BSh	24.68	-3.96	43.63	79.83	200.10	110.42	99.45
Cobar	BSh	26.79	-6.89	37.12	82.79	144.56	54.82	68.41
Kalgoorlie-Boulder	BSh	23.84	-7.33	40.16	78.88	305.20	211.04	149.14
Longreach	BSh	28.17	-5.47	46.71	80.54	117.31	36.49	61.80
Tennant Creek	BSh	29.12	-8.72	49.64	74.73	289.80	196.16	146.31
Mildura	BSk	22.32	-11.21	39.77	74.48	355.84	259.23	173.65
Alice Springs	BWh	26.19	-8.52	48.71	78.26	291.03	196.02	146.12
Learmonth	BWh	38.72	5.32	57.49	74.53	298.27	208.25	155.38
Woomera	BWh	29.78	-16.05	40.07	69.89	188.00	93.10	90.31
Rockhampton	Cfa	17.99	-10.12	40.11	69.72	315.40	226.06	155.42
Wagga Wagga	Cfa	19.04	-9.34	37.69	76.92	290.57	194.83	140.20
Cape Grim	Cfb	12.98	-15.70	34.10	45.02	576.94	481.99	281.78
Melbourne	Cfb	11.15	-11.11	29.94	70.08	377.52	283.18	180.14
Adelaide	Csa	16.74	-11.05	34.46	76.75	346.70	252.32	166.98
Geraldton	Csa	26.26	-6.27	50.35	71.42	256.86	163.95	130.38
Mt Gambier	Csb	12.93	-9.70	31.32	72.13	253.67	160.43	119.18
Improved	93%	15	18	19	19	18	17	18
Marginal	1%	1	0	0	0	0	0	0
Worse	6%	3	1	0	0	1	2	1

Table 4.16 shows the National BoM model offers a better estimate for diffuse fraction over the National BRL model with 70% of the indicators showing improvement. The majority of the marginally worse statistics are associated with rRMSE and R^2. However,

Table 4.16: Satellite data statistical indicators for diffuse fraction under National BRL model (with BoM variability parameter) (compared to National BRL model)

Location	KG Zone	Statistical Indicators (%)						
		MeAPE	rMBE	rRMSE	R^2	KSI	OVER	CPI
Cairns	Am	23.98	-12.97	44.55	57.03	303.13	210.29	150.63
Darwin	Aw	21.15	-13.16	42.26	67.06	349.02	251.65	171.30
Townsville	Aw	21.03	-20.20	52.15	59.34	234.38	137.41	119.02
Broome	BSh	24.50	-4.22	43.86	79.62	199.46	110.16	99.34
Cobar	BSh	26.67	-7.01	37.34	82.59	143.84	54.27	68.20
Kalgoorlie-Boulder	BSh	23.90	-7.29	40.31	78.72	304.38	210.38	148.85
Longreach	BSh	27.78	-5.63	46.86	80.41	116.62	35.95	61.57
Tennant Creek	BSh	29.39	-8.72	49.82	74.55	287.80	193.98	145.35
Mildura	BSk	21.87	-11.05	39.73	74.54	350.67	254.19	171.08
Alice Springs	BWh	26.05	-8.49	48.92	78.07	290.34	195.26	145.86
Learmonth	BWh	38.11	4.93	57.29	74.71	295.05	204.90	153.63
Woomera	BWh	29.23	-16.04	39.93	70.10	186.42	92.11	89.60
Rockhampton	Cfa	17.90	-10.03	40.20	69.58	314.24	224.69	154.83
Wagga Wagga	Cfa	18.93	-9.10	37.64	76.99	286.61	191.08	138.24
Cape Grim	Cfb	12.93	-15.48	34.03	45.22	568.99	474.22	277.82
Melbourne	Cfb	11.17	-10.94	29.91	70.14	371.67	277.88	177.34
Adelaide	Csa	16.32	-10.89	34.46	76.74	343.60	248.86	165.35
Geraldton	Csa	25.70	-6.26	50.47	71.29	254.07	160.92	128.98
Mt Gambier	Csb	12.63	-9.64	31.41	71.97	252.66	159.29	118.69
Improved	70%	14	13	6	6	18	18	18
Marginal	29%	5	6	13	13	0	0	1
Worse	2%	0	0	0	0	1	1	0

Table 4.17: Statistical indicators for diffuse fraction under Köppen-Geiger zone BRL model (with BoM variability parameter) (compared to National BoM model)

Location	KG Zone	Statistical Indicators (%)						
		MeAPE	rMBE	rRMSE	R^2	KSI	OVER	CPI
Cairns	Am	24.25	-12.44	44.54	57.05	308.71	215.52	153.33
Darwin	Aw	22.00	-16.92	44.09	64.14	443.69	346.12	219.50
Townsville	Aw	22.43	-23.45	54.39	55.78	272.02	174.86	138.91
Broome	BSh	21.69	-9.06	45.08	78.48	209.57	115.53	103.81
Cobar	BSh	23.70	-10.74	39.09	80.92	155.00	62.23	73.85
Kalgoorlie-Boulder	BSh	21.14	-10.85	41.82	77.10	327.58	232.12	160.84
Longreach	BSh	23.99	-10.94	48.75	78.80	118.40	29.73	61.41
Tennant Creek	BSh	25.49	-13.28	51.61	72.68	312.00	214.84	157.52
Mildura	BSk	25.41	-11.87	40.72	73.25	403.30	306.54	197.82
Alice Springs	BWh	24.02	-9.90	49.22	77.80	280.71	185.75	141.22
Learmonth	BWh	34.36	2.67	56.90	75.06	270.94	180.94	141.42
Woomera	BWh	26.88	-16.89	40.14	69.79	185.58	91.22	89.27
Rockhampton	Cfa	20.92	-9.69	40.35	69.36	353.82	261.50	174.00
Wagga Wagga	Cfa	22.65	-8.85	38.04	76.50	327.65	231.82	158.89
Cape Grim	Cfb	11.74	-12.13	32.45	50.20	474.96	379.72	229.90
Melbourne	Cfb	10.81	-7.43	28.48	72.93	296.25	201.48	138.67
Adelaide	Csa	16.32	-8.25	33.07	78.58	294.32	199.89	140.09
Geraldton	Csa	27.46	-2.71	49.81	72.03	233.27	141.40	118.57
Mt Gambier	Csb	13.37	-12.43	32.91	69.23	315.55	221.82	150.79
Improved	41%	11	8	6	6	7	8	8
Marginal	23%	5	2	12	10	1	0	0
Worse	37%	3	9	1	3	11	11	11

the almost universal improvement in KSI, OVER and CPI suggest the National BoM model may be considered to be superior.

Given the superior statistical performance of the National BoM model over the National BRL model, the Köppen-Geiger zone BRL model is compared against the National BoM model in Table 4.17. The statistical indicators associated with the Köppen-Geiger model do not support the adoption of a Köppen-Geiger zone BRL model without improvement to the global irradiation satellite model of BoM. Without such an improvement, localization of the BRL model may be concluded to be inappropriate. Only 41% of the indicators exhibit an improvement while 37% show a clearly worse performance. The majority of the worse indicators relate to rMBE, KSI, OVER and CPI across multiple Köppen-Geiger zones.

Consequently, it may be concluded that there is no benefit in applying a climate classification system to the BRL models when considering satellite-based data estimates without improvement to the global irradiation satellite model employed by BoM. However, the better performance of the new National BRL model with variability parameter justifies the adoption of a new national-level model. The adjusted BRL parameters with a variability term, as detailed in Table 4.18, are proposed for application to the AREMI GHI data set.

Table 4.18: BRL model parameters for satellite-based global estimates

Model	β_0 (constant)	β_1 (k_T)	β_2 (AST)	β_3 (α)	β_4 (K_T)	β_5 (υ)
National BoM	-7.108	9.598	0.01416	-0.00743	2.813	-0.343

4.4.2 Direct Normal Irradiation

Table 4.19 shows the statistical indicators associated with the DNI estimate of the original AREMI data set. Table 4.20 shows a comparison of the new National BRL model applied to AREMI GHI data against the original AREMI DNI statistics. Similar to the ground-based results, the development of a National BRL level based on high quality filtered data, results in a closer match to ground estimates than the original AREMI DNI estimates. Only three of the statistics demonstrate a clearly worse result than the original AREMI DNI data set and only four statistics exhibit a marginally worse outcome.

A comparison of the new National BoM model against the new National BRL model is shown in Table 4.21. In contrast to the results for diffuse fraction in Section 4.4.1, the variability factor shows a worse performance than the persistence factor with only 41% of the statistics showing improvement.

Table 4.22 shows the results for the Köppen-Geiger zone BRL model. Similar to diffuse fraction in Section 4.4.1, no clear improvements are introduced by climatological classification considerations in BRL model development applied to satellite-based data. On 44% of the statistical indicators see an improvement. The indicators exhibiting a worse performance are spread across the climatological zones, inhibiting the potential to at least apply the Köppen-Geiger models to a subset of climatologies.

Table 4.19: Statistical indicators for original AREMI DNI data set

Location	KG Zone	Statistical Indicators (%)							$\overline{I_{bn}}$
		MeAPE	rMBE	rRMSE	R^2	KSI	OVER	CPI	
Cairns	Am	27.40	-17.79	47.24	51.67	355.56	270.57	180.15	421
Darwin	Aw	25.49	-16.21	44.78	63.02	424.08	327.17	210.20	477
Townsville	Aw	29.00	-26.14	55.45	54.02	284.73	184.95	145.15	541
Broome	BSh	27.02	-10.39	47.52	76.08	230.54	139.54	116.28	626
Cobar	BSh	23.44	-14.15	41.23	78.77	152.37	60.65	73.87	569
Kalgoorlie-Boulder	BSh	22.82	-14.16	42.97	75.83	341.78	245.08	168.20	551
Longreach	BSh	29.65	-12.64	51.17	76.64	117.39	29.96	62.42	683
Tennant Creek	BSh	31.01	-16.40	54.63	69.39	342.51	242.77	173.64	633
Mildura	BSk	23.59	-18.42	42.87	70.36	434.01	334.44	213.55	498
Alice Springs	BWh	26.47	-16.13	52.30	74.93	310.33	212.74	156.92	659
Learmonth	BWh	35.77	-2.18	58.91	73.26	276.79	185.25	144.97	722
Woomera	BWh	24.68	-22.00	43.32	64.82	208.78	115.14	102.64	457
Rockhampton	Cfa	22.52	-15.32	42.85	65.44	409.70	311.92	201.83	458
Wagga Wagga	Cfa	24.41	-16.25	40.67	73.13	403.03	299.66	196.01	500
Cape Grim	Cfb	19.04	-20.51	36.99	35.30	747.88	646.74	367.15	251
Melbourne	Cfb	17.32	-16.08	32.28	65.20	543.93	441.12	262.41	314
Adelaide	Csa	22.74	-16.95	37.36	72.66	469.45	367.38	227.89	448
Geraldton	Csa	28.07	-13.52	52.87	68.48	283.30	189.57	144.65	607
Mt Gambier	Csb	18.74	-16.67	34.68	65.83	413.61	310.58	198.39	352

Table 4.20: Satellite data statistical indicators for DNI under National BRL model (compared to original AREMI DNI data set)

Location	KG Zone	Statistical Indicators (%)						
		MeAPE	rMBE	rRMSE	R^2	KSI	OVER	CPI
Cairns	Am	55.93	11.53	60.65	59.50	165.91	92.21	94.86
Darwin	Aw	22.19	13.10	45.69	65.35	35.01	8.09	33.62
Townsville	Aw	14.20	14.63	45.78	61.90	116.60	33.38	60.38
Broome	BSh	10.41	2.00	27.11	78.56	162.93	75.18	73.08
Cobar	BSh	15.86	2.26	31.39	84.11	97.86	53.84	53.62
Kalgoorlie-Boulder	BSh	17.00	2.26	35.31	80.80	377.00	281.68	182.33
Longreach	BSh	10.44	0.34	23.94	80.69	110.30	42.51	50.17
Tennant Creek	BSh	11.79	2.75	31.41	74.97	174.17	117.48	88.62
Mildura	BSk	28.82	7.85	42.17	77.01	266.19	170.90	130.35
Alice Springs	BWh	10.33	1.58	28.71	79.15	249.71	163.49	117.66
Learmonth	BWh	11.80	-5.70	27.08	71.29	308.04	240.61	150.70
Woomera	BWh	45.15	14.81	48.17	74.81	130.61	42.01	67.24
Rockhampton	Cfa	36.41	7.71	49.22	69.83	342.99	251.31	173.19
Wagga Wagga	Cfa	27.73	5.92	39.97	78.33	347.91	254.43	170.57
Cape Grim	Cfb	280.07	40.15	100.69	50.10	185.72	93.57	120.16
Melbourne	Cfb	109.62	20.10	65.05	73.37	462.67	366.72	239.87
Adelaide	Csa	46.35	9.57	43.79	79.84	380.16	284.48	188.05
Geraldton	Csa	14.06	0.90	36.04	72.72	181.66	121.33	93.77
Mt Gambier	Csb	75.53	14.15	59.61	74.86	191.20	96.00	101.61
Improved	95%	16	18	19	19	18	18	18
Marginal	3%	3	0	0	0	0	0	1
Worse	2%	0	1	0	0	1	1	0

Table 4.21: Satellite data statistical indicators for DNI under National BRL model (with BoM variability parameter) (compared to National BRL model)

Location	KG Zone	Statistical Indicators (%)						
		MeAPE	rMBE	rRMSE	R^2	KSI	OVER	CPI
Cairns	Am	54.53	11.58	60.68	59.46	164.39	90.73	94.12
Darwin	Aw	22.28	13.23	45.82	65.15	34.25	7.42	33.33
Townsville	Aw	14.73	14.71	45.94	61.63	114.70	31.92	59.63
Broome	BSh	10.36	2.14	27.21	78.40	159.16	72.03	71.40
Cobar	BSh	15.77	2.34	31.49	84.00	97.90	53.21	53.52
Kalgoorlie-Boulder	BSh	17.15	2.23	35.42	80.68	377.85	282.59	182.82
Longreach	BSh	10.30	0.41	23.98	80.63	109.75	41.73	49.86
Tennant Creek	BSh	11.88	2.77	31.51	74.82	173.70	116.06	88.19
Mildura	BSk	28.61	7.75	42.17	77.01	268.18	172.72	131.31
Alice Springs	BWh	10.40	1.56	28.81	79.01	250.47	163.70	117.95
Learmonth	BWh	11.70	-5.54	26.98	71.50	303.36	236.36	148.42
Woomera	BWh	43.00	14.83	48.03	74.97	129.44	41.05	66.63
Rockhampton	Cfa	36.44	7.63	49.31	69.72	344.80	253.07	174.12
Wagga Wagga	Cfa	27.05	5.73	39.97	78.33	351.96	258.55	172.61
Cape Grim	Cfb	283.08	39.66	100.64	50.15	190.98	98.83	122.77
Melbourne	Cfb	110.92	19.75	65.07	73.35	467.55	371.66	242.34
Adelaide	Csa	46.48	9.42	43.81	79.81	383.35	287.67	189.66
Geraldton	Csa	14.20	0.93	36.09	72.64	180.02	119.69	92.98
Mt Gambier	Csb	76.27	14.05	59.80	74.71	192.63	97.51	102.43
Improved	41%	8	10	4	4	9	10	10
Marginal	47%	10	9	15	15	6	2	6
Worse	11%	1	0	0	0	4	7	3

Table 4.22: Satellite data statistical indicators for DNI under Köppen-Geiger zone BRL model (compared to National BoM model)

Location	KG Zone	Statistical Indicators (%)						
		MeAPE	rMBE	rRMSE	R^2	KSI	OVER	CPI
Cairns	Am	55.26	11.00	60.79	59.32	173.45	99.79	98.70
Darwin	Aw	22.55	15.90	46.86	63.55	77.12	12.53	45.84
Townsville	Aw	13.85	16.53	46.89	60.02	141.09	53.23	72.03
Broome	BSh	9.75	4.48	27.54	77.87	94.84	26.09	44.00
Cobar	BSh	14.71	4.80	32.13	83.35	93.47	42.33	50.01
Kalgoorlie-Boulder	BSh	16.20	4.75	35.97	80.08	320.48	225.50	154.48
Longreach	BSh	9.16	2.59	24.34	80.05	105.27	30.53	46.12
Tennant Creek	BSh	10.90	5.11	32.05	73.94	129.92	82.66	69.17
Mildura	BSk	29.60	8.27	42.74	76.38	262.63	168.30	129.10
Alice Springs	BWh	9.70	2.47	28.73	79.13	225.28	140.87	105.90
Learmonth	BWh	10.98	-4.62	26.69	72.10	277.83	210.59	135.45
Woomera	BWh	45.28	16.06	48.33	74.65	127.93	39.29	65.97
Rockhampton	Cfa	37.99	7.39	49.27	69.77	351.73	259.78	177.51
Wagga Wagga	Cfa	27.94	5.62	40.20	78.08	355.07	261.67	174.29
Cape Grim	Cfb	196.94	31.97	97.14	53.55	271.62	178.51	161.10
Melbourne	Cfb	90.83	13.61	62.91	75.09	552.21	455.37	283.35
Adelaide	Csa	44.44	6.95	42.86	80.68	430.10	333.45	212.32
Geraldton	Csa	15.12	-1.15	35.98	72.82	216.28	146.44	108.67
Mt Gambier	Csb	88.91	17.54	61.02	73.66	160.24	66.44	87.18
Improved	44%	12	7	5	5	10	10	10
Marginal	28%	6	3	14	14	0	0	0
Worse	28%	1	9	0	0	9	9	9

4.5 Discussion

The performance of the BRL model based on Köppen-Geiger climate zones shows some potential for ground-based measurement applications. However, the low spatial density of ground-based monitoring in Australia results in no more than four stations operating in any one zone. For most zones, only two stations are present while some zones only have one station with a relatively short measurement history (Mildura and Cairns). Additionally, not all climate zones identified in Table 3.7 have a BoM OMS station. Consequently, it is not possible to fit a Köppen-Geiger classification BRL model to these areas. However, the relatively small geographical size of these areas means only a small percentage of the Australian continent is ineligible for a Köppen-Geiger zone BRL model.

It is apparent from the small campaign data for some stations and low spatial density of monitoring, the zone correlations have room for improvement. The establishment of additional monitoring stations particularly for warm temperature ('C') and equatorial ('A') main climates, would enable the development of higher accuracy Köppen-Geiger BRL models within which the majority of the Australian population resides.

With reference to Table 4.8 and Table 4.13 in Sections 4.3.1 and 4.3.2 respectively, it can be seen that the majority of the clearly under-performing metrics for ground-based DHI and DNI estimates are associated with just three measurement locations – Townsville, Kalgoorlie-Boulder and Wagga Wagga. The lower performance for Townsville may be explained by the relatively short measurement campaign compared to Darwin as the other weather station within the Köppen-Geiger categorisation of 'Aw'. The Townsville data set consists of only 20% of the targeted two-years of randomly sampled data. Similar observations can be drawn for the DNI results.

Speculative explanations for Wagga Wagga and Kalgoorlie-Boulder are not as apparent. Köppen-Geiger zone re-categorisation trials were conducted to assess if the BRL model adjustments based on adjacent zones present a more applicable representation of local solar irradiation characteristics. However, the results for Wagga Wagga after re-categorisation as 'Cfb' and 'BSk' did not demonstrate any improvement. Kalgoorlie-Boulder showed some improvement through a 'BWh' categorisation.

It is evident that despite the demonstrably improved performance of the Köppen-Geiger BRL models for diffuse fraction applied to ground-based GHI data in general, the low spatial density of ground-based solar irradiation measurement stations within Australia results in model under-performance in some locations. For zones exhibiting such behaviour, deferral to the National BRL model may be more appropriate. The identification of such areas is non-trivial and requires consideration of separation distance. For example, for locations in the state of New South Wales within which Wagga Wagga is situated, it may be more appropriate to apply the National BRL model for 'CSa' classified areas, whereas in Queensland, within which Rockhampton is located, the Köppen-Geiger model may be retained.

Despite the deficiencies discussed above, the results presented in this research provide sufficient evidence to justify the application of adjusted BRL models for ground-based data – first in a national context through the application of rigorous quality control regimes to

tune BRL parameters, and secondly based on Köppen-Geiger zone classifications.

The statistical indicators associated with the satellite-based data results, as presented in Sections 4.4.1 and 4.4.2, are markedly worse in comparison to the ground-based assessment. The low correlation between ground-based measurements and satellite diffuse fraction and DNI estimates through the BRL model may be attributed to the larger errors associated with the GHI estimates within the AREMI data set. Referring to Figure 4.40 (left), the AREMI GHI estimates show an over-estimation bias, an issue that is magnified through the application of the BoM BRL model to estimate DNI. The amplification effect on DNI bias from GHI error can be better observed through examination of average daily profiles for winter and summer months in Darwin. As shown in Figure 4.41, the GHI error (left) is reduced compared to the full year. Consequently, the DNI estimate (right) provides a closer match to the ground-measured data. Conversely, for the summer months GHI error is larger leading to considerably larger DNI bias. The effect is more pronounced for the data from Adelaide with the winter average daily profile (Figure 4.44) exhibiting pronounced bias, particularly in the late afternoon as the the GHI AREMI observation deviates markedly from the ground measurement. The summer DNI estimates present a closer match to ground data, coinciding with a closer GHI approximation (Figure 4.45).

It may therefore be concluded that without improvement to the global irradiation satellite model of [57] employed by BoM, the over-estimation of global irradiation results in amplification of bias when estimating diffuse fraction and DNI irradiation following the application of the BRL model.

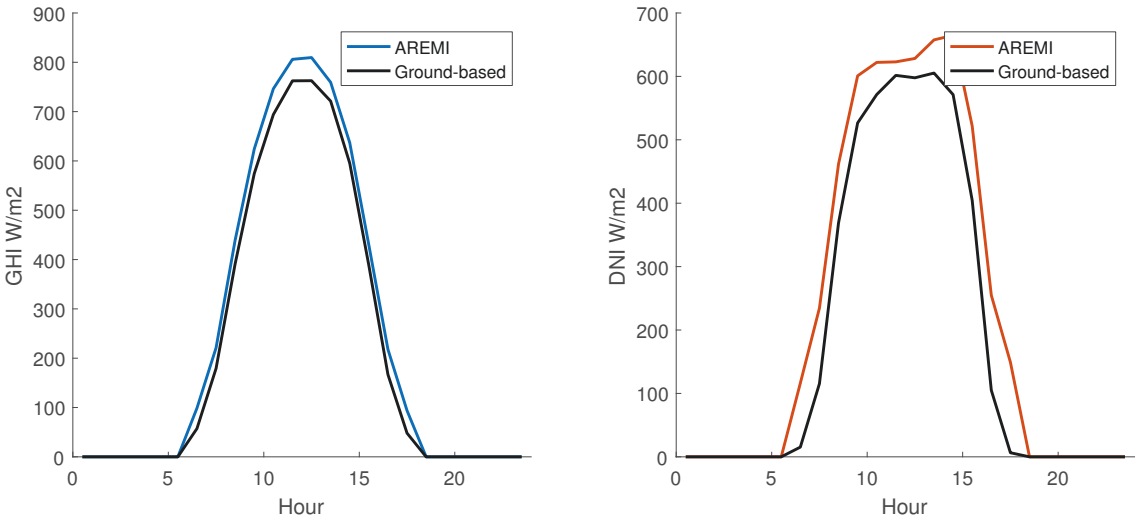

Figure 4.40: Darwin average hourly profile of AREMI GHI (left) and DNI (right) after filtering

The results presented in Section 4.4.1 and 4.4.2 show there is no improvement introduced through the application of Köppen-Geiger zone based BRL parameters to satellite data. However, the demonstrably better performance of the new National BRL model for diffuse fraction and DNI estimation after applying the quality control process of Section 4.2.1 justifies the adoption of a new National BRL model. The results for diffuse fraction and DNI present opposing arguments for the adoption of a variability term, as is

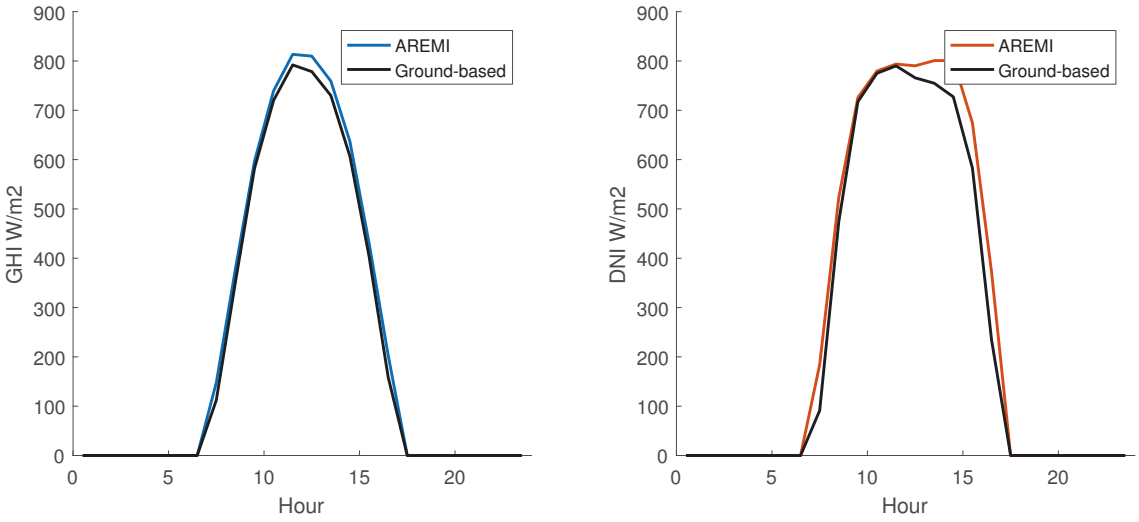

Figure 4.41: Darwin average winter hourly profile of AREMI GHI (left) and DNI (right) after filtering

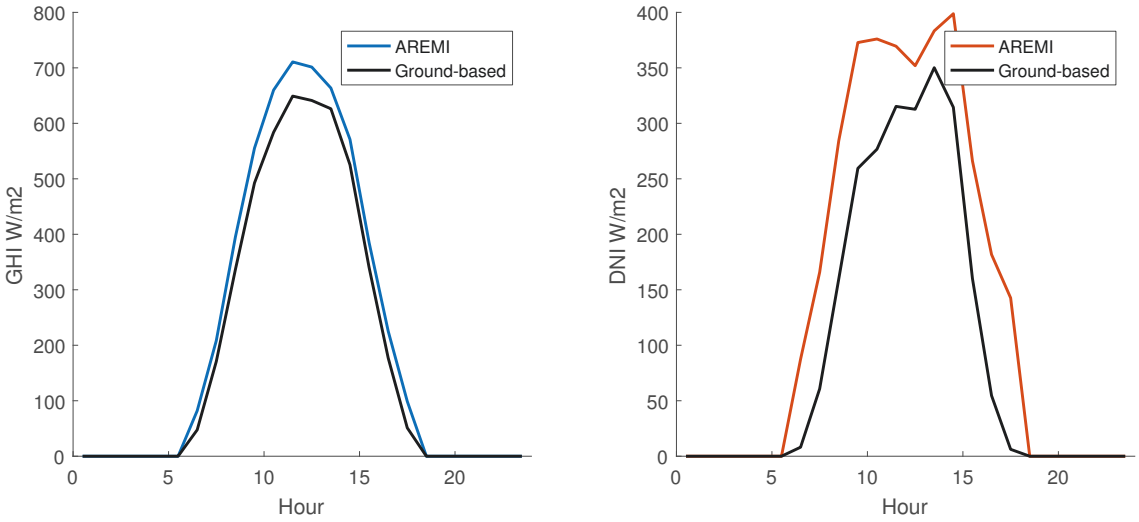

Figure 4.42: Darwin average summer hourly profile of AREMI GHI (left) and DNI (right) after filtering

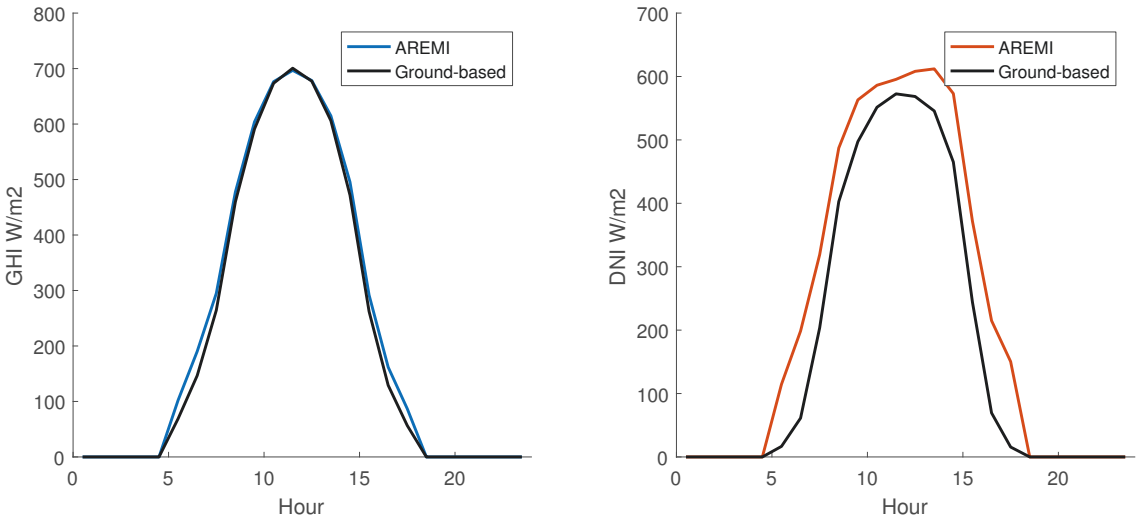

Figure 4.43: Adelaide average hourly profile of AREMI GHI (left) and DNI (right) after filtering

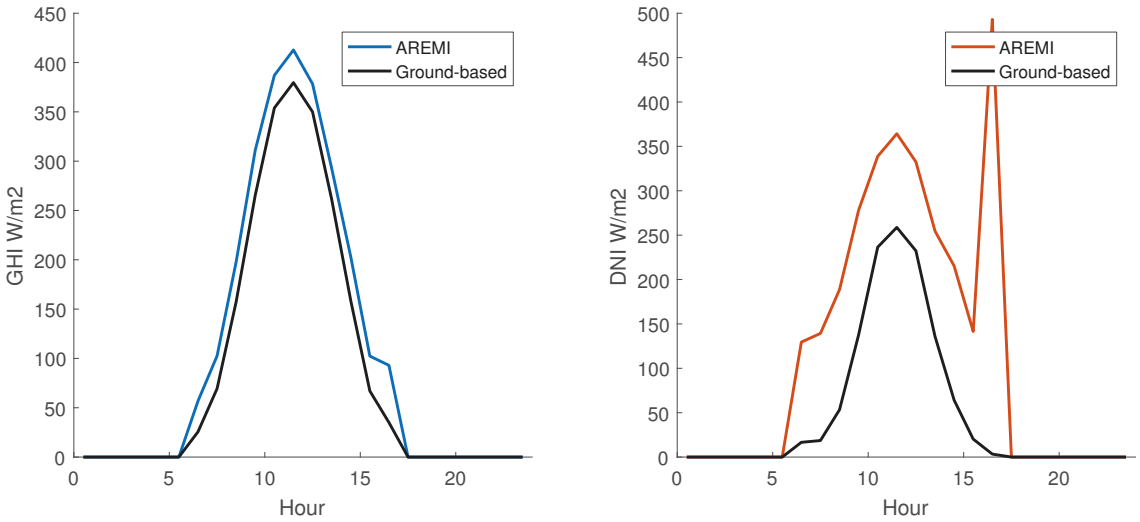

Figure 4.44: Adelaide average winter hourly profile of AREMI GHI (left) and DNI (right) after filtering

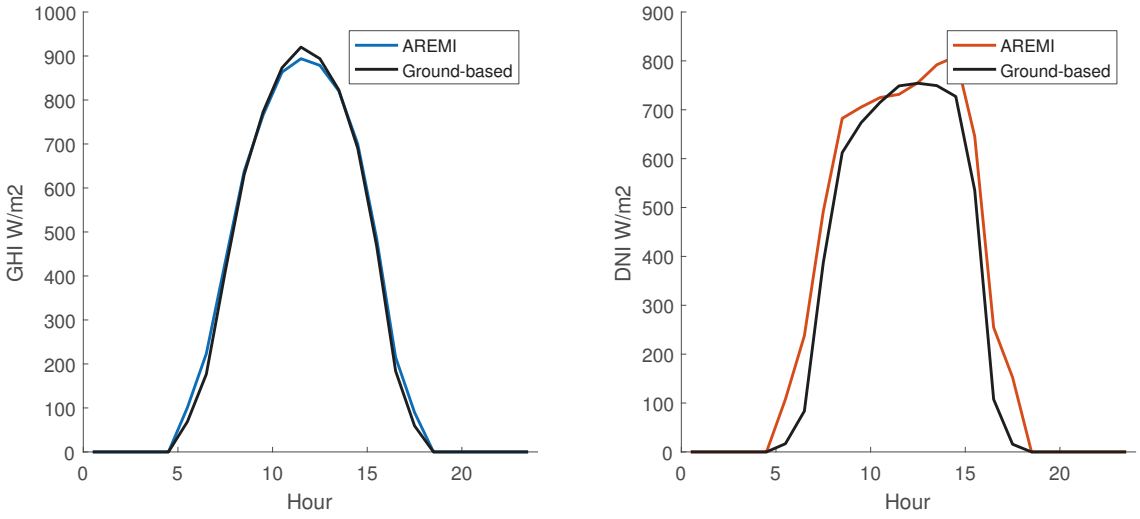

Figure 4.45: Adelaide average summer hourly profile of AREMI GHI (left) and DNI (right) after filtering

the case for diffuse fraction, or a persistence term, as is the case for DNI. For solar PV applications where accurate knowledge of diffuse irradiation is important for transposition models in order to calculate plane-of-array irradiation (discussed further in Section 3.5), it can be argued that it may be more appropriate to adopt the National BoM model.

4.6 Summary

The original research presented in this chapter aimed to improve estimates of diffuse irradiation components from global horizontal irradiation data measurements. The Köppen-Geiger climate classification system was proposed for application to diffuse irradiation models and investigated to establish the potential to improve modelling accuracy through climatological characteristic considerations of specific locations.

Rigorous data quality control steps were defined to establish a high quality tuning data set to facilitate the development of new BRL diffuse models. Using data from the Australian Bureau of Meteorology's one minute solar measurement station network, a new National BRL model was developed for ground-based measurements. Through the calculation of statistical indicators including mean absolute percentage error, mean bias error, coefficient of correlation, root mean square error, Kolmogorov-Smirnov Integral and the construction of cumulative distribution functions, the performance of the new model variant was established and compared against the original BRL model. The new National BRL model was shown to almost universally out-perform the original BRL model. The filtered data were then used to develop Köppen-Geiger zone specific BRL models. Similar analysis found strong support for the adoption of a specific climate classification models to improve diffuse irradiation estimates. New National and Köppen-Geiger BRL parameters were proposed for application to Australian ground-based global horizontal irradiation data in the absence of diffuse and direct irradiation estimates.

The low spatial and temporal density of ground-based irradiation measurements was proposed as a potential contributor to reduced performance in Köppen-Geiger models for some locations. An opportunity for improvement through the establishment of additional measurement locations within each Köppen-Geiger zone, particularly on the coastal fringes of eastern Australia where the majority of the population resides, was identified. As an intermediate solution, deferral to the new National BRL model was proposed in instances where the Köppen-Geiger models are shown to be inferior.

Due to the limited ground coverage of global horizontal irradiation estimates, satellite-based irradiation estimates were investigated. Hourly satellite measured irradiation data from 1990 to 2015 processed by BoM and made available through the AREMI database were examined for potential improvement through the development of new National BRL and Köppen-Geiger BRL models. The Australian BoM uses a variant of the BRL model to process data within its hourly solar insolation database, which takes into account clearness index variability as opposed to a persistence factor. The BoM variability was also investigated for potential model improvements.

Based on a similar data quality control and statistical analysis approach, the results found in this research do not support the adoption of Köppen-Geiger zone BRL models

for satellite-based estimates without improvement to the global irradiation satellite model employed for the AREMI data set. However, a new National BRL model based on the BoM BRL model variant was found to present a closer approximation to ground-based measurements than the original AREMI data set.

In the next chapter, synthetic hourly irradiation from daily irradiation data as previously presented in Section 3.2.9 are first utilised as part of a design optimisation strategy to reduce lifetime energy costs based on specific consideration of temporal energy consumption profiles. The new National BRL diffuse irradiation model developed in this chapter is leveraged in the more advanced system and market analyses presented in Chapter 6 and Chapter 8.

Chapter 5

PV Design Optimisation

Over the last decade the solar PV industry has undergone significant technological improvement and enormous growth in installed capacity. As market penetration increases, primarily driven by the continued reduction in technology costs, installation incentive schemes will be reduced or removed altogether.

The reduction and removal of incentive schemes are not the only disrupting factor to the small-scale PV industry. The penetration and system characteristics of residential PV systems have the potential to be significantly influenced by the introduction of smart meters and other smart grid technologies. Enabled by smart meters, the implementation of dynamic tariff structures will require due consideration of a customer's temporal energy consumption habits.

The SGSC project commissioned by the Australian Government between 2012 and 2014 [1] and other independent research conducted by the Grattan Institute [29] in 2015 [1] found a real and immediate business case for the introduction of dynamic tariffs. Focusing on temporal energy demand, dynamic tariffs were deemed necessary to remove the cross-subsidies existing between non-PV owners and PV owners. Under such an environment, the uptake of small-scale PV in Australia was projected to exhibit continued growth. However, in response to the recommended tariff restructures, a reduction in average size of new residential systems was forecast to occur [1].

An optimisation strategy for residential PV systems is developed in this chapter. The maximisation of the net benefit achieved through reduced imported energy costs is set as the underlying objective. Within a competitive retail electricity market with various tariff structures including flat and dynamic TOU rates, the best plan is not self-evident. The research presented in this chapter is principally focused towards leveraging temporal energy consumption data facilitated by smart meters to develop a customer specific evaluation based on other influential factors such as location, prevailing solar irradiation and available retail electricity plans. The traditional PV installation objective to maximise gross energy generation is challenged and demonstrated to not necessarily be the most cost-effective approach. The ultimate objective of this research is to remove the uncertainty in system specification and retail electricity plan selection in a competitive retail market and dynamic regulatory environment.

While PV system design optimisation may be undertaken using many existing software

platforms, widespread application of optimisation techniques at the residential consumer level using real-world high temporal resolution smart meter consumption data has not previously been investigated in an Australian context. The novelty of this research lies in the large sample size application of design optimisation techniques to establish market trends in different geographical and electricity network areas. The research presented in this thesis is intended to establish viability trends for PV systems in the Australian electricity market including drawing comparisons against recently installed PV systems and highlighting the economic efficacy of such systems.

As a basis for the optimisation problem defined in this chapter, a PV array energy yield model using the solar irradiation models presented in Chapter 3 is defined. Particle swarm optimisation (PSO) is used as the underlying optimisation algorithm, given its speed and simplicity of application to non-linear problems. The standard canonical algorithm is modified first through the introduction of a penalty function and then through the introduction of a hypercube nearest vertex approach previously established in literature to enable the handling of constraints.

Actual solar irradiation data from selected Australian locations, smart meter data from the SGSC project and electricity plans from three large Australian retailers are applied to the optimisation problem to demonstrate the potential investment value of optimally selected PV systems. Although the assessment presented in this chapter is undertaken in an Australian context, the principles and analysis methodology are applicable to any location or country.

5.1 Literature Review

Solar power generation, particularly PV, has undergone enormous growth over the last decade. The growth can be primarily attributed to technological improvements and the introduction of government incentives such as rebates and feed-in tariffs [29,184]. However, less tangible factors such as increased end-user energy awareness and an increased public perception of the potentially damaging impacts of unrestrained carbon emissions have also led to a dramatic increase in the number of rooftop PV installations. The cumulative installed capacity of small-scale PV systems in Australian up to July 2019 was 9.1 GW as shown in Figure 5.1 [185], increasing from just 8,000 homes with solar PV in 2007 [186].

The countries leading the PV uptake on an installed capacity basis include China, Japan, United States, Germany, India, Itay and the United Kingdom [187]. By 2018, China had installed over 175 GW of solar PV, almost three times more than any other country as shown in Figure 5.2 [186].

One of the primary disadvantages associated with PV is fluctuating and intermittent power output. Solar energy is entirely weather dependent and consequently experiences frequent periods of generation well below system ratings. PV panels are only able to generate energy during daylight hours, typically reaching peak output around midday. Periods of maximum load demand typically occur during the morning and in the early evening. Therefore, there is generally a misalignment between the period of maximum

generation and the period of maximum load demand as shown in Figure 5.3.

5.1.1 Photovoltaic Technologies and Materials

PV cells are specially manufactured semiconductor diodes designed to absorb photons to create electron-hole pairs in the semiconductor material [188]. The pn-junction formed by appropriately doping the semiconductor material creates an electric field which separates the electron-hole pairs [189]. Absorption of photons elevates electrons from the valence band into the conduction band, leaving behind holes in the valence band [189]. Once

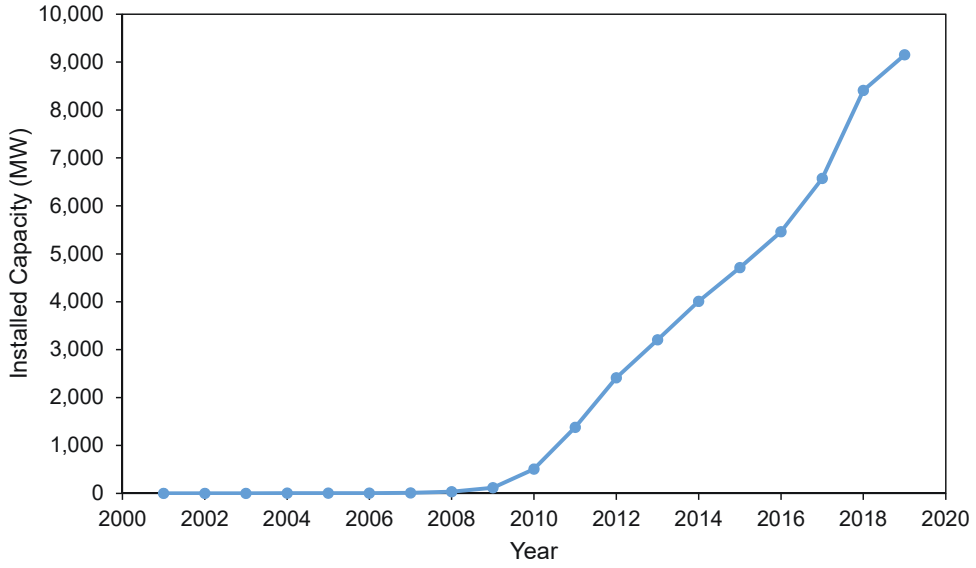

Figure 5.1: Installed cumulative capacity of small-scale solar installations in Australia to July 2019. Source data: Clear Energy Regulator [185]

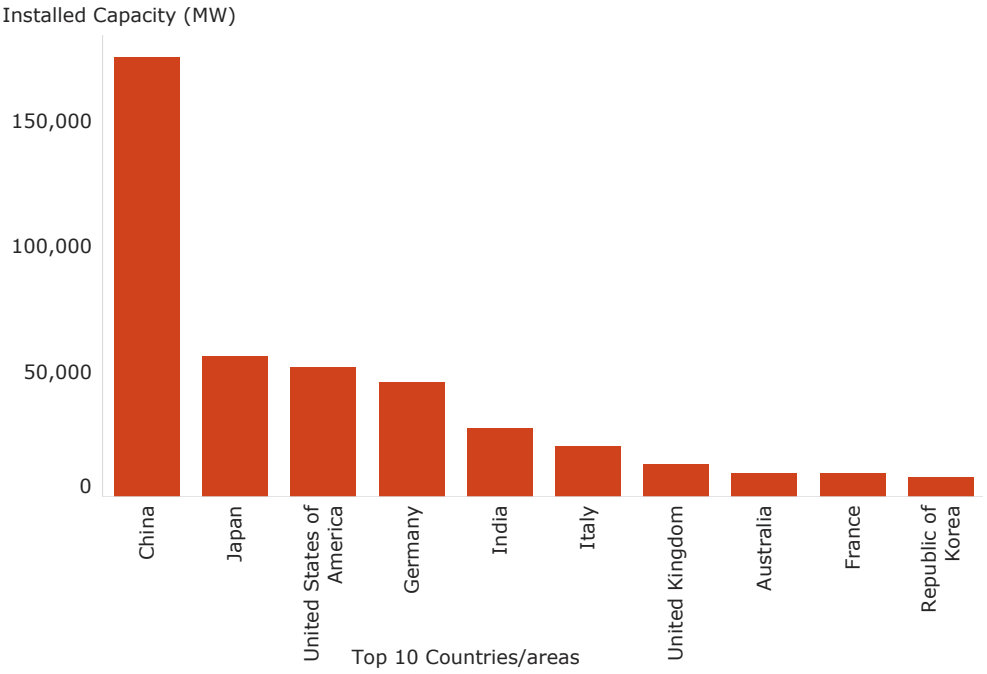

Figure 5.2: Global solar PV installed capacity up to 2018. Source: IRENA [187]

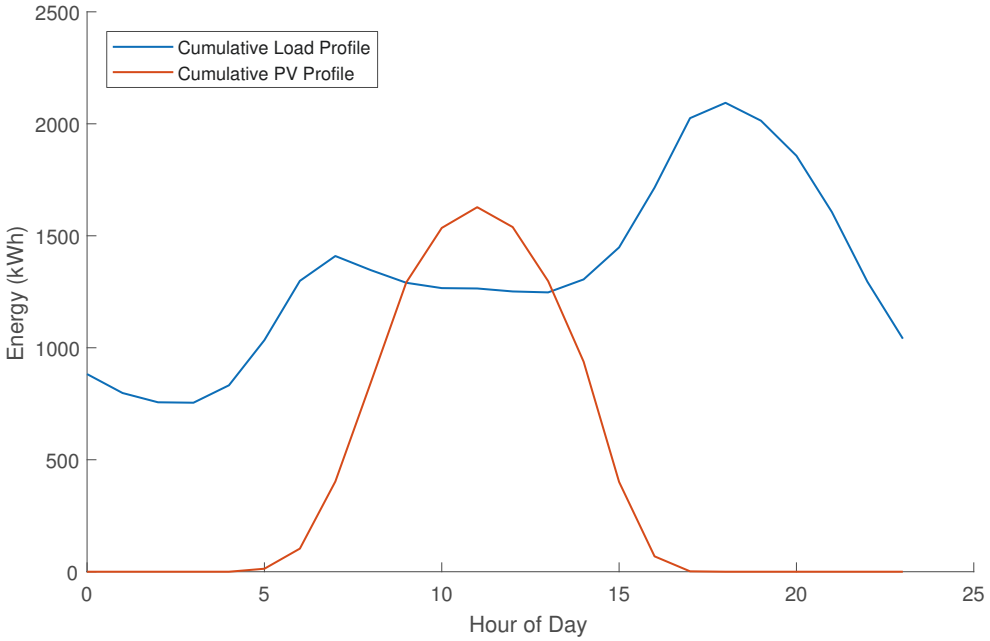

Figure 5.3: Example average hourly cumulative load and cumulative PV generation profiles for a group of electricity consumers

the charge carriers are separated into these regions, they are able to participate in the conduction process when an external electrical circuit is completed [189].

A multitude of PV materials and topologies exists from basic single junction cells to III-V multi-junction cells designed to enable photon absorption from a wide band of the radiation spectrum [190]. However, for the vast majority of current terrestrial solar applications, PV cells are constructed from three main technologies – monocrystalline silicon, multicrystalline (also referred to as polycrystalline) silicon and thin-film materials. Each technology has its own advantages and disadvantages in terms of manufacturing cost, efficiency and temperature performance.

Monocrystalline PV cells are constructed from thin wafers cut from a single silicon crystal [189]. As monocrystalline silicon exhibits a near perfect crystal lattice, it exhibits the highest efficiency per unit area at standard test conditions. Due to the energy intensive process to produce pure silicon ingots, monocrystalline PV cells are more expensive to produce than multicrystalline cells which are produced by cooling melted silicon in a crucible at a controlled rate [189]. The final multicrystalline product has a non-uniform crystal structure, however the structure still enables the cells to exhibit similar performance characteristics to monocrystalline.

Thin-film cells refer to a range of technologies and chemistries including amorphous silicon, cadmium telluride (CdTe) and copper indium gallium selenide (CIGS). Thin-film technologies have vastly improved in recent years [184] to the point that they are now cost competitive with crystalline cells, particularly in warmer environments. Of the thin-film technologies, CdTe is the most competitive and has seen the largest commercial penetration [191].

Thin-film cells are a direct semiconductor meaning they have valence and conduction bands that are aligned with respect to band gap momentum. Consequently, photons near

the band gap energy are likely to be readily absorbed without requiring momentum in addition to their energy [188,189]. In contrast, indirect semiconductors such as crystalline silicon feature band misalignment with respect to momentum, resulting in inefficient absorption of photons near the band gap energy. Due to their efficient photon absorption, thin-film cells can be manufactured with significantly reduced semiconductor thickness when compared to crystalline silicon cells resulting in material and cost savings.

5.1.2 Geographic Location of PV systems

Designing a PV system requires consideration of geographical location and environmental conditions in order to determine the requirements of the physical installation to achieve optimality. The latitude of the location has a significant influence on the alignment of the PV panels with respect to the horizontal plane. Generally, PV panels in the northern hemisphere should face south whereas panels in the southern hemisphere should face north [157].

Variation in the angle of incidence of solar irradiation during different seasons of the year complicates the orientation of the panels [189]. During winter, the sun is lower in the sky than in summer, requiring an increased angle of tilt further towards the vertical. When PV systems are installed without solar tracking, as is the case in the vast majority of small-scale PV installations, the season on which to base the PV panel orientation is largely dependent on the seasonal load profile of the consumer and the ability to participate in solar feed-in schemes [157]. However, the optimal solution is not always transparent. For example, a hypothetical installation may require more electrical energy for heating during winter than cooling in summer. This would initially imply that a PV system should be designed and oriented for maximum utilisation during winter. However, summer months typically yield an increased level of system utilisation through more daylight hours and a higher average hourly solar irradiance. If a PV system is installed such that it can feed-in to the electricity grid and therefore take advantage of feed-in tariffs, the optimal system arrangement could be one designed for summer months, despite the hypothetical higher winter load.

The lack of transparency regarding the optimal system arrangement is a key driver for the PV system design optimisation tool investigated in this research. Optimal alignment of solar panels have been investigated extensively in literature [157,189,192–194]. However optimisation of PV panel orientation combined with detailed load profiles obtained through smart metering devices, has not be investigated to any significant extent.

5.1.3 PV Installation Incentive Schemes

As market penetration increases for PV, primarily driven by the continued reduction in technology costs, installation incentive schemes are expected to reduce or be removed altogether. In an Australian context, PV systems contribute to the Australian Government's Renewable Energy Target (RET) and are therefore eligible for certain incentives depending on the size of the system installed. For systems of 100 kW or less, PV systems are deemed to be part of the SRES. Historically, the Solar Bonus Scheme (SBS) incentivised

the installation of PV through a generous feed-in tariff (FiT). The SBS encouraged investors to install large PV systems aiming to generate as much energy as possible during peak solar irradiation hours. However, the SBS in Australia, under which the FiT was initially set to be 60 c/kWh and later reduced to 20 c/kWh, was closed to new customers in 2011 and officially ended in 2016.

An assessment of the Australian Government Clean Energy Regulator (CER) database [195] revealed a relatively large national average size of 5.11 kW for new systems installed between January 2015 and August 2016. However, due to closure of the SBS, the newly installed larger systems are ineligible for the high FiTs mandated under the SBS and subsequently the payback periods are increasingly reliant on the cost savings achieved through self-consumption of PV generated energy.

Systems installed as part of the SRES continue to receive incentives in the form of upfront small-scale technology certificates (STCs) [196]. Current policy is to retain the SRES in the medium term, however the magnitude of the effective rebate will be gradually reduced between 2017–2030 [197], complicating the investment decision process.

PV systems may still be eligible to receive FiTs from an energy retailer, however current Australian FiTs are no longer mandated but rather set by individual retailers. As an example, the benchmark range for FiTs in New South Wales was 4.7–6.1 c/kWh in 2015–2016 [198] and increased to 8.5–10.4 c/kWh in 2019–2020 [199], still significantly less than those offered under the SBS.

For PV systems larger than 100 kW, incentives are provided through large-scale generation certificates (LGC) [196]. PV system developers commonly enter into a negotiated power purchase agreement (PPA) with an interested electricity off-taker, most commonly energy retailers but also large corporations with a high demand for energy. Under a PPA, the price to purchase LGCs from the PV installation is typically built into the total price paid for grid-exported energy.

The research presented in this thesis investigates solar PV modelling of residential and commercial PV systems in the context of current Australian market conditions and the incentive schemes developed to achieve the RET. Chapters 5, 6 and 8 consider FiTs and STCs for design optimisation of small-scale systems. Chapter 7 investigates the optimisation of solar PV under incentive schemes for both small-scale and large-scale systems.

5.1.4 PV System Optimisation

The optimisation of PV systems have been extensively researched in literature [200, 201]. A variety of optimisation methodologies have been utilised including numerical methods [157, 202] and metaheuristic methods such as genetic algorithms [203–207] and PSO [176, 208–212]. In recent times, research has focused heavily towards hybrid renewable energy systems and microgrids [204, 205, 207, 212, 213]. However, given hybrid systems predominantly find applications in medium to large-scale energy systems, the objectives, assumptions and methodology are not well-suited to small-scale residential systems. Consequently, limited research exists relating to a comprehensive market assessment for economic optimisation in residential PV applications.

Self-consumption and load matching of PV to residential loads have been investigated in [202, 203, 214]. Widen et al. [202] assessed load matching of PV combined with demand side management and energy storage systems through consideration of customer load profiles. However, it was acknowledged that no consideration was given to economic performance or optimal sizing of PV systems. Beck et al. [203] investigated the temporal resolution of smart meter load data on the self-consumption rate of PV generated electricity, developing an economic model to optimise the system size. However, a single standardised profile from an example PV system was applied to all analysed cases, thereby eliminating tilt and azimuth optimisation from the analysis.

The economic evaluation of PV systems has been extensively investigated. Many articles consider cost-benefit relationships through variations on a NPV analysis [157, 201, 203, 205, 206, 215–219]. Mulder et al. [215] investigated the dimensioning of PV-battery systems based on selling price and incentive conditions by utilising smart meter data from 65 Belgian households. Although smart meter data with a relatively high resolution (15 minutes) were used in the analysis, the temporal resolution was not leveraged; only cumulative annual generation and consumption profiles were considered.

Pillai et al. [217] investigated the near-term economic benefits of PV systems in the UK and India by determining the prosumer energy unit cost, equivalent to levelised cost of energy (LCOE). However, the analysis was based on a national average PV system size and monthly energy demand profile rather than the circumstances of an individual customer.

Despite the prevalence of existing literature focusing on PV system optimisation, no research has aimed to develop an encompassing design tool at the consumer level to inform prospective residential PV system owners through an integrated approach determining system size, orientation and the associated least cost retail electricity plan. With the integration of Smart Grid technologies, particularly the continued installation of smart meters and the introduction of dynamic electricity tariffs, such an optimisation tool is required to empower customers and provide confidence in the potential investment value of residential PV systems.

5.2 Photovoltaic Model

The PV energy yield model considered in this research is based on the model defined by Duffie and Beckman [115]. Using data provided on manufacturer data sheets under nominal operating cell temperature (NOCT) and standard test conditions (STC), the operating temperature of a particular PV module can be determined through (5.1):

$$T_c = T_a + (T_{NOCT} - 20) \cdot \frac{G_T}{800} \cdot (1 - \eta_{mpp,STC}) \tag{5.1}$$

where T_a is the ambient temperature, T_{NOCT} is the nominal operating cell temperature, G_T is the incident solar irradiance (i.e. power per unit area) and $\eta_{mpp,STC}$ is the maximum power point efficiency at standard test conditions.

The operating efficiency of the PV module at particular environmental conditions is

defined as:

$$\eta_{mpp} = \eta_{mpp,STC} + \mu_{mpp}(T_c - T_a) \tag{5.2}$$

where μ_{mpp} (%/°C) is the temperature coefficient of power provided on the module data sheet.

According to [115], the output power of a PV array at any particular instant, assuming the array has maximum power point tracking, can be described at a simple level as:

$$P_{pv} = A_c Z G_T \eta_{mpp} \eta_e D_y \tag{5.3}$$

where A_c is the PV module area, Z is the number of PV modules, η_e is the efficiency of the associated balance of plant (including the maximum power point tracking inverter and other loss associated equipment) and D_y is the PV module degradation factor in year y.

Most PV module manufacturers offer a linear power performance warranty whereby the module output degrades linearly over the warranty period. Consequently the degradation factor D_y can be expressed as follows:

$$D_y = D_1 - r_{deg}(y-1) \quad \text{for } 1 \leq y \leq Y \tag{5.4}$$

where r_{deg} is the manufacturer prescribed degradation rate and D_1 is the degradation factor in the first year (since performance equal to 100% of the rated output is not usually guaranteed).

If the instantaneous power is integrated over time and G_T is assumed to be constant over the period so that the hourly irradiation $I_T = G_T$, then the energy produced by the PV array over an hour is defined as:

$$E_{pv} = A_c Z I_T \eta_{mpp} \eta_e D_y \tag{5.5}$$

In (5.5), I_T is the hourly irradiation on the tilted plane defined by the HDKR model of (3.51) in Section 3.5.3. Equation (5.5) constitutes the underlying energy yield model used in the objective function of the optimisation problem defined in Section 5.4.1.

5.2.1 PV Maintenance Model

The cost of maintenance W_q must be accounted for when undertaking an NPV analysis. Although small-scale residential systems are largely maintenance free, periodic system inspections are required. Definitive guidelines for maintenance frequency and statistical costs have not been universally established. Consequently, in this research, maintenance is assumed to be carried out every five years at a cost of $200, a reasonable assumption provided the system is properly installed.

Furthermore, while PV modules are known to have relatively long operational lifespans (in excess of 20 years), inverters usually require replacement at least once over the lifetime of the system. In this research, inverter replacement has been assumed to occur after ten years of operation. Consequently, based on the assumptions above and recognising

that t is the number of billing periods per year, maintenance is therefore required every $5t$ (maintenance only) and $10t$ billing periods (maintenance plus inverter replacement). The maintenance costs defined by (5.6) are determined at the start of each billing period, where U_{inv} refers to the inverter replacement cost per watt peak ($/W$_p$) and $S_{pv}(Z)$ is the PV system cost defined later by (5.17). If maintenance is due, W_q defined by (5.6) forms a negative cash flow in the later-defined objective function of (5.12) for period q.

$$W_q(Z) = \begin{cases} 200 & \text{if } \frac{q-1}{5t} \in \mathbb{Z}^+,\ \frac{q-1}{10t} \notin \mathbb{Z}^+ \\ 200 + U_{inv}S_{pv}(Z) & \text{if } \frac{q-1}{10t} \in \mathbb{Z}^+ \\ 0 & \text{otherwise} \end{cases} \tag{5.6}$$

5.3 Economic Model

Due to the relatively long lifetime of PV systems, the time value of money must be considered. The option to invest in a PV system must be compared against other investment options that are realistically expected to earn a minimum rate of return. The time value of money is most commonly considered through a present value analysis. For a given investment option, future cash flows are discounted to yield their present value. Summation of the present value of each cash flow and subtracting the initial cost of the investment yields the NPV of the investment. NPV is therefore expressed as:

$$\text{NPV} = \sum_{q=1}^{Q} \frac{C_q}{(1 + r_{nom})^q} - C_0 \tag{5.7}$$

where C_0 is the initial investment cost, C_q is the cash flow in period q, Q is the number of billing periods and r_{nom} is the nominal discount rate. The discount rate is defined as the opportunity cost of capital – the return an investor reasonably expects to yield from well-defined alternative investment options. For the analysis presented in this chapter, the cost of capital is assumed to be 6% p.a., chosen to be reflective of standard investment options available to a typical home owner.

In addition to the time value of money, the purchasing power of the currency, which diminishes due to inflation, must also be considered. Inflation can be included in the economic model by modifying the nominal discount rate to yield a real discount rate defined by (5.8):

$$r_{real} = \frac{(1 + r_{nom})}{(1 + r_{inf})} - 1 \tag{5.8}$$

where r_{real} and r_{inf} are the real discount and inflation rates respectively. Assuming the more conservative inflation rate of 2% within the Reserve Bank of Australia's target range of 2–3% [220], the real discount rate considered in this research is 3.92%.

For retail electricity, typical billing periods are monthly or quarterly. Therefore the assumed annual rates must be converted to an effective rate based on the period of billing

as given by (5.9):

$$r_d = (1 + r_{real})^{1/t} - 1 \tag{5.9}$$

where r_d is the effective real discount rate for the period and t is the number of billing periods per year. For quarterly billing ($t = 4$), the effective quarterly rate, assuming $r_{real} = 3.92\%$, is $r_d = 0.97\%$.

Although NPV analysis is predominantly the primary metric for assessing investment options, the rate of return is also critically important to establish investment preferences among competing options. For the economic analysis considered in this research, the modified internal rate of return (MIRR) [221] as defined in (5.10) is used:

$$\text{MIRR} = \sqrt[Q]{\frac{\sum_{q=1}^{Q} C_q^+ (1 + r_{inv})^{(Q-q)}}{C_0 + \sum_{q=1}^{Q} C_q^- (1 + r_{fin})^q}} - 1 \tag{5.10}$$

where r_{inv} and r_{fin} are the re-investment and finance rates respectively (both assumed to be equivalent to r_d), while C_q^+ and C_q^- denote positive and negative cash flows respectively. Negative cash flows are associated with maintenance and equipment replacement costs in the context of a PV system.

Ideally, the MIRR should be greater than the cost of capital. In this research, an investment yielding such a return is defined as a 'viable' investment. However, despite the 'viable' investment definition, the intangible value associated with PV systems complicates the decision criteria – an investor may consider an MIRR slightly lower than the cost of capital to be acceptable in order to reduce their net carbon emissions. Thus, in the context of residential PV systems, the requirement for an MIRR greater than the cost of capital should not be seen as prescriptive, but used rather as a supporting metric for NPV to be balanced with an investor's desire to reduce their environmental footprint.

The final metric considered in this research is the payback period defined as:

$$P = A + \frac{B}{C} \tag{5.11}$$

where P is the payback period, A is the number of periods whereby the cumulative cash flow is negative, B is the residual cost to be paid back in period $A + 1$ and C is the total cash flow in period $A + 1$. A PV system may yield both a positive NPV and adequate MIRR over its design life, however if a particular investor intends to relocate before the expiration of the system life (thus prior to the realisation of any net benefit), knowledge of the payback period is crucial.

5.4 Photovoltaic System Optimisation Problem

The optimisation objective is to maximise the monetary savings achieved by installing an optimally sized and oriented PV system. The savings, defined as the difference between the cost of electricity with an optimised PV system under a given retail electricity plan, against a known lowest cost 'do nothing' plan, are quantified through the NPV analysis defined in Section 5.3. Through a comparison of the optimised systems for each of the

retail electricity plans available to an individual customer, the optimal system and tariff structure for a particular residence can be determined.

The defining equations for the optimisation problem and the subsequent analysis in this research are based in an Australian context. Irradiation and energy consumption data for a sample of Australian customers are used. Furthermore the economic parameters, system costs and available incentive schemes are reflective of the Australian PV industry. However, the problem is easily transferable to other national contexts given equivalent economic parameters, tariff structures and system costs.

5.4.1 Problem Definition

The optimisation problem considered in this research is defined as follows:

Given:

(i) Annual inflation of $r_{inf} = 2\%$

(ii) Maximum number of PV modules ($Z_{\max} = 30$)

(iii) PV cost per watt peak ($U_{pv} = \$2.37/\mathrm{W_p}$) [222]

(iv) Inverter replacement cost ($U_{inv} = \$0.35/\mathrm{W_p}$) [222]

(v) Quarterly billing frequency

(vi) A nominal annual discount rate of $r_{nom} = 6\%$, corresponding to a quarterly real effective rate of $r_d = 0.97\%$

(vii) Nominal annual electricity price growth of 4.04%, corresponding to a quarterly real effective rate of $r_e = 0.50\%$

(viii) PV system balance of plant efficiency $\eta_e = 90\%$

(ix) PV system lifespan of 20 years (which is considered to be conservative)

Find: Tilt angle β, azimuth angle γ, and number of modules Z

Objective:

$$\max_{\beta,\gamma,Z} NPV = \sum_{q=1}^{Q} \left[\frac{\Big(C_{base,q} - C_{pv,q}(\beta,\gamma,Z)\Big)\,(1+r_e)^q}{(1+r_d)^q} - \frac{W_q(Z)}{(1+r_d)^q} \right] - S_{pv}(Z) \tag{5.12}$$

Subject to:

$$0 \leq \beta \leq 180^\circ, \text{ for } \beta \in \mathbb{R} \tag{5.13a}$$

$$-180^\circ \leq \gamma \leq 180^\circ, \text{ for } \gamma \in \mathbb{R} \tag{5.13b}$$

$$0 \leq Z \leq Z_{\max}, \text{ for } Z \in \mathbb{Z}^+ \tag{5.13c}$$

In (5.12), $C_{pv,q}$ and $C_{base,q}$ refer to the cost of electricity with and without a PV system respectively within the billing period q (the difference of which constitutes the monetary savings achieved through the installation of PV). S_{pv} is the PV system cost, Q is the number of billing periods over the lifetime of the system and W_q is the maintenance cost in period q. Expressions for $C_{base,q}$, $C_{pv,q}$, S_{pv} and W_q are defined in (5.14), (5.15) and (5.6) respectively.

Equation (5.12) includes an additional growth factor $(1 + r_e)^q$ to allow for retail electricity price growth above (or below) the rate of inflation. In an Australian context since 1990, electricity price rises have significantly outpaced inflation on average by 2-3% per annum in real terms [223]. Consequently, electricity price growth is assumed to be 2% in real terms (or 4.04% in nominal terms), becoming $r_e = 0.5\%$ when converted to an effective quarterly rate for the quarterly billing assumed in this research.

$$C_{base,q} = \sum_{d=1}^{D_q} \left[\sum_{h=1}^{24} \left(T_{ret0,qdh} E_{load,qdh} \right) + T_{sc0,qd} \right] \tag{5.14}$$

$$\begin{aligned} C_{pv,q}(\beta, \gamma, Z) = \sum_{d=1}^{D_q} \Bigg\{ \sum_{h=1}^{H} \Big[& T_{ret,qdh} \max \left(0, E_{bal,qdh}(\beta, \gamma, Z) \right) \\ & - T_{fit,qdh} \max \left(0, -E_{bal,qdh}(\beta, \gamma, Z) \right) \Big] + T_{sc,qd} \Bigg\} \end{aligned} \tag{5.15}$$

$$E_{bal,qdh}(\beta, \gamma, Z) = E_{load,qdh} - E_{pv,qdh}(\beta, \gamma, Z) \tag{5.16}$$

In (5.14) and (5.15), for hour h of day d in billing period q (with D_q days in the billing period), $T_{ret0,qdh}$ and $T_{ret,qdh}$ represent the retail tariffs associated with grid imported electricity under a base plan (i.e. lowest cost 'do nothing' plan) and an alternatively trialled plan respectively; $E_{bal,qdh}$ is the balance of net energy flow defined in (5.16) as the difference between load energy $E_{load,qdh}$ and the PV generated energy $E_{pv,qdh}$; and $T_{fit,qdh}$ is the PV FiT. $T_{sc0,qd}$ and $T_{sc,qd}$ are the daily electricity supply charges for the base plan and tested plan respectively.

The total PV system cost S_{pv} for a system of rated power $P_{pv,rat}$, defined in (5.17), can be reduced through government initiated rebates and incentive schemes. In an Australian context, the total sytem cost to the investor is reduced through an effective rebate provided under the SRES. Under this scheme, STCs (Small-scale Technology Certificates defined in Section 5.1.3, not the standard test conditions previously referenced in this chapter) are generated and traded on an open market as a commodity to be ultimately purchased by liable entities (usually energy retailers) [197]. The quantity of certificates generated depends on the size, location and length of time the system is expected to contribute to the SRES. In 2016, certificates were generated for up to 15 years yielding a contribution lifetime of $M_{life} = 15$ [224]. The location multiplier is assumed to be $M_{loc} = 1.382$ for the locations assessed in this research [224]. In this chapter, the PV investor is assumed

to receive $C_{STC} = \$32$ for each certificate.

$$S_{pv}(Z) = U_{pv}P_{pv,rat}(Z) - M_{life}M_{loc}P_{pv,rat}(Z)C_{STC} \tag{5.17}$$

5.4.2 Optimisation Method

PSO has seen many applications in PV optimisation problems due to the complex non-linear equations involved and its excellent performance under such conditions [200]. For this research, PSO is selected due to its speed, global search performance and relative simplicity of application [225].

Originally developed by Kennedy and Eberhart [226], PSO simulates the social interaction within bird flocks and fish schools to achieve a global objective in the absence of centralised control [225]. Each swarm agent is represented as a particle with infinitesimal volume that flies through the solution space with J-dimensional position and velocity vectors, where J is equivalent to the number of optimisation parameters in the problem (i.e. $J = 3$ in this research). Consequently for the i^{th} particle in the n^{th} iteration, the position and velocity vectors $\mathbf{x}_{i,n}$ and $\mathbf{v}_{i,n}$ are respectively defined as:

$$\mathbf{x}_{i,n} = (x^1_{i,n}, x^2_{i,n}, x^3_{i,n}) = (\beta_{i,n}, \gamma_{i,n}, Z_{i,n}) \tag{5.18}$$

$$\mathbf{v}_{i,n} = (v^1_{i,n}, v^2_{i,n}, v^3_{i,n}) \tag{5.19}$$

In iteration $n+1$, updates of the dimensional components of position ($x^j_{i,n}$) and velocity ($v^j_{i,n}$) for each particle are performed through knowledge of the global best position within the swarm and the personal best position for each particle. The component-wise updates for each particle are defined by (5.20) and (5.21):

$$v^j_{i,n+1} = \chi\left[v^j_{i,n} + c_1 r^j_{i,n}\left(P^j_{i,n} - x^j_{i,n}\right) + c_2 R^j_{i,n}\left(G^j_{i,n} - x^j_{i,n}\right)\right] \tag{5.20}$$

$$x^j_{i,n+1} = x^j_{i,n} + v^j_{i,n+1} \tag{5.21}$$

where, c_1 and c_2 are acceleration coefficients, $r^j_{i,n}$ and $R^j_{i,n}$ are two sequences of uniformly distributed random numbers over $(0, 1)$, $P^j_{i,n}$ is the personal best position and $G^j_{i,n}$ is the global best position of the swarm, for particle i in dimension j. A modification of the original PSO algorithm is performed through the inclusion of a constriction factor term χ which gives significantly improved convergence performance [225]. Equation (5.20) is consequently termed PSO with constriction factor (PSO-Co), one of the two basic algorithms defined as canonical PSO [225]. In this research, c_1, c_2 and χ were set according to the recommendations of [225], defined to be 2.05, 2.05 and 0.729 respectively.

The algorithm continues until the termination conditions are met, i.e. the global best position is found (to an accepted level of accuracy) or the maximum number of iterations N has been reached, as defined by the user.

A flow chart of the PSO algorithm applied to the optimisation problem defined in Section 5.4.1 is presented in Figure 5.4. The standard PSO processes are represented as colourless cells. To differentiate the standard PSO procedures from the unique application

explored in this research, the optimisation problem and underlying models defined in Section 5.2 and Section 5.4.1 are represented by the blue cells.

A common method to handle optimisation constraints is to introduce a penalty function into the objective function [227] so that the revised objective function takes the form:

$$F(\mathbf{x}) = f(\mathbf{x}) + H(\mathbf{x}, n) \tag{5.22}$$

where $f(\mathbf{x})$ is the original objective function defined by (5.12) and $H(\mathbf{x}, n)$ is the penalty function. In this research, in order to manage the size and orientation constraints of a PV system, $H(\mathbf{x}, n)$ takes the form defined by Parsopoulos and Vrahatis [228] and further explored by Sun et al. [227] such that:

$$H(\mathbf{x}, n) = h(n) \sum_{k=1}^{K} \psi\left(\lambda_k(\mathbf{x})\right) \lambda_k(\mathbf{x})^{\alpha\left(\lambda_k(\mathbf{x})\right)} \tag{5.23}$$

The terms in (5.23) include a relative violated function of the constraints $\lambda_k(\cdot)$ (so that the penalty function is zero when all optimisation parameters are within their associated constraints); a multi-stage assignment function $\psi(\cdot)$ (which scales the penalty depending on the value of $\lambda_k(\cdot)$; a power function $\alpha(\cdot)$; and a dynamically modified penalty value $h(n)$ based on the iteration number. In (5.23), K refers to the number of constraints in the optimisation problem and subsequently for the problem defined in Section 5.4.1, $K = 3$.

The penalty parameters of (5.23) are problem dependent [228]. In this research, the values considered by Parsopoulos and Vrahatis in [228] were used with a few minor modifications to improve convergence performance. The penalty parameters used in this research are defined in (5.24a)–(5.24d) as follows:

$$h(n) = n\sqrt{n} \tag{5.24a}$$

$$\lambda_k(\mathbf{x}) = \max\left(0, g_k(\mathbf{x})\right) \tag{5.24b}$$

$$\alpha(\lambda_k(\mathbf{x})) = \begin{cases} 1 & \text{for } \lambda_k(\mathbf{x}) < 1 \\ 2 & \text{otherwise} \end{cases} \tag{5.24c}$$

$$\psi\left(\lambda_k(\mathbf{x})\right) = \begin{cases} 10 & \text{for } \lambda_k(\mathbf{x}) \leq 0.01 \\ 20 & \text{for } 0.01 < \lambda_k(\mathbf{x}) \leq 0.1 \\ 100 & \text{for } 0.1 < \lambda_k(\mathbf{x}) \leq 1 \\ 300 & \text{otherwise} \end{cases} \tag{5.24d}$$

where $g_k(\mathbf{x})$ are the constraint functions of the defined optimisation problem reformulated in the form $g_k(\mathbf{x}) \leq 0$. The constraints of (5.13) re-written in the form $g_k(\mathbf{x}) \leq 0$ therefore

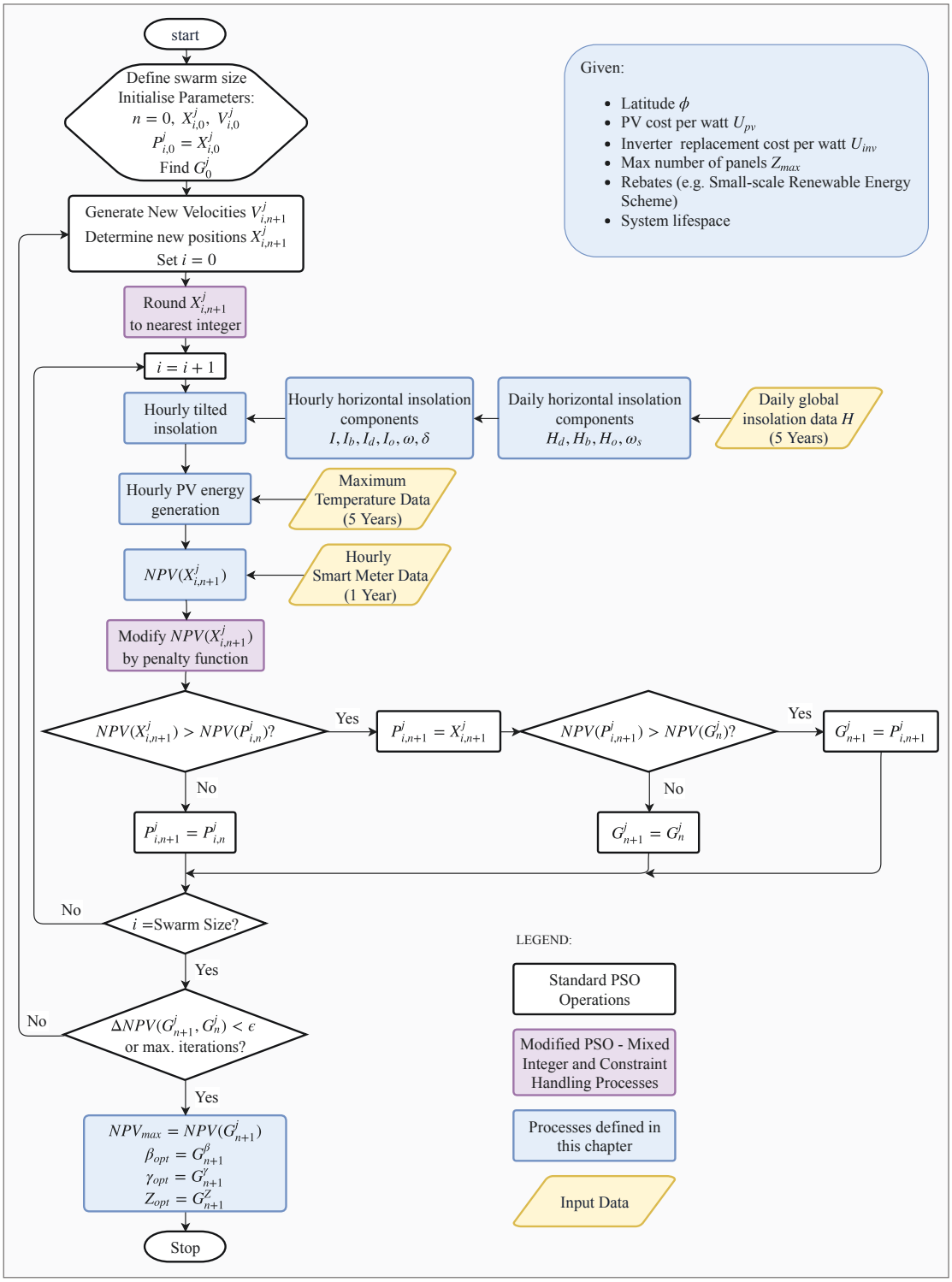

Figure 5.4: Optimisation problem flow chart

become:

$$g_1(\mathbf{x}) = |\beta - 90| - 90 \leq 0 \text{ for } \beta \in \mathbb{R} \tag{5.25a}$$

$$g_2(\mathbf{x}) = |\gamma| - 180 \leq 0 \text{ for } \gamma \in \mathbb{R} \tag{5.25b}$$

$$g_3(\mathbf{x}) = |Z - \frac{Z_{\max}}{2}| - \frac{Z_{\max}}{2} \leq 0 \text{ for } Z \in \mathbb{Z}^+ \tag{5.25c}$$

Referring to (5.25a)–(5.25c), it should be noted that the optimisation variable Z is limited to integer values while β and γ may take any real value within the domain of the constraints. Consequently, the optimisation problem may be classified as a mixed-integer non-linear programming (MINLP) problem.

In order to handle the integer constraints, the method adopted by Chowdhury et al. [229] was utilised whereby the continuous and discrete components of the particles are first separated. The locations of the discrete components are approximated by the nearest vertex of a local hypercube in J-dimensional space [229]. More simply, the particle's discrete components are approximated in each dimension by rounding to the nearest integer value. All components, both continuous and discrete, are then evaluated according to (5.20) and (5.21).

The constrained mixed-integer modifications to the standard canonical PSO algorithm are identified as purple cells in the flow chart of Figure 5.4. It should be noted that although tilt β and azimuth γ are not restricted to integer values, such accuracy is difficult to achieve and unnecessary given the insignificant energy gains achievable. Consequently, the nearest vertex approach was also applied for the tilt and azimuth parameters in the subsequent analysis.

A population size of $M = 20$ was applied. To ensure convergence, an iteration limitation of 1000 was also applied. Convergence was deemed to be achieved after 30 consecutive iterations where no change in the global best solution was observed. The PSO algorithm was developed and simulated in Matlab version R2015b using an Intel i7-4790 3.6 GHz CPU. An average solution time of 41.56 seconds was observed for Customer 1, taking on average 29.2 iterations.

5.4.3 Input Data

Between 2012 and 2014, the SGSC project collected smart meter energy data for approximately 13,700 residences in the state of New South Wales, Australia [1]. In 2015, the data were made publicly available by the Australian Government Department of Industry, Innovation and Science [230], presenting an ideal data source to investigate the optimisation of residential PV installations.

Given the extensive time required to process the large amount of customer data available, a sample of customers was randomly selected to test the optimisation strategy developed in Section 5.4.1. The sample includes four residences from both rural and urban regions and a larger focus group of 120 residences from the city of Newcastle. The sample of Newcastle residences is divided into three relative energy consumption categories with 40 members each, based on the 3-quantiles of the distribution of yearly energy consumption

E_{year}. For the sample of residences selected, the categories are defined as:

Low:	$E_{year} \leq 3,590.5$ (kWh/year)
Medium:	$3,590.5 < E_{year} \leq 6,122.6$ (kWh/year)
High:	$E_{year} > 6,122.6$ (kWh/year)

Satellite-derived daily global horizontal irradiation data from the nearest BoM weather stations are utilised in the analysis, accessed from the CDO database [55]. To reduce the likelihood of under-estimation or over-estimation of irradiation due to anomalous meteorological years, data from five consecutive years between 2011 and 2015 are utilised. Using (3.5) and (3.43), the daily data were processed to derive estimated hourly irradiation components. This process is necessary to enable PV energy yield estimates to correlate with the hourly smart meter energy consumption data utilised in this research.

Hourly ambient temperature data are not available in the CDO database for the assessed weather station locations. Consequently, the ambient temperatures for PV array operation are assumed to be the measured daily maximum temperature for all hours of operation, yielding conservative estimates for PV performance. Temperature data for the same five year period as the irradiation data were also accessed from the CDO database [55].

The energy tariffs used in this research are based on the available standing offers in September 2016 from three of the largest energy retailers in Australia. The four customers considered in the initial analysis are located within the same distribution network jurisdiction as Newcastle. Consequently, the available retail plans for these customers are

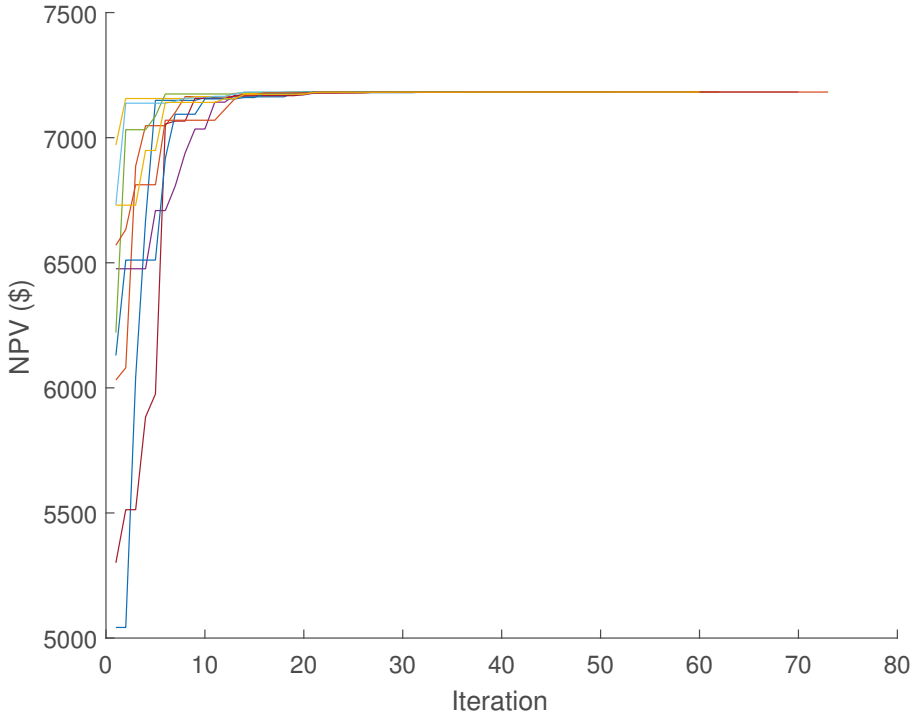

Figure 5.5: Optimisation convergence with ten repetitions (Customer 1)

assumed to be equivalent to those of Newcastle. For each retailer, a flat tariff and a TOU tariff are considered for which example rate profiles are shown in Figure 5.6. It should be noted that variable weekend TOU rates and incremental flat tariffs based on cumulative energy consumption within a given period are also considered but have been omitted in Figure 5.6 for clarity. Detailed tariff tables for the retail electricity plans assumed in this research are provided in Table A.1 to Table A.4.

5.4.3.1 Equipment Assumptions

The PV arrays are modelled as Trina Solar TSM-250PD05.05 250 W polycrystalline PV modules. The relevant performance characteristics are detailed in Table C.1.

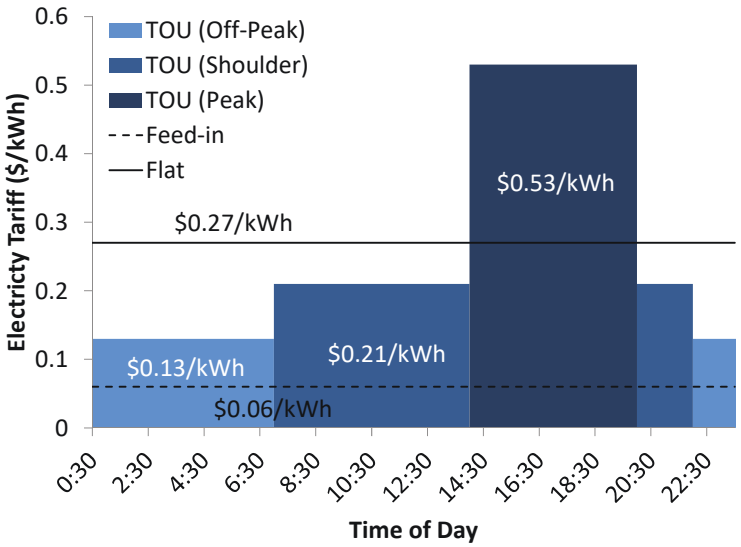

Figure 5.6: Typical electricity tariff structures

5.5 Optimisation Results

5.5.1 Four Residences

Table 5.1 summarises the results of the optimisation problem of Section 5.4.1 for four residences arbitrarily selected from the SGSC database. The identities of each of retailer are withheld and are designated as either Retailer A, B or C.

Referring to Table 5.1, it can be seen that for all retail electricity plans, an investment in PV yields a positive NPV. For each customer, the retail plan and associated optimised PV system giving the highest NPV are highlighted in grey.

For Customers 1, 2 and 4, at least one retail electricity plan, combined with an optimised PV system, results in a positive NPV and a MIRR greater than the nominal cost of capital (6%), thus indicating a viable investment. The optimal system for Customer 3 results in an MIRR of 5.81%; less than the required rate of return and thus indicating PV is a non-optimal financial investment option.

Table 5.1: Comparison of optimised PV systems for different retail electricity plans and different customers.

Customer	Retailer	Tariff	Size (kW)	Tilt	Azimuth	NPV	MIRR	Payback (Years)	Plan Savings
1	A	TOU	6.77	31°	21°	$7,182	6.01%	12	$254
	A	Flat	6.52	31°	2°	$7,257	6.10%	11.6	$329
	B	TOU	7.02	31°	21°	$7,543	6.03%	12	$614
	B	Flat	6.52	31°	1°	$7,815	6.24%	11	$887
	C	TOU	7.02	31°	21°	$7,189	5.94%	12.3	$260
	C	Flat	6.77	31°	2°	$6,928	5.94%	12.3	$0
2	A	TOU	6.52	28°	32°	$8,849	6.51%	10	$2,127
	A	Flat	5.26	25°	9°	$7,258	6.54%	9.8	$536
	B	TOU	7.02	28°	33°	$9,427	6.49%	10	$2,705
	B	Flat	5.51	25°	9°	$7,693	6.57%	9.8	$971
	C	TOU	7.02	28°	33°	$9,008	6.39%	10.6	$2,286
	C	Flat	5.26	26°	8°	$6,722	6.38%	10.6	$0
3	A	TOU	2.51	30°	29°	$447	4.25%	18.5	$0
	A	Flat	2.26	28°	5°	$1,720	5.48%	13.7	$1,273
	B	TOU	2.76	31°	30°	$652	4.37%	18	$205
	B	Flat	2.26	28°	5°	$2,129	5.81%	12.9	$1,682
	C	TOU	2.76	31°	30°	$456	4.21%	18.5	$9
	C	Flat	2.26	28°	5°	$1,670	5.44%	13.7	$1,223
4	A	TOU	3	27°	32°	$3,993	6.46%	10.1	$174
	A	Flat	2.76	25°	4°	$3,903	6.61%	9.6	$84
	B	TOU	3.26	27°	32°	$4,321	6.46%	10.1	$502
	B	Flat	2.76	25°	3°	$4,331	6.85%	8.8	$513
	C	TOU	3.26	27°	33°	$4,127	6.36%	10.6	$309
	C	Flat	2.76	25°	4°	$3,819	6.56%	9.9	$0

The payback periods of the optimal systems ranges from 8.8–12.9 years, well within the assumed lifetime of the PV system of 20 years.

In Table 5.1, the PV systems are generally oriented towards the west, with TOU plans having a marginal increase in tilt angle compared with flat plans. For the customers assessed, periods of peak electricity demand occur in the afternoon/evening. Consequently, the orientation of the optimised PV systems appear to be biased towards afternoon solar hours. While this is easily rationalised for TOU plans, for flat tariffs one would initially expect the PV systems to be aligned due north (or south for the northern hemisphere), towards the mid-day sun and the solar energetic maximum. However, due to the comparatively low feed-in tariffs offered by the retailers assessed, the azimuths of the PV systems under flat plans are also slightly biased towards the afternoon peak in order to reduce the cost of grid-imported electricity and the comparatively high cost attached to it.

The final column of Table 5.1 summarises the comparative savings that can be achieved through the correct choice of retail electricity plan. Referring to Customer 2 and comparing the highest NPV solution (Retailer B, TOU) with the worst solution (Retailer C, flat), an increase in NPV of $2,705 is achieved. This represents a substantial saving, demonstrating the necessity to choose the most cost effective plan for a customer's particular circumstances.

The sensitivity of NPV to system size was assessed for Customer 3 and graphically presented in Figure 5.7. The peak of each curve corresponds to the optimal systems recorded in Table 5.1, further highlighted by the dotted vertical and horizontal lines. It is immediately discernible in Figure 5.7 that a significant reduction in NPV occurs as the PV system size increase beyond the optimal. Even if an investor has the available capital to install a substantially sized system, the NPV of such an investment may be far less than an alternative smaller optimised system.

The sensitivity of NPV to tilt and azimuth is demonstrated by the contour plot of Figure 5.8 for Customer 2. While a significant impact on NPV can be observed for systems with tilts approaching the vertical and oriented facing far west or east, for orientations in the vicinity of the optimal position, NPV can be seen to be only marginally effected. Therefore it can be concluded that tilt and azimuth have limited contributions to the achievable NPV, provided the tilt and azimuth are within $\pm 10^\circ$ and $\pm 20^\circ$ of the optimal angles respectively.

Remark 5.1 *While the design optimisation methodology developed in this chapter enables tilt and azimuth to be optimally selected in addition to system size, it is important to note that in most instances, residential consumers typically have limited installation flexibility, particularly from an azimuth perspective. While fixed-tilt racking options are available, racking allowing selectable tilts and azimuths are not generally practical for roof surfaces facing far from north, i.e. west or east sides of a roof. Consequently, the tilt and azimuth optimisation parameters may have limited practicality for many residential consumers.*

However, the results presented in this section show NPV to be relatively insensitive to tilt and azimuth within a wide central-angle range suggesting the lack of design flexibility may in many circumstances have limited effect. The roof pitch on most residential

premises enable an underlying tilt to be achieved, moving the installation closer to a local, if not global, optimum. Consequently, where tilting of PV arrays to optimal angles induces increased installation difficulty, leveraging the pre-existing roof pitch may be sufficient to achieve a good, albeit sub-optimal, economic outcome through optimisation of size only. The methodology established in this chapter is intended to provide the greatest level of design flexibility in the first instance, however additional constraints on tilt and azimuth in (5.13) are straight forward to implement should the installation circumstance require so.

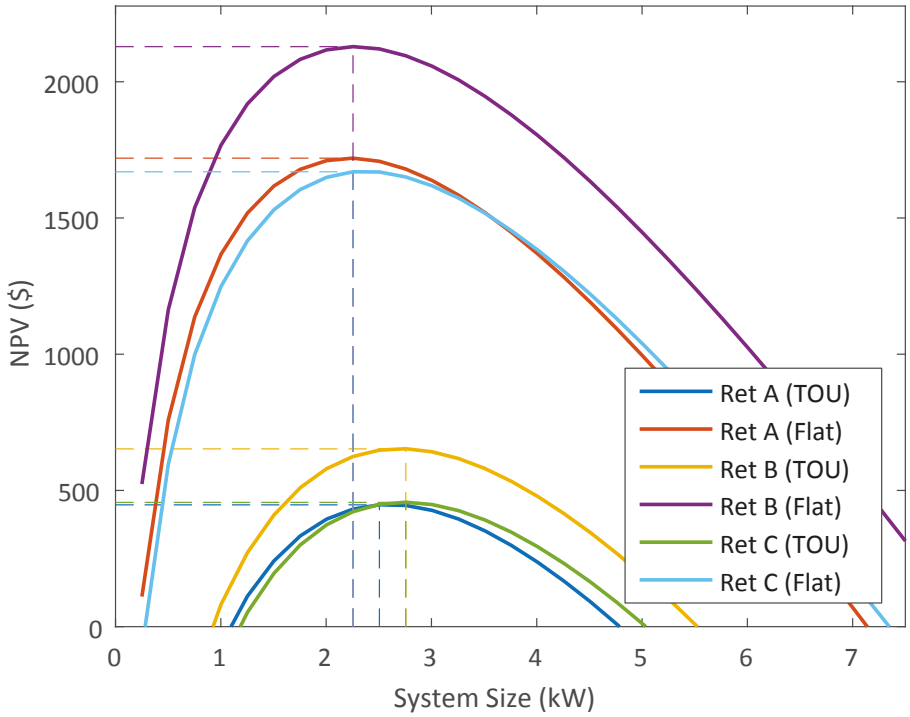

Figure 5.7: NPV sensitivity to system size (Customer 3)

5.5.2 Large Sample

A wider sample size was considered using energy consumption data for 120 customers in the city of Newcastle, New South Wales, Australia. Using the methodology established in Section 5.4, PV systems were optimised for each customer.

A breakdown of the proportional contribution of each optimisation parameter to the total NPV under TOU and flat plans is provided in Figure 5.9. The contribution of azimuth angle is larger for TOU plans than flat plans, however the contribution is still limited, with only a 5% increase in NPV achieved under TOU plans. Therefore it can be concluded that even with PV systems optimally aligned further west (or east) based on the temporal energy usage profile, only small gains in net benefit can be achieved. Due to the difficulties customising azimuth angles on residential rooftops, the additional effort and cost may not be justifiable given the limited benefit.

A proportional breakdown of the optimal retail plans is given in Figure 5.10. The optimal plans observed include both flat and TOU plans from Retailer B and a flat plan

[a]Total percentages are greater than 100% for the low and high energy charts due to rounding error

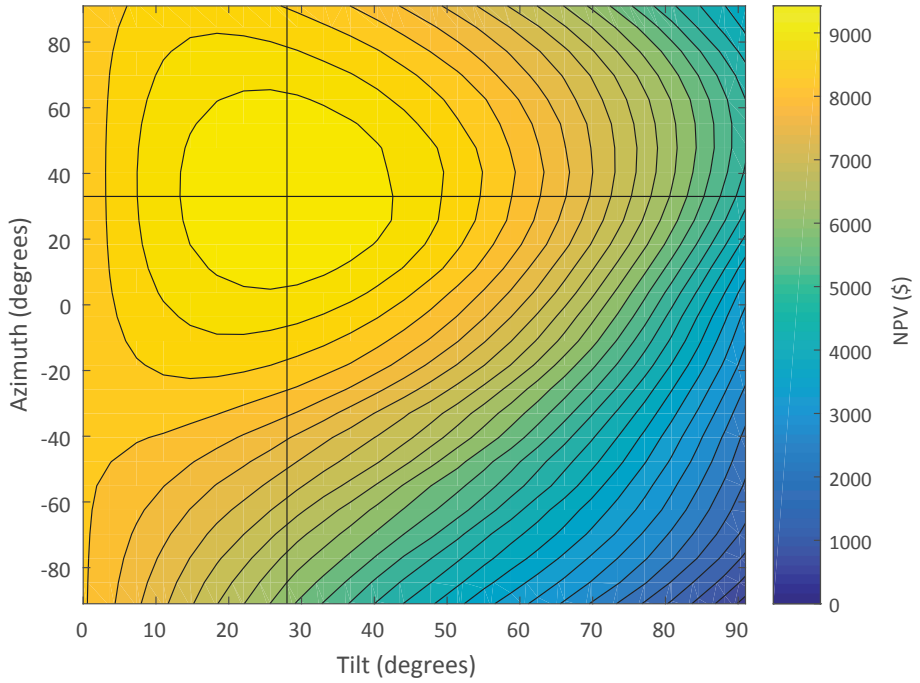

Figure 5.8: NPV sensitivity to tilt and azimuth (Customer 2)

from Retailer C. Amongst the sample of 120 customers, no retail plan from Retailer A can be seen to yield the highest NPV.

It is immediately evident in Figure 5.10 that the flat plan from Retailer B is the best choice plan for the majority of low energy residences, with the potential to secure 88% of the market amongst the 40 selected customers. As energy consumption increases, the TOU plan from Retailer B seizes a progressively higher proportion of the market from 13% (low energy) to 45% (high energy), with a combined market percentage of 32.7% across the entire population.

Box plots showing the inter-quartile ranges of key economic performance metrics are presented in Figure 5.11(a)–(e) with the sample population categorised based on relative

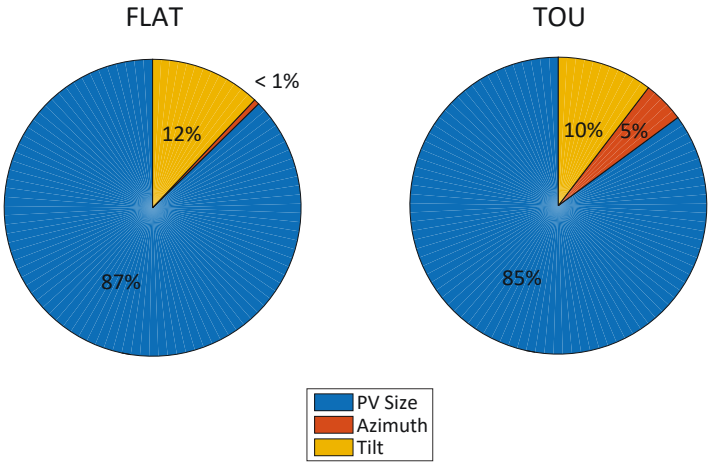

Figure 5.9: Average contribution of each optimisation parameter to total NPV for all Newcastle customers

cumulative energy consumption profile. The median and interquartile ranges for each economic parameter are further summarised in Table 5.2.

Referring to Figure 5.11(a) and Table 5.2, the median NPV and inter-quartile ranges amongst the sample of customers clearly increase as the energy consumption category increases. For customers with low energy usage, the median NPV for an optimised PV system is \$1,471 over 20 years representing an average saving of \$74 per year in 2016 currency. In comparison, the median NPV for medium and high energy consumers can be seen to be \$3,230 and \$6,269 respectively, representing savings of roughly \$162 and \$313 per year. It should be highlighted that these average savings represent the real achievable savings after factoring in all costs.

From a population perspective, the median PV system sizes and NPVs are closely related, demonstrated by the similar trends in the box plots of Figure 5.11(a) and Figure 5.11(b). As summarised in Table 5.2, the median sizes for low, medium and high energy customers are 1.38 kW, 2.88 kW and 5.26 kW respectively. It is apparent based on the median value and the inter-quartile ranges that the size of optimised PV systems is larger for customers with higher energy consumption.

Table 5.2: Summary of median values and associated inter-quartile (IQR) ranges for key economic metrics for each energy consumption range in Newcastle

Metric	Median (IQR)		
	Low	Medium	High
NPV (\$)	1,471 (1166)	3,230 (1264)	6,269 (2647)
Size (kW)	1.38 (0.75)	2.88 (0.88)	5.26 (1.88)
Plan savings (\$)	829 (423)	1,269 (1365)	1,969 (2564)
MIRR (%)	6.02 (0.59)	6.15 (0.59)	6.34 (0.72)
Payback (years)	12.1 (2.5)	11.5 (2.6)	10.5 (3)

To test if the low, medium and high distributions are in fact different, hypothesis tests were undertaken on the mean of each sample via the t-test as detailed in Appendix B.

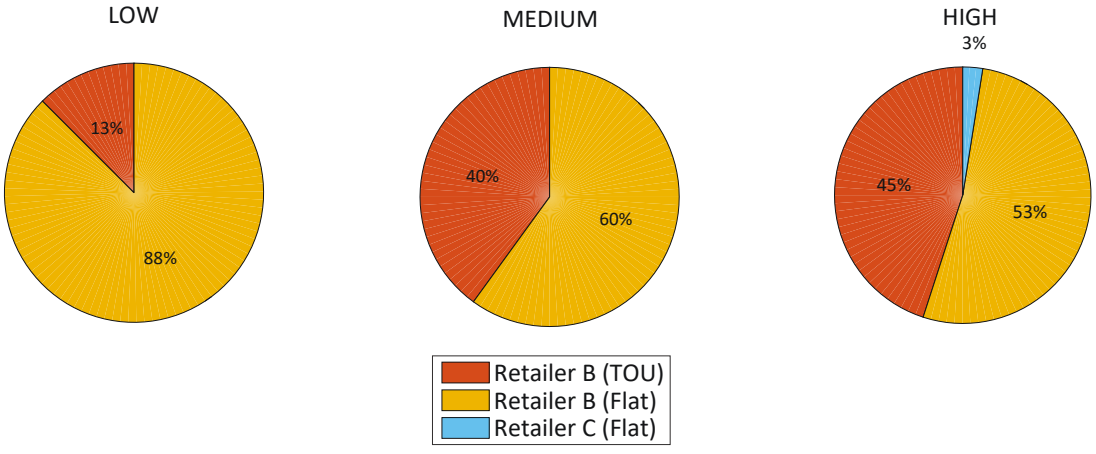

Figure 5.10: Proportion of lowest cost energy retailers for Newcastle residences with low, medium and high energy consumption[a]

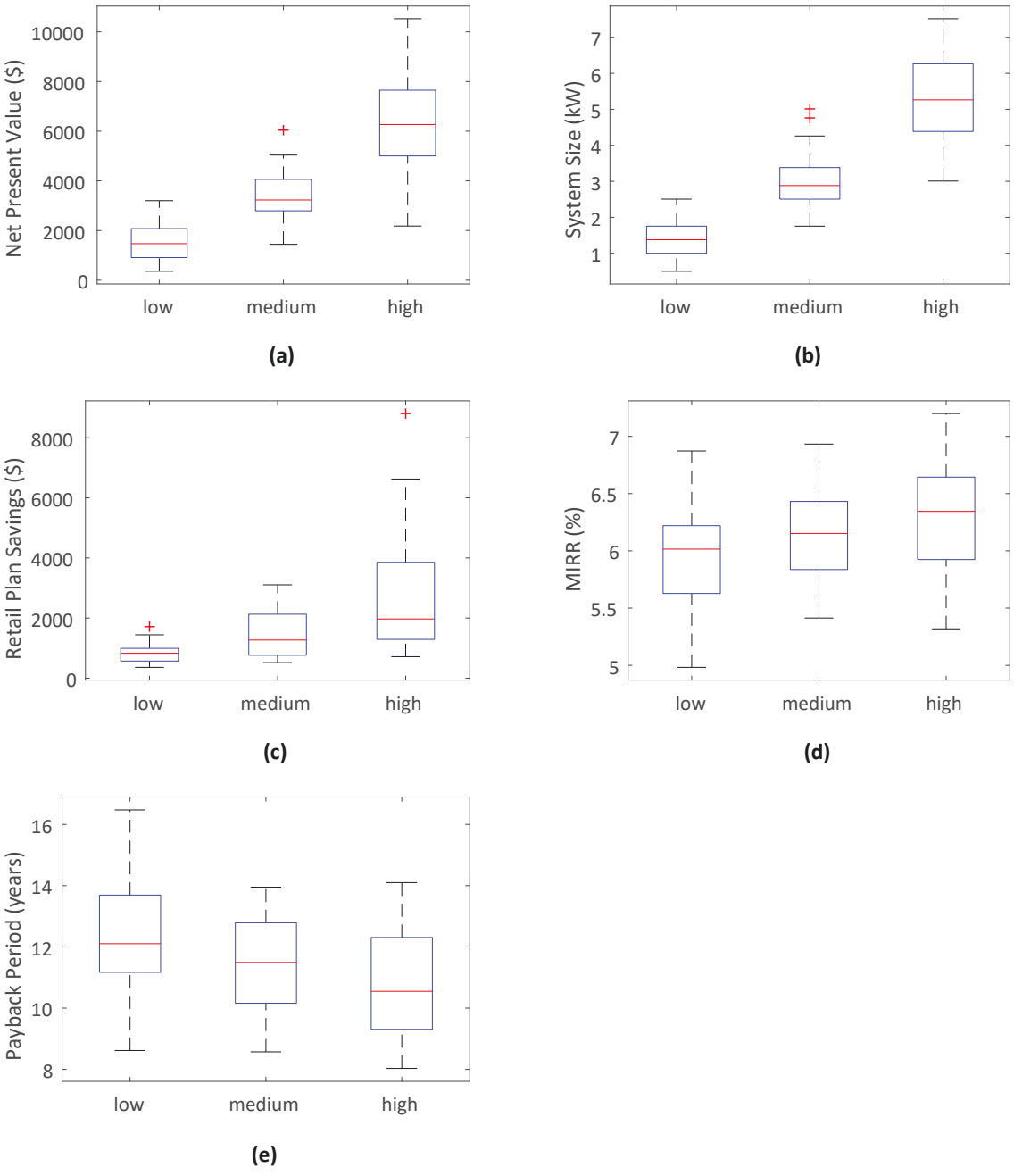

Figure 5.11: Box plots for (a) NPV, (b) system size, (c) plan selection savings, (d) MIRR and (e) payback period for Newcastle residences with low, medium and high energy consumption profiles

For the null hypothesis, the means of two samples were considered to be equal (implying equivalence between the distributions); the alternative hypothesis therefore being unequal means. A summary of the subsequent results of the hypothesis tests is provided in Table B.1. For NPV and PV system size, the p-values were found to be less than the 5% significance level for both test cases Low/Medium and Medium/High. Therefore, the null hypothesis was rejected leading to the conclusion that the mean optimal system size of medium consumers is larger than that of low customers, and less than that of high consumers based on the box plot trends, i.e. the average size for the PV systems is larger for households that consume more energy. However, given the large sample variance evidenced by the wide inter-quartile ranges summarised in Table 5.2, particularly for high consumption customers, no prescriptive PV system size can be established for each consumption category. Thus a process to optimally select a PV system, such as the one explored in this research, must be undertaken to avoid uneconomical system selection.

Figure 5.11(c) summarises the savings potential achieved through correct retail electricity plan selection. The metric represents the difference in NPV between a system optimised for the highest cost energy plan and the lowest cost (optimal) plan given a customer's particular energy profile. Based on the magnitude of potential savings, the importance of correct plan selection (achieved through detailed consideration of a customer's particular circumstances) is clearly evident. Referring to the median values summarised in Table 5.2, potential savings are in the range of 31% (high energy) to 56% (low energy) relative to the median achievable NPV. Consequently, it can be concluded that correct plan selection is a critical consideration to be made in conjunction with optimal selection of the PV system size and orientation.

As previously mentioned in Section 5.3, despite the obvious net benefit achievable through the installation of PV, MIRR is also a key consideration when establishing the viability of the investment. Referring to Figure 5.11(d), the MIRR ranges observed for the three consumption categories are similar, with a marginal increase in median MIRR as consumption increases. However, significant overlap in the inter-quartiles ranges signals difficulty in establishing a clear differentiator between the distributions. Indeed, when conducting hypothesis testing on the mean of the MIRR distributions, as summarised in Table B.1, the null hypotheses can not be rejected at the 5% significance level. Consequently, no assertions can be made regarding differences in the MIRRs between the consumption categories.

Table 5.3: Proportion of Newcastle customers where PV is financially attractive (acceptable MIRR)

Energy Consumption	MIRR > 6%	MIRR > 5.5%
Low	53%	88%
Medium	63%	98%
High	65%	88%
All	60%	91%

Based on the MIRR metric, investing in PV may be deemed to be a 'non-viable'

financial investment option for a large proportion of customers. Referring to Table 5.3, only 60% of customers have a return on investment above 6% for an optimised PV system. However relaxation of the MIRR may be considered acceptable for many customers given the intangible value associated with PV systems. After relaxing the acceptable MIRR rate to 5.5%, the proportion of customers with 'viable' PV investment options increases to 91%.

Referring to Figure 5.11(e), slightly shorter median payback periods can be observed as energy consumption increases. However, similar to MIRR, no differences can be conclusively established between the payback periods of medium and high customers due to a failure to reject the null hypotheses. It should be noted that the null hypothesis was rejected at the 5% level for the low and medium comparison. Consequently, it can be concluded that the mean payback period is less for consumers with medium and high energy consumption than that of low consumers. From a population perspective, customers with a higher relative energy consumption profile are more likely to achieve an earlier payback on their investment.

Despite all customers achieving investment payback prior to the assumed system end-of-life (20 years), a number of installations have payback periods in excess of 14 years. Such a period may be unacceptably long for many investors. Shorter payback periods may be achieved by introducing an additional constraint on the system lifetime prior to optimisation. Such a lifetime constraint will result in a different PV system size and orientation, ultimately yielding a lower NPV compared to the 20-year period considered in this research. However, if the investor intends to relocate after a predetermined period, thereby foregoing the residual value in the PV system, such a consideration is justifiable.

The higher NPVs coupled with shorter payback periods observed in this section indicate households with higher energy consumption have a greater justification to install a PV system, a relatively intuitive expectation. However, the results also suggest that under Australian regulatory environments and incentive schemes, PV system optimisation becomes increasingly important for households with lower energy consumption to avoid ineffective system selection. The lower NPVs seen for low energy households, indicate a higher sensitivity to sub-optimal sizing, potentially removing the viability of PV altogether without due assessment.

5.5.3 Other Locations

To gain a wider appreciation of the optimised economic performance characteristics of PV systems, the optimisation strategy was applied to four additional Australian locations. As the state of New South Wales has three electricity distributors, the investigation was extended to hypothetical customers from the cities of Tamworth and Parramatta within the other two networks to complement the investigation in Section 5.5.2. Furthermore, the cities of Melbourne and Brisbane, in the states of Victoria and Queensland respectively, were also investigated due to their geographic and regulatory separation from New South Wales. As smart meter data for the other locations were not available for this research, the data for the same 120 customers used in the Newcastle analysis were again applied. It

Table 5.4: Comparison of mean economic performance and system characteristics for optimised PV systems in different locations

Location	A		B		C		NPV	Size	CER data	Plan savings	Payback	MIRR
	TOU	Flat	TOU	Flat	TOU	Flat		(kW)	(kW)		(years)	>6%
Newcastle	–	–	32.50%	66.70%	–	0.80%	$3,741	3.22	5.41	$1,632	12.3	60%
Brisbane	–	7.5%	54.20%	–	31.70%	6.70%	$4,418	3.68	5.74	$1,295	11.9	69.20%
Melbourne	–	20%	80%	–	–	–	$3,803	2.72	4.42	$2,374	11.7	75%
Parramatta	–	86.7%	0.80%	–	12.50%	–	$3,699	3.3	5.68	$1,972	12.5	58.30%
Tamworth	97.5%	–	2.50%	–	–	–	$5,545	4.06	5.83	$3,772	11.3	77.50%

should be noted that the assumption of homogeneous load profiles between the different locations has inherent shortcomings as the average load profile for the Newcastle area does not necessarily translate to the other locations. However, the analysis methodology remains valid and it is conceivable that similar load profiles may be individually observed in different locations.

A summary of the mean economic performance and system characteristics for optimised systems in each location is provided in Table 5.4. Brisbane exhibits the greatest plan diversity, featuring four of the six plans assessed and a mixture of TOU and flat tariffs as the lowest cost plans for certain customers. In contrast, Tamworth customers receive the greatest benefit from TOU tariff structures only, with the vast majority from Retailer A (97.5%). For all locations assessed, the achievable savings through correct plan selection prior to system optimisation are significant. For Brisbane customers, plan savings of $1,295 on average are observed while savings of $3,772 are possible in Tamworth.

Referring to the NPV column, the mean net benefit achievable through system optimisation varies significantly amongst the five locations. Comparing the highest NPV city of Tamworth with the lowest NPV city of Parramatta, customers with the sampled load profiles on average receive an additional benefit of $1,846.

The proportion of customers with 'viable' PV investment opportunities also varies between the locations assessed. Parramatta exhibits the lowest with 58.3% of customers having 'viable' opportunities whereas Tamworth exhibits the greatest proportion at 77.5%. Interestingly, a relatively high proportion of customers in Melbourne are found to have a 'viable' PV investment. Although not demonstrated in this research, Melbourne has the lowest historical average irradiation levels amongst the locations assessed. Consequently the intuitive assumption would be to expect a lower PV investment value. However, through a combination of optimal PV system selection and comparatively high prevailing retail electricity costs, PV systems are found to be a 'viable' investment for 75% of the hypothetical Melbourne customers assessed.

The mean installed system sizes for the locations assessed from January 2015 to August 2016 are also provided in Table 5.4 based on CER data [195]. A comparison between the mean optimised PV sizes found in this research and the historical CER data shows significant over-sizing for each of the locations assessed – approximately 2 kW on average. This conclusion can be drawn as no significant policy changes have been made relating to small-scale PV systems since 2011–2012. Therefore, the systems installed in 2015-2016 were exposed to identical incentives to those considered in the optimisation problem investigated in this research. These results corroborate the size reduction forecasts of the SGSC project [1] and the Grattan Institute [29] previously discussed in Chapter 2.

5.6 Updates to PV Model

For the subsequent chapters presented in this thesis, a revised PV energy yield model from the one established in (5.5) was considered to capture additional loss factors associated with PV systems. Efficiency factors similar to the ones considered by Copper et al. [231]

are applied to (5.5) to yield a revised generated DC energy for PV systems defined as:

$$E_{pv,dc} = A_c Z I_T \eta_{mpp} \zeta_{pv} \eta_{soil} \eta_{mm} \eta_{dc,wire} \tag{5.26}$$

where η_{soil}, η_{mm} and $\eta_{dc,wire}$ are the efficiencies due to panel soiling, module mismatch and DC wiring losses, assumed to be 99%, 98% and 98% respectively in this research.

Converting the the DC energy to AC through an inverter gives the total energy generated by the PV system as AC power to be:

$$E_{pv,ac} = E_{pv,dc} \eta_{inv} \eta_{ac,wire} \tag{5.27}$$

where $\eta_{ac,wire}$ is the efficiency due to AC wiring losses, assumed to be 99%, and η_{inv} is the inverter losses. Different values for the inverter efficiency are considered in subsequent chapters.

The updated PV model of (5.27) is considered in the large customer sample assessment of Chapter 6 Section 6.4.2, the case study presented in Chapter 7 and the P2P energy trading simulation of Chapter 8.

5.7 Summary

The introduction of smart grid technologies and the phased removal of incentive schemes is likely to further complicate the cost-effective selection and integration of residential PV systems in the future. The continued increase in smart meter market penetration allows high temporal resolution data to be leveraged by electricity customers in order to make informed PV investment decisions. Consequently, an optimisation tool is required to maximize the investment value of PV systems and avoid ineffective capital spending.

In this chapter, such an optimisation strategy was explored. A model for PV energy production, as well as underlying economic models based on an NPV analysis, were defined as key components of the optimisation objective function.

An algorithm based on canonical PSO was developed to include a penalty function to enable the handling of parameter constraints. A hypercube nearest-vertex approach was incorporated to facilitate the inclusion of discrete parameters such as the number of PV modules in the system.

The optimisation methodology was tested in an Australian context, using real-world hourly smart meter and irradiation data applied to currently available incentive schemes and retail electricity plans.

With realistically defined economic parameters, a positive NPV was achievable for all customers assessed. Net present value, system size and savings achievable through correct retail plan selection were all found to increase between the low, medium and high annual electricity consumption brackets defined in the chapter. However, ‘viable’ PV investment opportunities were not universally observed for all customers, with at most 77.5% of customers amongst the locations assessed yielding a return greater than the cost of capital.

A wide variety of optimal retail plans was observed, from the extreme of 97.5% from one retailer in one city to a diverse array of plans and tariff structures in others.

A sensitivity analysis on individual customers demonstrated the significant negative impact of non-optimal sizing on the value of the investment, particularly for over-sized systems. However, a sensitivity analysis conducted on tilt and azimuth found limited effect on the net benefit for deviations within $\pm 10^\circ$ and $\pm 20^\circ$ respectively. Furthermore, optimal azimuth selection was found to contribute to less than 1% of the potential net benefit for flat tariffs and just 5% for TOU tariffs. Consequently, azimuth was therefore deemed non-critical and the optimisation problem can be reduced to the two dimensions of tilt and size.

Finally, the average optimal system sizes for the customers and locations assessed were found to be significantly less than the average size installed in 2015 and 2016 by 2 kW on average. The observed disparity between recent practices within the Australian residential PV industry and the characteristics of the optimised systems found in this chapter highlights the necessity for an economic optimisation strategy to be routinely implemented prior to the decision to invest.

Chapter 6 extends the design optimisation problem investigated in this chapter to consider the introduction of BESSs under a hybrid PV-BESS system configuration.

Chapter 6

BESS Design Optimisation

Battery energy storage systems for residential applications, particularly lithium-ion based batteries, have undergone rapid development in the past five years. A range of stationary energy storage devices from manufacturers including Tesla Motors, Enphase, Mercedez Benz, Samsung and LG have been recently introduced to the market. In Australia, average annual electricity prices have risen 4.5% over the last 10 years [223], 2.5% higher than the inflation rate target [220]. Consequently, the application of BESSs to complement existing rooftop PV systems or the installation of new hybrid PV-BESS solutions are of particular interest to energy consumers aiming to reduce their net electricity costs.

The performance of PV-BESS systems in reducing energy costs have been investigated in [203, 215, 232, 233] where various PV and BESS sizes were tested under various tariffs [232, 233], incentive schemes [215] and temporal resolution of energy consumption data [203]. However, existing research has been primarily structured around typical PV-BESS systems and consumption profiles, rather than investigating strategies to enable individual customers to optimise a system based on their own circumstances.

In this chapter, the optimisation methodology developed in Chapter 5 is updated with a modified objective function for hybrid PV-BESS systems. The aim is to assist potential PV-BESS investors in determining the economic efficacy of a hybrid PV-BESS system. Models for BESS energy flow, installation cost and maintenance cost are developed and integrated with the models for solar irradiation and PV energy output considered in previous chapters. Together, the energy flow and system cost models form key components of the underlying optimisation problem. In order to maximise the net benefit of a hybrid system, the PV power rating, PV orientation, retail electricity plan and currently available retail BESS products are optimally selected. BESS operating modes are also considered to establish the most cost-effective operation profile. The objective function is formulated as a NPV evaluation of the electricity cost savings that can be achieved through the introduction of a hybrid PV-BESS system compared to a known lowest-cost retail electricity plan.

A form of PSO, referred to as quantum-behaved PSO (QPSO), is utilised due to its fast convergence speed, handling of optimisation parameter constraints and simplicity of implementation. The algorithm is tested in an Australian context for three residences in the state of New South Wales using one year of hourly energy data and five years

of irradiation data from BoM. TOU retail electricity plans from three large Australian retailers as well as current PV and retail BESS pricing are applied in order to establish the feasibility of installing a PV-BESS system under prevailing market conditions.

The analysis is then expanded to a sample of 100 customers with the new National BRL diffuse model developed in Chapter 4 applied as an input to the updated PV energy yield model of Section 5.6. A more rigorous climatological data methodology is presented, capturing the complete measurement campaign history of the AREMI and CDO databases through the development of a TMY data set for irradiation and the estimation of hourly temperatures from daily maxima and minima.

6.1 BESS Model

The BESS models defined in this section are structured based on manufacturer warranties and guarantees to establish the economic benefit the owner can expect over the lifetime of the system. While BESS systems may be reasonably expected to perform beyond the warranty period, no documentation is available in the public domain quantifying the end-of-life performance characteristics. Consequently, the model developed and presented in this section may be expected to be conservative from a lifetime energy throughput perspective. However, given the significant capital required to purchase and install a BESS system, a conservative assumption is justifiable and for an economically viable system, the purchaser should reasonable expect to receive a payback within the warranty period.

The performance of battery systems, regardless of technology, degrade over time. The maximum capacity of a BESS can be expected to decrease over its lifetime due to a number of factors, a primary contributor for which is the number of charge/discharge cycles undergone. The energy storage capacity degradation rate ζ_{batt} (kWh/cycle) can be defined as:

$$\zeta_{batt} = \frac{C_{\max 0} - C_{EOL}}{Y_{EOL}} \tag{6.1}$$

where $C_{\max 0}$, C_{EOL} and Y_{EOL} are the initial maximum capacity, end-of-life maximum capacity and cycle life respectively. In this research, these values are based on specifications provided in manufacturer data sheets.

The maximum capacity $C_{\max,qdh}$ available at the start of each hour h, in day d and billing period q, is assumed to be a linear function of the number of operational cycles Y_{qdh} in the previous hour such that:

$$C_{\max,qdh} = C_{\max,qd(h-1)} - Y_{qd(h-1)}\zeta_{batt} \tag{6.2}$$

It should be noted that Y_{qdh} generally represents only a partial cycle for hourly intervals and therefore represents a fraction of the energy throughput of a full discharge/charge

cycle. Y_{qdh} is defined as follows:

$$Y_{qdh} = \frac{E_{bpv,qdh} + E_{bg,qdh} + E_{bd,qdh}}{2\delta C_{\max,qdh}} \tag{6.3}$$

where $E_{bd,qdh}$, $E_{bpv,qdh}$ and $E_{bg,qdh}$ are the discharge, PV-charge and grid-charge energy flows respectively and δ is the maximum depth of discharge.

The available capacity at the start of each hour is a function of the capacity at the start of the previous hour and the total charge/discharge energy that has flowed to/from the battery cells in the previous hour. The available capacity C_{qdh} is therefore defined as:

$$C_{qdh} = C_{qd(h-1)} - E_{bd,qd(h-1)} + E_{bpv,qd(h-1)} + E_{bg,qd(h-1)} \tag{6.4}$$

The charge and discharge energy flow terms in (6.4) are defined in (6.5)–(6.7) as follows:

$$\begin{aligned} E_{bpv,qdh} = \max \Bigg\{ \min \Big[& C_{\max,qdh} - C_{qdh}, \left(E_{pv,qdh} - E_{load,qdh}\right)(1-F), \\ & R_{\max}(1-F) \Big], 0 \Bigg\} \end{aligned} \tag{6.5}$$

$$\begin{aligned} E_{bg,qdh} = \max \Bigg\{ \min \Big[& C_{\max,qdh} - C_{qdh}, R_{\max}(1-F) \Big] (M_3 + M_4) I_{op,qdh} \\ & - E_{bpv,qdh}, 0 \Bigg\} \end{aligned} \tag{6.6}$$

$$\begin{aligned} E_{bd,qdh} = \max \Bigg\{ \min \Bigg[& C_{qdh} - C_{\max,qdh}(1-\delta), \frac{E_{load,qdh} - E_{pv,qdh}}{1-F}, R_{\max} \Bigg] \\ & \times \Big[(M_2 + M_4) I_{sh,qdh} + I_{pk,qdh} \Big], 0 \Bigg\} \end{aligned} \tag{6.7}$$

In (6.5)–(6.7), $E_{pv,qdh}$, $E_{load,qdh}$ and $R_{\max}$ are the PV generated energy as defined in (5.5) or (5.27), energy requirement of the underlying load and rated continuous charge/discharge rate respectively. $I_{op,qdh}$, $I_{sh,qdh}$, $I_{pk,qdh}$ and terms of the form M_x are BESS operation control variables defined later in Section 6.1.1.

It should be noted that the charge energy flow terms $E_{bpv,qdh}$ and $E_{bg,qdh}$ are considered to be the net additional charge to a BESS after losses while the discharge energy term $E_{bd,qdh}$ is the total energy discharged from the BESS, representative of both the energy delivered to the load and the discharge losses. The charge and discharge losses have been accounted for through the inclusion of a loss factor $F = (1 - \eta_{batt})/2$ where η_{batt} is the BESS round-trip efficiency.

Referring to (6.5), the charge contribution from PV can be expected to follow one of three scenarios. In the instance where the current BESS capacity is nearing maximum

and the energy required to 'top-up' the BESS is less than the surplus PV energy, the PV charge contribution is equal to the magnitude of the depleted charge, shown as the first term in (6.5). Note that the PV system must also supply charge losses which are treated as a separate load, defined later in (6.9)–(6.11). In the instance where the battery charge required to reach maximum capacity is greater than the surplus PV energy, the second term of (6.5) allows the entirety of the remaining surplus PV energy to charge the battery. The actual charge increase of the battery is limited due to charging losses, quantified through the application of a loss factor term $(1 - F)$. Finally, battery charging and discharging, is limited by a maximum charge and discharge rate $R_{\max}$. Consequently, where the available surplus PV energy exceeds $R_{\max}$, the total charged energy is limited to $R_{\max}$ less the charge losses. The actual charge energy applied is determined through the application of a 'min' function on the three terms. A 'max' function with an additional zero term is added to ensure the equation holds true when no surplus PV energy is available for BESS charging.

In (6.6), the energy charge from the grid is defined similarly as the charge from PV in (6.5). The charge energy is defined as either the maximum charge rate less battery losses, or the amount of depleted capacity. The total amount of charge required is reduced by the amount of charge already provided by the PV system. One notable difference between (6.5) and (6.6) is the presence of charge control operators, M_3, M_4 and $I_{op,qdh}$, defined later in Section 6.1.1 as previously mentioned.

The discharge energy equation (6.7), is in many respects a reverse of (6.5) but with discharge control operators similar to (6.6). The energy discharged follows one of three scenarios – either the remaining available capacity in the battery taking into consideration the maximum depth of discharge δ, the remaining load where available PV energy is insufficient or the maximum discharge rate of the battery. Under the second scenario, the amount of energy discharged to meet the load requirements is greater than the actual load requirement due to discharge losses. Hence the divisor $(1 - F)$ is introduced.

The total energy loss associated with the BESS charging and discharging terms of (6.5)–(6.7) is defined as:

$$E_{bloss,qdh} = E_{bpvloss,qdh} + E_{bgloss,qdh} + E_{bdloss,qdh} \tag{6.8}$$

where $E_{bpvloss,qdh}$, $E_{bgloss,qdh}$ and $E_{bdloss,qdh}$ are the losses during PV-charge, grid-charge and discharge respectively and are defined in (6.9)–(6.11) as:

$$E_{bpvloss,qdh} = \max\left[\min\left(\frac{C_{\max,qdh} - C_{qdh}}{1-F}, E_{pv,qdh} - E_{load,qdh}, R_{\max}\right), 0\right] F \tag{6.9}$$

$$\begin{aligned} E_{bgloss,qdh} = \max\Bigg[&\min\left(\frac{C_{\max,qdh} - C_{qdh}}{1-F}, R_{\max}\right)(M_3 + M_4)\, I_{op,qdh} \\ &- \frac{E_{bpv,qdh}}{1-F}, 0\Bigg] F \end{aligned} \tag{6.10}$$

$$E_{bdloss,qdh} = E_{bd,qdh}F \tag{6.11}$$

6.1.1 Operation Modes

In addition to increasing the self-consumption ratio of PV generated energy (by effectively translating PV generated energy to non-generation periods), a BESS can also be used to perform energy arbitrage by charging during low cost off-peak hours and discharging during peak periods. In this research, a review of various BESS operating modes is undertaken to determine the most economically efficient mode for each residence assessed. The operating modes considered are defined as follows:

- **Mode 1:** PV generation shifting. Discharge in peak only.
- **Mode 2:** PV generation shifting. Discharge during shoulder and peak periods.
- **Mode 3:** Energy arbitrage and PV generation shifting. Discharge in peak only.
- **Mode 4:** Energy arbitrage and PV generation shifting. Discharge during shoulder and peak periods.

As previously indicated, (6.6), (6.7), (6.10) and (6.11) are controlled by the operation mode variables M_1, M_2, M_3 and M_4 where:

$$M_x = \begin{cases} 1 & \text{if in Mode } x \text{ where } x \in \{1,2,3,4\} \\ 0 & \text{otherwise} \end{cases} \tag{6.12}$$

The variables $I_{op,qdh}$, $I_{sh,qdh}$ and $I_{pk,qdh}$ control BESS charge and discharge based on the tariff period within which a particular hour lies and take the form:

$$I_{op,qdh} = \begin{cases} 1 & \text{if } h \in \{\text{off-peak hours}\} \\ 0 & \text{otherwise} \end{cases} \tag{6.13}$$

with similar equations for $I_{sh,qdh}$ and $I_{pk,qdh}$ for shoulder and peak hours respectively.

The final component of the BESS model is the cost, defined simply as:

$$S_b = U_b X \tag{6.14}$$

where U_b is the price per battery and X is the number of battery units installed in the BESS.

6.1.2 BESS Maintenance Model

During the lifetime of a PV-BESS system, periodic maintenance as well as battery and inverter replacements are required. In this research, the lifespans of PV modules and inverters/batteries are assumed to be 20 years and 10 years respectively. Consequently,

with t billing periods per year, inverters/batteries will require replacement after $10t$ billing periods. Furthermore periodic maintenance is assumed to occur every $5t$ billing periods. The system maintenance costs are therefore defined as:

$$W_q = \begin{cases} 200 \text{ if } \frac{q-1}{5t} \in \mathbb{Z}^+, \ \frac{q-1}{10t} \notin \mathbb{Z}^+ \\ 400 + \kappa_{inv} U_{inv} S_{pv} + \kappa_b S_b \text{ if } \frac{q-1}{10t} \in \mathbb{Z}^+ \\ 0 \text{ otherwise} \end{cases} \tag{6.15}$$

where U_{inv} is the inverter replacement cost ($/W$_{ac}$) and κ_{inv} and κ_b are cost reduction rates for the inverter and batteries. Given a current average per unit inverter cost of US$0.29/W$_{ac}$ [234], the per unit PV inverter costs are assumed to be U_{inv} = AU$0.41/W$_{ac}$ (assuming AUD/USD exchange rate of 0.7). The cost of inverters and batteries are forecast to reduce significantly over the next 10 years with reductions of 31% and 53% respectively between 2015–2025 [235]. Consequently, the cost reduction factors in (6.15) are assumed to be $\kappa_{inv} = 0.69$ and $\kappa_b = 0.47$.

6.2 PV Model

Two assessments are presented in Section 5.5 – a small sample assessment of three customers sampled from the the SGSC project and a larger sample of 100 customers. For the preliminary small sample assessment, the simple PV energy yield model previously defined in (5.5) is considered.

For the large sample assessment, the more advanced model defined at the end of Chapter 5 as (5.27), accounting for additional loss factors including soiling and module mismatch among others, is applied.

The model for PV system cost previously defined in (5.17) is considered for both the small and large sample assessments conducted in this chapter. The exception is a revision to the STC price of C_{STC} = $34 based on a revised market assessment provided in [236].

The analysis presented in this chapter also considers revised system unit prices to capture price differences at different system sizes. The cost per watt peak U_{pv} is based on data provided in [236] for March 2016 which were published to be (in AUD) $3.20, $3.00, $2.55, $2.35 and $2.20 for 1 kW, 1.5 kW, 3 kW, 5 kW and 10 kW rated systems respectively. When solving the optimisation problem presented in Section 6.3, the price corresponding to the closest system size is used.

6.3 Hybrid PV-BESS Optimisation Problem

The objective of this research is to maximise the electricity cost savings achieved through optimal selection of a hybrid PV-BESS system based on high resolution smart meter load data and prevailing economic and PV-BESS market conditions. Cost savings are quantified through an NPV analysis performed on the difference in electricity costs between a known lowest-cost retail electricity plan and a hybrid PV-BESS system combined with other

currently available retail electricity plans.

As previously indicated in Section 6.1, hourly evaluations of the energy flows are conducted for each hour h in day d and billing period q. Maximising the net benefit over all the billing periods Q in the lifetime of the system is the objective of the optimisation problem as defined below.

6.3.1 Problem Definition

Given:

(i) Annual inflation of $r_{inf} = 2\%$

(ii) Maximum number of PV modules ($Z_{max} = 30$)

(iii) Quarterly billing frequency

(iv) A nominal annual discount rate of $r_{nom} = 6\%$, corresponding to a quarterly real effective rate of $r_d = 0.97\%$

(v) Nominal annual electricity price growth of 4.04%, corresponding to a quarterly real effective rate of $r_e = 0.50\%$

(vi) PV system balance of plant efficiency $\eta_e = 90\%$

(vii) PV system lifespan of 20 years (which is considered to be conservative)

Find: Tilt angle β, azimuth angle γ, number of PV panels Z and number of batteries X

Objective:

$$\max_{\beta,\gamma,Z,X} NPV = \sum_{q=1}^{Q} \frac{\left(C_{base,q} - C_{pvbatt,q}\right)(1+r_e)^{q-1}}{(1+r_d)^q} - \sum_{q=1}^{Q} \frac{W_q}{(1+r_d)^q} - \left(S_{pv} + S_b\right) \tag{6.16}$$

Subject to:

$$0 \leq \beta \leq 180 \quad \text{for } \beta \in \mathbb{R} \tag{6.17a}$$

$$-180 < \gamma \leq 180 \quad \text{for } \gamma \in \mathbb{R} \tag{6.17b}$$

$$0 \leq Z \leq Z_{\max} \quad \text{for } Z \in \mathbb{Z}^+ \tag{6.17c}$$

$$0 \leq X \leq X_{\max} \quad \text{for } X \in \mathbb{Z}^+ \tag{6.17d}$$

In (6.16), $C_{pvbatt,q}$ and $C_{base,q}$ are the cost of electricity with and without a PV-BESS system within the quarter billing period q.

The terms $C_{base,q}$ and $C_{pvbatt,q}$ are defined as:

$$C_{base,q} = \sum_{d=1}^{D_q} \left(\sum_{h=1}^{24} T_{ret0,qdh} E_{load,qdh} + T_{sc0,qd} \right) \tag{6.18}$$

$$C_{pvbatt,q} = \sum_{d=1}^{D_q} \left\{ \sum_{h=1}^{24} \left[T_{ret,qdh} \max\left(0, E_{bal,qdh}\right) - T_{fit,qdh} \max\left(0, -E_{bal,qdh}\right) \right] + T_{sc,qd} \right\} \tag{6.19}$$

where $T_{ret0,qdh}$ and $T_{ret,qdh}$ are the grid imported retail electricity tariff of the base plan and tested plan respectively for the h^{th} hour of day d with D_q days in the billing period, $T_{sc0,qd}$ and $T_{sc,qd}$ are the daily electricity supply charges for the base plan and tested plan respectively, $T_{fit,qdh}$ is the PV feed-in tariff and $E_{bal,qdh}$ is the net energy flow balance of the terms defined in Section 6.1, expressed as:

$$E_{bal,qdh} = E_{load,qdh} - E_{pv,qdh} - E_{bd,qdh} + E_{bpv,qdh} + E_{bg,qdh} + E_{bloss,qdh} \tag{6.20}$$

As the optimisation parameters Z and X are limited to integer values (with respective maximums $Z_{\max}$ and $X_{\max}$ determined by the customer's available space restrictions), while β and γ may take any real value within the domain of the constraints, the problem is classified as an MINLP problem.

6.3.2 Optimisation Method

To solve the MINLP problem defined in 6.3.1, a modified version of the PSO algorithm previously described in Section 5.4.2, known as QPSO as denoted by Sun et al. [225] was applied. QPSO is a relatively simple probabilistic algorithm using the mean best position of the particle swarm to improve the global search capability [225]. QPSO requires fewer parameter adjustments between problems and handles parameter constraints naturally with no specific modifications required to the algorithm compared to traditional PSO.

QPSO varies markedly from traditional PSO as velocity vectors are no longer used [225]. The principle of state superposition and uncertainty through the application of a quantum delta potential well model was first introduced in [237] to govern particle position updates. The concept was based on trajectory analysis which determined that to guarantee a global solution, the particle must converge to its local attractor $p_{i,n}^j$ [225] defined as:

$$p_{i,n}^j = \phi_{i,n}^j P_{i,n}^j + \left(1 - \phi_{i,n}^j\right) G_{i,n}^j \tag{6.21}$$

where $G_{i,n}^j$ is the global best position of the swarm and $P_{i,n}^j$ is the personal best position of a particle, while $\phi_{i,n}^j = c1 r_{i,n}^j / (c1 r_{i,n}^j + c2 R_{i,n}^j)$ and $r_{i,n}^j$ and $R_{i,n}^j$ are random numbers from a uniform distribution. Noting that typically $c1 = c2$ in PSO [238], $\phi_{i,n}^j$ may therefore be

sampled as a random variable from $U(0,1)$.

Under the model, the particles are treated as spin-less with a particular energy in J-dimensional Hilbert space [225, 238]. To ensure the particles remain in a bound state to guarantee a solution, a one-dimensional delta potential well model centred on the local attractor $p_{i,n}^j$ [225] for each dimension j is considered to ensure convergence [237]. The delta potential well represents the probability of a particle i appearing in a position $\mathbf{x}_i$. Under such an assumption, the characteristics of the particle are represented by a position dependent wave function ψ with a position probability density $|\psi|^2$ [238] defined by:

$$\left|\psi\left(x_{i,n}^j - p_{i,n}^j\right)\right|^2 = \frac{1}{L_{i,n}^j} e^{-2\left|x_{i,n}^j - p_{i,n}^j\right|/L_{i,n}^j} \tag{6.22}$$

where the parameter $L_{i,n}^j$ is the characteristic length of the delta potential well – the key parameter governing the search scope of the particle [227]. To facilitate good performance of the QPSO algorithm, two search strategies exist to determine the characteristic length $L_{i,n}^j$ [225]. The first strategy is referred to as quantum delta potential well-based PSO (QDPSO), as originally developed in [237], and has been shown to demonstrate satisfactory performance [225]. Under this strategy, $L_{i,n}^j = 2\alpha\left|x_{i,n}^j - p_{i,n}^j\right|$ leading to the following stochastic evolution equation:

$$x_{i,n+1}^j = p_{i,n}^j \pm \frac{L_{i,n}^j}{2} \ln \frac{1}{u_{i,n+1}^j} \tag{6.23}$$

where $u_{i,n+1}^j$ is sampled from the uniform distribution $U(0,1)$. However, QDPSO has also been shown to be sensitive to the selection of α [225].

The second strategy for determining $L_{i,n}^j$ is an evolution of the QDPSO model and represents the typical definition of QPSO. The concept of a mean best position [239] is considered whereby the mean best position acts as the 'centre of gravity position' for all the particles [239,240]. For M particles with J dimensions and for each particle $i \in \{1,\ldots,M\}$ with dimension $j \in \{1,\ldots,J\}$, the mean best position is defined as:

$$C_{i,n}^j = \sum_{i=1}^{M} \frac{P_{i,n}^j}{M} \tag{6.24}$$

The intention of the second strategy is to scale the distance from the current position to a global mean best point $C_{i,n}^j$, thereby controlling the value of $L_{i,n}^j$ [225]. The position of a particle in the n^{th} iteration $x_{i,n}$ is updated according to (6.25):

$$x_{i,n+1}^j = p_{i,n}^j \pm \alpha\left|x_{i,n}^j - C_{i,n}^j\right| \ln \frac{1}{u_{i,n+1}^j} \tag{6.25}$$

The parameter α is referred to as the contraction-expansion coefficient and is set so as to balance the local and global search performance of the algorithm [238]. In contrast to traditional PSO, α is the only parameter requiring adjustment for a specific optimisation

problem in QPSO.

For the optimisation problem with objective function (6.16), (6.25) was considered as the defining position update equation. The value of α was varied each iteration in the range between 1 and 0.5 based on the example provided in [225] whereby:

$$\alpha = (1 - 0.5)\frac{(N - n)}{N} + 0.5 \tag{6.26}$$

To provide an acceptable balance between optimisation speed and accuracy for the purposes of the analysis presented in this chapter, a particle swarm of $M = 10$ particles with a maximum number of iterations of $N = 50$ was implemented. In order to handle the discrete parameters Z and X denoting the number of PV panels and number of batteries respectively, the hypercube nearest-vertex approach of [229] previously considered in Chapter 5 was again utilised.

Figure 6.1 and Figure 6.2 show the solution convergence over ten repetitions for two test customers. For each of the repetitions performed, the same solution was found.

The QPSO algorithm was developed and simulated in Matlab version R2015b using an Intel i7-4790 3.6 GHz CPU. Average solution times of 147.54 seconds and 149.54 seconds were observed for Customer X and Y respectively. The increase in solution time compared to the results recorded in Section 5.4.2 may be principally attributed to the increased complexity of the objective function, requiring sequential BESS energy calculations for each hour over a 20 year horizon. It can be see that the number of iterations taken to reach the optimal solution is approximately 15 with QPSO; similar to, if not slightly faster, than traditional PSO in Chapter 5, but with a significantly simplified optimisation algorithm. Convergence plots for the two test customers are provided in Figures 6.1 and 6.2.

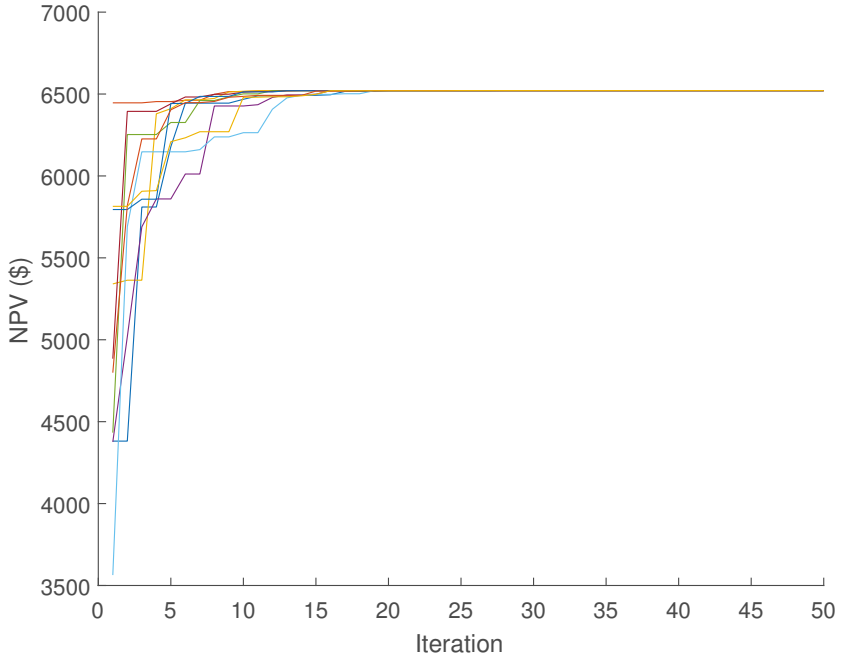

Figure 6.1: Optimisation convergence with ten repetitions (Customer X)

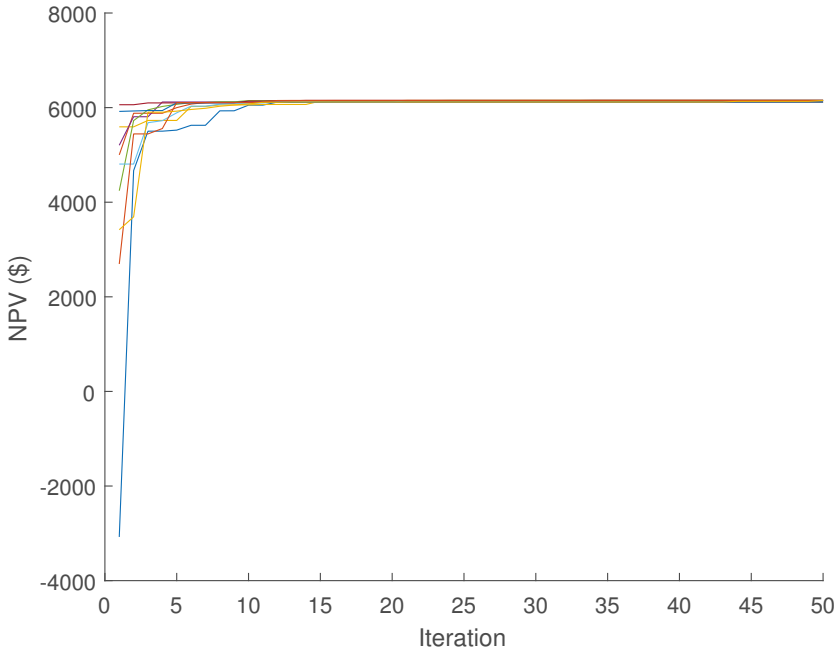

Figure 6.2: Optimisation convergence with ten repetitions (Customer Y)

6.3.3 Input Data

The electricity tariff structures tested in the optimisation problem were based on real 2016 TOU rates from three large Australian retailers, EnergyAustralia, Origin Energy and AGL. The retail tariffs considered in this research are provided in Appendix A Table A.3 and Table A.4.

6.3.3.1 Small Sample

Electricity consumption data measured over a one-year period for a small initial sample of three arbitrarily selected customers from the SGSC project are used in the analysis. Daily irradiation and ambient temperature data over a five-year period for each location were derived from the BoM CDO database [55]. The daily irradiation data were converted to hourly data using the same methodology established in Chapter 3 and Chapter 5. The weather station data considered for the small sample analysis is provided in Table 6.1.

Table 6.1: Weather station data considered in the small sample assessment

Analysis Sample	Station Name	BoM Station ID	Latitude (°)	Longitude (°)	Elevation (m)	Year Open
Small	Cessnock Airport AWS	61260	-32.79	151.34	61	1968
	Lake Macquarie AWS	61412	-33.09	151.46	6	2008
	Scone Airport AWS	61363	-32.03	150.83	221	1988

6.3.3.2 Large Sample

The second stage of the analysis considers a larger sample of 100 customers from the SGSC project. The updated PV energy yield model of (5.27) is applied with some minor

additional adjustments including a change to monthly billing for q, an inflation rate change to $r_{inf} = 2.5\%$ and nominal electricity price growth of 4.5%. Although the adjustments are minor and do not yield appreciably different results to the small sample analysis, the changes have been transparently identified for posterity. Furthermore, the inverter efficiency η_{inv} included in (5.27) is assumed to be 96%, representative of typical residential PV inverters.

The new National BRL model for satellite-based data measurement developed in Chapter 4 is used given the strong results of the statistical assessment undertaken in Section 4.4.1.

The previous research presented in Chapter 5 assumed the ambient temperature to be equal to the maximum daily temperature for the purposes of PV module losses due to temperature. This assumption yields conservative results from an electricity cost saving perspective. In the next section, an improvement to ambient temperature assumptions is introduced by estimating hourly temperature data from daily maximum and minimum temperature data.

6.3.3.3 Hourly Temperature Estimates from Daily Extremes

Hourly temperature data are typically unavailable for the vast majority of locations. Numerous empirical models have been developed to estimate hourly temperatures from daily minimum and maximum data. Reicosky et al. [241], assessed five methods including the hourly model defined by de Wit [242] presented as a subroutine in Rootsimu v4.0 [243]. The de Wit model constructs the hourly temperature estimates from minimum and maximum temperature measurements within a particular day as well as the minimum temperature from the next day. The minimum and maximum values are used to construct a piece-wise sinusoidal function constructed in two parts – from sunrise to 2 pm and from 2 pm to sunrise of the next day. The model assumes the maximum and minimum daily temperatures ($T_{\max}$ and $T_{\min}$) occur at 2 pm and sunrise respectively [241]. Following statistical analysis applied to four years of data, the method of de Wit was concluded to be the most accurate method [241].

Based on the model comparison undertaken in [241], the de Wit [242,243] temperature model was applied as an input to the PV energy yield model considered in this chapter. The ambient temperature T_a at each hour based on the de Wit model is defined as follows:

$$T_a = \begin{cases} a + b\cos\left(\frac{\pi h'}{10+h_{rise}}\right) & \text{for } 0 \leq h < h_{rise} \\ a + b\cos\left(\frac{\pi h'}{10+h_{rise}}\right) & \text{for } 14 < h < 24 \\ a - b\cos\left[\frac{\pi(h-h_{rise})}{14-h_{rise}}\right] & otherwise \end{cases} \tag{6.27}$$

where $a = (T_{\max} + T_{\min})/2$, $b = (T_{\max} - T_{\min})/2$, h is hour of the day, h_{rise} is the sunrise hour angle and $h' = h + 10$ if $h < h_{rise}$ and $h' = h - 14$ if $h > 14$. It should be noted that for $h > 14$, $T_{\min}$ of the next day is used to determine T_a for the remaining hours of each day.

6.3.3.4 Typical Meteorological Year Development

In contrast to the methodology applied in Chapter 5 and for the small sample of customers in Section 6.3.3.1, the weather data (both hourly irradiation and estimated hourly temperature) were subjected to a more rigorous process to better represent typical climatological data based on long-term irradiation and temperature measurements.

As opposed to applying five consecutive years of weather data over the period of 2011–2015, typical meteorological year data sets were developed following the procedure detailed in the flow chart of Figure 6.3.

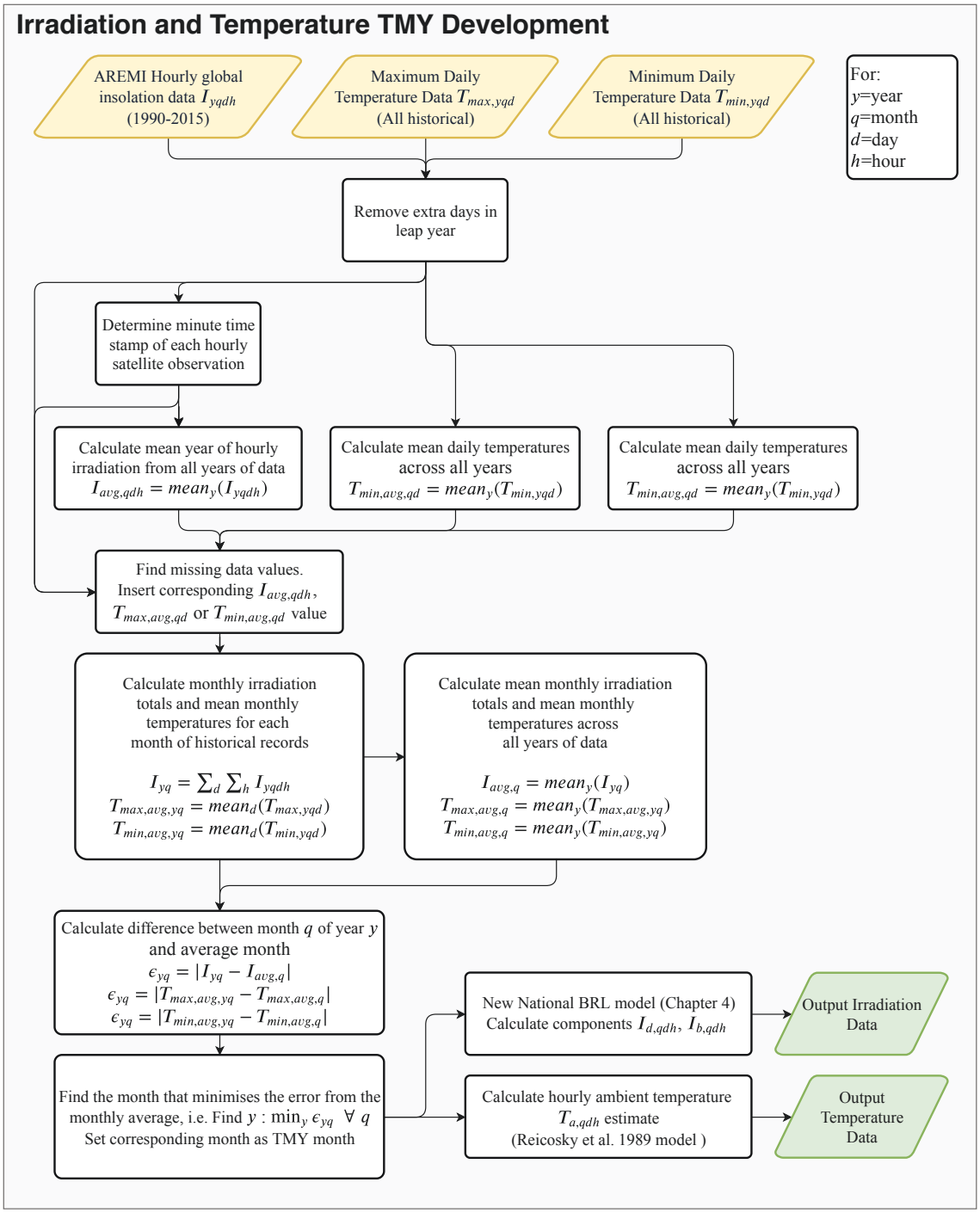

Figure 6.3: TMY development flow chart

The weather station location details assumed in this research is defined in Table 6.2. The full campaign history of AREMI irradiation data between 1990 and 2015 were used to develop the TMY data sets. In the first step, all extra leap year days were removed from consideration. The second step was applicable to irradiation data only, whereby the time stamps of the satellite observations were determined through consultation with the lookup table previously defined in Section 4.2.3. In the third step, average hourly irradiation and daily maximum and minimum temperatures were calculated to establish a representative average year. The average year values were used in place of missing data values.

Table 6.2: Weather station data considered in the large sample assessment

Analysis Sample	Station Name	BoM Station ID	Latitude (°)	Longitude (°)	Elevation (m)	Year Open
Large	Newcastle University	61390	-32.89	151.71	21	1998

Average monthly irradiation totals and average monthly maximum and minimum temperatures were the calculated. The average values for each month during the entire measurement campaign were then compared against an average representative month. The absolute value of the error between the two values was determined, the minimum of which corresponds to the typical monthly value. The process was repeated until all twelve months of the TMY data set were determined. The resultant full irradiation TMY data set and an example period showing direct and direct irradiation components are presented in Figure 6.4. The estimated temperature TMY dataset is shown in Figure 6.5.

A comparison of the average hourly irradiation profiles between the TMY data set using the new National BRL diffuse model of Chapter 4 and hourly data derived from daily data in the 2011–2015 date range is shown in Figure 6.6. It can be seen that the the TMY data set has slightly higher average global irradiation values than observed in the 2011–2015 period. Furthermore, the models defined in (3.39) to (3.43) estimating hourly irradiation data from daily data predict less direct irradiation in the middle of the day compared to the hourly based BRL model.

6.3.3.5 Equipment Assumptions

The PV modules considered for the small sample analysis were modelled based on 280 W Trina Solar TSM-PC05A(II) polycrystalline modules, applicable parameters for which are provided in Appendix C Table C.2. For the large sample analysis, the 300 W Trina Solar TSM-PD06A polycrystalline modules detailed in Appendix C Table C.4 were considered, to provide a more uniform comparison with the analysis presented in later in Chapter 8.

Two BESSs were considered in this research – the Tesla Motors 13.5 kWh 5 kW Powerwall 2 and the more modular 1.2 kWh 260 W Enphase AC Battery. Values for the BESS model parameters defined in Section 6.1 including δ, Y_{life}, Y_{EOL}, C_{EOL} and η_{batt} were based on the manufacturer data sheets [244] and [245] for the Tesla and Enphase systems respectively. Applicable data sheet parameters are detailed in Appendix D Table D.1. The fully installed cost of the Powerwall 2 is assumed to be AU$10,000 [246] in this chapter, while the cost of the Enphase BESS is approximately AU$2,000 [247].

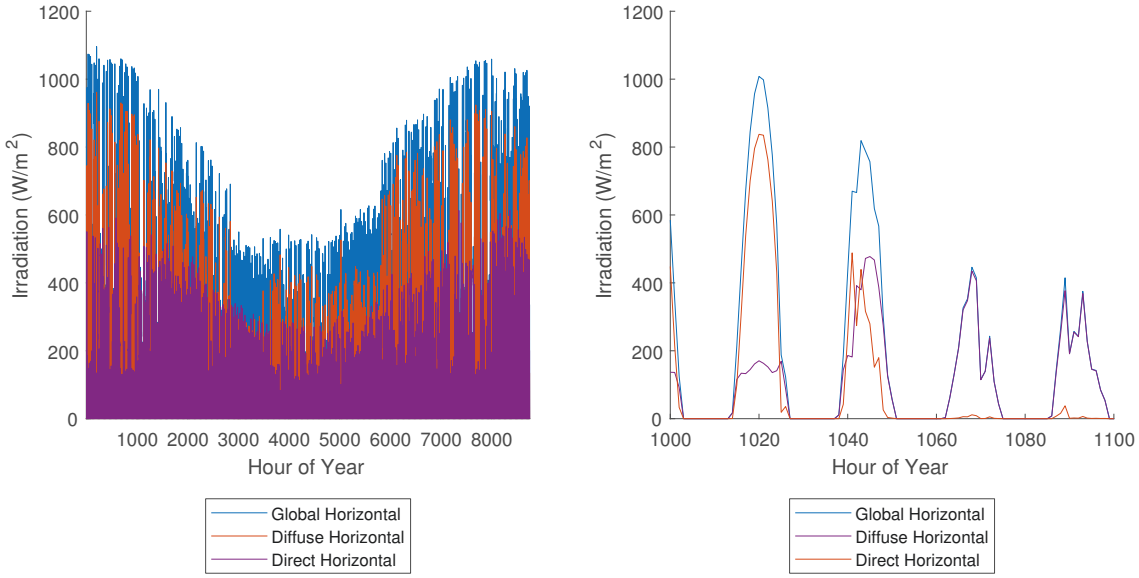

Figure 6.4: TMY global, diffuse and direct irradiation data set for Newcastle based on AREMI data

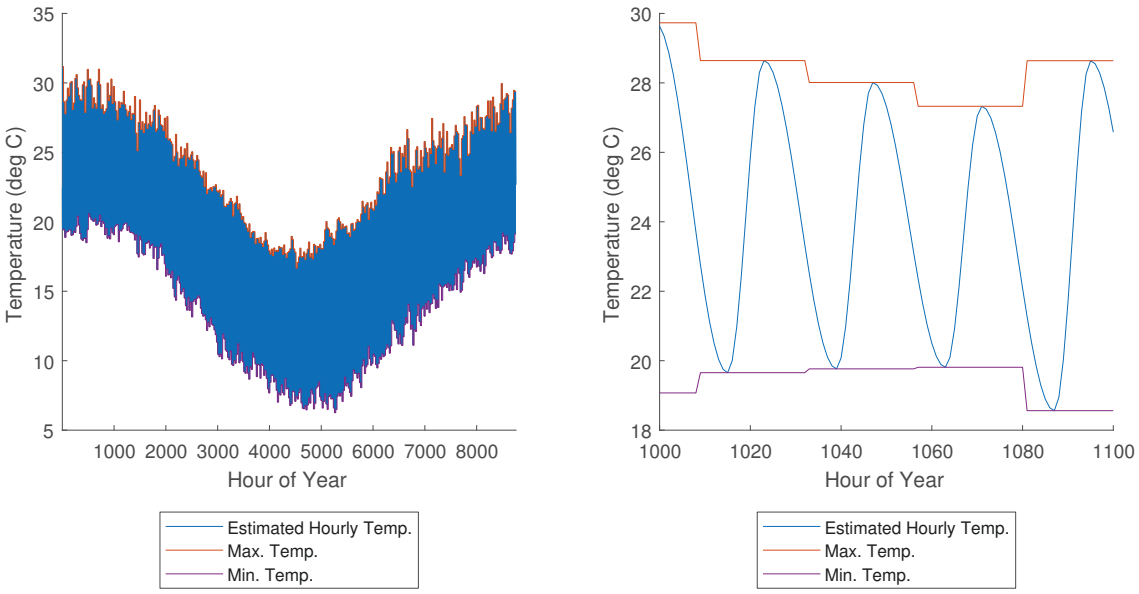

Figure 6.5: TMY hourly temperatures estimated from daily extremes for Newcastle based on CDO data

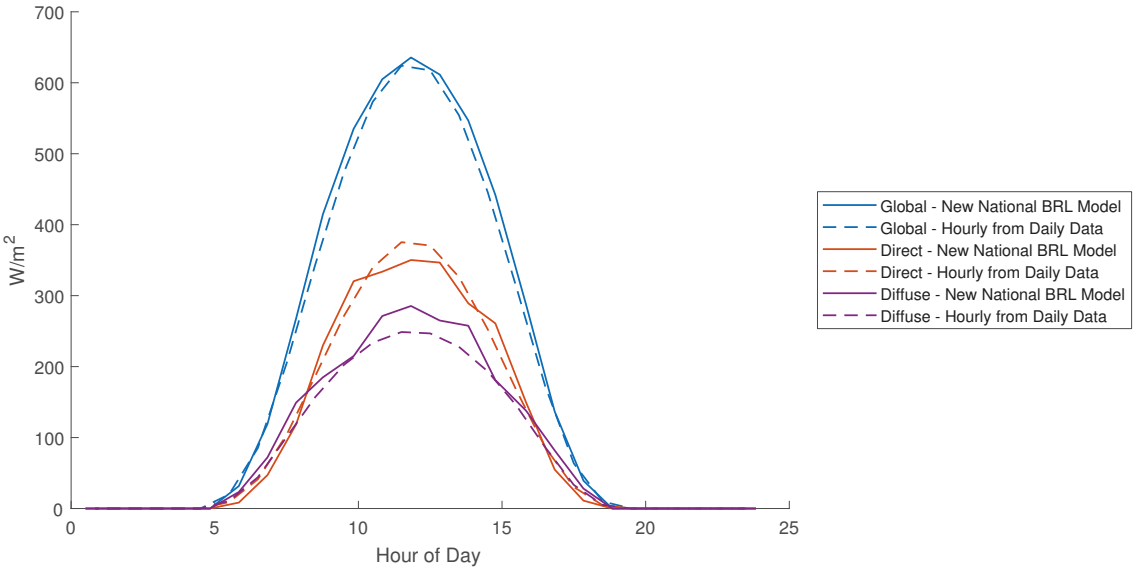

Figure 6.6: Average hourly TMY irradiation from AREMI and hourly data derived from daily data from the CDO database in the period 2011–2015 for Newcastle

6.4 Results

6.4.1 Small Sample

Table 6.3 shows a summary of the optimised PV-BESS systems for each customer under retail electricity plans from three large retailers. For each customer, Retailer B is found to provide the greatest benefit. For Customer 1, the maximum system size of 8.4 kW ($Z_{\max} = 30$, 280 W PV panels) is reached, while Customer 3 is also seen to potentially benefit from a relatively large PV system of 7.56 kW. In contrast, the optimal PV system for Customer 2 is found to be a far smaller system at 4.2 kW. The optimal tilt and azimuth angles also vary for each customer but are within a 20-30 degree range. However, importantly for the customers assessed, no instance can be seen whereby an energy storage system yields an economic benefit higher than a PV-only system based on current BESS pricing.

To determine the price point at which a hybrid PV-BESS system becomes an economically beneficial option for each customer, an NPV sensitivity analysis was undertaken on BESS pricing. Referring to Figure 6.7, systems consisting of either the Tesla Powerwall 2 or an Enphase AC Battery become viable for Customer 1 when unit costs are reduced to 70% of 2016 pricing. Customers 2 and 3 first see a benefit from the small, more modular Enphase system at the 60-70% price point but do not see a benefit from a larger Tesla system until pricing reaches 30-40% of current levels.

Figure 6.8 shows the number of batteries that constitute the optimal system as BESS prices are decreased. For the more modular Enphase BESS, an increase in battery quantity is observed for each customer as prices decrease. Customer 1, having a relatively high energy demand, would benefit the most from a larger number of Enphase batteries at each price point compared to the other two customers. In contrast, Customer 3 would not benefit from additional batteries until the 50% price point is reached, after which the customer could can take immediate advantage of additional units as prices continue to decrease. However, for the larger Tesla system, a single battery was found to be sufficient for all customers under all BESS price scenarios with one exception being an additional battery for Customer 1 at the 10% price point.

Table 6.3: Characteristics and economic performance of optimised PV-BESSs for different retail electricity plans

Customer	Retailer	BESS Size (kWh)	PV Size (kW_p)	Tilt	Azimuth	NPV	MIRR	Payback (Years)
1	A	0	8.4	29°	30°	$10,534	7.39%	9.3
	B	0	8.4	29°	30°	$11,153	7.52%	9
	C	0	8.4	29°	30°	$10,745	7.44%	9
2	A	0	4.2	31°	26°	$672	4.88%	18.4
	B	0	4.2	31°	26°	$917	5.04%	17.8
	C	0	4.2	31°	26°	$732	4.92%	18.2
3	A	0	7.56	29°	25°	$4,601	6.06%	13.8
	B	0	7.56	29°	25°	$5,044	6.19%	13.6
	C	0	7.56	30°	26°	$4,870	6.14%	13.6

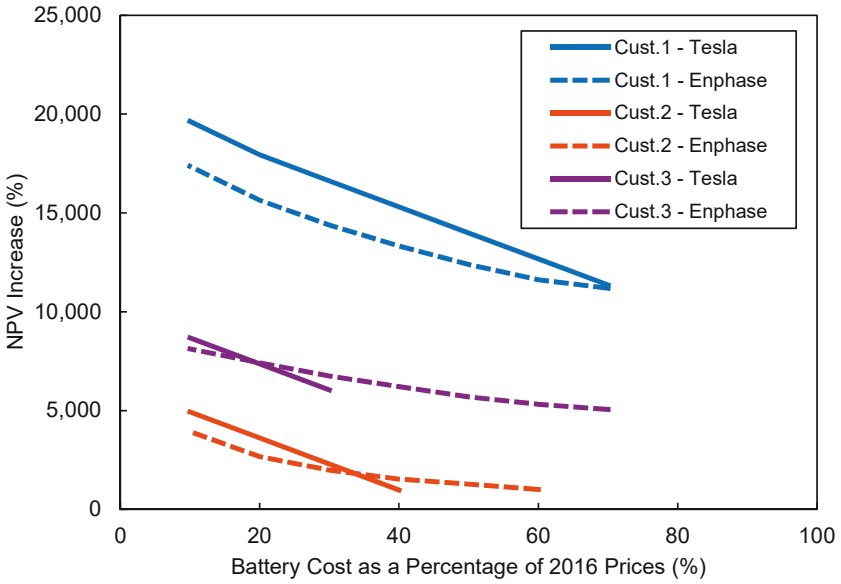

Figure 6.7: NPV sensitivity to BESS installed cost (Retailer B, Operation Mode 2)

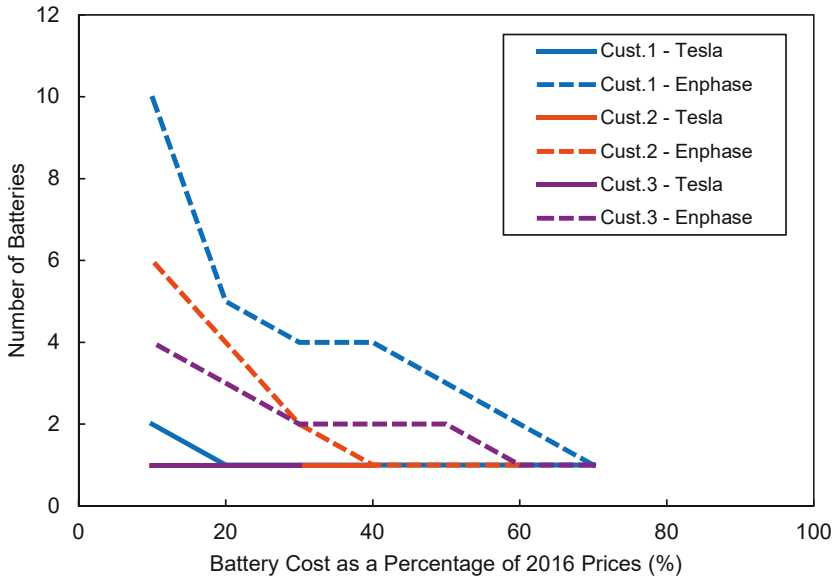

Figure 6.8: Number of batteries in PV-BESS system for varying installed BESS costs (Retailer B, Operation Mode 2)

Table 6.4 summarises the effect of BESS operation mode on the NPV for each customer. The table considers a significantly deflated BESS pricing scenario of 10% of 2016 installation costs whereby energy arbitrage would yield its greatest benefit among the price points considered in this research. In all instances, Mode 2 can be seen to produce the highest NPV, i.e. the BESS operating to maximise self-consumption of PV generated energy in shoulder and peak periods with no energy arbitrage. Consequently, even with significantly deflated BESS costs, under current TOU electricity tariffs and with electricity prices continuing to increase at current rates, a BESS system engaging in energy arbitrage is not found to provide any additional economic benefit than a BESS system purely used for PV generation load shifting.

Table 6.4: Economic performance under different BESS operating modes (Tesla Powerwall 2, cost = 10% of 2016 prices)

Customer	Operating Mode	BESS Size (kWh)	PV Size (kW_p)	NPV
1	1	27	8.4	\$17,446
	2	27	8.4	\$19,637
	3	27	7.56	\$16,721
	4	27	8.4	\$18,102
2	1	13.5	4.2	\$3.80
	2	13.5	4.2	\$4,931
	3	13.5	4.2	\$3,269
	4	13.5	4.2	\$4,232
3	1	13.5	4.2	\$7,313
	2	13.5	4.2	\$8,678
	3	13.5	4.2	\$6,785
	4	13.5	4.2	\$7,652

6.4.2 Large Sample

BESS operating Mode 2 and Mode 4, as detailed in Section 6.1.1, were tested on a larger sample of 100 customers selected from the SGSC project. An adjustment was made to the Tesla Powerwall 2 cost, increasing from \$10,000 to \$12,350 to more accurately reflect recent manufacturer price guidance [248].

The optimisation methodology was applied to three BESS price levels – current system pricing (100%), a price reduction to 70% and a 50% price reduction. Referring to Figure 6.9(a), only four customers can be seen to benefit from a BESS, each of which is a Tesla Powerwall 2, while 93% of customers benefit from a PV system.

When the BESS prices are reduced to 70% of the original price assumption, the proportion of customers with an optimal design configuration featuring a BESS greatly increases to 67% as shown in Figure 6.9(b). Furthermore, the split between the larger Powerwall 2 BESS and much smaller Enphase system is approximately equal. Furthermore, larger PV systems are almost uniformly coupled with the larger Powerwall 2 battery, while the Enphase battery is typically featured in PV systems within the 2.4 kW to 6.9 kW range. A slight anomaly can be observed in relation to the proportion of customers featuring an optimised PV system, which has dropped to 92% from 93% in Figure 6.9(a). Further investigation revealed the PV system no longer featured in the 70% BESS price case was initially a very small system at 0.6 kW, with a corresponding NPV of just \$30. Consequently, it may be concluded that the optimisation algorithm did not have sufficient time to reach the optimal solution in this case. However, given the relatively small NPV error compared to the 20-year analysis horizon, the balance between speed and accuracy may be considered acceptable.

Figure 6.9(c) shows the NPV when BESS prices are reduced by 50%. The proportion of customers with a PV system and the distribution of optimal system sizes can be seen to remain relatively unchanged compared to the previous two cases. However, 93% of customers can be observed to benefit for a BESS. The split between the Powerwall 2 and Enphase systems remains relatively even, with a clear trend towards the small battery for PV systems of 6 kW and lower.

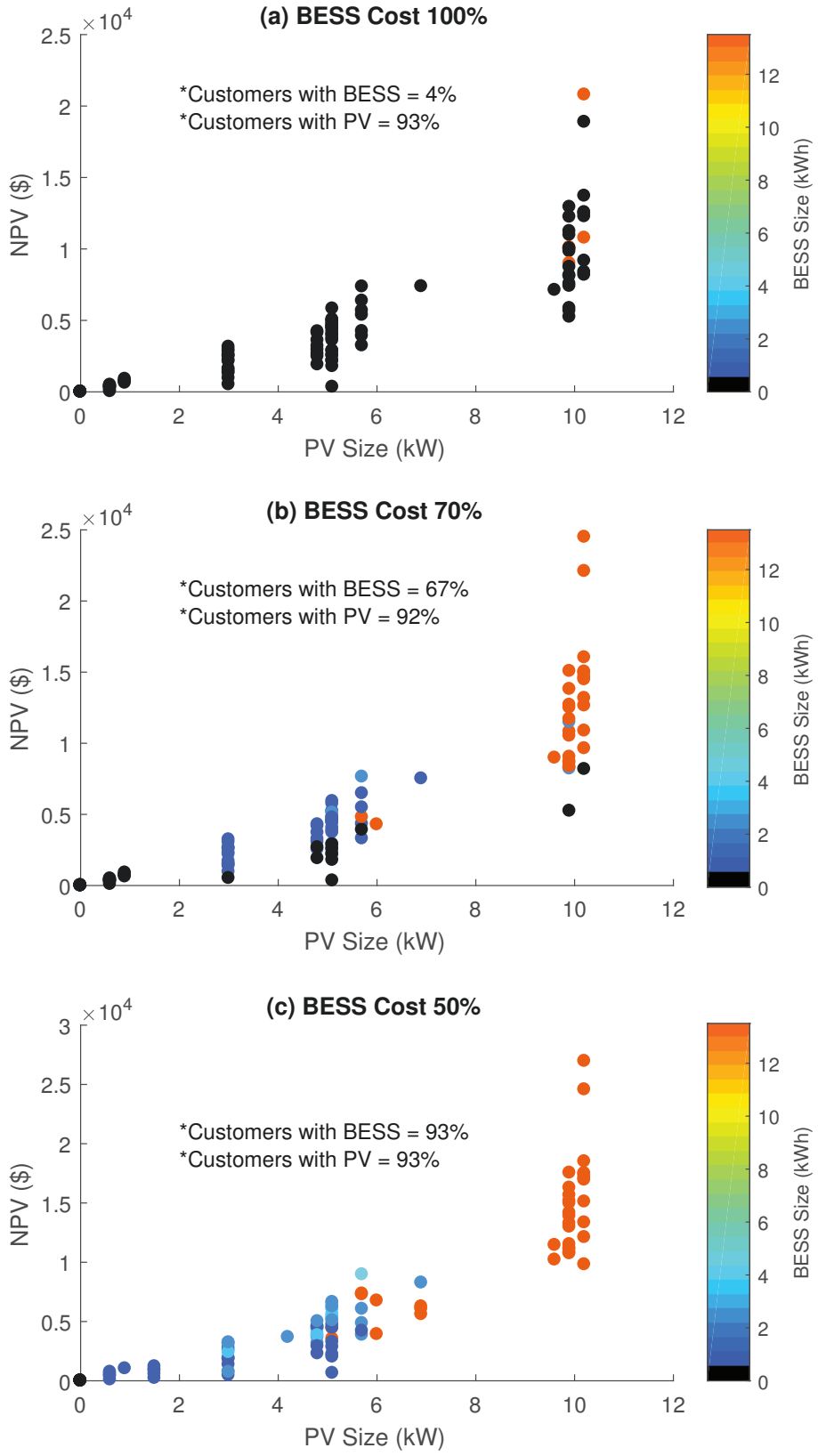

Figure 6.9: NPV, PV size and BESS size for a sample of 100 customers at (a) 100%, (b) 70% and (c) 50% BESS reference price levels

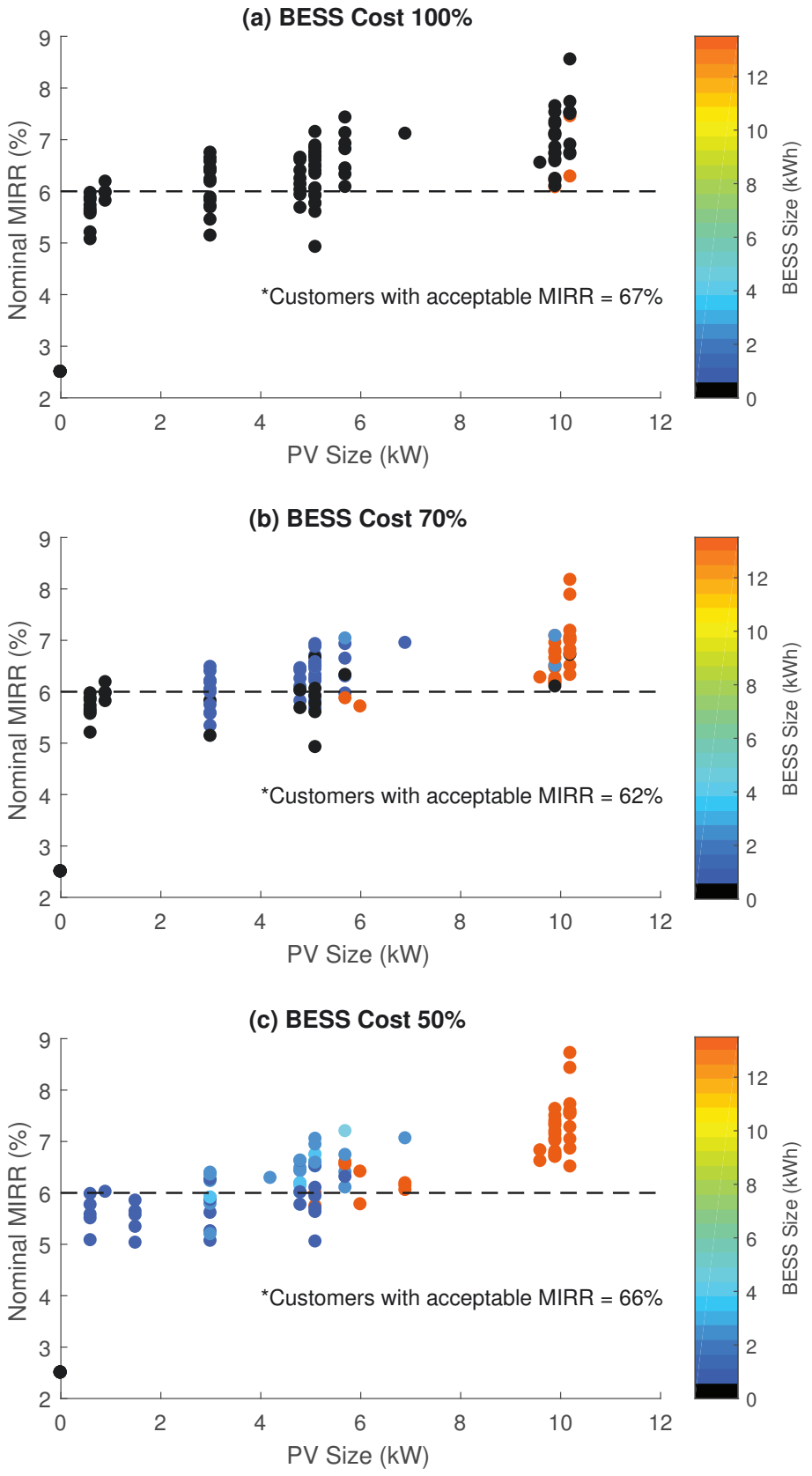

Figure 6.10: MIRR, PV size and BESS size for a sample of 100 customers at (a) 100%, (b) 70% and (c) 50% BESS reference price levels

Some customers can be seen to have a non-zero NPV without the installation of a PV system or a BESS in Figure 6.9. This cost saving is achieved through optimal electricity retail plan alone.

Figure 6.10 shows the distribution of the nominal MIRR for each customer at the three BESS price levels previously considered. For each level, the proportion of customers with a nominal MIRR above the acceptable 6% level (given the nominal discount rate of 6% assumed in this research), remains relatively unchanged – around 62–67%. The deviation in acceptable MIRR proportion may be attributed to certain customers on the 'economic fringe' between a PV-only system and a PV-BESS solution, leading to an increase in NPV, at the expense of a comparatively large initial system cost increase effecting the rate of return. The proportion recovers somewhat when the BESS price level reduces further to 50% as shown in Figure 6.10(c). However, overall it cannot be concluded that a reduction in BESS pricing presents a clear trend in the nominal MIRR received on the investment.

The proportions of the lowest cost base plans prior to optimal PV-BESS selection from Retailers A, B and C are presented in Figure 6.11. Approximately 65% of customers can be seen to benefit from prior selection of the plan from Retailer A, while 35% benefit from Retailer B. No customers were found to initially benefit from the Retailer C plan.

Following the application of the optimisation algorithm for each customer, a comparison of the proportion of the optimal retail plans for three BESS reference price levels is presented in Figure 6.12. The plan featured in the majority of optimal solutions can be seen to have transitioned from Retailer A to Retailer B. With BESS costs at 100% of the reference price, 91% of customers benefit most by selecting Retailer B, compared to 35% in the previous case of Figure 6.11. As BESS costs are reduced, the proportion of customers with Retailer B plans increases slightly, with only 5% benefiting from Retailer A at the 50% BESS cost level. Figure 6.11 and Figure 6.12 provide a clear demonstration of the necessity to consider available retail plans during the selection of a PV-BESS system. The optimal retail plan for a load-only customer is not necessarily the best option when a PV-BESS system is installed.

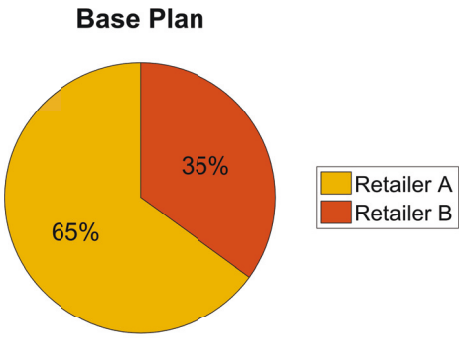

Figure 6.11: Proportion of base case lowest cost retail plans amongst 100 test customers

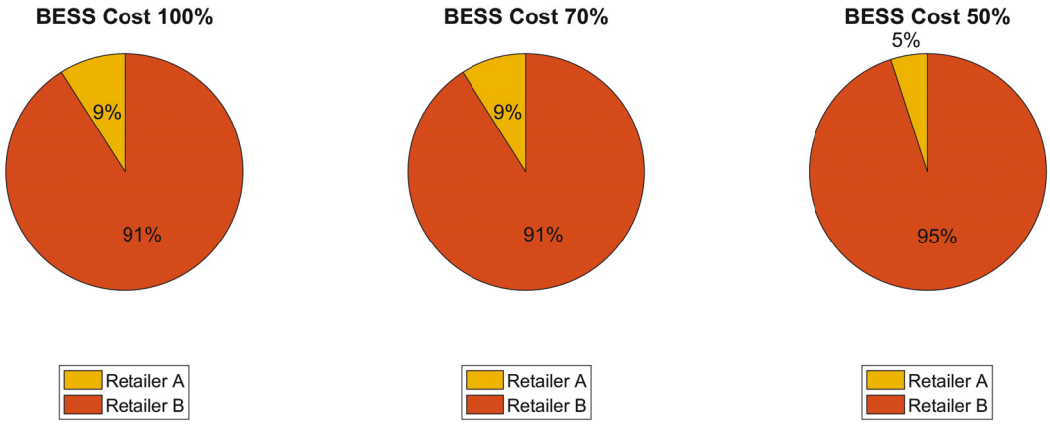

Figure 6.12: Proportion of lowest cost retail plans amongst 100 test customers with a PV-BESS installed at three different BESS price levels

6.5 Summary

Significant price reductions in PV and battery systems have sparked considerable interest in hybrid PV-BESS solutions at the residential level. However, optimal system selection is critical to ensure the economic viability of such systems for a particular customer's energy requirements.

An optimisation tool was developed in this chapter and applied to three real-world electricity customers. Based on current PV and battery system prices, no battery system was found to be economically viable for the residences assessed, however optimised PV-only systems were found to yield a net benefit for all customers.

A sensitivity analysis was conducted on battery pricing to determine the price point at which a hybrid PV-BESS would yield a net benefit improvement. The results showed that significant price reductions to 60-70% of current prices are required before the tested customers could take advantage of an energy storage system. It was also concluded that customers can generally take advantage of a modular system of smaller batteries earlier than a bulk energy storage system. Additionally, the results indicated that the current size of the Tesla Powerwall 2 battery is large enough for most energy storage needs even with battery prices at significantly deflated levels.

For the three customers selected, various battery operating modes were examined to determine the most economically beneficial operation. No instances were found whereby energy arbitrage yielded a greater benefit than purely maximising PV self-consumption. This observation continued to hold at all battery pricing levels.

The analysis was expanded to a wider sample of 100 customers. It was found that only four customers would benefit from a BESS system at current pricing, with the proportion increasing to 93% if BESS costs were reduced to 50% of current pricing. The proportion of customers with an MIRR exceeding the cost of capital under each price scenario was found to remain relatively constant across each of the BESS price scenarios.

Finally, the necessity to identify the most cost-effective retail electricity plan following the installation of a PV-BESS system was established. Without a PV-BESS, the majority of customers were found to benefit most from Retailer A, whereas when a PV-BESS system

is installed, the most cost-effective plan changed to Retailer B for 91% of customers.

Chapter 7 presents a case study assessment of the PV-BESS design optimisation methodology developed in this chapter applied to the TransGrid iDemand real-world microgrid system. The PV-BESS design optimisation methodology is further extended in Chapter 8 to consider the introduction of P2P energy trading to assess system design impacts effecting economic returns.

Chapter 7

Case Study

The economic performance of a hybrid PV-BESS is primarily dependent on the prevailing climatological and market conditions under which the proposed system is intended to operate and the underlying load which it is intended to supply. In an Australian context, PV systems contribute to the Australian Government's RET and are therefore eligible for certain incentives depending on the size of the system installed. For systems of 100 kW or less, PV systems are deemed to be part of the SRES and receive incentives in the form of upfront STCs [196]. Additionally, feed-in tariffs from an energy retailer may also be made available. However, STCs are scheduled to be phased out by 2030, complicating the investment decision process.

For PV systems larger than 100 kW, incentives are provided through the Large-Scale Renewable Energy Target in the form of LGC) [196]. PV system developers or owners generally enter into a negotiated PPA, most commonly with energy retailers. Under a PPA, the price to purchase LGCs from the PV installation is typically built into the total price paid for grid-exported energy. In the analysis presented in this chapter, PPA prices from \$60/MWh to \$140/MWh are considered to determine the effect on the economic viability of hybrid PV-BESSs.

A case study based on TransGrid's iDemand project, featuring a 53 kW polycrystalline PV array combined with a 400 kWh lithium polymer battery system [249], is presented in this chapter. TransGrid is the owner and operator of New South Wales' high voltage transmission network. The iDemand system was developed as a demand management innovation project to enable "researchers to investigate optimal integration of batteries, load and local generation" [249]. A block diagram of the TransGrid iDemand AC system is provided in Figure 7.1.

Operational data from the iDemand system are first used to validate the accuracy of the adopted PV energy yield model and then applied to hypothetical installations over a nine-year period to enable the determination of the opportune investment year and the characteristics and performance of the corresponding optimised system, including whether to install a small-scale or large-scale system given the different incentive schemes on offer.

In this chapter, PV energy yield and battery lifetime operation models based on hourly satellite irradiation and estimated hourly temperatures from daily temperature data are considered. The objective function of the underlying optimisation problem is formulated

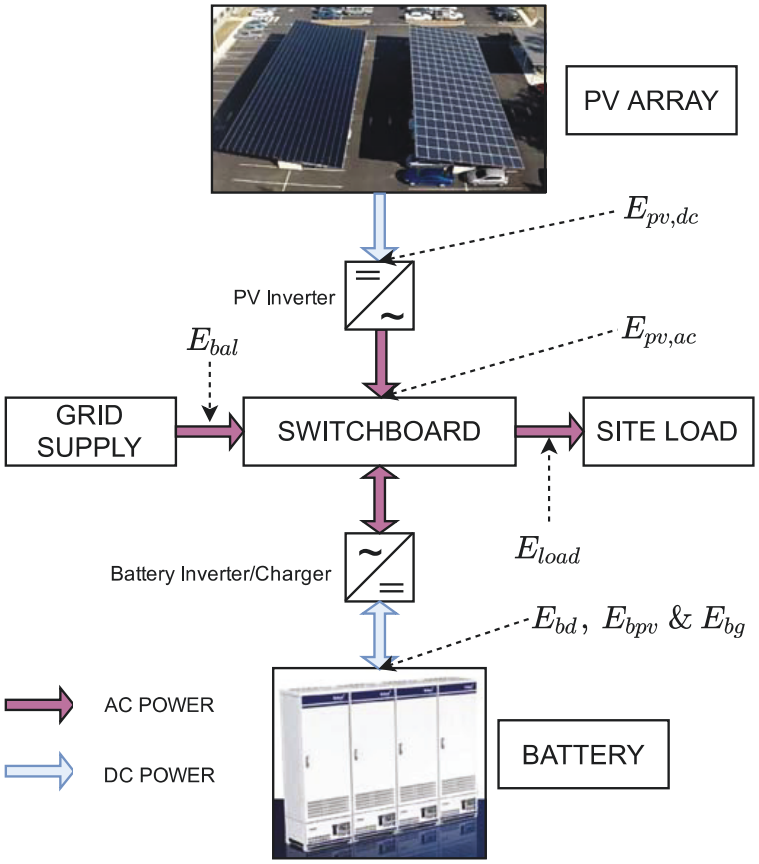

Figure 7.1: TransGrid iDemand AC system

as an NPV maximisation of energy cost savings achieved through the introduction of an optimally sized and oriented PV-BESS as previously defined in Chapter 6. Consideration is given to forecast technology cost reductions and electricity tariff increases.

7.1 Weather and PV Energy Models

7.1.1 Hourly Irradiation

As detailed in Chapter 3, BoM maintains a database of hourly and daily irradiation data from satellite observations. While direct access to the hourly data is available subject to a fee, the hourly data from 1990 to 2015 are publicly available via the AREMI spatial data platform [63]. The data includes global horizontal irradiation (I) and direct normal irradiation (I_{bn}) which are related through the following equation:

$$I = I_{bn}\cos(\theta_z) + I_d \tag{7.1}$$

where I_d is the diffuse horizontal irradiation and θ_z is the solar zenith angle the equation for which was previously established in (3.11). Consequently through rearranging (7.1), I_d can be directly estimated from the AREMI data as discussed in detail in Chapter 4.

Remark 7.1 *It should be noted that for the analysis presented in this chapter, neither the improved National BRL developed in Chapter 4 or the TMY data set methodology defined*

in Section 6.3.3.4 were applied as each were developed subsequent to the research presented in this chapter.

7.1.2 Hourly Temperature

The BoM CDO database contains daily maximum and minimum temperature data for thousands of weather locations within Australia. Data for the station closest to TransGrid's iDemand site (less than 4.5 km away) were applied to the methodology defined in Section 6.3.3.3 to estimate hourly temperature from daily minimum and maximum temperatures.

7.1.3 PV Energy Yield

After obtaining hourly irradiation components based on satellite data the transposition model is required to estimate the irradiation on the plane-of-array of a PV system. The HDKR transposition model previously considered in Chapter 5 and Chapter 6 is again applied, repeated below as (7.2) for convenience:

$$I_T = (I_b + A_i I_d)\, R_b + I_d(1 - A_i) \left(\frac{1+\cos\beta}{2}\right) \left[1 + f \sin^3\left(\frac{\beta}{2}\right)\right] + I\rho_g \left(\frac{1-\cos\beta}{2}\right) \tag{7.2}$$

In (7.2), I_b and I_d are the hourly direct and diffuse irradiation on the horizontal plane respectively, $A_i = I_b/I_o$, $f = \sqrt{I_b/I}$, I is the hourly global horizontal irradiation, I_o is the hourly extra-terrestrial irradiation, ρ_g is the ground reflectance and R_b is the ratio of tilted to horizontal direct irradiation. Importantly, R_b is a function of panel tilt β and panel azimuth γ, the equations for which are presented at length in Section 3.2.

Although not repeated in detail in this section, the analysis presented in this chapter (and for the the subsequent Chapter 8) consider an Incident Angle Modifier (IAM), as defined by De Soto et al. [250] to account for reflected radiation off the PV panel glass surface.

The PV energy yield model defined by (5.27) in Section 5.6 is considered in this case study, taking as an input the irradiation model for I_T defined in (7.2).

7.2 Optimisation Problem

7.2.1 Economic Assumptions

A nominal discount rate of 10% per annum is considered in this research, representative of the cost of capital that may be expected for a large corporation such as TransGrid. Annual inflation is assumed to be 2.5% while nominal electricity price growth is taken to be 4.5%.

For large-scale commercial and industrial customers, electricity charges are typically billed monthly. Consequently, the real discount rate and electricity price growth (taking

inflation into account) converted to monthly effective rates are $r_d = 0.59\%$ and $r_e = 0.16\%$ respectively.

The analysis presented in this research considers forecast PV system, battery and battery inverter costs between 2017 and 2025. The forecast costs are based on three price scenarios as defined by Brinsmead et al. [235], designated as minimum, base and maximum price scenarios.

7.2.2 Problem Definition

The optimisation problem is near identical to the problem defined in Section 6.3.1 with the previous objective function defined by (6.16). However, for industrial customers such as TransGrid, the tariff structures are slightly different and include an additional demand charge during each billing period. Consequently, the $C_{base,q}$ and $C_{pvbatt,q}$ terms previously defined in (6.18) and (6.19) are modified to include the demand charge $T_{DC,q}$ applied to the maximum demand $P_{\max,pvbatt,q}$ and $P_{\max,q}$ with and without a PV-BESS system respectively as shown in (7.3) and (7.4):

$$C_{base,q} = \sum_{d=1}^{D_q} \left(\sum_{h=1}^{24} T_{ret,qdh} E_{load,qdh} + T_{sc,qd} \right) + T_{DC,q} P_{\max,q} \tag{7.3}$$

$$C_{pvbatt,q} = \sum_{d=1}^{D_q} \left\{ \sum_{h=1}^{24} \left[T_{ret,qdh} \max\left(0, E_{bal,qdh}\right) - T_{pv,qdh} \max\left(0, -E_{bal,qdh}\right) \right] + T_{sc,qd} \right\} + T_{DC,q} P_{\max,pvbatt,q} \tag{7.4}$$

The $E_{bal,qdh}$ expression remains the same as (6.20). For systems of size $\leq$100 kW, $T_{pv,qdh}$ is the retailer PV feed-in tariff (6c/kWh) and for large-scale systems (>100 kW) $T_{pv,qdh}$ is the supply rate as agreed in the PPA (ranging from \$60/MWh to \$140/MWh). It should be noted that the same daily supply term $T_{sc,qd}$ is considered in (7.3) and (7.4) and therefore has no impact on the NPV as only a single retail electricity tariff is considered in the analysis presented in this chapter. Calculating the cost savings as the difference between the base cost and cost with a PV-BESS system results in the daily supply charges cancelling out.

As the problem is in the form of a MINLP problem, meta-heuristic methods are employed to solve the problem. A modified version of QPSO, known as comprehensive learning quantum-behaved particle swarm optimization (CLQPSO) is employed. As previously discussed in Chapter 6, QPSO has been shown have a better global search performance than traditional PSO with fewer parameter adjustments [225].

For the problem presented in Chapter 6, despite the fast convergence as previously shown in Figure 6.1 and Figure 6.2, premature convergence was experienced in some instances, whereby the swarm became stuck in local optima thereby requiring numerous repetitions for each customer to be undertaken in order to increase certainty of optimality.

To discourage such premature converge, one technique proposed by [251], referred to as comprehensive learning, has been applied to QPSO in [252]. Under traditional PSO, a particle learns from its personal as well as the global best positions simultaneously [251]. Liang et al. [251] noted that limiting the social learning aspects to the global best position leads to fast convergence but comes at the risk of entrapment in local optima, particularly for multi-modal problems.

Under the comprehensive learning strategy proposed in [251], in a particular dimension j, a particle is given the opportunity to learn from the personal best positions of all the particles, including its own $P^j_{i,n}$. The potential to learn is based on a prescribed learning probability $P_{c,i}$ which varies for each particle, proposed in [251] as follows:

$$P_{c,i} = 0.05 + \frac{0.45e^{10(i-1)/(M-1)}}{e^{10} - 1} \tag{7.5}$$

where M is the swarm population size.

For each dimension j of a particle i, a random number is generated and compared against the probability $P_{c,i}$. If the random number is greater than $P_{c,i}$, the particle will learn from its own $P^j_{i,n}$. If the random number is less than $P_{c,i}$, two separate particles are randomly chosen and the fitness values compared. The winning particle is used as the learning exemplar. In the instance where the exemplars in each dimension are a particle's own $P^j_{i,n}$, then a random dimension in another randomly selected particle is chosen to learn from. The learning process is continued until the particle position no longer improves for a prescribed number of iterations, referred to as the refreshing gap which was set to be $m = 7$ in [251].

Long et al. [252] extended the formulation of QPSO to include the comprehensive learning component of [251]. In QPSO, the comprehensive learning strategy is applied to the particle swarm prior to the calculation of the mean best position $C^j_{i,n}$ as defined in (6.24). To solve the objective function (6.16) as applied to the problem defined in this chapter, the maximum number of iterations was set to be $N = 50$ to ensure the optimisation process was completed in a reasonably time frame with a swarm size of $M = 10$. The refreshing gap of $m = 7$ and the learning probability $P_{c,i}$ as defined in (7.5) were also applied. The optimization problem was solved using Matlab 2017a.

Figure 7.2 and Figure 7.3 show the solution convergence for the CLQPSO algorithm for ten repetitions against the same two test customers considered in Chapter 6. Comparing the number of iterations to reach a solution against the QPSO algorithm as shown in Figure 6.1 and Figure 6.2, it can be seen that the CLQPSO algorithm takes longer, approximately 10-15 more iterations for the problem considered in this research. It can also be seen that the final NPV solutions reached after each repetition are almost, but not quite, identical for each customer. The maximum error from the highest NPV solution found was determined to be 0.0289% and 0.0086% for Figure 7.2 and Figure 7.3 respectively. Therefore, it is clear the CLQPSO algorithm did not quite have enough time to reach the global optimal solution. However, given the error is very small this is considered reasonable.

Although the QPSO algorithm can be seen to be generally faster to reach a solution,

the chance of getting stuck in local optima, which was sometimes observed using QPSO in the research undertaken in Chapter 6, is a problem of some concern. To reduce the probability of such an occurrence, the trade-off in speed to avoid premature global convergence is considered necessary thereby justifying the application of the CLQPSO algorithm.

The QPSO algorithm was developed and simulated in Matlab version R2017b using an Intel i7-4790 3.6 GHz CPU. Average solution times of 186.69 seconds and 199.65 seconds were observed for the same Customer X and Y assessed in Chapter 6 respectively. An increase in solution time of approximately 30-40% due to the comprehensive learning component may therefore be expected. It can be seen that the number of iterations taken to reach the optimal solution is approximately 10 more than the 15 iterations taken for QPSO. Convergence plots for the two test customers are provided in Figures 7.2 and 7.3.

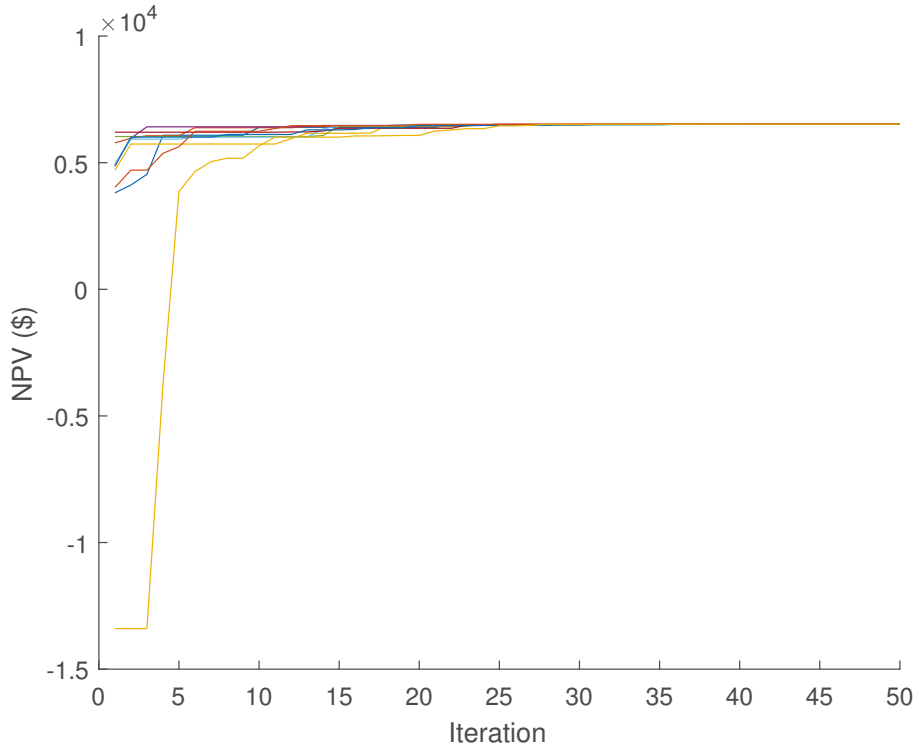

Figure 7.2: Optimisation convergence with ten repetitions (Customer X)

7.2.3 Input Data and Equipment Details

For this research, the inverter losses are assumed to be in accordance with the SMA STP17000TL model inverters installed in the iDemand system. The characteristics of the PV modules and batteries considered in this analysis are shown in Appendix C Table C.3 and Appendix D Table D.2. The energy costs associated with the terms $T_{ret,qdh}$, $T_{sc,qd}$ and $T_{DC,q}$ are shown in Appendix A Table A.5.

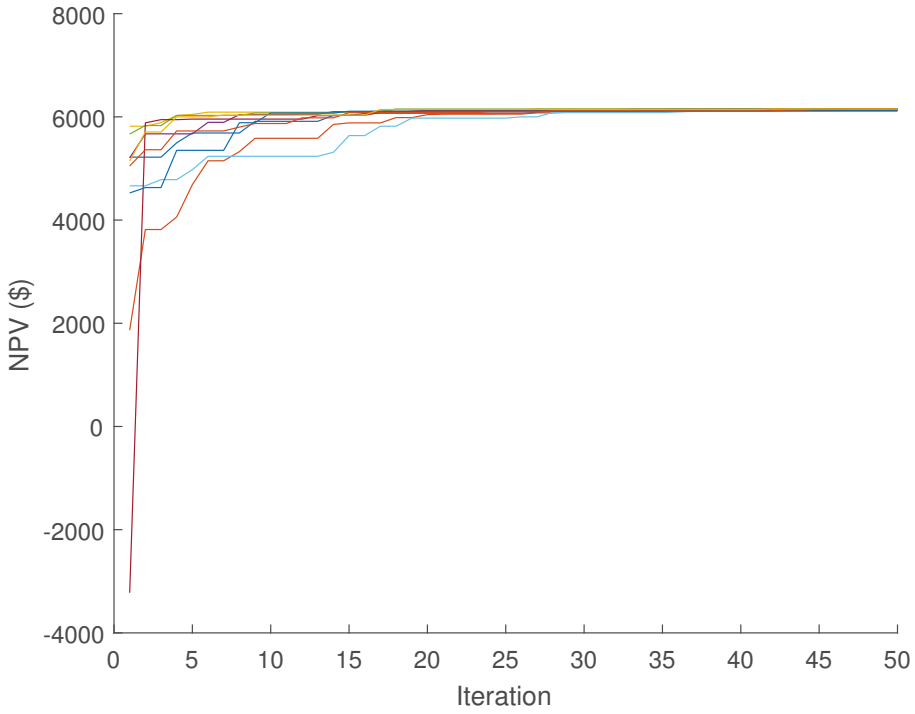

Figure 7.3: Optimisation convergence with ten repetitions (Customer Y)

7.3 Results

7.3.1 Energy Model Comparison

A comparison of average hourly AC power generated from the 53 kW polycrystalline silicon PV array installed in the iDemand system and the energy production model considered in this research is presented in Figure 7.4. Plots for energy production for months centred around winter and summer, as well as a full year of production are shown. For the full year of production, the energy model appears to slightly under-estimate energy production in the early afternoon hours and over-estimates production in the mid-morning hours. The overall rMBE for the full year of AC production is 0.02% as shown in Table 7.1.

The over-estimation during early morning can be attributed to shading events in winter, clearly observed in the winter plots of Figure 7.4. The model inaccuracy due to shading events is further demonstrated by the rMBE and rRMSE statistics summarised in Table 7.1 which are the worst for the three periods assessed. The overall accuracy of the PV energy yield model is perhaps better represented by the statistics for the summer period whereby the rRMSE is the lowest amongst periods assessed and the overall rMBE for AC energy is -2.9%.

The overall effect of energy yield model inaccuracy on the determination of economic performance of a PV system is shown in Table 7.2. The model underestimates electricity cost savings by just 1.57%, thereby presenting a conservative estimate. Based on the relatively low error, a reasonable degree of confidence in the accuracy of the PV energy yield model can be held for the purposes of economic optimisation.

The average hourly load profiles in different seasons are also shown in Figure 7.4.

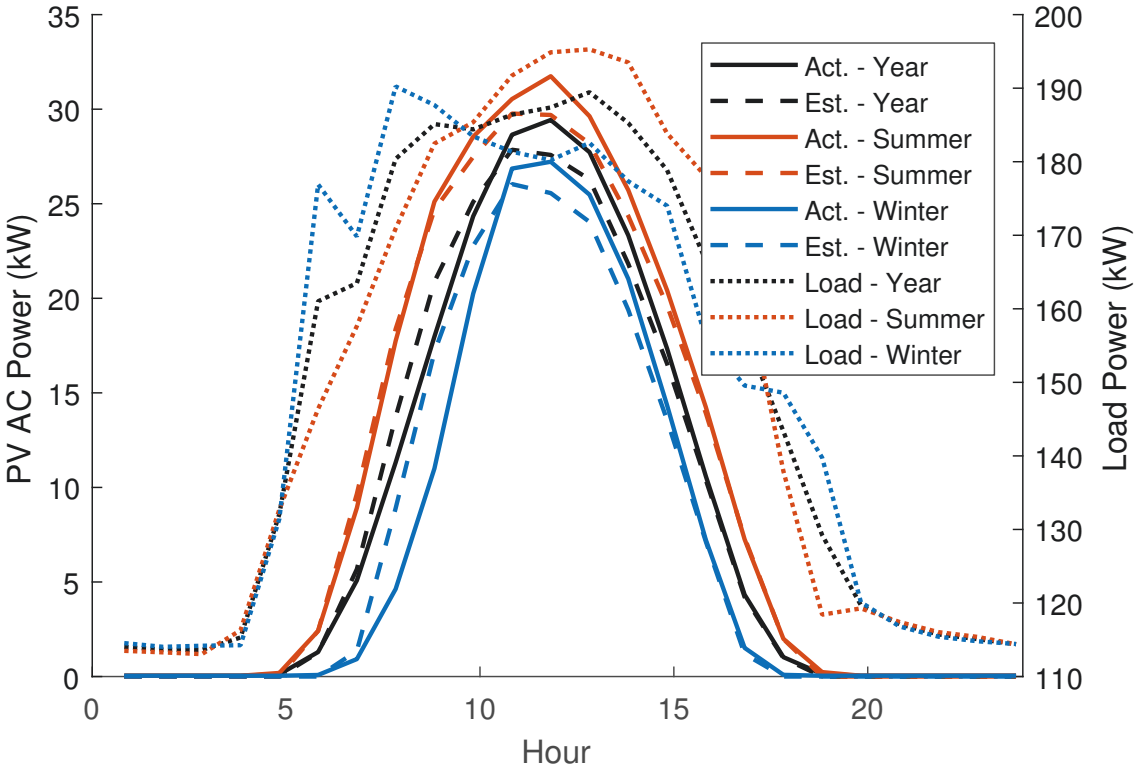

Figure 7.4: Comparison of average hourly estimated AC generation versus actual measured AC generation in 2015

Table 7.1: Statistics for measured versus modelled energy production of the iDemand system

Period	AC Energy		DC Energy	
	rMBE (%)	rRMSE (%)	rMBE (%)	rRMSE (%)
Year	-0.02	24.18	-0.36	24.19
Summer	-2.9	20.69	-3.24	20.81
Winter	4.36	29.34	4.01	29.22

Clearly there is a strong alignment between the hours of electricity demand and the hours of energy generation. The significance of this load profile is further discussed in Section 7.4.

7.3.2 Optimisation Results

Following the application of the optimisation algorithm applied to the TransGrid iDemand data and the economic scenarios considered, no hybrid PV-BESS was found to yield an economic benefit greater than a PV-only system. Consequently, the results presented and discussed in the remainder of this research refer to a PV-only system.

Referring to Figure 7.5, the NPV achieved for an optimised system steadily increases

Table 7.2: NPV of energy cost savings (actual and estimated) of the iDemand system (2015)

NPV (Actual)	NPV (Estimated)	Error (%)
$10,210	$10,049	-1.57

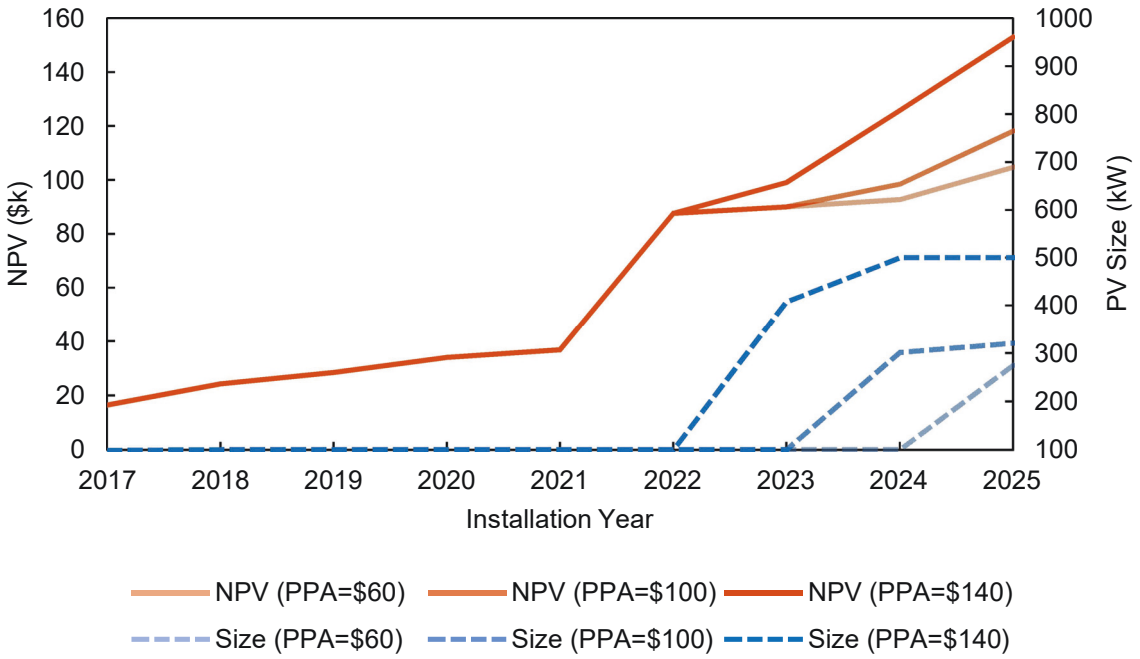

Figure 7.5: Optimal PV array sizes and associated NPVs evaluated for a range of PPAs forecast for future years of installation

with installation year due to reduction in system costs under the base PV system cost scenario of [235]. For the high price case of a PPA=$140/MWh shown in Figure 7.5, it can be seen that the optimal system size for the load profile considered is a 100 kW PV system, the maximum achievable under the small-scale renewable energy scheme, up until 2022. Between 2022 and 2025, the optimal system from an NPV perspective changes to be a large-scale system. At this point, the NPV and system size trajectories diverge depending on the negotiated exported energy price under a various PPAs. It should be noted that the distinct NPV increase from 2021 to 2022 is due to a significant PV price drop as forecast by Brinsmead et al. [235] and is unrelated to the pricing scenario and PPA energy price.

Referring to Figure 7.6, the MIRR for an investment in PV steadily increases as system prices are expected to decrease overtime. Due to the forecast price drop in 2022, the MIRR increases rapidly before reducing once again as the optimal system is deemed to be a large-scale scale system. The inverse is true for the payback period. It should be noted that under the base system pricing scenario featured in Figures 7.5 and 7.6, the maximum MIRR achieved for the NPV optimised PV systems is around 9.5%, less than the cost of capital of 10%. Consequently, without considering carbon reduction motives, under the economic assumptions considered in this research, investment in a PV system does not present the most efficient investment option. However, a relaxation of the discount rate, would yield a higher rate of return and therefore the investment in a PV system may be deemed economically viable. Furthermore, other market participants may have higher retail electricity costs than those assumed in Table A.5, rendering a PV system more economically viable.

The optimal NPV and PV system size trajectories for the three pricing scenarios

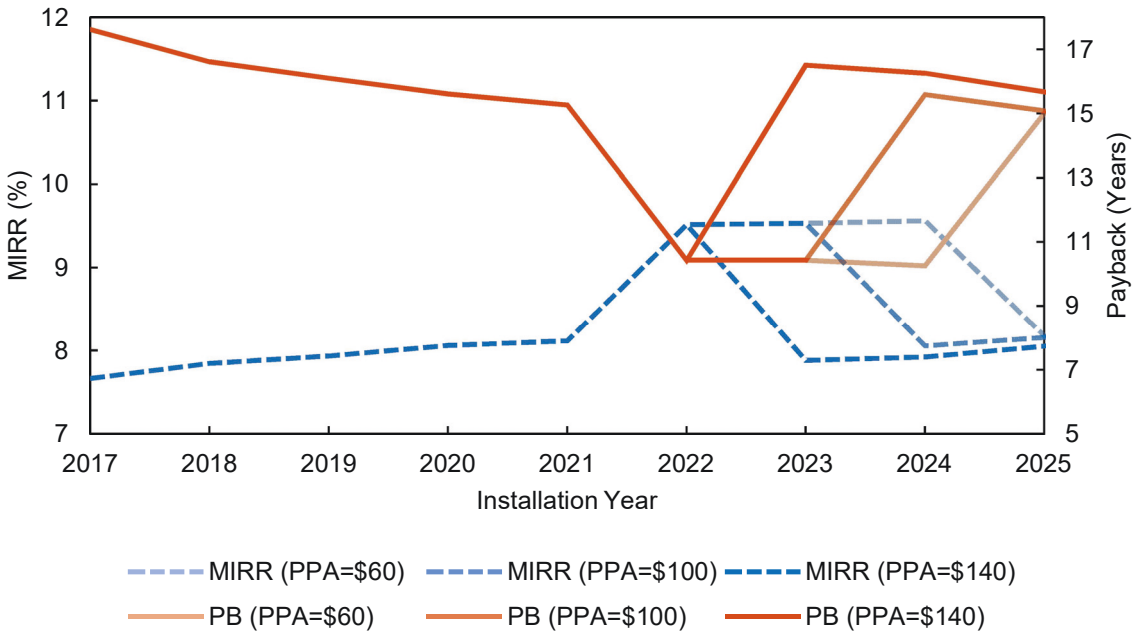

Figure 7.6: MIRR and payback periods of optimised systems for a range PPAs forecast for future years of installation

considered in this research are overlaid in Figures 7.7 and 7.8 respectively. Under the minimum and base price scenarios, the optimal system size is 100 kW until 2020 and 2022 respectively whereby a larger system is the most beneficial. The shaded regions represent the range of PPA energy prices considered in this research – the lower bound represents \$60/MWh and the upper bound \$140/MWh. However, under the maximum price scenario, the optimal size for all installation years is almost uniform at 100 kW with the exception of the initial year 2017. Due to especially high PV system costs modelled for 2017 under the maximum pricing scenario, the optimal size is only 4.5 kW. This is an unrealistic scenario as the industry pricing is currently tracking well below the assumed price point.

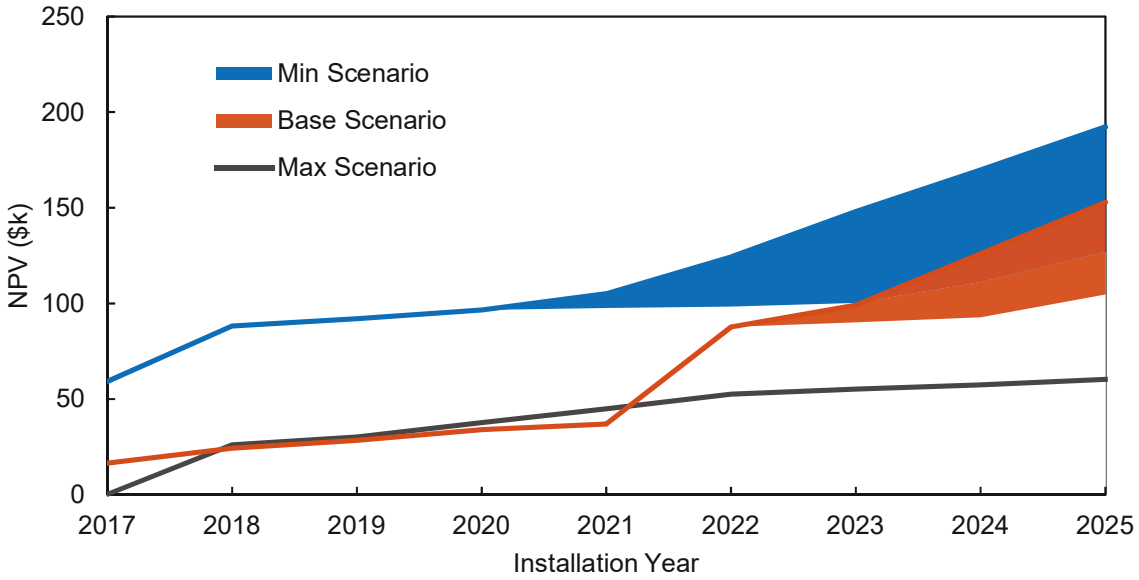

Figure 7.7: Comparison of optimised NPVs for three component pricing scenarios (min, base and max). Overlaid shaded areas represent the range of PPAs considered (lower bound represents \$60/MWh, the upper bound represents \$140/MWh)

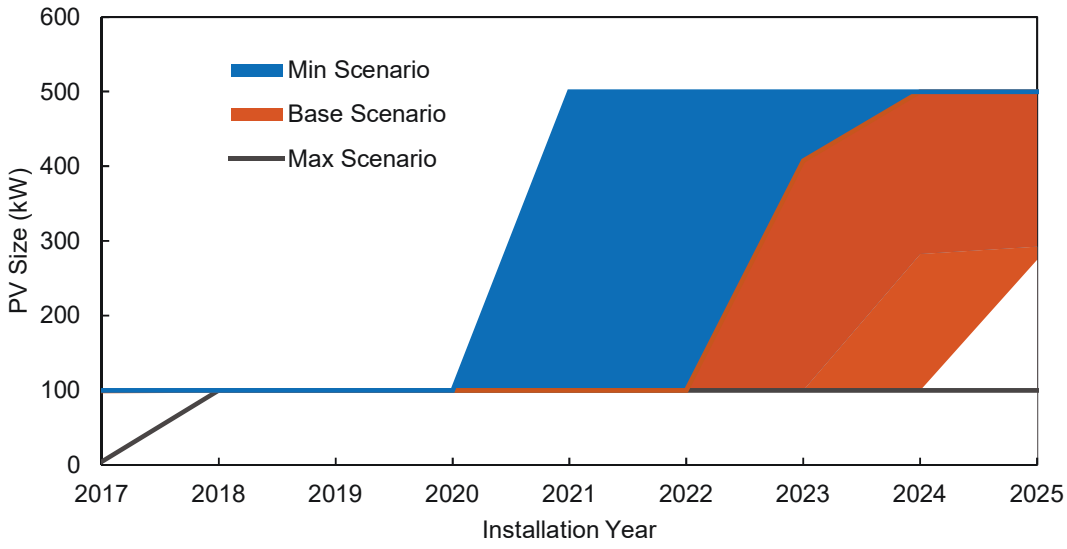

Figure 7.8: Comparison of optimal system sizes for three component pricing scenarios (min, base and max). Overlaid shaded areas represent the range of PPAs considered (lower bound represents \$60/MWh, upper bound represents \$140/MWh)

7.4 Discussion

It should be noted that hourly irradiation measurements from satellite observations do not necessarily coincide with the beginning of the hour. In the instance of MTSAT-2 observations at a latitude of -35°, the observation occurs 49.5 seconds after the beginning of the hour [56]. As the irradiation observations are required to align with the time stamp for the load data, significant errors may be introduced if the resolution of load data is too coarse. To achieve a reasonable correlation between data time stamps, minutely load data are preferable.

As stated in Section 7.3.2, no battery system was found to provide an economic benefit higher than a PV-only system. This may be attributed to two primary factors. Firstly, the electricity costs as detailed in Table A.5 are particularly low when compared to the residential consumer market. Consequently, the relatively low energy cost savings achieved through avoided grid-imported energy are not sufficient to out-weigh the high capital costs of a battery system. Secondly, as shown in Figure 7.4, the hours of load demand strongly align with the hours of PV generation. Therefore, the benefit achieved through shifting PV generated energy to evening or early morning hours is far less than directly meeting demand during the day time period which typically correspond to higher network prices, particularly in the afternoon. The combination of these two factors indicate that under the load profile and tariffs conditions representative of TransGrid's operations, a hybrid PV-BESS is not the most economically efficient arrangement.

7.5 Summary

PV energy yield models and battery operation models were developed as key components of an optimization algorithm to determine the hybrid PV-BESS with the most economic value for a load based on TransGrid's iDemand system. The energy yield model was found to have an acceptable accuracy and shown to underestimate the potential annual energy cost savings by just 1.57%.

Implementation of the optimization algorithm revealed no battery system would yield an economic benefit greater than a PV-only system for installation years between 2017 and 2025. Under the system pricing scenarios considered, the optimal system was found to be a small-scale system until 2020 after which a transition to a large-scale system would yield the highest NPV depending on the pricing scenario considered.

The results presented in this chapter demonstrate the necessity to optimize PV-BESS systems as an integral component of the investment decision process.

Chapter 8

DER Design Optimisation for Peer-to-Peer Energy Trading

Desire for flexibility and empowerment to choose renewable electricity sources at the consumer level has driven the introduction of collaborative economy concepts in electricity markets [7]. Electricity networks and markets are transitioning from traditional centralised generation to decentralised structures as a means to transition to a low carbon society that is "consumer-centred" [253], facilitated by the widespread introduction of DER. Sharing economy concepts popularised in the mobile app era by Uber for transportation and Airbnb for hospitality services are now under investigation for extension to electricity markets [254]. The concept that energy can be traded between self-organised peers and groups [8], either as independent producers or community-based structures [7], is expected to be facilitated by the introduction of physical microgrids or transactive energy enabling soft technologies such as distributed ledger technologies (DLTs).

Existing retail arrangements do not capture the value provided by DER and in some cases discourage PV investment [255]. The temporal and spatial variations between DER and individual consumers [255] are not accounted for under network tariff structures that have not traditionally accurately reflected the cost to deliver services to each customer [256].

P2P energy trading, also referred to as local electricity trading [255, 257], virtual net metering [258] or transactive energy [259], is a concept whereby bilateral agreements or contracts are established between two electricity peers for the exchange of electricity at an agreed price and for an agreed time [7]. P2P trading is not restricted to large traditional generators and industrial consumers but can be applied to all levels of the network including single household consumers or prosumers, in the case where energy customers also have installed DERs such as rooftop solar PV, batteries or micro wind turbines.

P2P research is still in its infancy with no agreement on the most efficient data sharing and processing structures [260] or fair market designs that enable the development of local energy trading [261, 262]. The coordination of loads between peers does not necessarily require centralised control, such as the role played by an aggregator through cloud-based systems [263]. DLTs are an example of distributed transaction management between peers

whereby each peer holds a copy of the transaction log thus removing the need for central management [264]. DLTs provide "real value when multiple organisations have a stake in shared data and processes" [265]. The management of each stake is handled by smart contracts, which are defined programs that govern the ledger rules and are triggered when transaction conditions have been met [264]. To faciliate smart contracts, particularly for the benefit of P2P trading, DLTs must be secure and demonstrate consensus (proof of agreement), provenance (auditable) and immutabability (tamper-proof) [265]. Blockchain, as a form of DLT, has received increasing attention for P2P trading applications with over 140 research projects and startups emerging in the energy sector [264].

In this chapter, P2P trading is investigated from the perspective of a prospective investor in small-scale DERs at the residential level. A lifetime assessment of DERs consisting of solar PV and battery systems is undertaken in the context of a P2P market consisting of over 2,200 participants with real load consumption profiles derived from the SGSC project data. The energy flow models previously developed in Chapter 5 and Chapter 6 are modified to enable potential DER investors to participate in P2P transactions. The hypothetical P2P market simulation is tested under various scenarios to identify trends in optimal PV-BESS system sizes and the potential economic returns available.

8.1 Literature Review

The first application of the P2P concept to power systems was introduced in 2007 [7]. In recent years, particularly since 2016, the number of research projects and trials has rapidly increased, coinciding with increased consumer appetite to utilise low carbon energy sources and leverage DERs.

Sousa et al. [7] present a comprehensive review of consumer-centric electricity markets noting that other recent studies have focused solely on market prospects or technical aspects. The review aimed to provide an understanding of all aspects of the transition to the consumer. Three P2P market designs are presented – full P2P, community-based P2P and hybrid P2P.

Full P2P, in which peers or agents directly negotiate with each other, is gaining significant momentum [7]. Under full P2P, the negotiation process can, and is indeed expected to, result in a different price for every trade. Through the use of DLT, privacy is assured with only power and energy quantities and the associated price signals shared between agents [7]. Under a full P2P design, the delivery of energy can be truly aligned with customer preferences, whether sourcing green energy only or achieving the lowest possible price for the individual customer. The primary disadvantage of full P2P is the problem of scalability associated with the negotiation process due to the quantity and frequency of potential transactions [7, 265]. As an example, the Brooklyn Microgrid project, discussed further in Section 8.1.3, observed scalability limitations for the Ethereum blockchain DLT, requiring the establishment of a bespoke blockchain for the project [266].

Under community-based structures, a community manager, also referred to as an aggreggator or trader, is established to handle trading between the participants or manage trades outside the community on behalf of the participants. The main definition of a

community is a group of participants sharing a common goal, such as carbon footprint reduction through purchase of remotely generated green energy [7] or auctioning of local available stored energy [267]. Consequently, community structures are well suited to microgrid architectures or for a local group of participants. The market is structured to benefit the entire community rather than focusing at the individual level. However, there are times when the preferences and expectations for particular members are not met as they may not align with the community interests [7].

Full P2P and community designs can be combined to form hybrid topologies. As described by Sousa et al. [7], at the upper layer peers or energy collectives can trade directly with each other, while on the bottom layer a community manager overseas trading within the community. The graphical representation of a hybrid P2P structure is presented in Figure 8.1 as detailed in [7]. The primary advantages of hybrid structures include a wider energy choice than community structures, increased cooperation between agents and fewer scalability issues due to the reduced communication and computational effort required.

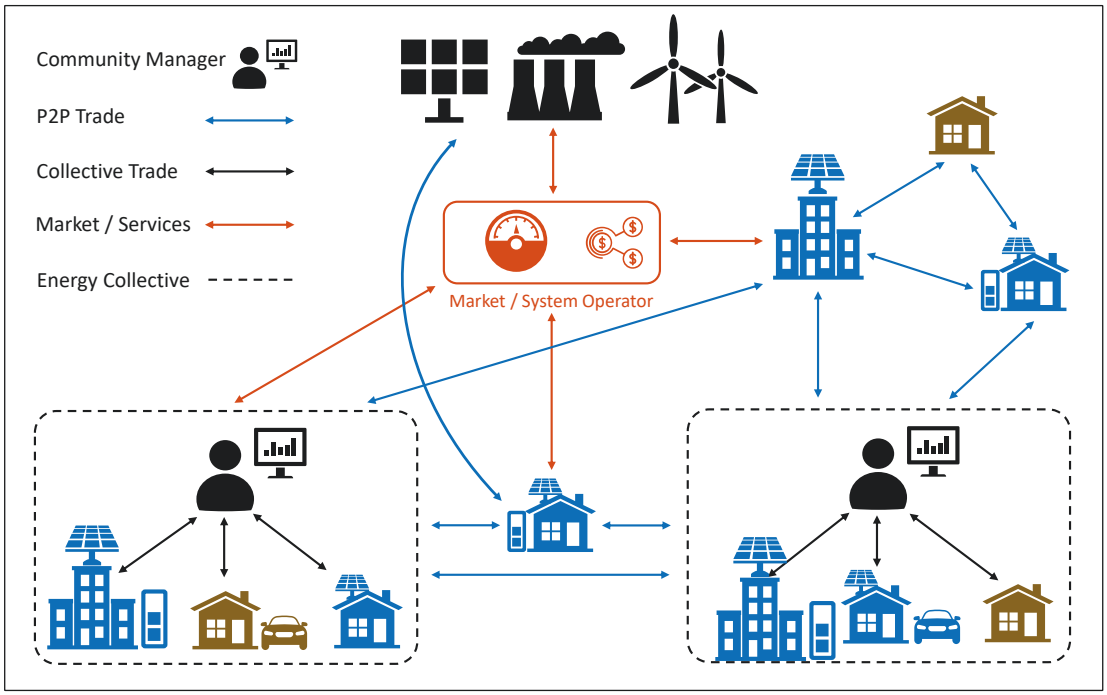

Figure 8.1: Hybrid P2P market design adapted from Sousa et a. [7]

In [7], a test case of the three high level P2P structures was conducted on the IEEE 14-bus system. It was found that a full P2P architecture resulted in the highest local consumption of DERs while the hybrid topology presented reasonable trade-offs to improve social welfare (i.e. mutual economic benefit) through transactions with other communities. The hybrid P2P system was therefore considered to be the most compatible with the existing network and is more predictable to grid operators than full P2P [7].

In [268], a hierarchical architecture was proposed to identify and characterise the key elements of P2P energy trading. A three-dimensional achitecture was proposed with four key layers – the business layer (referred to in [7] as the market layer), control layer, in-

formation and communications technology (ICT) layer and finally the power grid layer. The second dimension details the size of the trading group, first starting with a single customer, then scaling up to microgids, cells of microgrids and finally entire regions consisting of multiple cells. The final dimension relates to time related components of the transaction process from bidding, to energy exchange and finally to financial settlement.

In [268], a P2P trading platform was proposed focusing on the business layer for a grid-connected low-voltage microgrid. The research novelty is claimed to be prosumer modelling as opposed to modelling of agents categorised solely as either generators or consumers. In [268], P2P energy trading to maximise economic benefit is the sole consideration, as opposed to other research whereby physical support of microgrids to improve reliability and stability are considered. The system was simulated using game theory to reach Nash equilibrium as a solution of a non-cooperative game with multiple players [268]. Under the simulation, solar PV and later wind turbines were modelled along with flexible demand scheduling through electric hot water heaters. However, no consideration was given to energy storage systems.

8.1.1 Optimisation of P2P Participation

Optimal peer-to-peer trading decisions have received significant attention in recent literature largely from a community or microgrid perspective such as in [7, 261, 262, 268–274]. Although less prevalent, some research focused on P2P optimisation for single residences [260,263,268]. In [263] and [260], cost optimisation in smart homes with demand-side management (DSM) was investigated for energy sharing. The research aimed to address unfair cost and benefit distributions for P2P trades under microgrid structures with the aim to enforce pareto optimality whereby no household is worse-off in order to benefit others. In [263], Alam et al. first considered integrating P2P trading with DSM. Multi-objective optimisation and pareto optimality constraints were used to minimise costs for a microgrid of individual households, whilst also minimising the import from the grid. In [260], Alam et al. showed the cost savings associated with energy storage and renewable penetration rate scenarios do not always increase linearly, but rather decrease after a saturation point. In [263], only two households were considered, while the study in [260] was limited to 40 households with three different PV system and battery sizes. In [263], the evaluation was only performed over 8 one-hour periods while [260] considered a single 24-hour window.

Long et al. [275] determined the optimal capacity of DERs including solar PV and combined heat and power systems to balance supply and demand for local low-voltage networks in a P2P trading environment. Customers were clustered based on their load profiles and the optimal DER was determined to balance low-voltage networks.

Münsing et al. [271] found the optimal schedule for a mix of battery loads [269]. However, investigation of the influences of DER size, penetration rates, market signals or customer preference was not undertaken [269].

In [269], an optimisation model to maximise the cumulative economic benefits amongst a group of households with PV and battery systems under a P2P trading environment was considered. Limited previous research was identified to be focused towards the optimisa-

tion of operational decisions, such as when to export and store energy, and strong influence they have on energy costs [269]. The study aimed to assist stakeholders in establishing an assessment of the techno-economic trade-off of P2P. A large heterogeneous group of households participating in a P2P market was assessed, whereby trading and physical constraints were considered. Four groups of customers were included in the analysis consisting of PV only, battery only, no DER and a combination of both PV and battery DERs.

Reservation prices were considered for each prosumer or consumer as part of the energy bidding process, with the price including a margin that can be user adjustable, enabling the participant to sufficiently cover the investment cost (the analysis considered a consumer margin of 10%). With this mechanism, the market was expected to self-stabilise [269].

Sensitivity analyses were conducted on four parameters – P2P trader margin, size of participant PV systems, different FiT rates and PV market penetration rates. Local use-of-system (LUoS) network charges, as considered in [255] and discussed in Section 8.1.2, were assumed to be included in the aggregator margin and therefore effectively shared between trading peers as in [255]. Results showed that significant savings were possible through P2P. However, it was identified that prospective owners need to be aware of the highly sensitive impacts of PV penetration rates on savings from P2P trading to ensure that installation costs of DERs are justifiable. The results of this research highlight the value in optimal selecting system size based on market conditions such as trading mechanisms, penetration rate and cumulative energy profiles of participants. The research presented in this thesis aims to address this problem.

The research in [269] included a number of analysis exemptions and approximations. Battery depth of discharge and degradation were not considered in the levelised cost of storage for the battery. Load profiles were based on a single profile randomly scaled to represent a set of households. Only a single retail plan was considered, with some randomness introduced in pricing based on a normal distribution as opposed to actual retail rates. Finally, the levelised cost of electricity for solar PV was based on industry averages. However, as shown in Chapter 5, investment returns are customer specific and dependent on the temporal load profile to establish self-consumption and export potential. In this research, the above deficiencies are addressed as detailed further in Section 8.1.6.

The time frames investigated for P2P trading analysis vary significantly in literature – from hours or a few days [260, 263, 270–274, 276], to a few weeks [261, 269, 275] and to over one or two years [7, 255, 262, 275]. However, based on the literature review undertaken for the research presented in this thesis, no investigations have focused on the assessment of the full investment lifetime of DERs under a P2P trading environment.

Furthermore, the scale of participation previously investigated also varies widely. Only a few participants were considered in [262, 263, 270] while tens of participants were investigated in [7, 260, 268, 271–273, 275, 276]. Large-scale analyses such as those undertaken in [255, 269, 274] whereby hundreds of peers were modelled are less prevalent but necessary to establish the wider market impacts of P2P trading. This research aims to undertake a large-scale assessment of P2P participation in the Australian NEM.

8.1.2 P2P Market Designs

The policy of the European Union places end-users firmly in the middle of the transition to a low carbon society [253]. Removal of regulatory barriers and incentivising the establishment of local trading markets are considered to be necessary to transition the current electricity market to a prosumer-centred market [253, 261, 262]. Numerous market designs and mechanisms have been considered for P2P trading, with no consensus yet reached on the most efficient approach [261, 262]. In Australia, a number of studies have been undertaken to evaluate potential trading environments and market structures with consideration given to cost-reflective tariffs structures [256, 277, 278] and charges representative of the fractional network use of service to facilitate local trades [255, 257, 279]. However, valuing the contribution of DERs towards reduced network costs and lower carbon emissions is a complex undertaking. For example, local generation network credits incentivising local energy trading have been considered and rejected by regulators [280]. Cost-reflective tariffs structures are further discussed in Section 8.1.5.

Liu et al. [270] developed an energy sharing model based on a supply and demand ratio (SDR) to drive the internal pricing of a microgrid with P2P prosumers with installed PV systems. An aggregator was used to coordinate the energy sharing with common buy and sell pricing applied to all prosumers and consumers. To encourage increased energy sharing, demand response was used to adjust power consumption based on SDR indicators. For example, as SDR is inversely proportional to price, when the SDR ratio is low, buyers would aim to reduce power in order to reduce the buying price. Similarly, sellers would also want to reduce self-consumption to sell more energy at a higher price.

Zhou et al. [272], undertook an evaluation of P2P sharing mechanisms including SDR, mid-market rate (MMR) and bill sharing. The SDR mechanism developed by Liu et al. [270] was found to out-perform the other mechanisms. Evaluation indexes such as a value tapping, participant willingness and equality of cost, energy balance, power flatness and self-sufficiency were also considered.

Long et al. [273] undertook a similar assessment for bill sharing and MMR as in [272]. A third scheme referred to as an auction-based pricing strategy, similar to the methodology of [255, 269], was also investigated, whereby reservation prices were set for each consumer or prosumer defining the bid prices and offers. The final P2P trade price was defined by the auction clearing price, determined by the intersection of the supply and demand curves. A community of ten households, five with PV, were trialled in a case study.

Auction-based pricing was also investigated in [267, 281, 282]. Kang et al. [281] introduced a double auction mechanism for P2P trades amongst plug-in hybrid electric vehicles, whereby both the buyers and sellers bid to trade energy via an auctioneer, representing a P2P market trader or aggregator.

A review of various auction-theoretic and game-theoretic approaches for P2P trading is presented in [282] and includes a clear description of a double auction process. For each trading interval, consumers and prosumers bid their offers to participate in P2P trading. Consumers bid the maximum price at which they are willing to purchase P2P energy while the prosumers bid their minimum sale price for their installed DER. These bid prices are

referred to as the reservation prices [255, 269]. The highest consumer reservation price is allocated energy first followed by a merit-order dispatch of progressively lower bidders. The final allocated consumer reservation price defines the clearing price of the P2P auction for that trading interval. Consumers and prosumers that are unable to offer over or undercut the clearing price respectively are excluded from the P2P trading interval and instead exchange energy with other sources, e.g. electricity retailers.

Tushar et al. [267] apply a modified version of a Vickrey auction by integrating a Stackelberg game between the auctioneer and bidders to facilitate stored energy trades between residential units and facility controllers of apartment buildings. In a Vickrey auction, the clearing price is defined as the second highest reservation price amongst the participants selected to enter into the P2P trades, in this case the reservation price of the energy storage owner's. However, this would adversely impact owner revenue. Consequently, a Stackelberg game is used to strike a balance between the auction price, which is somewhere between the Vickrey price and the maximum owner bid price, and the amount of energy each owner is willing to trade.

Long et al. [274] investigated P2P energy sharing where only energy measurement at the point of common coupling with the main grid and a one-way communication path were required to minimise the energy costs of a community. Supply and demand management were handled by a proposed two-stage aggregated control methodology of distributed prosumer batteries within the community to minimise grid export and therefore maximise self-consumption within the community. Data from smart meters at each household were used to calculate the SDR for each time period. SDR was then used as the pricing mechanism to determine the P2P trading prices with an additional compensation price added for prosumer sales as a variant on the original formulation of [270].

Lüth et al. [262] considered alternative market designs to incentivise local energy trading with the aim of addressing the questions – what is the value of batteries towards P2P trades and what market features are required? Batteries installed at prosumer residences and a central community battery were both tested within a flexi-user market and pool hub market established for each battery configuration with the objective of minimising the community energy costs. Nine months of energy consumption data were applied to the analysis with the communities modelled consisting of just four representative houses. The P2P prices were set based on the willingness of the consumer to pay.

In [270], day-ahead markets were established for energy sharing models in a P2P network. As stated in [276], forward pricing is expected to become more important as microgrids and managed networks are more widely integrated. Morstyn et al. [276] further expanded the consideration of forward price markets with proposed bilateral real-time and day-ahead contract networks. A distributed price-adjustment process was established to find a set of an agreed network of contracts between prosumers, suppliers (similar to retailers or aggregators) and generators (i.e. traditional large-scale generation). The unwillingness to deviate from the agreed network of contracts ensures price stability.

A framework to integrate prosumers into day-ahead and intraday wholesale electricity markets is proposed in [261]. The research aimed to evaluate the value of P2P in day-ahead

and intraday markets and how battery systems contribute towards demand flexibility. In the first stage, the community commits to bidding into the day-ahead market based on the combined uncertainty of DERs and wholesale spot prices. In the second stage, intraday P2P trades are used to balance supply and demand. P2P prices are set between the FiT and grid day-ahead price and are assumed to be equal to the grid price less the transmission component of the network tariff, similar to the methodology of the virtual trial in [265].

The potential value of DERs is not believed to be adequately reflected under current market structures by Roy et al. [255]. The potential for DERs to reduce energy consumption amongst consumers and to enable the deferral of network augmentations are not considered to be adequately reflected under existing tariff structures and incentive schemes [255]. Within the context of the Australian NEM, P2P was proposed and investigated in [255] as a solution to better utilise DERs. The impacts on consumers, prosumers, retailers and the Distribution Network Service Provider (DNSP) were assessed.

Under the methodology established in [255], an aggregator is assumed to facilitate the transactions while peers share an LUoS charge, representing associated network costs for the levels of the network actually used to facilitate the energy exchange. The pricing mechanism assumed was based on the Australian wholesale market, relying on the revealed preferences of P2P participants to determine the traded quantity. The reservation prices at which buyers and sellers are willing to trade are revealed and used to establish the market clearing price and traded quantities.

In [255], three tests under P2P trading are investigated. The first test investigated the overall effect of P2P trading. A hypothetical group of 1000 customers (based on 3 years of data from 300 Ausgrid customers, half of which had PV systems installed) were modelled with a 15% solar PV penetration. Due to the low supply of solar, high P2P demand results in a large uplift to prosumer revenue due to higher P2P clearing prices compared to FiTs. Consumers were not found to materially benefit and would rely on the free issue of smart meters to participate. In Test 2, solar PV penetration rates were examined. With penetrations above 50%, investments in solar PV were found to be less under P2P than BAU. Under Test 3, aggregator margins up to 40% were found to have virtually no impact on the quantity of P2P trades due to the large price differential between retail tariffs and FiTs. However it was found that fewer consumer-only customers would participate. Beyond 40%, traded quantities began to drop.

8.1.3 International Trial P2P Projects

Numerous pilot projects and trials have been established investigating the operation and benefits of P2P energy trading. Zhang et al. [283] present a review of existing P2P trading projects identifying projects that focus purely on business models and others consisting of business models combined with technology aspects such as ICT and control. Sousa et al. [7] also provide a brief summary of market design specific projects along with projects considering the implementation and trading platform requirements for P2P energy transactions. In [7], two key business areas are noted as (i) P2P exchange of energy surplus

between local participants and (ii) enabling consumers to directly choose local DERs.

Piclo (formerly Open Utility) [284], based in the United Kingdom, enables local commercial consumers to purchase electricity from local small-scale renewables [265]. Under the structure, electricity meter data, generator pricing and consumer preferences are leveraged by a matching algorithm via an online platform [268] to rationalise demand and supply over half-hourly intervals [268, 283].

Vandebron [285] is an online platform in the Netherlands allowing small independent energy producers such as farmers with solar PV and wind turbines to sell energy to households [265]. Vandebron, similar to Good Energy via the Piclo platform [284], is a retailer encouraging consumer and prosumers to exchange energy [268]. Prosumers with surplus DER generation are incentivised to provide the energy to the Vandebron platform through lower consumption electricity rates [268].

Similar to Piclo and Vandebron, Powerpeers is another online platform enabling participants to trade energy services through a subscription fee [265]. The platform is backed by Vattenfall, the largest utility in the Nordic region.

The transmission system operator Tennet in the Netherlands and parts of Germany has undertaken two successful blockchain trial projects [286]. With blockchain development partner IBM, flexibility services in both energy and demand [265] were provided through Tesla electric vehicles and household batteries.

The Brooklyn Microgrid [287] is a local energy marketplace faciliated by LO3 Energy's online platform Exergy, enabling P2P transactions to be conducted autonomously in near real-time. Bilateral contracts between peers are established through a proprietary blockchain DLT whereby prosumers are able to auction surplus generation via an online platform and mobile app to consumers willing to purchase the energy [259].

SonnenCommunity is a community based project by battery manufacturer Sonnen whereby members store surplus energy, selling to other members when required at a low-price tariff defined by Sonnen [268]. German regulation prohibits the feed-in of DERs during periods of grid over supply [265]. Consequently, the SonnenCommunity manages supply and demand to share energy between participants via a virtual energy pool [288] with a zero net exchange of energy between consumers [265].

8.1.4 Trial P2P Projects in Australia

Given the research presented in this thesis is based on Australian electricity market considerations and assessed against Australian customers and locations, a review of P2P projects and trials conducted in Australia is presented in this section. Numerous projects have been undertaken in Australia either through private investment or under government grants provided through agencies such as ARENA. Many of the projects are still in progress and the results are not yet publicly available.

A virtual trial of P2P energy trading using a distributed ledger technology was assessed by AGL in 2017 with funding from ARENA [265]. With assistance provided by consultant partners MHC Consult and IBM, the project was split into two stages. The first stage established and assessed a virtual trading model while the second stage reviewed the

benefits and limitations of DLT technologies such as blockchain. Historical half-hourly data from AGL's customer base consisting of 85 consumer and 27 prosumer homes in Melbourne, Victoria were used for the Stage 1 assessment. A single summer weekday was selected to demonstrate the model and methodology. The trial assumed each participant was economically rational, thereby aiming to improve personal economic benefit. The benefits were modelled to be distributed fairly across the P2P participants in prosumer and consumer groups, proportional to their generation or consumption profiles. Bilateral contracts between peers were not investigated in the research but rather a central P2P administrator managing a P2P cost stack was assumed, consisting of:

- P2P export price (higher than the retailer feed-in tariff)
- Variable network charges (removal of partial network costs during P2P trading periods)
- P2P administration fees (assumed to be 1 c/kWh)
- Fixed network and retail daily charge fees (excluded from analysis as same charges are applied whether in P2P market or BAU market).

Three hypothetical scenarios were modelled assessing network price modifications, customer load profile changes and market competition effecting P2P market development. The first scenario focused solely on variable network charges through the assumed elimination of the transmission component, referred to in Australia as the transmission use-of-system (TUoS), as local DER generation does not require direct access to the transmission network. The second scenario assessed the influence of customer load shifting to better align with local DER profiles whilst also considering the elimination of TUoS. Finally, the third scenario considered the entrance of a low-cost P2P market entrant handling the transactions (with an administration charge of 2 c/kWh), shifting revenue away from the incumbent retailer during DER generation periods.

The virtual trial found P2P trading can, under specific conditions, provide financial benefit to both consumers and prosumers. Consumer preferences, for example local green energy from family or friends, were also postulated to drive further value. The study concluded that modifications to network prices based on location and time of generation enables the establishment of a P2P market. Using storage and DSM to shift load to local DERs was also found to unlock more P2P market value while a new low-cost P2P administration entrant gave the greatest benefit to customers (potentially supported by an existing registered retailer).

Stage 2 provided a technical assessment of DLT enabling P2P trading, with blockchain specifically investigated. It was noted that DLTs have issues when applied to high-frequency high-volume transactions, as storing all prosumer/consumer transactions would be cost-prohibitive in a full-scale market [265]. Consequently, a compromise was proposed to only store trading instructions and parameters from prosumers/consumers and a history of net aggregated volumes of trading positions between retailers and contracted prosumers/consumers.

In March 2018, LO3 Energy, with ARENA funding, commenced a microgrid feasibility study trial in the La Trobe Valley of Victoria Australia [289]. The trial aimed to assess the viability of a local electricity marketplace trading energy and demand response services amongst participants. The marketplace was facilitated by LO3 Energy's blockchain-based digital ledger platform Exergy [259] with participants including dairy farmers, residences, commercial and industrial customers.

The Enexa trial facilitated by LO3 Energy [259] aimed to introduce transactive energy in South Australia's Riverland, linking commercial customers with renewable energy sources and pricing. The project goal aimed to expand the regional boundaries and ultimately provide services to residential consumers.

Greensync, with ARENA funding, developed the decentralised energy exchange platform deX [290]. The market-based platform enables physical coordination and dispatch of DERs amongst market participants including homeowners, businesses, retailers and energy networks. The platform lists buyers and sellers, records agreements between participants whilst managing event handling and verifying contractual obligations. Functionality to build-in P2P transactions into deX is planned, however the developers remain technology agnostic regarding DLTs such as blockchain. A multitude of foundation partners including equipment manufacturers, consultants and research bodies provided input to help define the principles and establish the pilot marketplace. The pilot trial successfully demonstrated the ability to respond to dynamic, time-related and location-based prices. The deX platform is currently under commercial scale trials through Simply Energy's ARENA funded virtual power plant (VPP) in Adelaide, South Australia [291]. The VPP consists of Tesla Powerwall 2 batteries installed in 1,200 homes providing 6 MW of energy storage. An additional 2 MW of demand response capability facilitated by commercial businesses is also included in the VPP trial.

Power Ledger has developed a platform based on the Ethereum blockchain that enables "trustless, transparent and interoperable" energy trading [254]. The platform development consists of two blockchain layers. The first blockchain layer facilitates POWR tokens enabling Application Hosts, such as utilities or retailers, to have access to the platform and to generate Sparkz (the second token) to be used by the consumer base. The second layer issues Sparkz tokens purchased through fiat currencies against escrowed POWR tokens via Smart Bonds and used by P2P customers for energy trades [254].

With funding provided by the Smart Cities and Suburbs Program of the Australian Government, the RENeW Nexus project aims to undertake a city-wide demonstration of energy and water trading facilitated by Power Ledger's blockchain platform [292]. Around 40 residences across Fremantle, Western Australia are participating in the projet [292], while trading of energy from a 5 MW solar farm and a grid-scale community-owned battery system is also under investigation [293].

Other P2P trial projects undertaken by Power Ledger include the White Gum Valley project in Perth, Western Australia and the Greenwood Solutions project in Melbourne, Victoria, aim to facilitate energy trades from solar PV systems between residents in strata developments [294].

8.1.5 Cost-Reflective Tariff Structures

The current top-down market structure whereby energy has traditionally flowed from centralised generation down to consumers is no longer applicable. Under this structure, network charges do not account for bi-directional energy flows due to the presence of high DER penetration rates. Prosumers currently receive a FiT for exported surplus generation however FiTs are paid only against the energy portion of the tariff and do not adequately reward prosumers for the typically local consumption by nearby customers and subsequently the use of only the local distribution network [279]. Concurrently, retailers must pay the full network charge to DNSPs [279] which is subsequently passed on to local consumers. Furthermore, the energy component of the consumer bill must be paid against the retailer's whole electricity contract book, not the FiT paid to the nearby prosumer as the most likely source of energy generation [279]. Consequently, cost-reflective tariff structures have received renewed focus in recent research [21, 256, 277–279], accounting for actual volumetric energy and power demand as well as consideration of local network utilisation.

Network tariffs at the level of small consumers have traditionally been volumetric and fixed, with little variance across geographical regions [278]. The uptake of energy-intensive appliances such as air-conditioning systems [278], along with the augmentations required to integrate high-level PV market penetration, have required additional investment in network infrastructure to manage increased peak-hour demands. Rising electricity prices have placed pressure on households which have in turn responded through reduced consumption and the installation of DERs to manage retail price exposure. The resultant further reduction in network capacity factors exacerbates the disparity between the network cost of service provision and the time of energy consumption. Consequently, cost-reflective tariffs have been proposed whereby customers are informed and capable of responding to network tariff price signals based on the direct impact the customer induces on the network. Cost-reflective tariffs thus represent fairer prices with minimised cross-subsidies and tariffs signalling efficient investment in the network and DERs [277].

In Australia, reform is already underway for cost-reflective network tariffs [279]. In 2014, the Australian Energy Market Commission (AEMC) amended the National Electricity Rules with a network pricing objective [277] to reflect the efficient costs to the DNSP to provide electricity services to customers [295]. However, the rule was not prescriptive in how to design cost-reflective tariffs [278]. Additional modifications have be proposed to include a capacity or demand charge component [277, 278], however in 2017 only a few distributors such as SA Power Networks had introduced a demand tariff structure. In [278], cost-reflective tariff designs with demand charges are investigated. The correlation between existing cost-reflective charge structures and peak contribution from a group of over 3,800 customers was found to be poor. An adjusted demand charge structure was proposed to move the demand component from one based on the customer's monthly peak to a charge based on customer demand coincident with the network peak demand. The coincident demand model was shown to be better aligned with the network pricing objective of the Australian Energy Regulator (AER). More recently, numerous Australian DNSPs,

including Ausgrid, Endeavour Energy and Essential Energy have, as part of the 2019–24 regulatory submisison, each presented an updated tariff structure statement (TSS) to the AER [296] which included a demand or capacity charge in some form, providing a better representation of the efficient costs of network service delivery.

In parallel to network tariff cost-reflective reform, the utilisation of local networks only by DERs, as opposed to traditional centralised generation requiring the full use of transmission and distribution networks, has been considered for potential tariff structure changes.

The introduction of a local generation network credit (LGNC) has been considered in a number of countries, whereby additional time-varying credits are effectively added to the standard FiT based on local network utilisation [279]. Rutovitz et al. [258] consider local generation credits whereby DERs exporting to the grid are rewarded with a volumetric credit linked to the time-of-day export. The LGNC concept was submitted to the AEMC for consideration as a regulatory change [279, 280]. However, the proposal was rejected, with the determination finding that the introduction of an LGNC would provide insufficient incentive to invest in DERs. Contrary to the objectives of local network utilisation, the introduction of LGNCs was expected to lead to higher consumer prices [280].

In [279], LGNCs were investigated with a probabilistic approach proposed to assess the potential value associated with PV and energy efficient appliances. It was postulated that the rule change determination of the AEMC [280] failed to account for two considerations. Firstly, the combination of LGNCs and targeted TOU charges would enable short-term peak shaving (which can be implemented in parallel with the refinement of cost-reflective tariff design). Secondly, LGNCs would also lead to reduced network expenditure by encouraging generation at peak times (similar to the effect of current TOU pricing) [279].

The concept of an LGNC was extended to a local network charge (LNC) in [257] whereby the network component of the electricity bill is reduced in recognition of the partial use of the distribution network when generators and consumers are locally situated. Trials were conducted to assess local energy trading and the application of LNCs for commercial scale generators against trialled net-metered loads either co-located within the same facility or distributed across a number of sites. The LNC could be applied as a reduced network charge for the consumer or a credit to the local generator. The generator credit was considered in modelling due to the complications associated with maintaining records of local transactions for local consumption of local generation [21]. However, as previously discussed, this issue may be alleviated cost-effectively through the implementation of DLTs. The LRMC, as the standard measure for establishing network tariffs and representing the annual cost of providing one unit of additional capacity to the network [257], was used to calculate the LNC. The calculation was in two parts with a base value provided by the LRMC and an additional time-varying tariff component. The base value for the LNC at each level of the network includes only the LRMC for the network levels upstream.

The LNC tariff component was based on two methodologies. The first was a volumetric

method whereby the peak and off-peak annual hourly likelihood are used to establish the tariff. For example, if peak hours are 90% likely to occur in 600 hours of the year, then the LNC peak volumetric tariff component (in \$/kWh) is (LRMC $\times$ 90%)/600. Note that as LRMC is defined in \$/kW, in order to provide a time-based distribution of cost over a year, typical practice is to convert it to an effective kWh value by dividing it by 8,760 (the number of hours in a standard year).

The second method consisted of both volumetric and capacity components. The split between volume and capacity was based on mirroring network usage tariff structures [21]. For example, a DNSP calculated split of 76:24 would result in 24% of the LRMC assigned to the capacity component which is in turn calculated by determining the number of days per year a peak is expected to occur. Consequently, the capacity component is charged in units of \$/kW/day based on the LRMC.

In [21], it was found that the capacity payment, dependent on the minimum generator availability during a particular period, did not adequately incentivise as it did not reward fractional contribution during peak periods. Consequently, a targeted version of the volumetric method, whereby the DNSP determines a smaller number of peak hours per year with a high probability of occurrence, is used to establish the peak LNC, thereby providing transparency for a generator to maintain availability [21].

It is important to note that the trial in [257] investigated medium-scale cogeneration, solar and wind with installed capacity greater than 150 kW. In [21], it was recommended that LNCs should not be made available to non-dispatchable generation or generation under 10 kW. However, it was also conceded that the introduction of batteries may influence the recommendation in the future.

8.1.6 Research Objective for P2P Trading

Existing research including [261, 262, 268, 269] has shown the potential benefit a prosumer can receive through providing access to existing DER systems under a P2P trading market. However, Nguyen et al. [269] identified that prospective investors would benefit from prior consideration of market conditions and the penetration rates of participant DERs when sizing systems. Based on the literature review undertaken for this research, the optimal system sizing and orientation of DER systems to maximise savings at the individual consumer level has not previously been investigated for P2P trading applications.

In this research, a novel lifetime assessment of DERs consisting of solar PV and battery systems trading in a P2P market is undertaken, with the objective of assessing the influence of design optimisation on market participation. An expansive P2P market assessment based on real-world electricity consumption data from over 2,200 residential premises is conducted, an assessment which to the author's knowledge has not yet been undertaken in the context the Ausralian NEM at such a scale with actual metered data. The data, gathered during the SGSC project, are utilised to establish a hypothetical group of energy trading peers. Previously, solar PV penetration rates have been considered in [255, 269, 272] while P2P trader margins have been considered in [255, 269]. Similar considerations are proposed for this research with sensitivity analyses undertaken for various DER penetra-

tion rate scenarios, P2P participant margins, commercially available BESS types, retailer plans and the inclusion/exclusion of FiTs and P2P trading.

Existing research on P2P trading with energy storage systems have not typically modelled key factors effecting lifetime storage cost including battery degradation and physical limits such as a depth of discharge. In [262, 269], no consideration was given to degradation or depth of discharge. In [260, 261, 274], minimum charge levels were considered however battery degradation was not accounted for. In this research, battery degradation and the associated cost of degradation, maximum depth of discharge and charge/discharge efficiencies are uniquely accounted for based on manufacturer warranties and data sheets.

The P2P trading mechanism considered in this research is based on the auction-based bidding scheme of [255, 265, 269, 273] with consideration given to the minimum returns expected by P2P participants. Although the supply and demand ratio market mechanism has previously been shown to outperform other mechanisms [268], such a mechanism is only applicable to a community-based structure where the grid import and export prices are the same for all participants. As the objective of this research is to optimise the economic benefit of an individual customer, the P2P market structure resembles either the full P2P or at least the hybrid structure defined in [7]. The minimum sell and maximum buy prices are not homogeneous for all participants as each customer can sign up to different retailers or aim to recover DER investment costs dependent on their personal circumstances. Therefore an auction-based scheme is more relevant and modelled in this chapter. A variant on the SDR ratio is proposed to manage the partial success of P2P bidding when participant bids coincide with the determined clearing price.

Residential and small business premises typically do not have the knowledge or technical capability to participate in networks of contracts involving multiple-agents, or to facilitate the load forecasts necessary for more advanced forward and adjustments markets. Consequently, this research focuses on post-delivery settlement of energy transactions through the use of DLT, rather than optimally scheduling and bidding DERs into the P2P market. Bilateral contracts between consumers and retailers in the form of electricity retail plans, as per existing BAU practice, are assumed to provide the necessary balancing for all energy not sourced through the P2P market.

In this research, given the recent focus of the AER to consider the efficient costs of electricity delivery, the recently developed cost-reflective tariffs by Ausgrid are uniquely considered in the context of a P2P market. The tariffs, which include a demand component, are expected to evolve over the next decade, coinciding with a future electricity market with high DER penetration rate scenarios and active P2P trading.

Finally, LUoS network charges are considered in this research, similar to [255, 269] and the virtual trial of [265]. Due to the difficulties in establishing the exact cost of the local network portion used for local P2P trading, the high level assumption of [265] is assumed, whereby the TUoS component is excluded from the network tariff component of the electricity bill. In [257], the customer is solely responsible for the LUoS while in [269], the LUoS is included as part of the P2P trader margin with no further quantification of the charge component. In this research, the methodology of [255] is applied whereby

the LUoS is assumed to be shared between the prosumer and the consumer to encourage customer participation.

8.2 P2P Market Model

The P2P market model considered in this research is based on double auction schemes similar to those presented in [255, 267, 269, 281, 282]. Under such schemes, both the buyer and seller of energy bid to participate in a P2P market facilitated by a P2P trader or aggregator via provision of a reservation price and an associated energy quantity.

In this research, a modified version of the P2P trading scheme considered in [255, 269] is applied. Under the methodology established in [255, 269], an aggregator is assumed to facilitate transactions while peers share the LUoS charge, representing the associated network costs for the levels of the network used to facilitate the energy exchange. Sharing the LUoS charge encourages P2P participation by reducing the network component of the energy costs to the consumer. Figure 8.2, adapted from [269], graphically depicts the financial agreements between market participants.

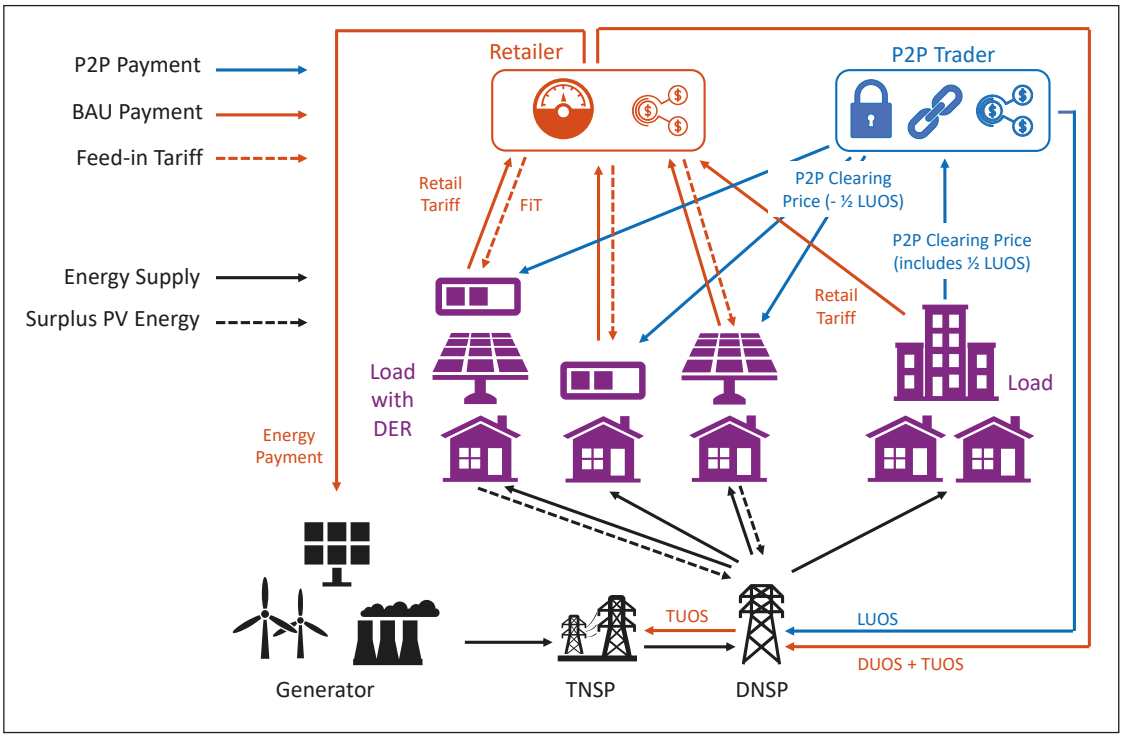

Figure 8.2: Block diagram of P2P energy supply and financial transactions adapted from Nguyen et al. [269]

Nguyen et al. [269] considered the LUoS to be included in the P2P trader margin. In this research, the LUoS charges are quantified and assumed to be equivalent to the Ausgrid distribution use-of-system (DUoS) charges under the TSS of the 2019-2024 regulatory period, detailed in Section 8.2.2. Furthermore, as trades of P2P energy within a single distribution network do not make use of the transmission network, TUoS charges are excluded from P2P trades in this research, as similarly considered in [21, 265]. The avoided

TUoS charges are quantified in this research based on the published estimates in the Ausgrid 2019–2024 TSS.

The P2P sale reservation prices $B_{pvsell,qdh}$ and $B_{BESSsell,qdh}$ for solar PV and BESS discharge respectively, in billing period q, day d and hour h, are defined as follows:

$$B_{pvsell,qdh} = \Big(T_{fit,qdh} + T_{luos,qdh}/2\Big)\,(1+\mu_{P2P})\,\big(1+\mu_T/2\big) \tag{8.1}$$

$$B_{BESSsell,qdh} = C_{degrad} + \Big(C_{c,qd(h-1)} + T_{luos,qdh}/2\Big)\,(1+\mu_{P2P})\,\big(1+\mu_T/2\big) \tag{8.2}$$

where $T_{fit,qdh}$, $T_{luos,qdh}$, μ_{P2P} and μ_T are the feed-in tariff from the electricity retailer, LUoS charge payable to the DNSP, the preferred sale margin of the P2P participant and the P2P trader margin respectively. In (8.2), the BESS sell bid is dependent on the effective battery degradation cost C_{degrad} associated with the discharge cycle and the cost of energy $C_{c,qd(h-1)}$ used to charge the battery up to the previous hour, $h-1$. Equations for C_{degrad} and $C_{c,qdh}$ are defined in Section 8.2.3.1.

The P2P buy reservation price is defined in (8.3) where $T_{tuos,qdh}$ is the TUoS charge payable for retailer purchased energy, which is no longer applicable to P2P energy trades.

$$B_{buy,qdh} = \frac{T_{ret,qdh} - T_{luos,qdh}/2 - T_{tuos,qdh}}{1+\mu_T/2} \tag{8.3}$$

Many reservation price bids submitted to the P2P trader can be expected to be equivalent due to the limited number of electricity retailers resulting in a limited number of retail [270] and feed-in tariffs.

In a P2P market, while the majority of successful bids remain unaffected, for final bidders where the bid price corresponds to the determined clearing price and energy, without appropriate handling, the energy balance between supply and demand can be violated. To ensure energy trade balances are not violated, the method of [269] is further modified by applying a supply and demand ratio based on the market mechanism defined in [270]. While the mechanism in [270] is used to dictate the P2P clearing for a P2P community, in this research, the supply and demand ratio is used to define the portion of energy shared between the final bidders, with the remainder of the energy requested or delivered is settled against the customer's retailer of choice. Definition of the supply and demand ratios, as well as a description of the P2P settlement process is provided in Section 8.2.1.

8.2.1 P2P Settlement

The pricing mechanism assumed in the auction strategy is based on the Australian wholesale market, relying on the revealed preferences of P2P participants to determine the traded quantity. The reservation prices at which buyers and sellers are willing to trade are revealed and used to establish the market clearing price and traded quantities. Under a double auction settlement scheme, P2P bids are settled based on merit order, with buy bids ordered from highest to lowest and sell bids from lowest to highest. The final sell reservation that is less than or equal to a buy reservation at an equivalent cumulative

energy level defines the clearing price of the trading interval. The market settlement steps are as follows:

(i) Calculate the import/export quantity for each customer.

(ii) Calculate the reservation price for the purchaser defined as the retail tariff less half the LUoS costs and half the P2P trader margin.

(iii) Calculate the reservation price for the seller defined as the retail tariff plus half the LUoS costs and half the P2P trader margin.

(iv) Create cumulative demand/supply tables with corresponding reservation prices.

(v) Find the intersection of the table entries, representing the clearing price and the electricity quantity traded.

The P2P settlement process can be described mathematically as follows. Consider J and K to be the number of unique buy and sell reservation prices arranged in merit order, where $x_{\rho,j}$ and $y_{\rho,k}$ represent the unique buy and sell prices, while $x_{\xi,j}$ and $y_{\xi,k}$ represent the corresponding cumulative bid energy for each $j \in \{1,\ldots,J\}$ and $k \in \{1,\ldots,K\}$. P2P settlement is achieved when, for $x_{\xi,j} > 0$ and $y_{\xi,k} > 0$, there exists a j and k, such that:

$$x_{\xi,j-1} < y_{\xi,k} \quad \text{and} \quad x_{\rho,j+1} < y_{\rho,k+1} \tag{8.4}$$

Should j and k be found, then the P2P clearing price is $T_{P2P,qdh} = y_{\rho,k}$ and the final buy bid successfully participating in the auction is $B_{BUY,qdh} = x_{\rho,j}$. For the determination of the energy cleared, consider the scenarios shown in Figure 8.3. In the first scenario of Figure 8.3(a), the P2P clearing price and energy quantity are $T_{P2P} = y_{\rho,k}$ and $E_{P2P} = y_{\xi,k}$ respectively. The final successful buy bid is $B_{BUY} = x_{\xi,j}$. Note that the cumulative energy of $x_{\xi,j}$ is greater than $E_{P2P} = y_{\xi,k}$, consequently only a portion of the buy bid position j is settled in the P2P market. In the case of Figure 8.3(b), the energy bid $y_{\xi,k}$ associated with the clearing price $T_{P2P} = y_{\rho,k}$, exceeds the energy bid $x_{\xi,j}$ associated with the final buy price $B_{BUY} = x_{\rho,j}$. Therefore only a portion of the energy in bid position k is sold in the P2P market. In Figure 8.3(c), the final successful buy and sell bid prices are equal. Consequently, the clearing price is $T_{P2P} = y_{\rho,k} = x_{\rho,j}$. Again only a portion of the final buy bid is settled in the P2P market. Finally in Figure 8.3(d), the final successful buy and sell bid energies are equal. Therefore, $E_{P2P} = x_{\xi,j} = y_{\xi,k}$ and under this scenario the entire energy quantity of the final buy and sell bids are settled in the P2P market.

Based on the examples shown in Fig 8.3, where j and k exist such that (8.4) is satisfied, the energy cleared in the P2P in billing period q, day d and hour h, is defined as:

$$E_{P2P,qdh} = \begin{cases} y_{\xi,k} & \text{if } x_{\xi,j} > y_{\xi,k} \\ x_{\xi,j} & \text{otherwise} \end{cases} \tag{8.5}$$

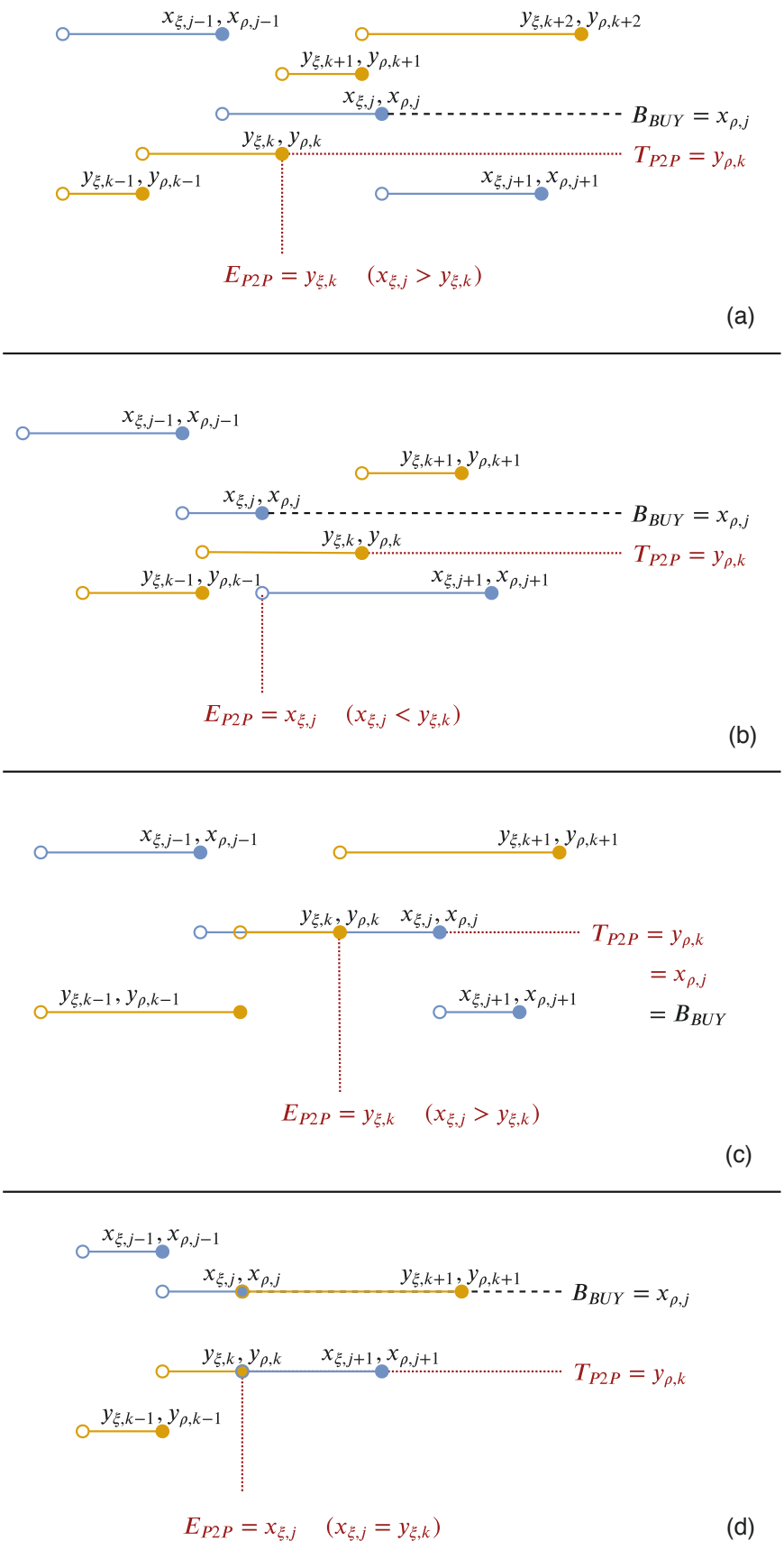

Figure 8.3: P2P energy supply demand settlement examples

The supply and demand ratio for final successful buy bids can be determined as follows:

$$R_{BUY,qdh} = \frac{E_{P2P,qdh} - x_{\xi,j-1}}{x_{\xi,j} - x_{\xi,j-1}} \tag{8.6}$$

The demand and supply ratio final successful sell bids is defined as:

$$R_{SELL,qdh} = \frac{E_{P2P,qdh} - y_{\xi,k-1}}{y_{\xi,k} - y_{\xi,k-1}} \tag{8.7}$$

To ensure a solution is found satisfying the condition (8.4), if it indeed exists, dummy values must be added in the first and last positions of the cumulative energy and price vectors. The starting and end positions for bidding vectors $\mathbf{x}_\xi = (x_{\xi,0}, \ldots, x_{\xi,J+1})$, $\mathbf{x}_\rho = (x_{\rho,0}, \ldots, x_{\rho,J+1})$, $\mathbf{y}_\xi = (y_{\xi,0}, \ldots, y_{\xi,K+1})$, $\mathbf{y}_\rho = (y_{\rho,0}, \ldots, y_{\rho,K+1})$ respectively are as follows:

$$\begin{array}{cccc} x_{\xi,0} = 0 & x_{\rho,0} = x_{\rho,1} & y_{\xi,0} = 0 & y_{\rho,0} = 0 \\ x_{\xi,J+1} = x_{\xi,J} & x_{\rho,J+1} = 0 & y_{\xi,K+1} = y_{\xi,K} & y_{\rho,K+1} = y_{\rho,K} \end{array} \tag{8.8}$$

For each P2P participant with buy and sell bids $B_{buy,qdh}$ and $B_{sell,qdh}$ respectively, the supply and demand ratio $R_{buy,qdh}$ (or demand and supply ratio $R_{sell,qdh}$ in the case of sell bids), can be defined as follows:

$$R_{buy,qdh} = \begin{cases} R_{BUY,qdh} & \text{if } B_{buy,qdh} = B_{BUY,qdh} \\ 1 & \text{if } B_{buy,qdh} > B_{BUY,qdh} \\ 0 & \text{otherwise} \end{cases} \tag{8.9}$$

$$R_{sell,qdh} = \begin{cases} R_{SELL,qdh} & \text{if } B_{sell,qdh} = T_{P2P,qdh} \\ 1 & \text{if } B_{sell,qdh} < T_{P2P,qdh} \\ 0 & \text{otherwise} \end{cases} \tag{8.10}$$

Note that the sell bid $B_{sell,qdh}$ is equal to either $B_{pvsell,qdh}$ or $B_{BESSsell,qdh}$, depending on success of each.

Equations (8.9) and (8.10) are used in the objective function of the optimisation problem defined in Section 8.4, to reflect the amount of energy successfully traded in the P2P market and settled against the retailer for a particular participant within a trading hour.

8.2.2 Distribution Network Tariff Structure

DNSPs are required to submit a TSS to the AER for review and determination prior to entering the next regulatory period, currently set every five years. The tariff structures of Ausgrid, as the DNSP applicable to the load data from the SGSC project, are assumed in this research.

In response to rule changes by the AEMC [277] directing DNSPs to reflect the efficient costs of network service delivery in tariff proposals, Ausgrid along with other distributors within the National Electricity Market are required to introduce cost-reflective pricing structures. The final proposal for the 2019–2024 regulatory period submitted by Ausgrid to the AER [297] included the introduction of demand tariffs for residential consumers for the first time [298]. Two primary structures were proposed:

- TOU demand tariff – Including TOU energy rates reflecting similar to traditional TOU tariff structures and a new daily demand charge component based on seasonal peak kW demand.
- Demand tariff – Including flat (low) energy rates and a large demand charge component.

In this research, the latest available TSS developed by Ausgrid [298–301], including TUoS and DUoS components forming an overall network use-of-system (NUoS) charge, is applied to the subsequently presented analysis, with each of the two tariff structures considered under particular scenarios. A summary of the Ausgrid network tariffs assumed is provided in Appendix A Table A.6.

8.2.3 Energy Flow Models

While the BESS energy flow model equations defined in Chapter 6 are largely still applicable under a P2P trading market, slight modifications to the original models are required, details for which are provided in this section. Previously, four operation modes were considered in Section 6.1.1, based around off-peak, shoulder and peak retail tariff periods. Under a P2P trading environment, the operation of the BESS, either charging or discharging, is based around the price signals associated with the P2P market. Therefore, the following amended modes of operation are considered:

- **Mode A:** Off-peak charging with discharging in shoulder and peak periods based on settlement against a sell reservation price.
- **Mode B:** Charging only via solar PV, discharging any time based on settlement against a buy reservation price.

The charge control operators defined in Section 6.1.1 are revised and simplified to the following parameters:

$$P_{d,qdh} = \begin{cases} 0 & \text{if } h \in \{\text{off-peak hours}\} \text{ and in Mode A} \\ 1 & \text{otherwise} \end{cases} \tag{8.11}$$

$$P_{c,qdh} = \begin{cases} 1 & \text{if } h \in \{\text{off-peak hours}\} \text{ and in Mode A} \\ 0 & \text{otherwise} \end{cases} \tag{8.12}$$

where P_c is the control signal for permission to charge and P_d is the control signal for permission to discharge. With the addition of the charge and discharge permission control signals, (6.5)–(6.7) defined in Chapter 6 are adjusted to (8.13)–(8.15) for BESS charging from PV, BESS charging from the grid (settled against the retailer or in the P2P market) and BESS discharging energies respectively.

$$E_{bpv,qdh} = \max\left\{\min\left[C_{\max,qdh} - C_{qdh}, \left(E_{pv,qdh} - E_{load,qdh}\right)(1-F), R_{\max}(1-F)\right], 0\right\} \tag{8.13}$$

$$E_{bg,qdh} = \max\left\{\min\left[C_{\max,qdh} - C_{qdh}, R_{\max}(1-F)\right] P_{c,qdh} - E_{bpv,qdh}, 0\right\} \tag{8.14}$$

$$E_{bd,qdh} = \max\left\{\min\left[C_{qdh} - C_{\max,qdh}(1-\delta), \frac{E_{load,qdh} - E_{pv,qdh}}{1-F}, R_{\max}\right] \times P_{d,qdh}, 0\right\} \tag{8.15}$$

The total energy loss term $E_{bloss,qdh}$ from (6.8) remains unchanged, repeated as (8.16) for convenience, along with the individual charge and discharge loss terms described in (8.17)–(8.19).

$$E_{bloss,qdh} = E_{bpvloss,qdh} + E_{bgloss,qdh} + E_{bdloss,qdh} \tag{8.16}$$

$$E_{bpvloss,qdh} = \max\left[\min\left(\frac{C_{\max,qdh} - C_{qdh}}{1-F}, E_{pv,qdh} - E_{load,qdh}, R_{\max}\right), 0\right] F \tag{8.17}$$

$$E_{bgloss,qdh} = \max\left[\min\left(\frac{C_{\max,qdh} - C_{qdh}}{1-F}, R_{\max}\right) P_{c,qdh} - \frac{E_{bpv,qdh}}{1-F}, 0\right] F \tag{8.18}$$

$$E_{bdloss,qdh} = E_{bd,qdh} F \tag{8.19}$$

where $E_{bpvloss,qdh}$, $E_{bgloss,qdh}$ and $E_{bdloss,qdh}$ are the losses during PV charging, grid charging and discharging respectively.

The PV AC generated energy $E_{pv,ac}$ for each hour period is calculated through the updated model of (5.27) presented in Section 5.6. The efficiency factors assumed in this chapter are identical to those considered in Section 5.6 with the exception of inverter efficiency η_{inv} which is assumed to be 96% for both PV and battery inverters where a particular BESS product does not come with an in-built inverter.

8.2.3.1 P2P Energy Bids

Additional energy terms associated with the P2P buy and sell bids are defined as follows:

$$E_{pvbid,qdh} = \max\left(E_{pv,qdh} - E_{load,qdh} - E_{bpv,qdh} - E_{bpvloss,qdh}, 0\right) \tag{8.20}$$

$$E_{bdbid,qdh} = \max\left\{\min\left[R_{\max} - E_{bd,qdh}, C_{qdh} - E_{bd,qdh} - C_{\max,qdh}\left(1-\delta\right)\right], 0\right\} \times P_{d,qdh}(1-F) \tag{8.21}$$

$$E_{buybid,qdh} = \max\left(E_{load,qdh} - E_{pv,qdh} + E_{bpv,qdh} + E_{bloss,qdh}, 0\right) \tag{8.22}$$

where $E_{pvbid,qdh}$ is the PV sell energy bid to the P2P trader associated with the previously defined $B_{pvsell,qdh}$ price, $E_{bdbid,qdh}$ is the BESS sell bid corresponding with a $B_{BESSsell,qdh}$ price and $E_{buybid,qdh}$ is the buy energy bid with the associated price $B_{buy,qdh}$. It should be noted that the BESS sell bid must account for battery energy loss, hence (8.21) is representative of the energy available at the output of the battery after losses. The additional loss term $E_{bdbidloss,qdh}$, defined in (8.23), is applicable should the BESS discharge bid be successful.

$$E_{bdbidloss,qdh} = \max\left\{\min\left[R_{\max} - E_{bd,qdh}, C_{qdh} - E_{bd,qdh} - C_{\max,qdh}\left(1-\delta\right)\right], 0\right\} \times P_{d,qdh}F \tag{8.23}$$

Following a successful bid, the total energy discharge (8.15) requires an update to reflect the P2P traded energy. Consequently, additional terms $E_{bdbid,qdh}$ and $E_{bdbidloss,qdh}$ must be added to (8.15), becoming (8.24). Note that the demand and supply ratio $R_{sell,qdh}$ is included in (8.24) to reflect the success of the P2P sell bid.

$$E_{bd,qdh} = \max\left\{\min\left[C_{qdh} - C_{\max,qdh}(1-\delta), \frac{E_{load,qdh} - E_{pv,qdh}}{1-F}, R_{\max}\right] \times P_{d,qdh}, 0\right\} + \left(E_{bdbid,qdh} + E_{bdbidloss,qdh}\right) R_{sell,qdh} \tag{8.24}$$

As previously identified in (8.2), the reservation price associated with BESS discharge bids is dependent of the cost to charge the BESS and the effective degradation cost associated with the discharge cycle. The average effective electricity tariff $T_{c,qdh}$ to charge the battery over the lifetime of the system is defined as:

$$T_{c,qdh} = \frac{C_{c,qdh}}{E_{through,qdh}} \tag{8.25}$$

where $C_{c,qdh}$ is the charge cost, $E_{through,qdh}$ is the cumulative energy throughput experienced by the battery up to period q, day d and hour h. $E_{through,qdh}$ and $C_{c,qdh}$ are defined in (8.26) and (8.27).

$$E_{through,qdh} = E_{through,qd(h-1)} + P_{c,qd(h-1)}\left(E_{bg,qd(h-1)} + E_{bgloss,qd(h-1)}\right) + E_{bpv,qd(h-1)} + E_{bpvloss,qd(h-1)} \tag{8.26}$$

$$C_{c,qdh} = T_{c,qd(h-1)}E_{through,qd(h-1)} + P_{c,qd(h-1)}\Big[T_{P2P,qd(h-1)}\left(1+\mu_T/2\right)R_{buy,qd(h-1)} + T_{ret,qd(h-1)}\left(1-R_{buy,qd(h-1)}\right)\Big]\left(E_{bg,qd(h-1)}+E_{bgloss,qd(h-1)}\right) + T_{fit,qd(h-1)}\left(E_{bpv,qd(h-1)}+E_{bpvloss,qd(h-1)}\right) \tag{8.27}$$

In (8.27), the total charge cost $C_{c,qdh}$ at hour h is dependent on the historical cost up to the previous hour period $h-1$, represented by the first addition term $T_{c,qd(h-1)}\times E_{through,qd(h-1)}$ and the cost of charge in the $h-1$ period. Consequently, the proportion of the energy bought from the P2P market and the retailer must be accounted for (represented by the middle addition term). Finally, where the battery is charged either partially or fully by the PV system, the forfeited FiT must be accounted for as the revenue stream is foregone in order to charge the battery for potential P2P sale in subsequent hours. This cost is accounted for in the final major addition term $T_{fit,qd(h-1)}(E_{bpv,qd(h-1)}+E_{bpvloss,qd(h-1)})$.

Equation (8.2) also includes a BESS degradation cost C_{degrad}, which is defined below as:

$$C_{degrad} = \frac{S_b}{E_{EOL}} \tag{8.28}$$

where S_b is the BESS cost previously defined in (6.14) and E_{EOL} is the total energy throughput of the battery before reaching end-of-life. Each charge/discharge cycle is assumed to reduce the maximum capacity of the BESS linearly with a battery degradation rate of ζ_{batt} defined previously in (6.1). The resulting lifetime degradation can be represented by an arithmetic series, the summation of which is represented by (8.29).

$$E_{EOL} = \frac{Y_{EOL}}{2\left[2C_{\max 0}\delta - \left(Y_{EOL}-1\right)\zeta_{batt}\right]} \tag{8.29}$$

where Y_{EOL} is the BESS cycle life, δ is depth of discharge and $C_{\max 0}$ is the initial maximum capacity.

8.2.4 DER Penetration Scenarios

In this research, the influence of DER penetration rates on the optimal DER system design is investigated. Three different DER penetration scenarios amongst P2P market participants are considered as follows:

1. 100% have solar PV and a BESS by year 5 and year 10 respectively
2. 100% have solar PV and 50% have a BESS by year 10 respectively with a continued linear uptake of BESSs until year 20.
3. 100% have solar PV and 50% have a BESS by year 20.

It is assumed that initially 50% and 10% of P2P market participants have PV and a BESS respectively. This assumption is justified given the widespread adoption of solar PV

in Australia and the increased likelihood of DER owners, as energy conscience consumers, to participate in a P2P market. Residential BESSs are in their relative infancy and consequently a far lower penetration percentage of 10% is assumed. While the initial BESS assumption is higher than the existing penetration rate in Australia in 2019, an increased appetite for BESS owners to participate in a P2P market, compared to other electricity consumers without DERs, is considered to be reasonable.

The DER uptake at the start of each simulation year over the 20-year P2P market horizon modelled in this research is assumed to follow a linear trajectory from the initial starting penetration percentages. A graphical representation of the three DER penetration scenarios is shown in Figure 8.4.

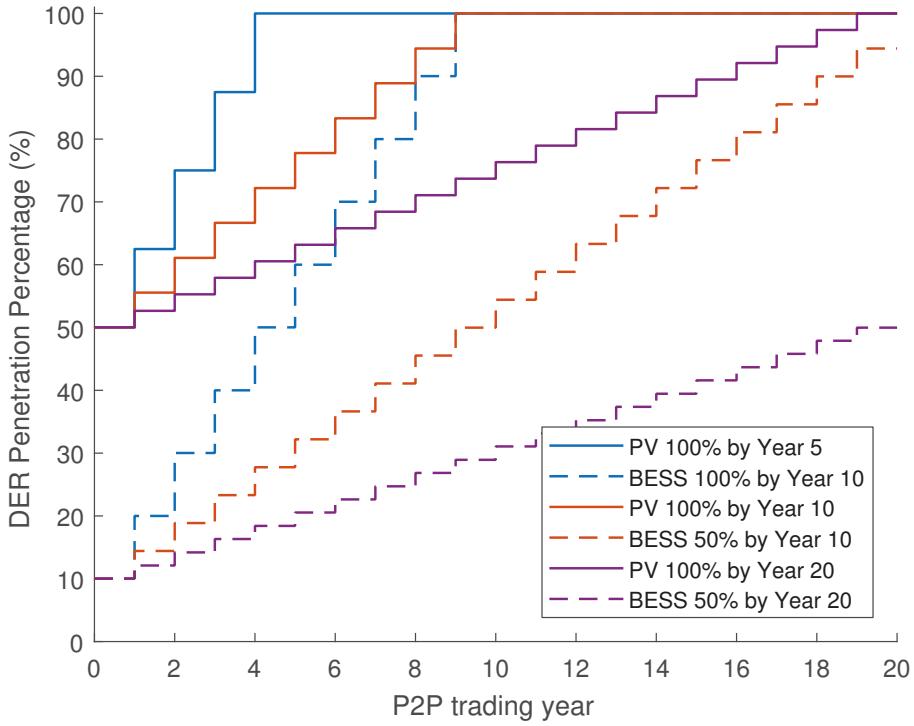

Figure 8.4: P2P market participant DER penetration rate scenarios

8.2.5 Weather Models

The new National BRL model for satellite-based data measurement developed in Chapter 4 was used, given the supporting statistical assessment presented in the chapter. Typical meteorological year data sets were developed for irradiation and temperature according to the methodology defined in Section 6.3.3.4.

8.2.5.1 Solar Irradiation Model

The new National BRL with BoM variability adjustment was applied based on the superior performance documented in Chapter 4 for satellite-based data measurements. The BRL model parameters defined in Table 8.1 were applied to the TMY irradiation data to determine the diffuse fraction. Equations (3.6) and (3.7) were then used to determine the direct irradiation component.

Table 8.1: BRL model parameters for satellite-based measurements

Model	β_0 (constant)	β_1 (k_T)	β_2 (AST)	β_3 (α)	β_4 (K_T)	β_5 (υ)
National BoM	-7.108	9.598	0.01416	-0.00743	2.813	-0.343

8.2.5.2 Temperature Model

Following the TMY data development process of Figure 6.3, the hourly temperature model of de Wit [242] as defined in Section 7.1, was applied to estimate hourly temperatures from the maximum and minimum daily temperature data.

8.2.6 Input Data

To simulate a large-scale P2P trading pool, representative load data for potential P2P participants were established through interrogating half-hourly smart meter data from 7,694 customers in the Ausgrid network acquired during the SGSC project. Section 8.3 summarises the data processing and customer selection methodology.

To represent the climatological variability across the Ausgrid network, ten different BoM weather stations capturing daily maximum and minimum temperature data were selected, summarised in Table 8.2, providing wide geographical coverage. Irradiation data corresponding to the coordinates of the weather stations were extracted from the AREMI database.

Table 8.2: Weather station data included in P2P trading model

Station Name	BoM Station ID	Latitude (°)	Longitude (°)	Elevation (m)	Year Open
Williamtown RAAF	61078	-32.79	151.84	8	1942
Paterson (Tocal AWS)	61250	-32.63	151.59	30	1967
Cessnock Airport AWS	61260	-32.79	151.34	61	1968
Scone Airport AWS	61363	-32.03	150.83	221	1988
Norah Head AWS	61366	-33.28	151.58	19	1989
Mangrove Mountain AWS	61375	-33.29	151.21	305	1994
Newcastle University	61390	-32.89	151.71	21	1998
Terry Hills AWS	66059	-33.69	151.23	199	2004
Sydney (Observatory Hill)	66062	-33.86	151.21	39	1858
Parramatta North (Masons Drive)	66124	-33.79	151.02	55	1965

Ten TOU retail plans available in 2019 were considered, including plans from the largest three retailers AGL, EnergyAustralia and Origin Energy within the Ausgrid network, to provide a representation of the retail plans servicing the majority of Ausgrid customers. The distribution network tariff structures considered in this chapter, as published in Ausgrid's 2019–2024 TSS and described in Section 8.2.2, were applied through an adjustment of the 2019 retail plans. The prevailing 2019 network tariffs were first removed from the peak, shoulder and off-peak energy rates and the proposed tariff structure for the next regulatory period added to the adjusted rates. Where a particular plan included a discount factor, the discount factor was then applied, along with the 10% Goods and Services Tax (GST) applicable in Australia. The resultant revised tariffs for each of

the electricity retailers considered in this research are provided in Appendix A Table A.7 against the two Ausgrid demand tariff forms 'Demand' and 'TOU Demand'.

The range of battery models considered in this research was extended from the Enphase AC Battery and the Tesla Powerwall 2 investigated in Chapter 6, to include an additional seven batteries available in 2019. Appendix D Table D.3 provides a summary of the BESS characteristics including parameters C_{MAX}, $R_{\max}$, C_{EOL}, Y_{EOL}, D, η_{batt}, C_{degrad} and U_b as well as battery, inverter and installation cost assumptions.

PV systems were modelled based on the Trina Solar TSM-300PD06H module characteristics summarised in Appendix C Table C.4.

PV system prices were based on the recent price guidance published by Solar Choice, an Australian based solar quote comparison provider [302]. Average monthly system costs from January 2018 until February 2019 were calculated based on published monthly 'median' and 'high' values. Table 8.3 provides a summary of the per unit system cost for various system sizes. The 'median' values were assumed for analysis presented in this chapter.

Table 8.3: Average residential solar PV system prices from Jan 2018 to Feb 2019. Source: Solar Choice [302]

	Size (kW)						
	1.5	2	3	4	5	7	10
Average 'Median' PV cost ($/W)	2.29	2.11	1.79	1.64	1.53	1.61	1.70
Average 'High' PV cost ($/W)	2.94	2.80	2.39	2.17	2.02	2.07	2.20

8.3 P2P Market Simulation

A subset of the SGSC customer database, characterised as load-only customers with no gross or net metered solar PV or any controlled loads, was extracted and filtered to ensure at least one full year of data were available. The program to roll-out smart meters to the SGSC participants was conducted over a number of months. As a result, the time ranges of the available customer data were not temporally coincident, with only partial years available for some customers. Consequently, for the purposes of this research and the development of a P2P market simulation, customers with at least the full 2013 calendar year of data were selected. Following this filtering process, the pool of available customers was reduced from 7,694 to 2,305. Where additional months of data were available for the selected customers, a representative load year was developed, similar to the development of the TMY weather data sets described in Section 8.2.5.

The process to construct a pool of participant customers to simulate a P2P market is outlined in the flow chart of Figure 8.5. Weather data for each customer are randomly assigned from the database of ten locations within the area covered by the SGSC project as defined in Section 8.2.6. To establish the P2P pool of participants, PV and BESS systems, the year of installation and an electricity retail plan are randomly assigned to each customer, based on the DER penetration percentage scenario defined in Section 8.2.4 assumed in the simulation. For certain P2P simulation cases, as defined later in this

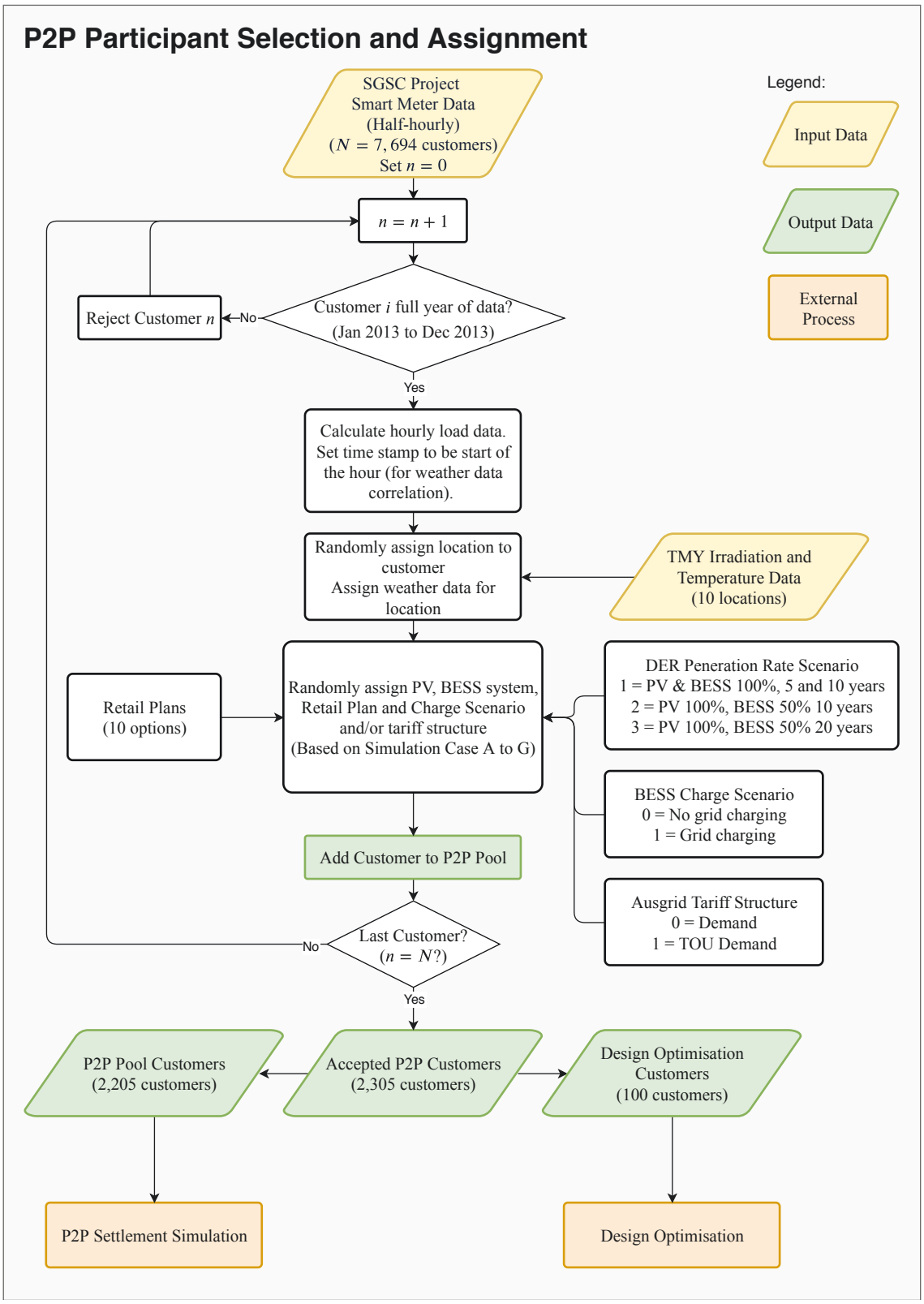

Figure 8.5: P2P participant selection process flow chart

section, the network tariff structure (defined in Section 8.2.2) and BESS charging mode (either Mode A or Mode B as defined in Section 8.2.3) are also randomly assigned.

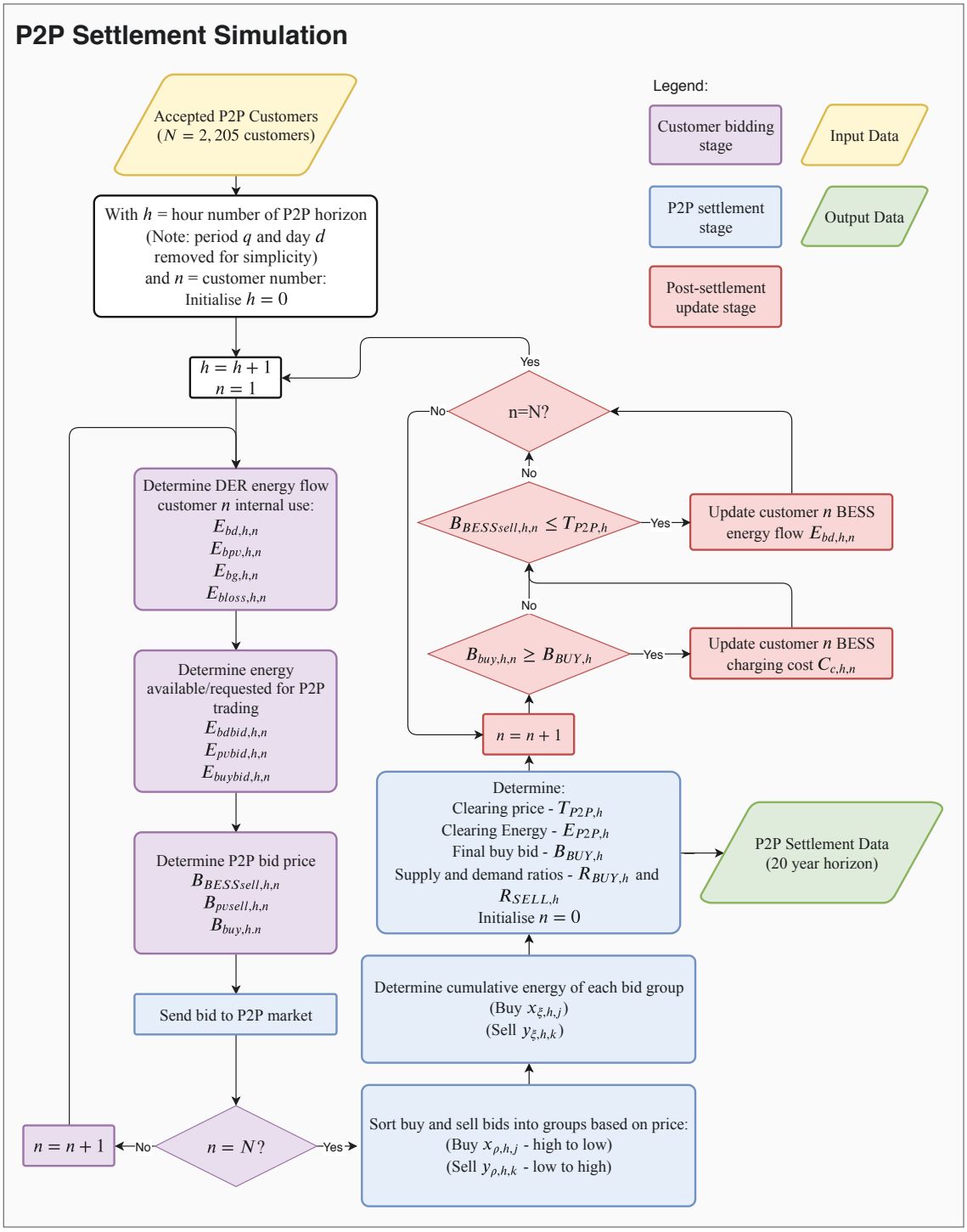

Figure 8.6: P2P market settlement flow chart

The PV size, tilt and azimuth are sampled from normal distributions with means (and standard deviations) of 4.5 kW (1.2 kW), 15° (5°) and 0° (20°) respectively. Note that the large standard deviation of azimuth is to capture the fact that many roof surfaces don't face north; in fact many PV units are installed on the west (90°) and east (-90°) surfaces due to space constraints. The maximum and minimum sizes of the PV systems

are limited to 10.2 kW and 2.1 kW respectively to ensure realistic sizes were modelled. The BESS and retail plan selected for each customer is sampled from a uniform distribution consisting of the nine BESS types and ten retail plans detailed in Appendix D Table D.3 and Appendix A Table A.7 respectively.

Following the completion of the customer selection and DER assignment process detailed in Figure 8.5, the pool of 2,205 P2P participants is passed into the P2P settlement simulation detailed in the flow chart of Figure 8.6. For the purpose of explanation simplification, the billing period q and day d terms are removed from subscript notation in this section.

In the 'Customer Bidding' stage, energy flow values are calculated for customer n, starting at hour $h = 1$. The desired P2P energy trades, $E_{bdbid,h}$, $E_{pvbid,h}$ and$E_{buybid,h}$ are determined, based on the DER surplus energy available or the energy supply deficiency. The P2P reservation prices associated with the energy bids are then calculated prior to sending the bid to the P2P trader. The process is repeated for each customer.

After the bids are determined for each customer in hour $h = 1$, the 'P2P Market Settlement' stage solves the supply and demand problem by sorting the buy and sell bids in merit order and identifying the intersection point as detailed in Section 8.2.1. After the P2P settlement conditions are established, the P2P settlement data, including clearing price $T_{P2P,h}$, clearing energy $E_{P2P,h}$, final buy bid $B_{BUY,h}$ and supply and demand ratios $R_{BUY,h}$ and $R_{SELL,h}$ are tabulated in a lookup table to be used as an input in the P2P trading design optimisation problem investigated in this chapter, as detailed in Section 8.4.

Following P2P market settlement, the success or failure of the bids is determined for each customer n in the 'Post-settlement Update' stage before proceeding to the $h+1$ hour where the process is repeated for all hours in the 20-year simulation horizon.

To facilitate a sensitivity analysis, numerous P2P market cases were simulated. Table 8.4 presents a summary of each P2P market simulation and the parameter values featured in each case. The impact of DER penetration rate scenarios is simulated through cases A, B and C while an increased P2P participant profit margin of 30% is simulated in case D. The influence of FiTs on P2P trading prices and energy quantities is investigated through case E where a FiT is no longer assumed to exist. Case F simulates electricity price increases returning to be in-line with the annual inflation rate, assumed to be 2.5%. Finally cases G and H investigate the influence of BESS price reductions on P2P trading. In addition to the input parameter values detailed in Table 8.4, the following additional inputs were considered across also eight market cases simulated:

- P2P trader margin u_T =20%
- BESS mode randomly assigned to be either A or B
- Battery types randomly assigned from the nine options detailed in Appendix D Table D.3
- Retail electricity plan randomly assigned from the ten options detailed in Appendix A Table A.7

- Ausgrid network tariff structure randomly assigned from the two options detailed in Appendix A Table A.6

Table 8.4: P2P market simulation cases

Case	DER Penetration Rate Scenario	P2P Sell Profit Margin (μ_{P2P})	Battery Cost	FiT	Nominal Electricity Cost Increase Rate
A	1	10%	100%	On	4.5%
B	2	10%	100%	On	4.5%
C	3	10%	100%	On	4.5%
D	2	30%	100%	On	4.5%
E	2	10%	100%	Off	4.5%
F	2	10%	100%	On	2.5% (inflation)
G	2	10%	70%	On	4.5%
H	2	10%	50%	On	4.5%

8.4 P2P Trading Optimisation Problem

The objective of the optimisation problem considered in this chapter is similar to the objectives previously considered in Chapters 5 and 6 – maximise electricity cost savings through the introduction of DERs against a known lowest cost retail electricity plan. The objective function (8.30) is therefore largely unchanged from the one considered in Chapter 6 with the exception of a subscript notation change from $C_{pvbatt,q}$ to $C_{der,q}$, representing the non-discounted lifetime cost of electricity with a DER system. The notation change is introduced to maintain consistency with the phraseology used in this chapter.

8.4.1 Problem Definition

As undertaken in the previous chapters, hourly evaluations of the energy flows are conducted for each hour h in day d and billing period q. Maximising the net benefit over all billing periods Q in the lifetime of the system under a P2P market trading environment is the objective of the optimisation problem defined as follows:

Given:

(i) Annual inflation of $r_{inf} = 2.5\%$

(ii) Maximum number of PV modules ($Z_{\max} = 34$)

(iii) Monthly billing frequency

(iv) A nominal annual discount rate of $r_{nom} = 6\%$, corresponding to a monthly real effective rate of $r_d = 0.28\%$

(v) Nominal annual electricity price growth of 4.5%, corresponding to a monthly real effective rate of $r_e = 0.16\%$

(vi) PV system lifespan of 20 years (which is considered to be conservative)

Find: Tilt angle β, azimuth angle γ, number of PV panels Z and number of batteries X

Objective:

$$\max_{\beta,\gamma,Z,X} NPV = \sum_{q=1}^{Q} \frac{\left(C_{base,q} - C_{der,q}\right)(1+r_e)^{q-1}}{(1+r_d)^q} - \sum_{q=1}^{Q} \frac{W_q}{(1+r_d)^q} - \left(S_{pv} + S_b\right) \tag{8.30}$$

Subject to:

$$0 \leq \beta \leq 180 \quad \text{for } \beta \in \mathbb{R} \tag{8.31a}$$

$$-180 < \gamma \leq 180 \quad \text{for } \gamma \in \mathbb{R} \tag{8.31b}$$

$$0 \leq Z \leq Z_{\max} \quad \text{for } Z \in \mathbb{Z}^+ \tag{8.31c}$$

$$0 \leq X \leq X_{\max} \quad \text{for } X \in \mathbb{Z}^+ \tag{8.31d}$$

In (8.30), the maintenance costs W_q are as previously defined in (6.15) while the BESS system cost S_b and the PV system cost S_{pv} are defined in Table D.3 lines 6–8 and Table 8.3 line 1 respectively. The terms $C_{base,q}$ and $C_{der,q}$ are defined as:

$$C_{base,q} = \sum_{d=1}^{D_q} \left(\sum_{h=1}^{24} T_{ret0,qdh} E_{load,qdh} + T_{DC0,qd} P_{\max,qd} + T_{sc0,qd} \right) \tag{8.32}$$

$$\begin{aligned} C_{der,q} = \sum_{d=1}^{D_q} \Bigg(\sum_{h=1}^{24} \Bigg\{ & \max\left(0, E_{bal,qdh}\right) \left[T_{ret,qdh}\left(1 - R_{buy,qdh}\right) + T_{P2P,qdh} R_{buy,qdh}\left(1 + \mu_T/2\right) \right] \\ & - \max\left(0, -E_{bal,qdh}\right) \left[T_{fit,qdh}\left(1 - R_{sell,qdh}\right) + T_{P2P,qdh} R_{sell,qdh} \right] \\ & + \max\left(0, -E_{bal,qdh}\right) \left(\frac{T_{P2P,qdh}\mu_T/2}{1+\mu_T/2} + \frac{T_{luos,qdh}}{2} \right) R_{sell,qdh} \Bigg\} \\ & + T_{DC,qd} P_{\max,der,qd} + T_{sc,qd} \Bigg) \end{aligned} \tag{8.33}$$

Equations (8.32) and (8.33) feature the demand charge terms ($T_{DC0,qd}P_{\max,qd}$) and ($T_{DC,qd}P_{\max,der,qd}$), similar to the term in (7.3) considered for an industrial consumer (TransGrid), but not previously considered at the residential scale in Chapters 5 and 6. A demand charge is introduced to the reflect the revised Ausgrid tariff structure proposal for the 2019–2024 regulatory period described in Section 8.2.2. $P_{\max,der,qd}$ and $P_{\max,qd}$ are the maximum load demand within the billing period with and without DERs respectively. $E_{bal,qdh}$ is the same net energy flow balance equation first introduced in Chapter 6 but with the updated energy flow terms defined in Section 8.2.3, the equation for which is repeated as (8.34) for convenience. All other terms, including D_q, $T_{ret0,qd}$, $T_{ret,qd}$, $T_{fit,qd}$,

$T_{sc0,qd}$, $T_{sc,qd}$ are as defined in previous chapters.

$$E_{bal,qdh} = E_{load,qdh} - E_{pv,qdh} - E_{bd,qdh} + E_{bpv,qdh} + E_{bg,qdh} + E_{bloss,qdh} \tag{8.34}$$

The comprehensive quantum-behaved particle swarm optimisation (CLQPSO) algorithm used in Chapter 7 was employed to solve the MINLP DER system design optimisation problem in the context of a P2P trading market. The problem was simulated and solved in Matlab version 2017b.

8.5 Trial Scenarios

In order to conduct sensitivity analyses around the various P2P market simulation inputs and assumptions, numerous trial scenarios were considered. Table 8.5 presents a summary of the scenarios investigated in this research. A base scenario was established whereby no P2P trading is implemented, representative of the BAU situation for P2P design optimisation as investigated in previous chapters. Scenarios 1a, 1b and 1c test the influence of various P2P market DER penetrations rates on optimal system design while Scenario 2 investigates the effect of increasing the P2P sale profit margin to 30%. The alternative Ausgrid demand tariff structure defined in Section 8.2.2 is investigated in Scenario 3 while Scenario 4 tests the impact of retail tariff plan variation against the known lowest cost plan without DERs. The implementation of different battery types and BESS cost reductions to 70% and 50% of current system pricing are investigated in Scenario 5. Scenario 6 tests BESS charging from the grid and charging from PV only while Scenario 7 investigates the influence on optimal DER design when FiTs are removed, both with and without a P2P trading environment. Finally, electricity price increases returning to the inflation rate are assessed.

Due to the large number of customers assessed, the multitude of scenarios considered and the length of time required to optimise a system, scenario sensitivity was tested around default assumptions detailed in Table 8.6. For each simulation scenario considered

Table 8.5: P2P sensitivity analysis scenarios

Scenario	Scenario Description	P2P Pool Simulation Case	Scenario Input Parameters
Base	**P2P Trading**	**N/A**	**Off**
1a	DER Penetration Rate Scenario	A	1
1b	DER Penetration Rate Scenario	B	2
1c	DER Penetration Rate Scenario	C	3
2	P2P Sell Profit Margin	D	30%
3	Ausgrid Tariff Structure	B	Demand
4	Retail Plan	B	1–10
5	Battery Type & Pricing	B,G,H	Type = 1–9, Pricing = 100%, 70%, 50%
6	BESS Mode	B	A
7a	FiT	E	Off
7b	FiT and P2P Trading	N/A	Off
8	Electricity Price Growth In-line with Inflation	F	4.50%

Table 8.6: Default customer parameters

Parameter	Value	Description
DER Penetration Rate Scenario	2	100% PV by year 10, 50% BESS by year 10.
P2P Sell Profit Margin	10%	Applied to both PV and BESS P2P energy sell trades.
BESS Cost	Current	100% of current (2019) retail prices.
Retail Plan	Base Plan	Lowest cost electricity retail plan without DERs or P2P market.
Battery Type	Soltaro 2	Representative of the lowest degradation cost C_{degrad} (refer to Appendix D)
Battery Mode	B	Charging only via PV, discharge any time if price signals are favourable.
Ausgrid Tariff Structure	TOU Demand	Closest representation to historical tariff structure included in Ausgrid 2019-24 TSS proposal.
P2P Trading	Applicable	
FiT	Applicable	

in Table 8.6 which tests particular input parameters, the default assumptions were applied for all other untested parameters.

8.6 Results

8.6.1 P2P Market Simulation Cases

An example of the P2P market supply and demand bids is presented in Figure 8.7 corresponding to Hour 7 of Year 1 under P2P market simulation Case B. Total P2P buy bids equate to around 635 kWh while 870 kWh are available for sale, either from surplus PV or surplus BESS energy. Although energy buy bids total 630 kWh, only 220 kWh of energy is traded between successful participants at a P2P clearing price of around \$0.12/kWh.

Remark 8.1 *In Figure 8.7, there is a visible discrepancy between the PV sell and BESS sell reservation prices. The maximum PV sell bid is approximately \$0.17/kWh, occurring around the cumulative bid energy of 530 kWh. The limited number of PV sell reservation prices is due to the low diversity of retail electricity plans considered in the P2P market simulation, with only 10 retailers and two network tariff structures modelled in this research. The increased diversity in the BESS sell bids, starting around \$0.34/kWh, is due to the historical BESS charge/discharge sequence unique to each BESS owner, resulting in a unique average cost for BESS charging.*

The P2P market simulation for Hour 15 of the final day in year 20 is provided in Figure 8.8. The diversity of the BESS sell prices is clearly higher due to the smoother sell reservation curve than the one seen in Figure 8.7, due to the longer operational time frame of the BESS systems leading to an increase in diversity of the average BESS charging costs experienced by each BESS owner. It is also evident in Figure 8.8 that due to BESS cost reductions some BESS systems are able to successfully bid into the P2P market. However, by comparing the highest buy bid with the energy quantity of the equivalent BESS sell bid, it is evident that for simulation Case B that only around 20% of the BESSs would successfully trade in the P2P if the quantity buy demands were incidentally higher.

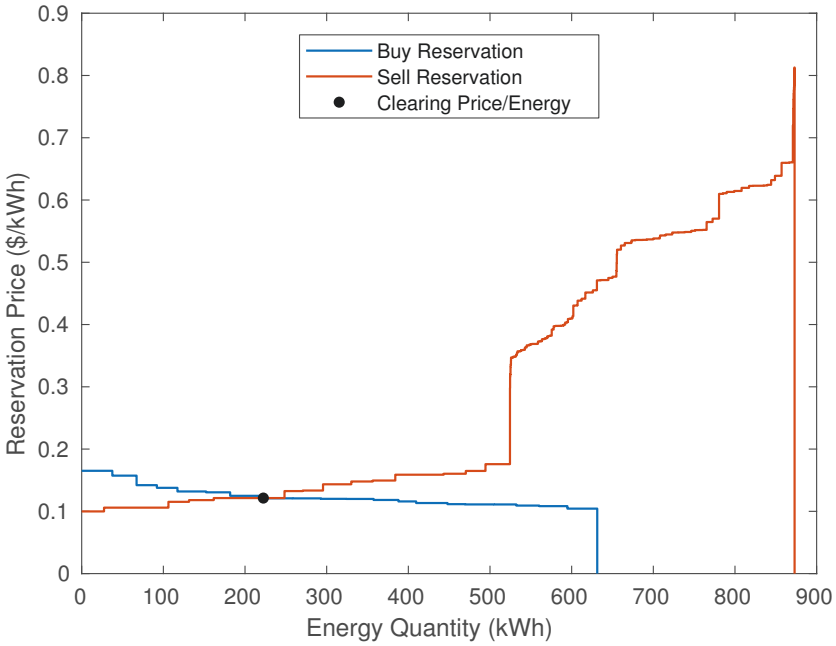

Figure 8.7: P2P settlement for Hour 7 in Year 1 (P2P simulation case B)

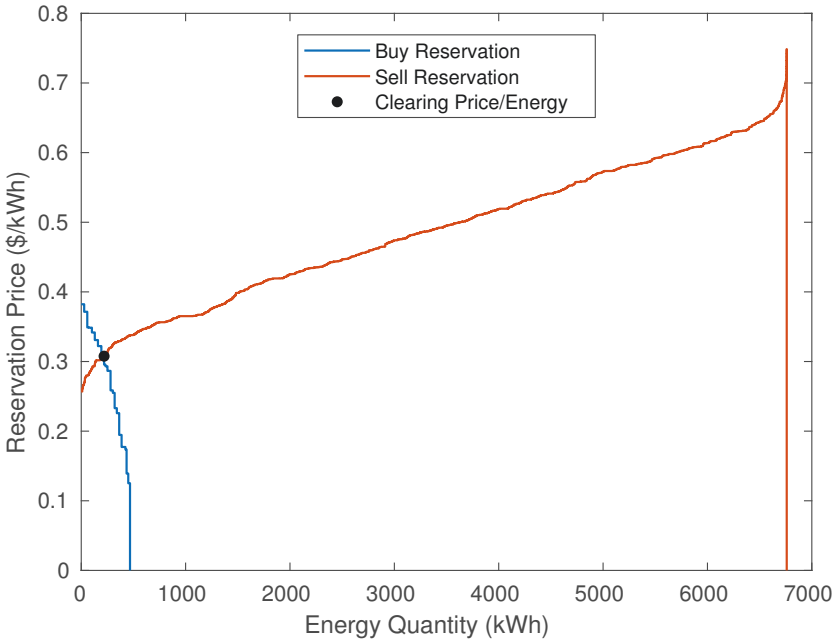

Figure 8.8: P2P settlement for Hour 15 in the final day of Year 20 (P2P simulation case B)

To provide further context towards the frequency and magnitude of P2P clearing prices within each hour of the day for simulation Year 1 and Year 20, heat maps are provided in Figure 8.9, corresponding to simulation Case B. The vast majority of P2P trades are undertaken between the hours 8 and 14, corresponding to a comparatively low clearing price. Referring to the price/hour heat map for Year 1, between hours 13 and 17 the trades can be generally seen fall into three distinct price ranges – \$0.11 to \$0.15, \$0.17 and \$0.22 to \$0.26. This is due to the coincidence of off-peak, shoulder and peak periods within these hours over the full course of the year. In Year 20, the clearing price range

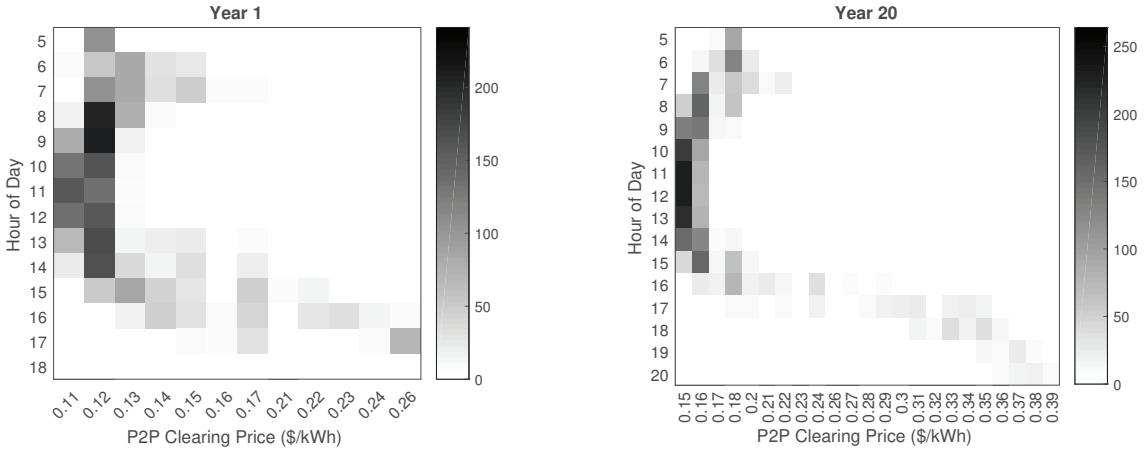

Figure 8.9: Heat map of P2P clearing prices for each hour of the day (P2P simulation case B)

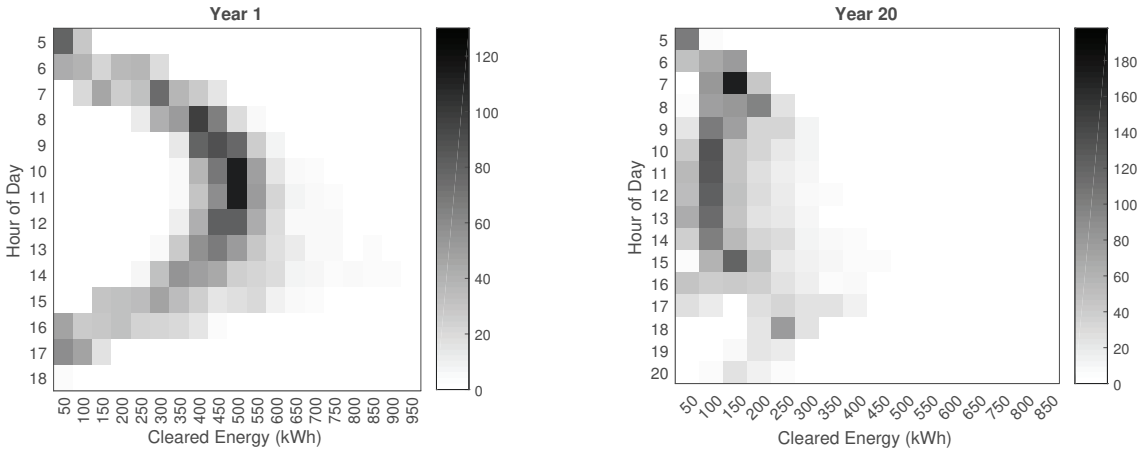

Figure 8.10: Heat map of P2P cleared energy for each hour of the day in Year 1 and Year 20 (P2P simulation case B)

is significantly wider, due to the success of some BESS sell trades. The price bands are fairly indistinct due to the variability in BESS systems average charging costs resulting in the sell reservation price diversity as seen in Figure 8.8.

The frequency and magnitude of energy trades for each hour of the day for simulation Year 1 and Year 20 are provided in Figure 8.10. In Year 1, the most frequent hourly trades occur within the bins of 450 kWh and 500 kWh. In Year 20, as all participants now have a PV system, the quantity of P2P energy traded reduces significantly, with the most frequent traded quantity being 150 kWh, occurring in Hour 7 of the day.

Figure 8.11 and Figure 8.12 show the heat maps of clearing price and cleared energy for each hour of the day respectively under Case D where the P2P seller margin is increased from 10% to 30%. Comparing Figure 8.11 to Figure 8.9 of Case B, it is evident the clearing prices have increased for most frequent occurrences at the low-end of the price rage under a higher seller margin scenario. However, at the high-end of the price range there is no further increase to the maximum clearing price. The effect of a 30% seller margin is limited to an increased frequency within the last bin of \$0.39/kWh in Year 20. It can also be seen by comparing Figure 8.12 and Figure 8.10 that the quantity of energy trades is reduced

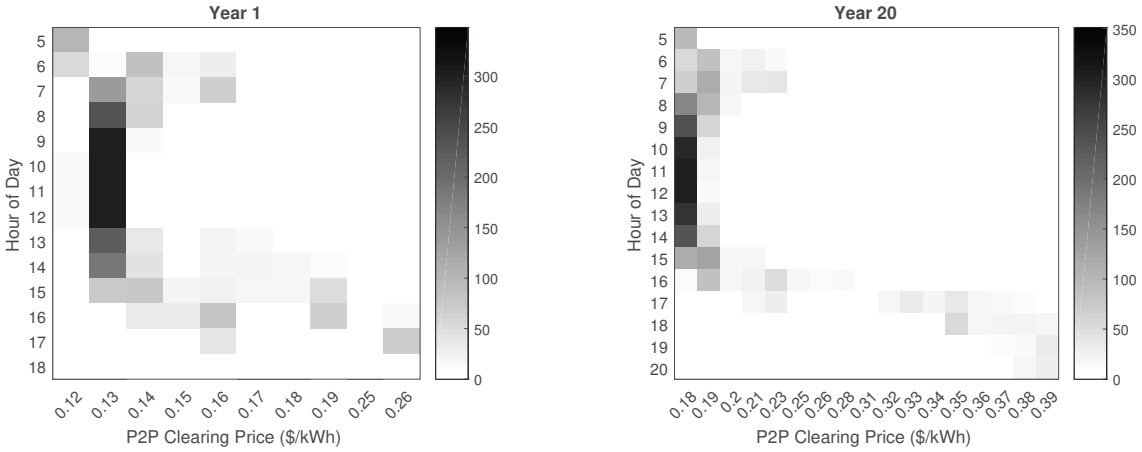

Figure 8.11: Heat map of P2P clearing prices for each hour of the day in Year 1 and Year 20 (P2P simulation case D)

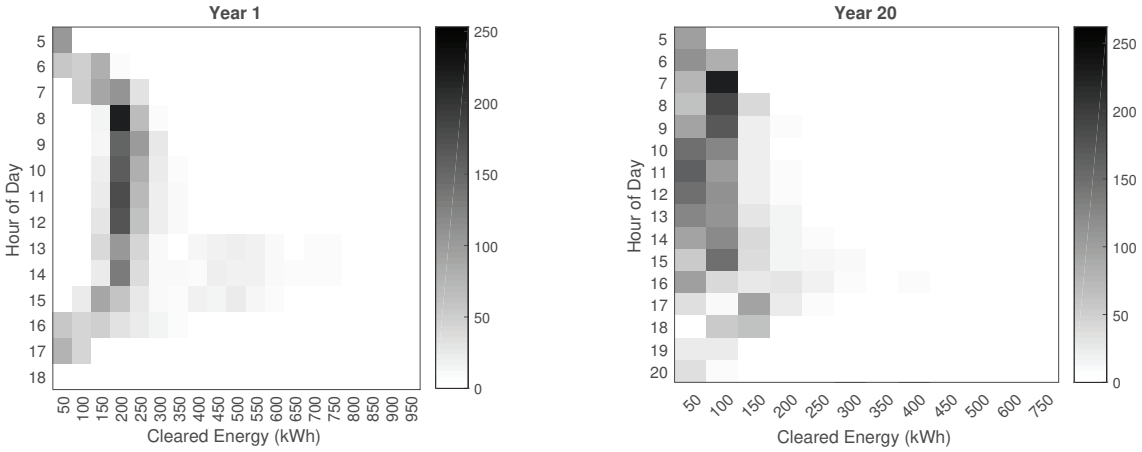

Figure 8.12: Heat map of P2P cleared energy for each hour of the day in Year 1 and Year 20 (P2P simulation case D)

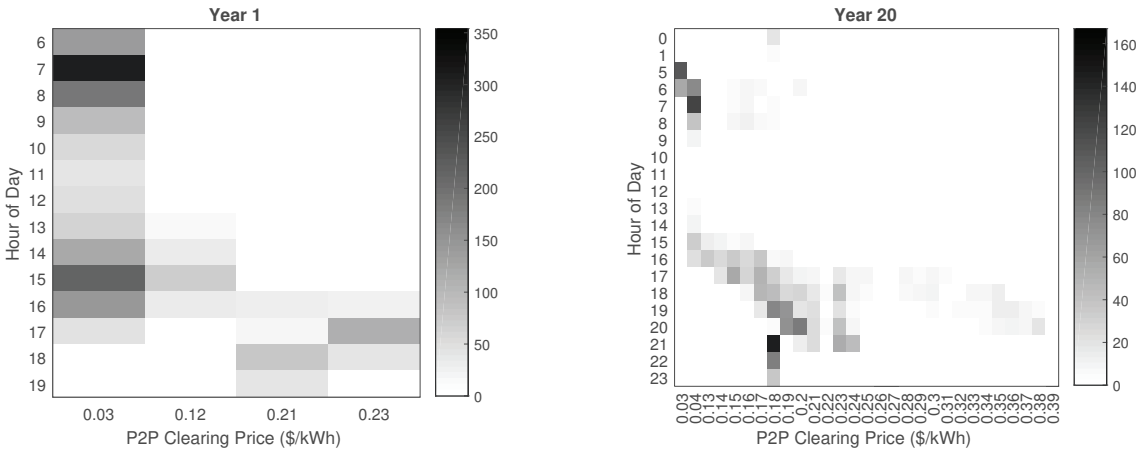

Figure 8.13: Heat map of P2P clearing prices for each hour of the day in Year 1 and Year 20 (P2P simulation case E)

with the adoption of a higher P2P seller margin. In Year 1, the most frequent hourly energy trade is 200 kWh for Case D, as opposed to the most frequent trades of 500 kWh for Case B.

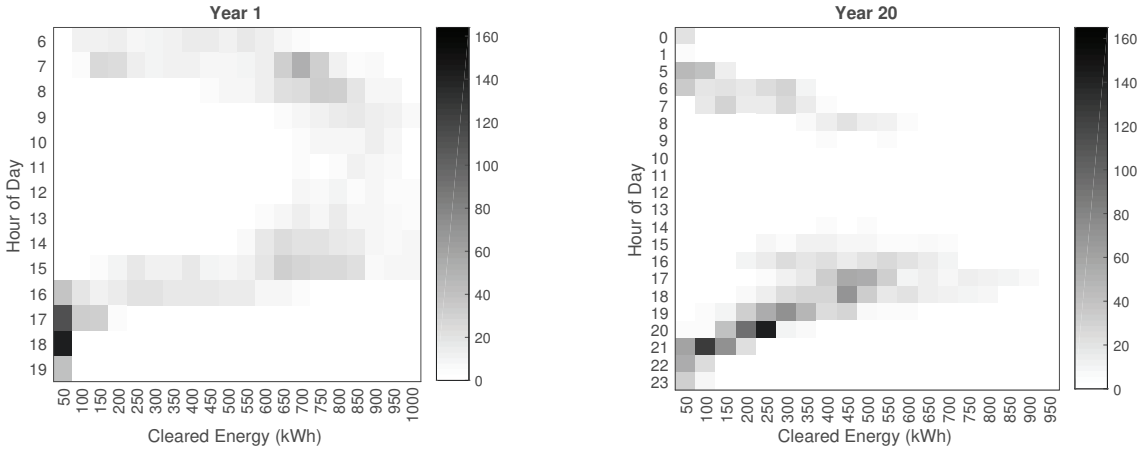

Figure 8.14: Heat map of P2P cleared energy for each hour of the day in Year 1 and Year 20 (P2P simulation case E)

Case E, whereby FiTs are no longer considered to be available, presents markedly different results to Case B and Case D. Referring to Figure 8.13, the clearing prices in Year 1 and Year 20 are significantly reduced as participants no longer wish to set a sell reservation price higher than the FiT given FiTs no longer exist. The scenario is indeed possible given the large number of PV systems currently installed in Australia which are expected to continue generating for many years to come. Due to the lower P2P clearing prices, the quantity of energy traded in each hour is significantly larger in Figure 8.14 compared to Cases B and D, with trades in a wider energy range up to 950 kWh for Year 1. Year 20 also exhibits an uplift in P2P trading compared to Case B and Case D, however similar to the previous two cases, the quantity of trades in the final simulation Year 20 is less than in Year 1. There is also a clear gap in the midday hours whereby fewer trades are made, compared to the evening hours where BESS sell trades are frequently successful. Further discussion is provided towards the end of the section.

Heat maps for each of the P2P market simulation cases are provided in Appendix E.1 for reference.

The average cumulative energy flows E_{load}, E_{pv}, E_{bpv}, E_{bd}, E_{bg} and E_{bloss} for the entire P2P market pool for simulation Case B are shown in Figure 8.15. In Year 1, the proportion of customers with a BESS system is low. Consequently, the charge and discharge energies are relatively insignificant compared to the average cumulative load and PV generation profiles. However, in Year 20 due to the increase in proportion of participants with a BESS installed, the cumulative charge and discharge energies are noticeably larger. Two discharge peaks are visible – the first in the morning following the off-peak charging period and the second much larger peak in the early evening hours. BESS charging occurs in two primary periods – night-time off-peak hours (for systems where off-peak charging is permitted under BESS Mode A) and during the sunlight hours of mid-morning. In Year 20, due to the saturation of solar PV installations, the cumulative PV generated energy exceeds the average load profile maximum by more than 100%.

Remark 8.2 *The over-installation of solar PV with respect to the maximum demand requirements of the underlying consumer load during sunlight hours poses significant diffi-*

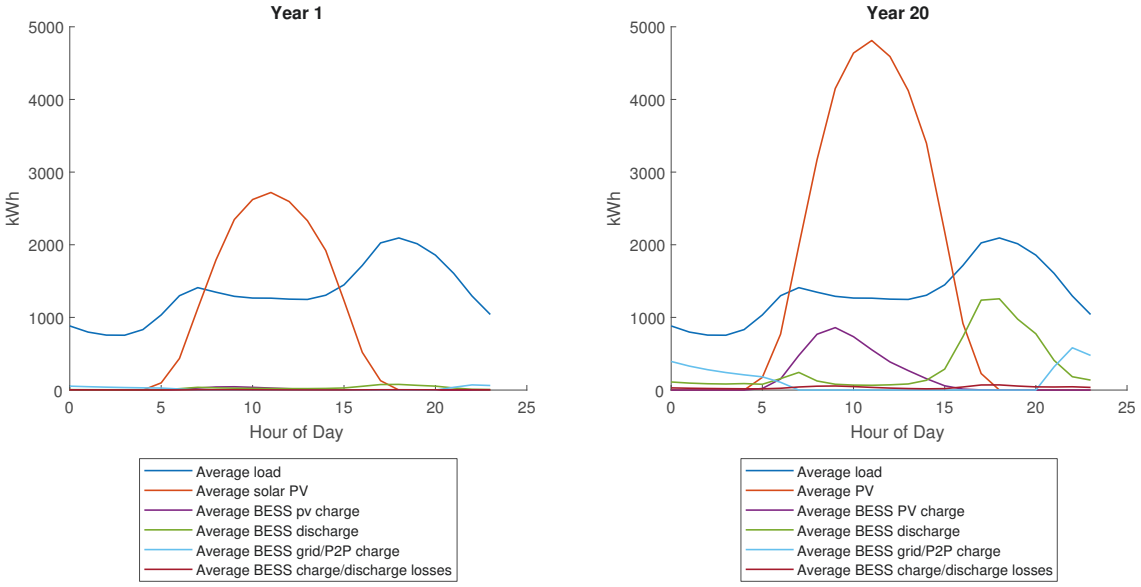

Figure 8.15: Average load and DER energy flows for P2P pool of participants in Year 1 and Year 20 (P2P simulation case B)

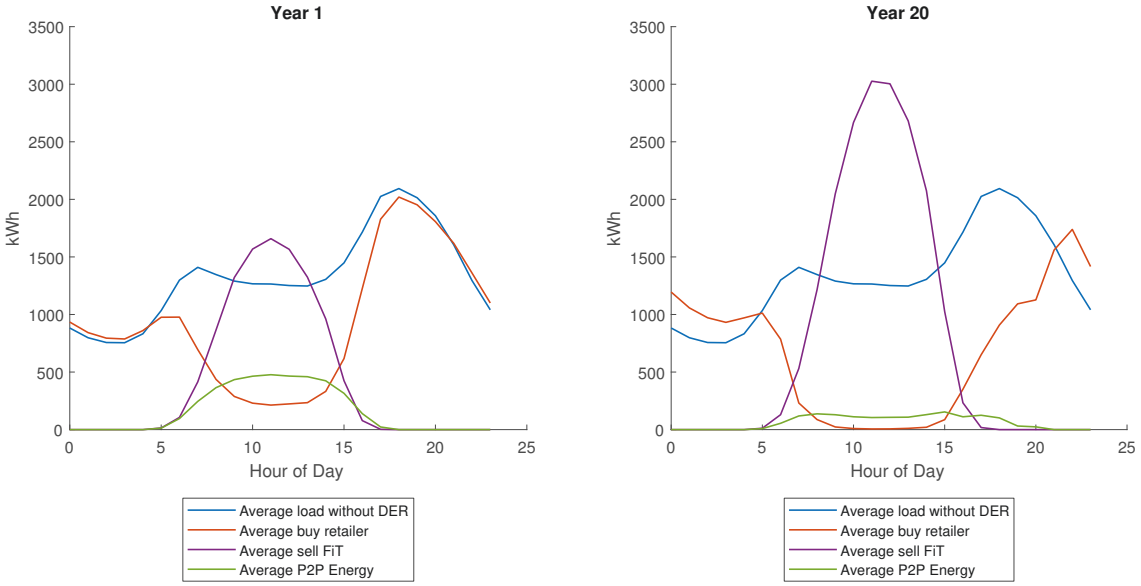

Figure 8.16: Average P2P and retail electricity energy sales across the participant pool in Year 1 and Year 20 (P2P simulation case B)

culties for DNSPs and electricity retailers. DNSPs must construct the electricity network to handle large reverse direction power flows, while electricity retailers are required to provide balance energy primarily during night and early morning/late afternoon hours. Such a situation is highly undesirable for electricity retailers as the generation portfolio would inevitably become less diverse. The viability of lower cost thermal energy as well as non-dispatchable renewable energy sources such as solar PV is removed from portfolios, instead favouring fast-start gas, hydroelectricity and other energy storage technologies.

Such considerations are not investigated in this research. However, it suffices to note that the likelihood of all electricity market customers exhibiting load and generation profiles similar to the P2P simulation of Figure 8.15 is low. Prior to such a scenario occurring

network wide, market corrections through curtailment of PV generation facilitated by smart inverters and/or adjustments to the DNSP hour definitions of off-peak, shoulder and peak periods may be expected. However, the assessment of DER operating scenarios in 20 years is difficult to forecast and therefore no contingency assumptions have been developed for this research.

Figure 8.16 shows the average cumulative energy purchased in the P2P market, energy purchased from electricity retailers and the energy sold to retailers via FiTs. In Year 1, maximum hourly average P2P purchased energy is around 450 kWh occurring in hour 11. The retail energy sale 'duck-curve' profile (so-named as it resembles the silhouette of a duck's head and tail in peak demand hours) can be seen to hollow out significantly in the central hours of the day with respect to the original average load profile. A slight increase in load during off-peak hours is also visible; a result of the introduction of BESSs requiring grid charging. In Year 20, the 'duck-curve' hollows further so that almost no electricity is sourced from the retailer between the hours of 8 and 15. Furthermore, off-peak demand is significantly increased, further exacerbating the network capacity factor issues.

Under simulation Case E where FiTs are removed from retail plans, Figure 8.17 shows that in Year 1, a much larger proportion of PV generated energy is sold through the P2P market compared to Case B in Figure 8.16, as previously observed in the heat map of Figure 8.14. In Year 20, a noticeable difference in P2P traded energy can be observed in the late afternoon hours by comparing Figure 8.16 and Figure 8.17. This is due to the low BESS sell reservation prices for systems charging from PV only as the FiT component of the charge cost described in (8.27) is zero. Consequently, the success of BESS discharge in the P2P market markedly increases, as discussed later. It should be noted surplus PV energy is still shown in Figure 8.17. Without appropriate curtailment the PV systems will continue to inject energy into the electricity grid, although without a financial benefit.

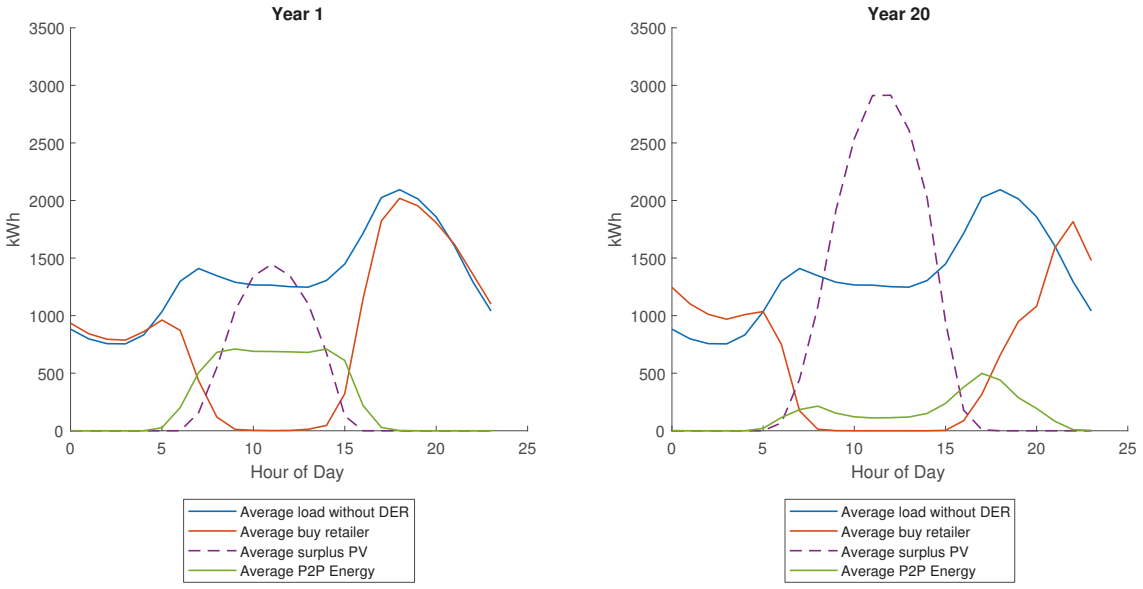

Figure 8.17: Average P2P and retail electricity energy sales across the participant pool in Year 1 and Year 20 (P2P simulation case E)

All P2P market simulation cases defined in Table 8.4 were calculated following the process outlined in the flow chart of Figure 8.6, result summaries for which are presented in Table 8.7 to Table 8.9. In Table 8.7, the total load energy (including the underlying load without DERs and the additional BESS grid-charge energy) over the entire 20-year simulation horizon is presented in units of gigawatt hours (GWh). Simulation Case A has the highest lifetime load due to the higher penetration of BESSs requiring grid charging. Comparing Cases A, B and C (corresponding to DER penetration rate scenarios 1, 2 and 3 respectively), the total load decreases from 253 GWh (Case A) to 241 GWh (Case C) due to the lower number of BESSs in the market and therefore the less demand for charge energy. The remaining cases have a similar total load to Case B, which is expected given each additional case was modelled to have the same DER penetration rate scenario as Case B.

A percentage breakdown of the energy purchased through the P2P pool and purchased from the retailer is also provided in Table 8.7. For each simulation case, less than 10.6% of the total load energy is sourced from the P2P market, with Case E resulting in the highest proportion of P2P energy trades. Due to the high proportion of participants with DER systems as the P2P simulation horizon progresses, a reduced number of energy trades occur. Consequently, the proportion of load energy bought through the P2P market in Year 1 can be expected to be higher than in Year 20, as previously observed in the energy/hour heat maps of Figure 8.10, Figure 8.12 and Figure 8.14. In contrast, over 44% of energy is purchased from the electricity retailer in all cases, primarily due to the unavailability of P2P trades during night time hours (no solar PV energy and BESSs charging against low off-peak retail tariffs). It should be noted that Case C has the highest proportion of retailer bought energy of all cases, as well as the highest proportion of P2P traded energy amongst the three DER penetration rate scenarios of Case A, Case B and Case C due to the reduced self-sufficiency of the Case C participants.

The proportion of total PV generated energy sold in the P2P market for each simulation case is presented in Table 8.8. A maximum percentage of 10.8% occurs for Case C, however the total volume of PV generated energy is less than the other cases. The next highest proportion can be seen for Case E, which is 2.6% higher than Case B featuring the same DER penetration rate scenario. Consequently, it may be concluded that based on

Table 8.7: P2P market simulation case settlement results – load energy

P2P Market Simulation Case	Average P2P Clearing Price ($/kWh)	Load		
		Total Load (GWh)	P2P Buy (%)	Retailer Buy (%)
A	0.148	281	4.8%	44.1%
B	0.151	264	6.6%	50.3%
C	0.155	250	9.1%	58.1%
D	0.163	264	3.5%	53.3%
E	0.071	266	10.6%	46.9%
F	0.151	264	6.6%	50.3%
G	0.152	265	6.6%	50.0%
H	0.155	265	7.0%	50.0%

Table 8.8: P2P market simulation case settlement results – PV energy

P2P Market	PV		
Simulation Case	Total PV (GWh)	P2P Sell (%)	Grid Feed-in (%)
A	253	5.0%	55.1%
B	239	7.1%	56.8%
C	204	10.8%	56.3%
D	239	3.8%	60.2%
E	239	9.7%	53.4%
F	239	7.1%	56.8%
G	239	6.8%	56.7%
H	239	7.0%	56.6%

Table 8.9: P2P market simulation case settlement results – BESS energy

P2P Market	BESS	
Simulation Case	Total Discharge (GWh)	P2P Sell (%)
A	44	1.7%
B	28	2.4%
C	16	3.6%
D	28	0.8%
E	30	16.8%
F	28	2.4%
G	29	4.1%
H	29	6.2%

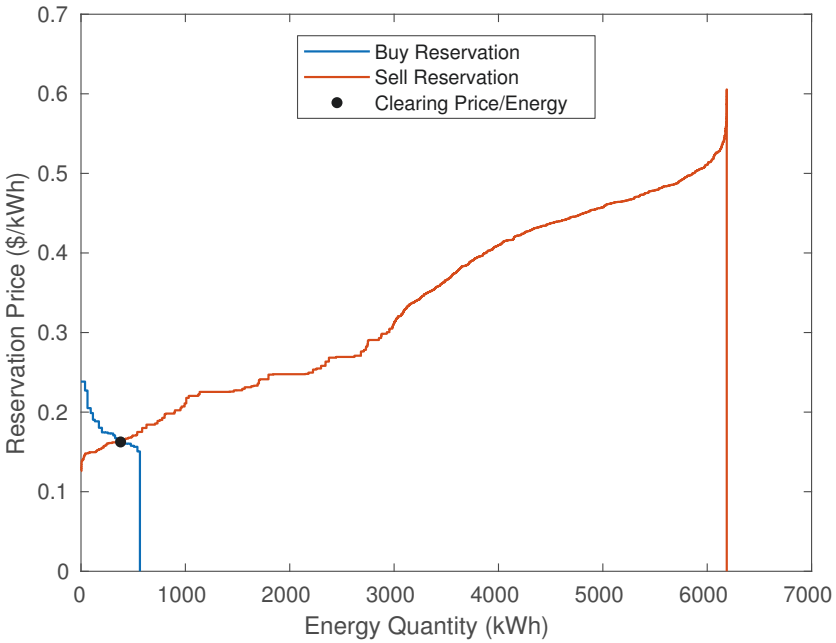

Figure 8.18: P2P settlement for an example hour in Year 20 (P2P simulation case E)

the cases presented in Table 8.4, removal of FiTs would result in an uplift in P2P trades of 2.6%. Case D shows the lowest proportion of successful P2P trades, clearly demonstrating the effect of higher P2P profit margins – a 3.3% reduction in P2P trading.

The simulation settlement results for BESS P2P energy trading are presented in Ta-

ble 8.9 which shows that generally BESS owners are rarely able to successfully conduct P2P trades based on the low percentages observed. The main exceptions exist for Cases E, G and H. Case E has the most success of sale, whereby 16.8% of BESS discharge energy is successfully sold. This is due to the low charging costs of the BESSs from the removal of FiTs resulting in low sell reservation prices, thus increasing the probability of sale. An example of a P2P clearing price corresponding to a BESS sell reservation price under Case E is provided in Figure 8.18.

The results of the design optimisation for 100 test customers against the P2P market trial scenarios detailed in Table 8.5 is presented in the next section.

8.6.2 DER Design Optimisation

A summary of the average NPV achieved following DER design optimisation for 100 P2P participants is presented in Figure 8.19. For each of the scenarios shown in Figure 8.19, it was found that the addition of a BESS system does not lead to an increase in NPV for any of the customers tested, similar to the results presented in Chapter 6. The average NPVs shown in Figure 8.19 result from PV-only DER systems. Consequently, the DER system yielding the greatest electricity cost savings consists of PV-only systems for all tested customers. With respect to the BAU base scenario, i.e. current PV system and BESS pricing, current retail electricity tariffs and FiTs and no P2P trading, the introduction of a P2P trading market results in a relatively small uplift of between 3% and 4% for each of the three DER penetration rate scenarios considered in this research, as shown for Scenarios 1a to 1c.

Remark 8.3 *Scenario 1a, representative of a high DER penetration rate scenario, corresponds to the greatest average NPV up-lift. This result is not necessarily intuitive as one would expect that higher penetration rate scenarios would lead to increased P2P trading competition and therefore less opportunity for additional revenue for the optimally designed participants, whereas the opposite can be seen to true in Figure 8.19. The reasoning lies in the fact that increased competition in the P2P market pool leads to a lower average P2P clearing price in market Case A compared to Case C as previously shown in Table 8.7. Table 8.10 shows summary totals of cumulative traded energy from the group of 100 participants with optimally designed DERs. Although the energy sold to the P2P market can be seen to increase from Scenario 1a to 1c, similarly for the P2P clearing price in Table 8.7 for market Cases A to C, the small uplift in PV revenue (10% above the FiT) is outweighed by the lower cost of purchased energy, of which the greater proportion is bought from the P2P market under Scenario 1a. As a result, a slightly higher NPV can be seen for Scenario 1a in Figure 8.19.*

Under Scenario 2, an increase in the P2P sell margin to 30% does not result in an appreciable uplift in NPV for the DER system owners tested. In Scenario 3, the tested customers receive on average a further 17% NPV uplift by adopting an Ausgrid demand tariff structure compared to Scenario 1b where participants have the alternative TOU demand tariff. Figure 8.20 and Figure 8.21 show a comparison of the average hourly

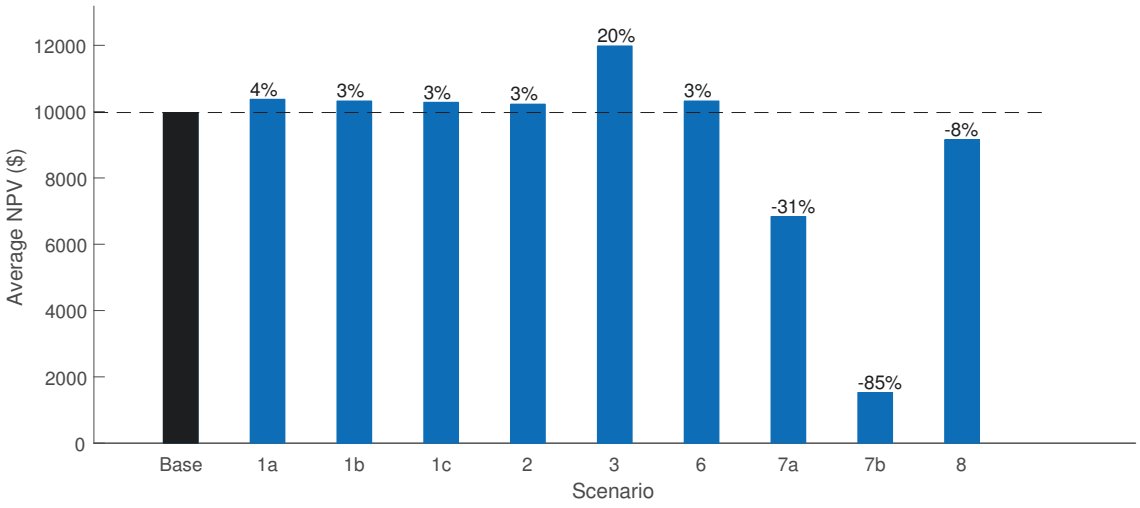

Figure 8.19: DER design optimisation average NPV for 100 trial customers (Scenarios 1a–3b and 6–8)

Table 8.10: Energy totals across 100 participants with optimally designed DERs (PV-only)

Scenario	Total Load (GWh)	Total PV (GWh)	Retailer (GWh)	FiT (GWh)	Total P2P Sell (PV-only) (GWh)	Total P2P Buy (GWh)
Base	10.83	28.57	6.36	24.10	0.00	0.00
1a	10.83	28.58	6.12	23.47	0.65	0.24
1b	10.83	28.57	6.18	23.31	0.81	0.19
1c	10.83	28.57	6.24	23.02	1.08	0.13
2	10.83	28.58	6.29	23.97	0.14	0.08
3	10.83	28.56	6.31	13.73	10.37	0.06
6	10.83	28.57	6.18	23.31	0.81	0.19
7a	10.83	0.00	6.31	0.00	0.00	4.52
7b	10.83	5.57	7.94	2.69	0.00	0.00
8	10.83	28.59	6.18	23.32	0.81	0.19

energy flow in years 1 and 20 of the simulation horizon for Scenarios 1b and 3 respectively. Referring to Figure 8.21, for Year 1 of Scenario 3 almost all surplus PV energy is sold in the P2P market, dropping significantly in Year 20. In contrast, Figure 8.20 shows that under Scenario 1b and a TOU demand tariff, the P2P participants are rarely successful in selling energy in the midday hours, instead selling some energy in the morning and late afternoon periods where retail and network prices are high and PV energy generation is low, albeit far less than in Scenario 3. Further discussion around the implications of these observations is provided in Section 8.7.

Average energy flow figures for each of the other test scenarios are included in Appendix E.2.

Due to the ineffectiveness of a BESS to further increase the NPV for any customer, the results of Scenario 6 (which tests BESS charge mode) are identical to Scenario 1b – neither charge mode matters as no BESSs are installed.

Referring to the results in Figure 8.19 for Scenario 7a, whereby no FiT is considered to be available in the P2P market, the NPV is reduced by 31%. Figure 8.22 shows the average size of the optimal DER (PV) configuration. Under Scenario 7a, the optimal configuration

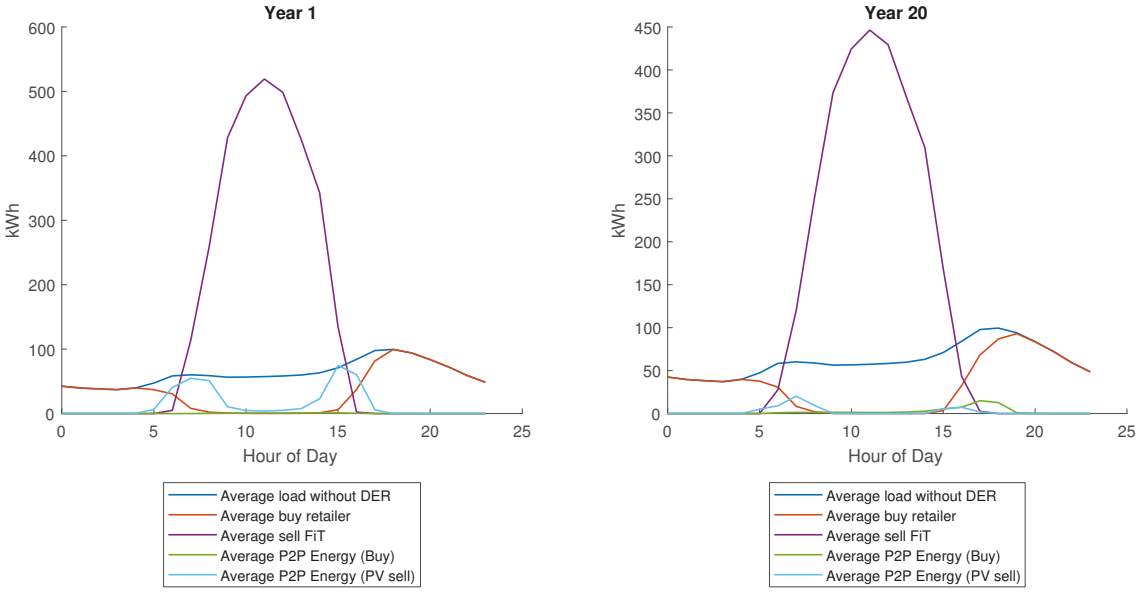

Figure 8.20: Average energy purchases and sales across 100 test customers in Year 1 and Year 20 (Scenario 1b)

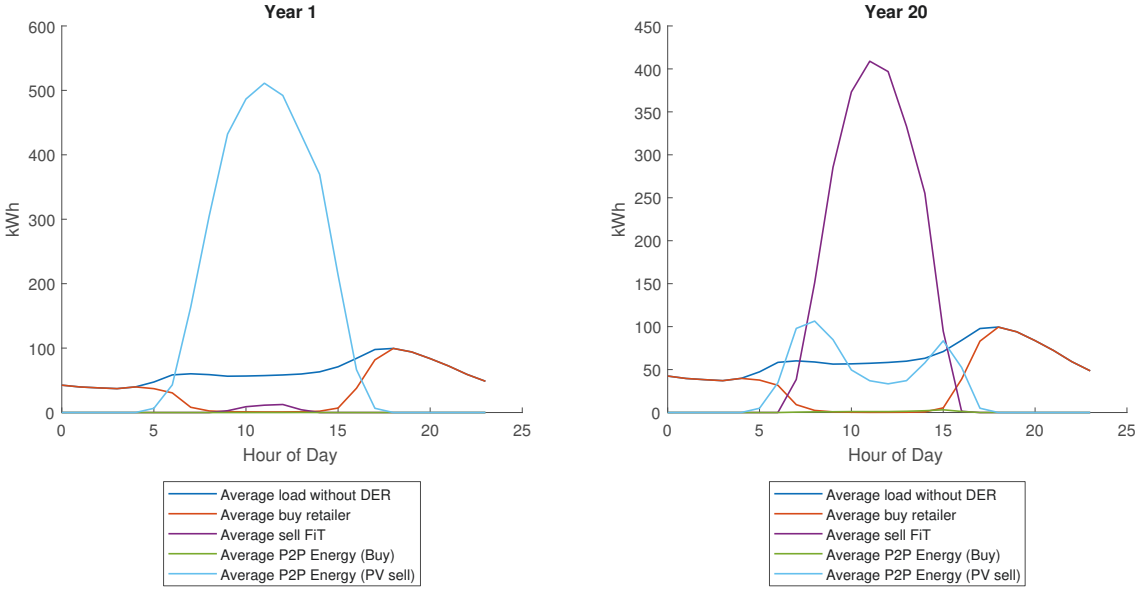

Figure 8.21: Average energy purchases and sales across 100 test customers in Year 1 and Year 20 (Scenario 3)

is to have no PV system as all. Instead, the net average benefit of around $7,000 observed in Figure 8.19 is achieved purely through purchasing low-cost P2P traded energy. While the long-term outlook for FiTs is debatable, it is not unreasonable to consider the possibility of FiT removal. Under such a scenario, participants with existing PV systems may seek to recover their investment cost through P2P trades. The results found in this research suggest prospective PV system investors should consider P2P trading market participation as an alternative to investing in PV. Further investigation focused towards the sensitivity of NPV to the removal of FiTs midway through the PV system lifespan is required.

With the removal of both FiT and P2P trading in Scenario 7b, the average optimal PV system can be seen in Figure 8.22 to reduce significantly from 10.2 kW in the base scenario,

to just over 2 kW, corresponding to an NPV reduction of 85% as shown in Figure 8.19. Under Scenario 8, whereby electricity price increases are modelled to match inflation, the NPV reduces by 8% on average due to the lower P2P trading prices that occur under such a scenario and lower underlying retail electricity costs making PV investment less beneficial.

Referring to Figure 8.22, the majority of scenarios show that the 100 test customers benefit the most by maximising the PV system size, which was modelled to be 10.2 kW in this research. Further discussion is provided in Section 8.7.

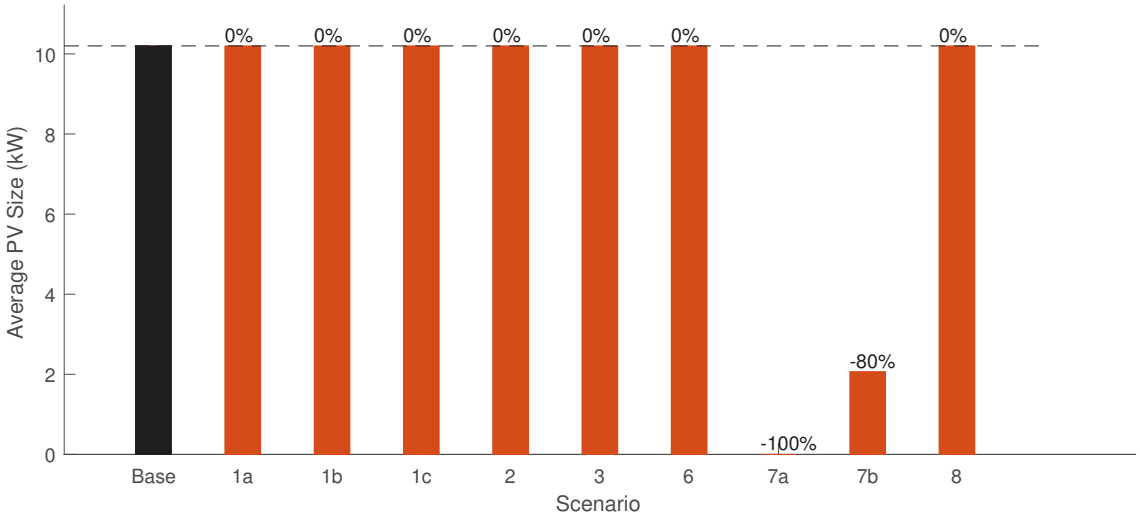

Figure 8.22: DER design optimisation average PV size for 100 trial customers (Scenarios 1a–3b and 6–8)

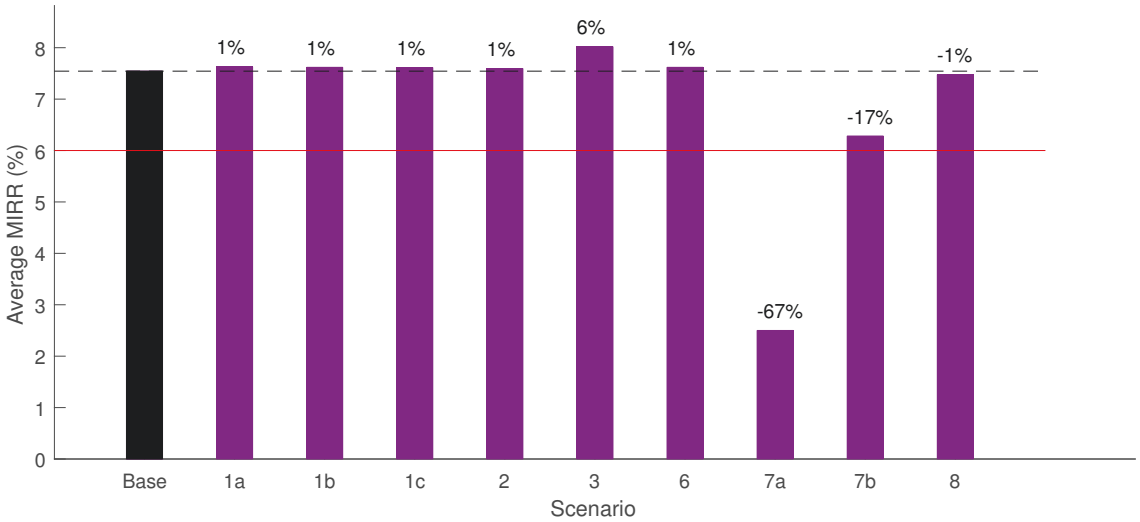

Figure 8.23: DER design optimisation average nominal MIRR for 100 trial customers (Scenarios 1a–3b and 6–8)

The average MIRRs for each of the scenarios are shown in Figure 8.23. Virtually no change is observed for Scenarios 1a, 1b, 1c, 2 and 6 with an increase of just 1% while Scenario 8 is reduced by just 1%. Scenario 3 results in an uplift of 6% due to the greater success of P2P sell trades while Scenario 7b leads to a 17% reduction. However, it should

be noted that the average MIRRs amongst the 100 participants investigated are greater than the 6% threshold (shown as a red) for all scenarios except Scenario 7a, demonstrating from an investment return perspective that investing in a PV system is worthwhile. In the case of Scenario 7a, comparing the MIRR against the 6% threshold is not valid as no capital is spent on DER systems under this scenario. The cost savings are achieved purely through access to an alternative electricity tariff platform.

The average NPVs for 50 customers under Scenario 4, whereby the financial benefit under different retail electricity plans is tested, are presented in Figure 8.24. For each of the retail tariff cases, the optimal system size was found to be 10.2 kW, matching the base case scenario. Only one participant was found to benefit from a BESS installation, corresponding to retail plan 5. By considering an alternative plan to the base plan when a DER system is not installed, it can be seen that the majority of plans yield an increased benefit. On average NPV is increased by up to 79% under Retail Plan 1. Referring to Figure 8.25, the MIRRs are also generally improved, with an MIRR up to 9% (corresponding to a 21% increase) observed for Retail Plan 1.

The sensitivity of NPV to different BESS types at different price levels is tested in Scenario 5. Figure 8.26 shows the BESS size required to achieve the optimal NPV for 100 customers under Scenario 5. In Figure 8.26(a), it can be seen that at current price levels (Scenario 1b), no BESS yields a greater benefit than a PV-only system. When pricing is reduced to 70%, again no BESS is seen to yield an improved benefit. However, at a 50% reduction level, some customers see an increased benefit from the installation of BESS systems, with a mix between the Tesla Powerwall 2 and the SolaX Triple Power 6.3 as the optimal configurations among the BESS options considered. Referring to Figure 8.27, each customer with a BESS achieves an MIRR exceeding 7%, well above the cost of capital threshold level of 6%. The result demonstrates investment in a BESS when prices are depreciated can be expected to yield a benefit from a return on investment perspective in addition to maximising NPV.

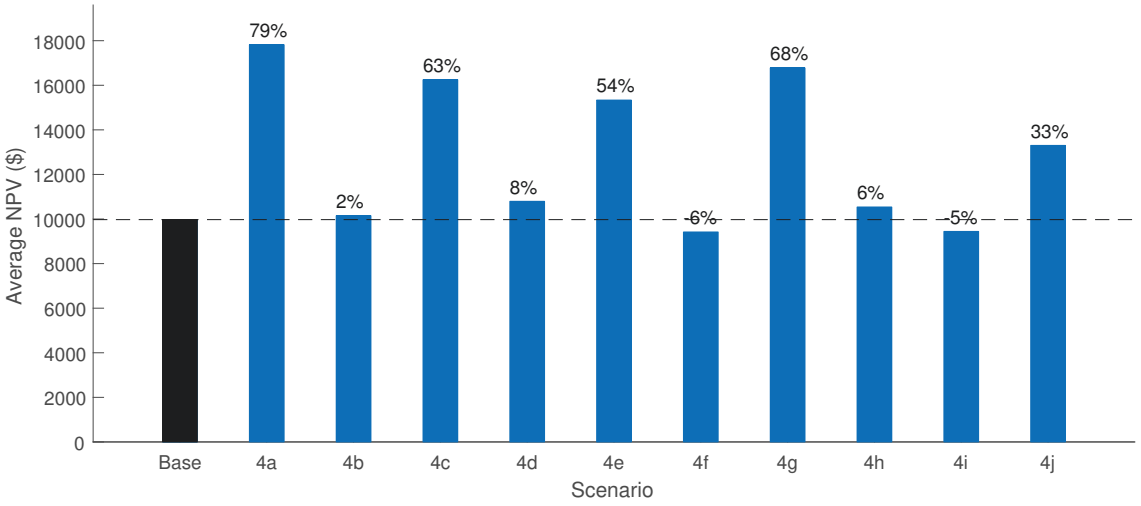

Figure 8.24: DER design optimisation average NPV for 50 trial customers under (Scenario 4: columns 4a–4j correspond to Retail Plan 1 – 10 respectively)

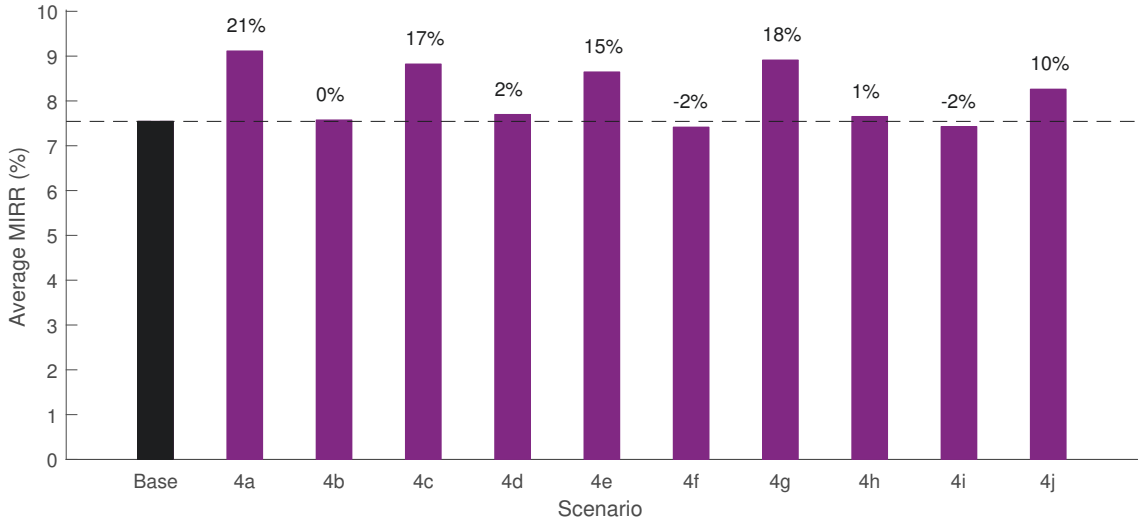

Figure 8.25: DER design optimisation average nominal MIRR for 50 trial customers (Scenario 4: columns 4a–4j correspond to Retail Plan 1 – 10 respectively)

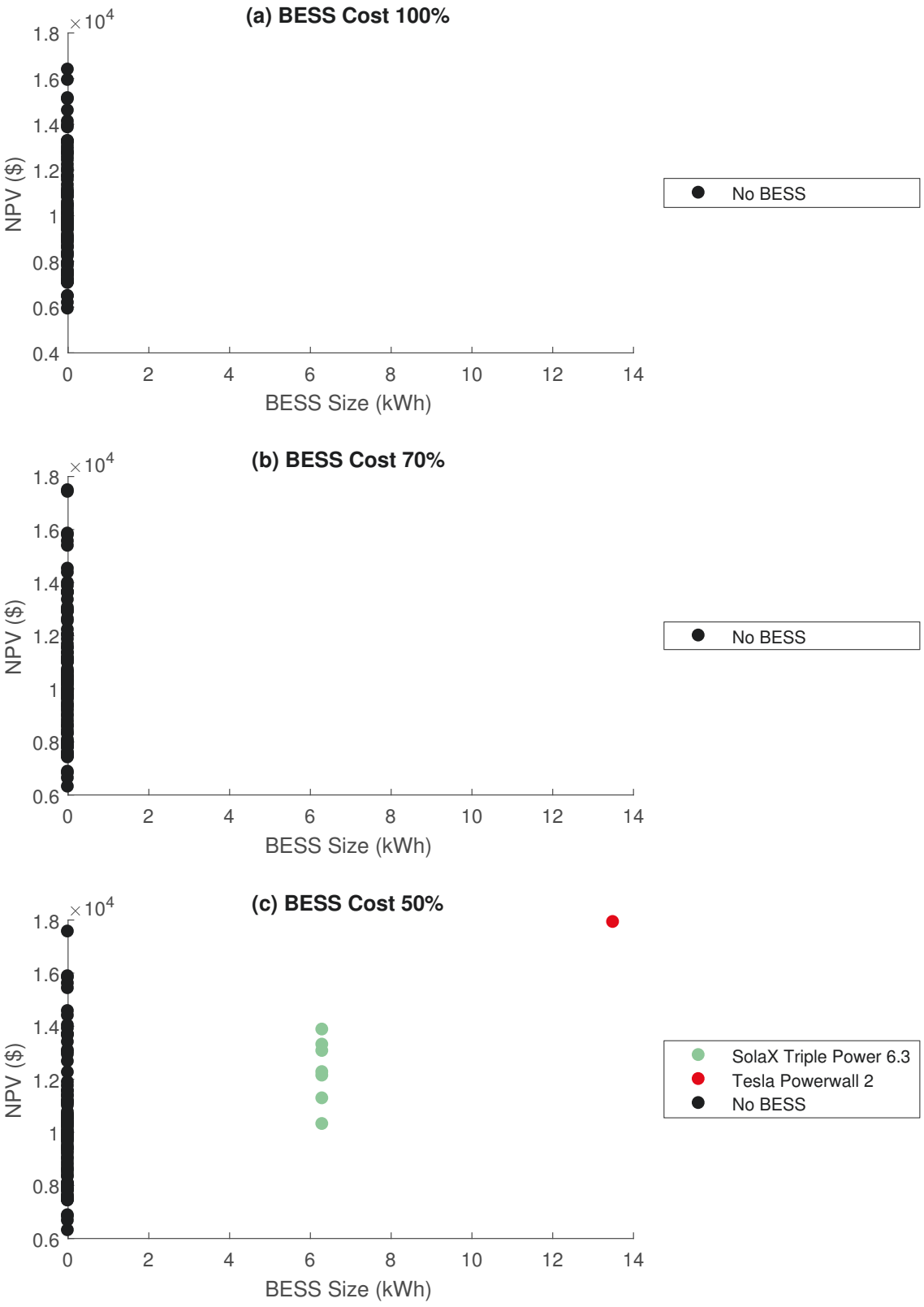

Figure 8.26: NPV and BESS size for a sample of 100 customers at (a) 100%, (b) 70% and (c) 50% BESS reference price levels (Scenario 5)

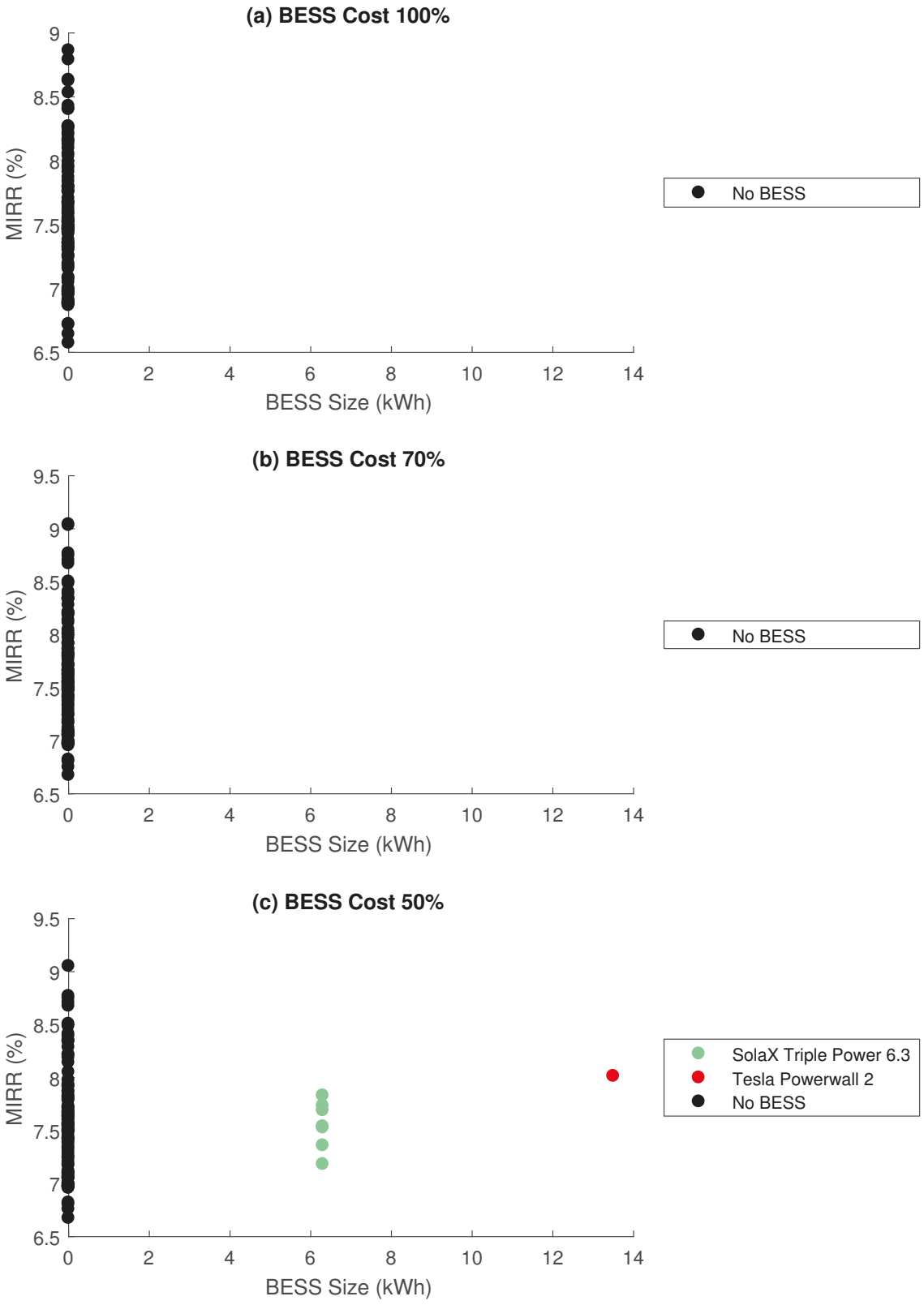

Figure 8.27: MIRR and BESS size for a sample of 100 customers at (a) 100%, (b) 70% and (c) 50% BESS reference price levels (Scenario 5)

8.7 Discussion

The results presented previously in Section 6.4.2 indicated that 4% of customers would benefit from a Tesla Powerwall 2 battery. However, the results in Section 8.6.2 show no customer to benefit from a BESS system under current pricing. The research undertaken for Chapter 6 assumed Powerwall 2 pricing to be $10,000 [246] whereas in late 2018, pricing was increased to the $12,350 [248, 303] level which was assumed in this chapter. More recently in July 2019, Powerwall 2 pricing was again reduced to $11,700 [304, 305]. The fluctuating Powerwall 2 pricing highlights the uncertainty facing prospective customers and therefore the necessity to apply the design optimisation methodology developed in this thesis as part of the investment decision process.

The average optimal PV system size found in Section 8.6.2 for the majority of scenarios was 10.2 kW, suggesting the customers would benefit most by maximising PV system size. The research presented in Chapter 5, based on 2016 pricing, resulted in a very different assessment, with average sizes in the range of 2.72 kW to 4.06 kW depending on installation location. While the Chapter 5 findings are valid for PV system pricing and electricity retail market scenario in the time range considered, the trend in upwards PV system sizes first observed in Chapter 6 before the final current market state considered in this chapter is clear. The size trend may be primarily attributed to significant PV system price reductions over the last three years coupled with a large increase in available FiTs.

The observation that the Ausgrid network demand tariff structure results in a cost-saving increase of 20%, compared to 3% for the equivalent assumptions under a TOU demand tariff suggests further research is required to assess the influences of various network tariff structures in a P2P trading environment. It should be noted that the P2P market model detailed in Section 8.2 may require further enhancement around sharing of network costs between buy and sell participants. Customers submitting buy bids based on a TOU demand tariff will on average submit higher bids than those on the demand tariff structure, thereby increasing the probability of a successful bid. Conversely, customers submitting sell bids under a demand tariff will have a greater probability of a successful trade. Consequently, on average the buy participant pays for half the TOU demand tariff whereas the sell participant will pay half the demand tariff. The implications on DNSP network cost recovery that this situation may impose require further investigation.

8.8 Summary

Existing research has shown the potential benefit a prosumer can receive through sharing energy in a P2P trading market [255, 257, 269]. However, it has previously been shown that prospective investors would benefit from prior consideration of market conditions and the penetration rate scenarios of participant DERs when sizing investments [269]. Based on the literature review undertaken for this research, the optimal system sizing and orientation of DER systems to maximise savings at the individual consumer level has not previously been investigated for P2P trading applications, nor has a full assessment of lifetime operation been undertaken.

In this chapter, P2P trading was investigated from the perspective of a prospective investor in small-scale DERs at the residential level. A lifetime assessment of DERs consisting of solar PV and battery systems was undertaken in the context of a P2P market consisting of over 2,200 participants with real load consumption profiles derived from the SGSC project data. Revision of the PV-BESS energy flow models developed in previous chapters was presented to enable potential DER investors to participate in P2P transactions.

The hypothetical P2P market simulation was tested under various market P2P simulation cases and input value scenarios to identify trends in optimal PV-BESS system design and the potential economic returns available. A double auction scheme was selected for P2P market settlement, given its suitability to full and hybrid P2P structures where each participant does not necessarily pay the same cost for electricity. The buy and sell reservation prices were constructed to account for recently introduced Australian network tariff structures as well as battery degradation and charging costs.

The results of the P2P market simulations for various trial cases revealed up to 10.8% of total PV generated energy within a pool of over 2,200 market participants could be traded in the P2P market. In a P2P market with BESS owner's bidding to sell available energy, it was found up to 3.6% of BESS discharge energy could be traded in the P2P market, observed under the slowest DER penetration rate scenario. In a trialled case where retailer-provided FiTs are removed, the success of BESS energy sale was found to increase, with 16.8% of total discharged energy sold in the P2P market, attributed to the lower sell reservation prices resulting from reduced battery charging costs.

A DER design optimisation methodology was developed for P2P energy trading and implemented for 100 test P2P market participants using CLQPSO as the underlying optimisation algorithm. It was found that under current retail electricity tariffs, FiTs and PV-BESS system pricing, prospective investors would benefit from a PV-only system in a P2P market. The optimal size for all participants was found to be 10.2 kW, corresponding to the upper end of the design size range considered. However, a scenario where FiTs were removed found participants would benefit most from P2P trading only. When P2P sale margins were increased to 30%, no appreciable impact on average NPV was observed.

The results of this research demonstrate the necessity to consider market conditions and DER system pricing, in particular BESS costs, when deciding to invest in a DER system operating in a P2P market scenario. While current PV system prices and FiTs suggest prospective investors would gain some additional benefit by participating in a P2P market, a clear reliance on FiTs to recover capital costs when sized to generate as much energy as possible was observed.

Chapter 9

Conclusion

Continued advances in PV and BESS technologies have made DERs an attractive option for residential energy consumers. Selecting an appropriate system is non-trivial due to the relatively high cost of batteries, a multitude of available retail electricity plans, the removal of incentive schemes and the impending introduction of disruptive technologies such as a peer-to-peer energy trading.

The introduction of Smart Grid technologies, particularly smart meters, enables consumers to leverage high temporal resolution energy consumption data to optimise system design based on an individual customer's circumstance. The results of the SGSC trial undertaken by the Australian Government and the recommendations published in current literature highlight the enormity of the paradigm shift towards integrating Smart Grid technologies and the difficulties in determining economically efficient energy strategies. The results further indicate there will be an ongoing need for comprehensive and reasoned decision making tools to ensure PV and energy storage systems are integrated to their maximum potential.

The research presented in this thesis leverages the real-world energy consumption data from the SGSC project to develop and demonstrate a design optimisation strategy enabling the economically efficient selection of PV and BESS system size, tilt, azimuth and retail electricity plan for residential DERs based on a customer's temporal load profile.

To enable the develop of energy yield models incorporated in the design optimisation methodology, a literature review of solar irradiation databases was undertaken in Chapter 3, with a particular focus on Australian applications. The AREMI spatial mapping platform, providing access to hourly data captured by BoM, was selected as the primary database for solar irradiation data and solar PV modelling in this research.

To enable the estimation of solar PV energy generation, as a central component of the research presented in this thesis, models for the transposition of solar irradiation on a horizontal plane to irradiation on a tilted plane were reviewed. The HDKR model was selected based on documented accuracy and reduced computational demand.

The BRL diffuse irradiation model, previously shown to be one of the more accurate models for Australian based applications, was identified for further improvement. Specific consideration of climatological zones based on the Köppen-Geiger climate classification system was introduced along with a review of data quality methodologies, establishing the

basis for the original research presented in this thesis.

In Chapter 4, the Köppen-Geiger climate classification system was proposed for application to diffuse irradiation models and investigated to establish the potential to improve modelling accuracy through climatological characteristic considerations of specific locations. Rigorous data quality control steps were defined to establish a high quality tuning data set to facilitate the development of new BRL diffuse models. Using data from the BoM OMS network, a new National BRL model and specific BRL models for each Köppen-Geiger zone were developed for ground-based measurements. Through the application of a rigorous statistical analysis process, the performance of the new models were established and compared against the original BRL model. The new National BRL model was shown to almost universally out-perform the original BRL model and strong support was found for the adoption of specific climate classification models to improve diffuse irradiation estimates. Based on the results presented in Chapter 4, new National and Köppen-Geiger BRL parameters were proposed for application to Australian ground-based global horizontal irradiation data in the absence of diffuse and direct irradiation estimates.

Due to the limited ground coverage of global horizontal irradiation estimates, irradiation estimates from satellite imagery were also investigated. Based on a similar data quality control and statistical analysis approach to that of the ground-based data analysis, the results found in this research did not support the adoption of Köppen-Geiger zone BRL models for satellite-based estimates. However, a new National BRL model based on the BoM BRL model variant was found to present a closer approximation to ground-based measurements than the original AREMI dataset.

The introduction of smart grid technologies and the phased removal of incentive schemes is likely to further complicate the cost-effective selection and integration of residential PV systems in the future. The continued increase in smart meter market penetration allows high temporal resolution data to be leveraged by electricity customers in order to make informed PV investment decisions. Consequently, an optimisation tool is required to avoid ineffective capital spending.

In Chapter 5, such a design optimisation strategy was developed to maximise the investment value of PV. Models for PV energy production, as well as underlying economic models based on an NPV analysis, were defined as key components of the optimisation objective function.

A version of the canonical particle swarm optimisation algorithm, modified to include a penalty function and a hypercube nearest-vertex approach to facilitate the inclusion of discrete parameters, was applied as the underlying optimisation algorithm. The optimisation methodology was tested in an Australian context, using real-world hourly smart meter and irradiation data applied to recently available incentive schemes and retail electricity plans.

With realistically defined economic parameters, a positive NPV was found to be achievable for all customers assessed. NPV, system size and savings achievable through correct retail plan selection were all found to increase between the low, medium and high annual electricity consumption brackets defined in the chapter. However ‘viable’ PV investment

opportunities were not universally observed for all customers, with at most 77.5% of customers amongst the locations assessed yielding a return greater than the cost of capital. A wide variety of optimal retail plans was observed, from the extreme of 97.5% from one retailer in one city to a diverse array of plans and tariffs structures in others.

A sensitivity analysis on individual customers demonstrated the significant negative impact of non-optimal sizing on the value of the investment, particularly for over-sized systems. However, a sensitivity analysis conducted on tilt and azimuth found limited effect on the net benefit for deviations within $\pm 10^{\circ}$ and $\pm 20^{\circ}$ respectively. Furthermore, optimal azimuth selection was found to contribute to less than 1% of the potential net benefit for flat tariffs and just 5% for TOU tariffs. Consequently, azimuth was therefore deemed as a non-critical parameter and the optimisation problem may be reduced to the two dimensions of tilt and size.

Finally, the average optimal system sizes for the customers and locations assessed were found to be significantly less than the average size installed in 2015 and 2016, approximately 2 kW on average. The observed disparity between practices within the Australian residential PV industry in 2016 and the characteristics of the optimised systems found in Chapter 5 highlighted the necessity for an economic optimisation strategy to be routinely implemented prior to the decision to invest.

In Chapter 6, the significant price reductions in PV and battery systems, sparking considerable interest in hybrid PV-BESS solutions at the residential level, was the motivation behind an adjustment of the design optimisation strategy initially developed in Chapter 5. Battery energy flow models were developed as the basis for a revised objective.

Subsequent analysis was initially applied to three real-world electricity customers before expansion to a larger sample of 100 consumers. For the small sample, based on PV and battery system prices at the time of research, no battery system was found to be economically viable for the residences assessed. However, optimised PV-only systems were found to yield a net benefit for all customers.

A sensitivity analysis was conducted on battery pricing to determine the price point at which a hybrid PV-BESS would yield a net benefit improvement. The results showed that significant price reductions to 60-70% of current prices are required before the tested customers could take advantage of an energy storage system.

For the three customers selected, various battery operating modes were examined to determine the most economically beneficial operation. No instance was found whereby energy arbitrage yielded a greater benefit than purely maximizing PV self-consumption. The observation continued to hold at all battery pricing levels.

The analysis was expanded to a wider sample of 100 customers, with battery prices investigated at three levels – 100%, 70% and 50% of the reference retail prices. It was found that at the 100% level, only 4% of customers would benefit from a Tesla Powerwall 2 system, with the proportion markedly increasing to 67% and 93% for the 70% and 50% levels respectively. The vast majority of customers were found to benefit from PV under all BESS pricing conditions.

To demonstrate the accuracy of the energy yield models developed, and to present an

alternative design optimisation assessment for a larger consumer, a case study based on the TransGrid iDemand project was undertaken in Chapter 7. Operational data from the iDemand system were used to validate the accuracy of the adopted PV energy yield model at a high level, which was ultimately shown to underestimate the potential annual energy cost savings by just 1.57%.

The operational data were then applied to hypothetical installations over a nine-year period to enable the determination of the opportune investment year and the characteristics and performance of the corresponding optimised system. Implementation of the optimisation algorithm revealed no battery system would yield an economic benefit greater than a PV-only system for installation years between 2017 and 2025. Under the system pricing scenarios considered, the optimal system was found to be a small-scale system until 2020 (incentivised through small-scale technology certificates), after which a transition to a large-scale system receiving large-scale generation certificates would yield the highest NPV depending on the pricing scenario considered. The results presented in Chapter 7 provided further support for the necessity to introduce a PV-battery system optimisation process as an integral part of the investment decision process.

A hypothetical P2P energy trading market was proposed in Chapter 8. The design optimisation methodology developed in Chapter 6 was revised to enable the potential net benefit achieved through P2P trading to be quantified. P2P market simulations were conducted to provide a sensitivity assessment around various market scenarios to identify trends in optimal PV-BESS system design. A double auction scheme was selected for P2P market settlement with consideration given to shared network tariffs based on recently introduced demand tariff structures in Australia. Battery degradation and charging costs were also modelled.

The results for the trial market cases amongst a pool of over 2,200 market participants revealed up to 10.8% of PV generated energy could be traded in the P2P market under the DER penetration rate scenarios modelled. Owners of BESSs were found to be less successful when bidding to sell available energy, however in the scenario where FiTs were removed, BESS energy sale success increased, with 16.8% of total discharged energy sold in the P2P market.

A DER design optimisation methodology was developed for P2P energy trading and implemented for 100 test P2P market participants using CLQPSO as the underlying optimisation algorithm. It was found that under current retail electricity tariffs, FiTs and PV-BESS system pricing, prospective investors would benefit from a PV system only, sized to maximise energy production. Under current market conditions and BESS prices, no BESS amongst a range of currently available products yielded a higher net benefit than a PV system only for any of the 100 test customers. The results of this research demonstrate the necessity to consider market conditions and DER system pricing, in particular BESS costs, when deciding to invest in a DER system operating in a P2P market scenario. While current PV system prices and FiTs suggest prospective investors would gain some additional benefit by participating in a P2P market, a clear reliance on FiTs to recover capital costs when sized to generate as much energy as possible was observed.

The research presented in this thesis shows a strong upwards trend in optimal PV system size over the last three years. The increase in optimal size can be primarily attributed to significant PV system price reductions over the last three years coupled with a large increase in available FiTs. While a prospective investor seeking to purchase a PV system in 2019 or 2020 may benefit from the larger systems found in Chapter 8, compared to investors in 2016 as presented in Chapter 5, the research presented in this thesis demonstrates the necessity to consider current and future retail electricity market and regulatory conditions prior to investing in a hybrid PV-BESS system. With the availability of smart meter data, consumers can leverage the value of high temporal resolution consumption data to inform investment decisions for their individual circumstance.

9.1 Future Work

Given the rapidly increasing maturity of the renewable energy industry, significant PV price reductions have been achieved since the commencement of the research presented in this thesis. While Chapter 8 largely captures current market conditions, there is scope to update the analyses presented in Chapters 5 and 6 to provide up-to-date regulatory, retail electricity and renewable energy industry context.

Additional research may be undertaken to investigate the influence of modelling uncertainty on the optimal design solutions, including input weather data uncertainty, energy measurement uncertainty and key PV-BESS datasheet performance metrics.

There is scope to investigate different battery operating modes in addition to the modes considered in Section 6.1.1 and Section 8.2.3 in future research. These modes may include peak lopping, scheduled operation and operation modes based on future load forecasts."

In relation to the research presented in Chapter 8, further work is proposed to assess additional P2P market analysis scenarios to expand upon the scenarios detailed in Table 8.5. Scenarios proposed for further consideration include:

- Investigation of appropriate management of different network tariff structures as discussed in Section 8.7;
- Sensitivity of NPV and return on investment towards reduced or future removal of FiTs, for instance a 50% reduction on existing tariffs, a situation which may transpire within the next 10 years given the high uptake of PV in Australia and the impending closure of the small-scale renewable energy scheme;
- Different PV system costs such as assessment against the 'high' range of system prices detailed in Table 8.3;
- Alternative DER penetration rate scenarios more closely aligned with the projected uptake of DERs in the Australian market; and
- Expand analysis to different distribution networks in the Australian NEM.

In Section 8.1.5, research on co-incident capacity charges proposed by [278] was reviewed. The proposal was introduced in response to recent guidance by the AER to

encourage networks to "send price signals that are more closely aligned with peak demand and utilisation on the network" [278]. There is potential to further expand the scenario analyses in Chapter 8 to investigate the impact on P2P energy trading when capacity charges are only applicable to events when the customer peak demand is coincident with the hourly network peak. Given the large sample of data available through the SGSC project, the network peaks to which the capacity charges would be applicable can be roughly identified, similar to the methodology implemented in [278].

Appendix A

Retail Electricity Tariffs

A.1 Retail Tariffs for 2016 - Chapters 5 and 6

The electricity tariffs assumed in these chapters are based on the standing offers available from Origin Energy, EnergyAustralia and AGL in September 2016. The flat tariff retail plans assumed in these chapters are summarized in Table A.1. In principle, under a flat tariff plan each energy unit at any time of day is billed uniformly at a single rate. However, a number of flat tariff plans considered in this analysis also include inclining block rates based on the total daily or quarterly energy consumption. The flat tariffs associated with each inclining energy block are shown in Table A.2.

The TOU tariff retail plans assumed are summarized in Table A.3 and the times for which each TOU tariff level is applicable are shown in Table A.4.

Table A.1: Flat tariffs for each retail plan and location considered (prices include 10% GST)

Retailer	Location	Flat Tariff 1 (c/kWh)	Flat Tariff 2 (c/kWh)	Flat Tariff 3 (c/kWh)	Daily Supply Charge (c/Day)	Feed-in Tariff (c/Day)
Origin Energy	Newcastle	27.005	26.51	24.2	88.66	6.0
	Parramatta	25.773	25.113	23.903	86.35	6.0
	Tamworth	26.62	26.191	25.773	149.6	6.0
	Melbourne	27.654	-	-	108.757	5.0
	Brisbane	25.586	-	-	128.117	6.0
EnergyAustralia	Newcastle	26.72571	26.1217	25.52869	83.9025	6.1
	Parramatta	28.02481	27.05923	25.20859	89.7644	6.1
	Tamworth	30.31237	29.74906	29.22029	152.6767	6.1
	Melbourne	27.654	-	-	115.5	5.0
	Brisbane	25.982	-	-	128.7	6.0
AGL	Newcastle	27.621	26.818	20.911	86.427	6.1
	Parramatta	27.104	26.587	26.367	85.217	6.1
	Tamworth	29.909	29.458	29.018	148.918	6.1
	Melbourne	27.225	-	-	120.868	5.0
	Brisbane	27.071	-	-	115.236	6.0

Table A.2: Energy blocks associated with each flat tariff rate for each retail electricity plan

Retailer	Location	Block 1	Block 2	Block 3
Origin Energy	Newcastle	First 10.9589 kWh/Day	Next 10.9589 kWh/Day	Remaining kWh/Day
	Parramatta	First 10.9589 kWh/Day	Next 8.2192 kWh/Day	Remaining kWh/Day
	Tamworth	First 10.9589 kWh/Day	Next 8.2192 kWh/Day	Remaining kWh/Day
	Melbourne	All kWh/Day	-	-
	Brisbane	All kWh/Day	-	-
EnergyAustralia	Newcastle	First 10.9589 kWh/Day	Next 10.9589 kWh/Day	Remaining kWh/Day
	Parramatta	First 10.9589 kWh/Day	Next 8.2192 kWh/Day	Remaining kWh/Day
	Tamworth	First 10.9589 kWh/Day	Next 8.2418 kWh/Day	Remaining kWh/Day
	Melbourne	All kWh/Day	-	-
	Brisbane	All kWh/Day	-	-
AGL	Newcastle	First 1000 kWh/Quarter	Next 1000 kWh/Quarter	Remaining kWh/Quarter
	Parramatta	First 1000 kWh/Quarter	Next 1000 kWh/Quarter	Remaining kWh/Quarter
	Tamworth	First 1000 kWh/Quarter	Next 1000 kWh/Quarter	Remaining kWh/Quarter
	Melbourne	All kWh/Day	-	-
	Brisbane	All kWh/Day	-	-

Table A.3: TOU tariffs for each retail plan and location considered (prices include 10% GST)

Retailer	Location	TOU Tariff 1 (c/kWh)	TOU Tariff 2 (c/kWh)	TOU Tariff 3 (c/kWh)	Daily Supply Charge (c/Day)	Feed-in Tariff (c/Day)
Origin Energy	Newcastle	52.8	21.45	13.2	99	6.0
	Parramatta	35.31	29.15	15.4	108.9	6.0
	Tamworth	31.35	31.35	18.15	149.6	6.0
	Melbourne	46.453	28.567	20.284	108.757	5.0
	Brisbane	33.803	24.365	19.767	128.117	6.0
EnergyAustralia	Newcastle	53.98844	21.62446	12.03719	95.6494	6.1
	Parramatta	38.1634	28.39265	14.3803	112.5366	6.1
	Tamworth	33.62293	33.62293	17.00116	153.1365	6.1
	Melbourne	35.222	-	17.842	113.3	5.0
	Brisbane	35.2	24.53	17.897	128.7	6.0
AGL	Newcastle	55.363	21.659	12.177	96.426	6.1
	Parramatta	36.245	29.7	14.465	109.439	6.1
	Tamworth	34.892	34.892	18.656	148.885	6.1
	Melbourne	34.727	27.225	20.559	120.615	5.0
	Brisbane	35.871	25.85	21.065	115.236	6.0

Table A.4: Hours of the day defining off-peak, shoulder and peak periods for each retail electricity plan (WD and WE denote weekday and weekend respectively)

Retailer	Location	Peak Period	Shoulder Period	Off-peak Period
Origin Energy	Newcastle	WD=(2pm-8pm)	WD=(7am-2pm,8pm-10pm) WE=(7am-10pm)	All other times
	Parramatta	WD=(1pm-8pm)	WD=(7am-1pm,8pm-10pm) WE=(7am-10pm)	All other times
	Tamworth	WD=(7am-9am,5pm-8pm)	WD=(9am-5pm,8pm-10pm)	All other times
	Melbourne	WD=(3pm-9pm)	WD=(7am-3pm,9pm-10pm) WE=(7am-10pm)	All other times
	Brisbane	WD=(4pm-8pm)	WD=(7am-4pm,8pm-10pm) WE=(7am-10pm)	All other times
EnergyAustralia	Newcastle	WD=(2pm-8pm)	WD=(7am-2pm,8pm-10pm) WE=(7am-10pm)	All other times
	Parramatta	WD=(1pm-8pm)	WD=(7am-1pm,8pm-10pm) WE=(7am-10pm)	All other times
	Tamworth	WD=(7am-9am,5pm-8pm)	WD=(9am-5pm,8pm-10pm)	All other times
	Melbourne	WD=(7am-11pm)	-	All other times
	Brisbane	WD=(4pm-8pm)	WD=(7am-4pm,8pm-10pm) WE=(7am-10pm)	All other times
AGL	Newcastle	WD=(2pm-8pm)	WD=(7am-2pm,8pm-10pm) WE=(7am-10pm)	All other times
	Parramatta	WD=(1pm-8pm)	WD=(7am-2pm,8pm-10pm) WE=(7am-10pm)	All other times
	Tamworth	WD=(7am-9am,5pm-8pm)	WD=(9am-5pm,8pm-10pm)	All other times
	Melbourne	WD=(3pm-9pm)	WD=(7am-3pm,9pm-10pm) WE=(7am-10pm)	All other times
	Brisbane	WD=(4pm-8pm)	WD=(7am-4pm,8pm-10pm) WE=(7am-10pm)	All other times

A.2 Example Business Retail Tariffs - Chapter 7

Table A.5: TransGrid iDemand retail electricity tariff assumptions (P = Peak, SH = Shoulder, OP = Off-peak)(prices exclude 10% GST)

Parameter	Charges	Rate			Unit
		P	SH	OP	
T_{ret}	Retailer Energy	6	6	4	c/kWh
	Distributor Energy	4.1124	3.0474	1.3178	c/kWh
	Administration		0.0378		c/kWh
	Ancillary Services		0.261		c/kWh
	LRET		0.381		c/kWh
	SRES		0.404		c/kWh
	NSW Energy Saving		0.082		c/kWh
T_{sc}	Network Access Charge		18.729		$/Meter/Day
	Meter Provision		2		$/Meter/Day
T_{DC}	Distributor Demand		10.4581		$/kVA

A.3 Ausgrid Network and Retailer Tariffs - Chapter 8

Table A.6: Ausgrid proposed 2019-2020 network tariffs (prices exclude 10% GST)

Tariff Component	Charge Component	Tariff Structure	
		TOU Demand	Demand
NUoS	Peak (c/kWh)	23.5336	3.0293
	Shoulder (c/kWh)	4.4199	3.0293
	Off-peak (c/kWh)	3.0859	3.0293
	Network Access Charge ($/day)	46.1155	37.1624
	Demand Charge (High Season) (c/kW/day)	4.0779	20.3897
	Demand Charge (Low Season) (c/kW/day)	4.0779	10.1949
DUoS & Climate Change Fund	Peak (c/kWh)	16.6295	1.3073
	Shoulder (c/kWh)	3.5148	1.3073
	Off-peak (c/kWh)	2.2504	1.3073
	Network Access Charge ($/day)	41.2955	32.3424
	Demand Charge (High Season) (c/kW/day)	4.0779	20.3897
	Demand Charge (Low Season) (c/kW/day)	4.0779	10.1949
TUoS	Peak (c/kWh)	6.9041	1.722
	Shoulder (c/kWh)	0.9051	1.722
	Off-peak (c/kWh)	0.8355	1.722
	Network Access Charge ($/day)	4.82	4.82
	Distribution Loss Factor (DLF)	1.048	1.048

Table A.7: Retail tariffs for 2019 associated with the Ausgrid network. Adjusted for the proposed 2019-2020 tariff structure statement (prices include 10% GST)

Tariff Structure	Bill Component	Retailer 1 EnergyAustralia	2 Origin Energy	3 AGL	4 Simply Energy	5 Red Energy	6 Alinta Energy	7 Dodo	8 ReAmped	9 Energy Locals	10 Powershop
Retail Plans 2019	Peak (c/kWh)	59.29	41.4	45.1	58.43	42.9	60.26	67.01	45.65	38.49	39.6
	Shoulder (c/kWh)	31.02	18.59	19.14	22.18	23.1	25.3	28.36	18.15	18.69	21.59
	Off-peak (c/kWh)	18.92	11.26	12.54	15	15.4	16.5	17.49	11.66	14.29	18.1
	Energy Discount (%)	26	0	0	18	10	30	30	0	0	15
	Daily Supply Charge (c/day)	106.04	106.54	102.4	96.44	110.11	105.6	111.2	99.66	140.8	120.47
	Solar FiT (c/kWh)	12.5	8	11.1	8	11.1	7.5	11.6	8	9	10.2
Ausgrid TOU Demand Tariff (2019-20) & Energy Discount	Peak (c/kWh)	42.75	39.88	43.58	46.67	37.24	41.12	45.85	44.13	36.97	32.37
	Shoulder (c/kWh)	21.23	16.26	16.81	16.28	18.69	16.08	18.22	15.82	16.36	16.37
	Off-peak (c/kWh)	14.46	11.88	13.16	12.81	14.42	11.98	12.68	12.28	14.91	15.91
	Daily Supply Charge (c/day)	107.01	107.51	103.38	97.41	111.08	106.57	112.13	100.63	141.77	121.44
	Demand (High Season) (c/kW/day)	4.49	4.49	4.49	4.49	4.49	4.49	4.49	4.49	4.49	4.49
	Demand (Low Season) (c/kW/day)	4.49	4.49	4.49	4.49	4.49	4.49	4.49	4.49	4.49	4.49
	Solar FiT (c/kWh)	12.5	8	11.1	8	11.1	7.5	11.6	8	9	10.2
Ausgrid Demand Tariff (2019-20) & Energy Discount	Peak (c/kWh)	25.26	16.25	19.95	27.29	15.97	24.57	29.30	20.50	13.34	12.28
	Shoulder (c/kWh)	20.04	14.66	15.21	14.96	17.25	14.96	17.10	14.22	14.76	15.01
	Off-peak (c/kWh)	14.41	11.81	13.09	12.75	14.36	11.94	12.63	12.21	14.84	15.85
	Daily Supply Charge (c/day)	97.16	97.66	93.53	87.56	101.23	96.72	102.28	90.78	131.92	111.59
	Demand (High Season) (c/kW/day)	22.43	22.43	22.43	22.43	22.43	22.43	22.43	22.43	22.43	22.43
	Demand (Low Season) (c/kW/day)	11.21	11.21	11.21	11.21	11.21	11.21	11.21	11.21	11.21	11.21
	Solar FiT (c/kWh)	12.5	8	11.1	8	11.1	7.5	11.6	8	9	10.2

Appendix B

Hypothesis Tests

The hypothesis testing methodology used in Chapter 5 is based on the p-value approach detailed in [306]. While hypothesis testing is usually established on the assumption of normally distributed populations with equal variance, if the sample sizes are sufficiently large for distributions exhibiting non-normal characteristics, such as skewness and unequal variance as apparent in Figure 5.11(a)–(e), then by the central limit theorem, the standard hypothesis testing methodology remains valid [306]. As the samples considered in this research each include 40 customers, the sample sizes are deemed sufficiently large to invoke the above statement.

Under the well defined p-value approach for the two-tailed t-test, if the p-value calculated for the sample test statistic t^* is less than the confidence level α (assumed to be 5% in this research), the null hypothesis (equal distribution means) is rejected, in favour of the alternative hypothesis (distribution means are not equal).

The results of the hypothesis tests undertaken for the analysis in Section 5.5.2 are summarized in Table B.1.

Table B.1: Summary of hypothesis tests for distributions of key performance and system metrics.

Tested samples	Metric	p-value	Reject null hyp. (@ $\alpha = 5\%$)
Low/medium	NPV	2.79×10^{-14}	Yes
	Size	1.63×10^{-17}	Yes
	Savings	1.26×10^{-5}	Yes
	MIRR	0.0818	No
	Payback	0.298	Yes
Medium/high	NPV	8.45×10^{-13}	Yes
	Size	7.07×10^{-15}	Yes
	Savings	3.31×10^{-4}	Yes
	MIRR	0.2109	No
	Payback	0.1075	No

Appendix C

PV Module Input Parameters

Applicable parameters of the PV module considered in the analysis presented in Chapters 5, 6, 7 and 8 are detailed in the subsequent tables.

Table C.1: PV module characteristics for Chapter 5

Parameter	Value
Make	Trina Solar
Model	TSM-250PD05.05
Type	Polycrystalline
Maximum Power @ STC	250 W
Efficiency ($\eta_{mpp,STC}$) @ STC	15.3
Power Temperature Coefficient (μ_{mpp})	-0.41
NOCT	44°C
Surface Area (A_c)	1.637 m^2
Initial Guarantee D_1	97
Degradation Rate r_{deg}	0.7

Table C.2: PV module characteristics for Chapter 6 (small sample)

Parameter	Value
Make	Trina Solar
Model	TSM-280PC05A(II)
Type	Polycrystalline
Maximum Power @ STC	280 W
Efficiency ($\eta_{mpp,STC}$) @ STC	17.1
Power Temperature Coefficient (μ_{mpp})	-0.39
NOCT	44°C
Surface Area (A_c)	1.637 m^2
Initial Guarantee D_1	97
Degradation Rate r_{deg}	0.7

Table C.3: PV module characteristics for Chapter 7

Make	Suntech
Model	STP250-20/Wd
Type	Polycrystalline
Maximum Power @ STC	250 W
Efficiency ($\eta_{mpp,STC}$) @ STC	15.4%
Power Temperature Coefficient (μ_{mpp})	-0.43
NOCT	45°C
Surface Area (A_c)	1.62688 m^2

Table C.4: PV module characteristics for Chapter 6 (large sample) and Chapter 8

Parameter	Value
Make	Trina Solar
Model	TSM-300PD06H
Type	Polycrystalline
Maximum Power @ STC	300 W
Efficiency ($\eta_{mpp,STC}$) @ STC	17.6
Power Temperature Coefficient (μ_{mpp})	-0.38
NOCT	41°C
Surface Area (A_c)	1.705 m^2
Initial Guarantee D_1	97
Degradation Rate r_{deg}	0.7

Appendix D

BESS Input Parameters

The battery system characteristics assumed for Chapter 6 and the TransGrid iDemand case study in Chapter 7 are provided in Table D.1 and Table D.2 respectively. The BESS characteristics considered in Chapter 8 are detailed in Table D.3 based on figures published in [248]. The final row was calculated using (6.1), (8.28) and (8.29).

Table D.1: System characteristics of two BESSs considered in Chapter 6

Make Model	Enphase AC Battery	Tesla Powerwall 2
Energy Capacity C_{MAX} (kWh)	1.2	13.5
Power Rating R_{max} (kW)	0.26	5.00
End-of-life Capacity C_{EOL} (kWh)	0.96	9.45
Cycle Life Y_{EOL}	3,650	3,650
Depth of Discharge D (%)	100	100
Battery Cost U_b (AUD)	$2,000	$10,000
Installation Cost	$0	$400
Battery Efficiency (Round-trip) (%)	0.96	-
Inverter Efficiency (Assumed) η_{inv} (%)	0.96	-
Total efficiency (η_{batt}) (%)	0.88	0.90

Table D.2: TransGrid iDemand BESS characteristics in Chapter 7

Manufacturer	Kokam
Model	KRI-H-3R4C-133
Nominal Charge/Discharge Power (R_{max})	133 kWh
Initial Maximum Useful Capacity (C_{max0})	126 kWh
End-of-life Capacity (C_{EOL})	75.6 kWh (60%)
Cycles (Y_{EOL})	8000
Depth of Discharge (D)	80%
Round-trip DC Efficiency (η_{batt})	95%
Assumed Warranty Period	10 years

Table D.3: System characteristics of nine BESSs available in 2019 assessed in Chapter 8

Make	Enphase	Soltaro	Soltaro	SolaX	SolaX	LG Chem	DCS	BYD	Tesla
Model	AC Battery	2	4.5	Triple Power 4.5	Triple Power 6.3	Resu 10	PV 10.0	B Box Pro 13.8	Powerwall 2
Reference Number	1	2	3	4	5	6	7	8	9
Energy Capacity C_{MAX} (kWh)	1.2	2	4.5	4.5	6.3	8.8	10.4	13.8	13.5
Power Rating R_{max} (kW)	0.26	2	4.5	2.5	2.5	5	5.2	12.8	5.00
End-of-life Capacity C_{EOL} (kWh)	0.96	1.8	4.05	4.05	5.67	5.28	9.36	9.52	9.45
Cycle Life Y_{EOL}	3,650	10,000	10,000	6,000	6,000	3,650	5,000	3,650	3,650
Depth of Discharge D (%)	100	90	90	90	90	100	100	100	100
Battery Cost U_b (AUD)	$2,000	$1,700	$4,200	$2,800	$4,000	$7,655	$8,900	$9,600	$12,350
Inverter Cost	$0	$694	$1,562	$868	$868	$1,735	$1,804	$4,442	$0
Installation Cost	$0	$400	$400	$400	$400	$400	$400	$400	$400
Battery Efficiency (Round-trip) (%)	0.96	0.97	0.97	0.95	0.95	0.95	0.98	0.953	-
Inverter Efficiency (Assumed) η_{inv} (%)	0.96	0.96	0.96	0.96	0.96	0.96	0.96	0.96	-
Total efficiency (η_{batt}) (%)	0.88	0.89	0.89	0.88	0.88	0.88	0.90	0.88	0.90
Degradation Cost (C_{degrad}) (c/kWh)	50.73	16.44	16.11	17.72	16.39	38.10	22.48	33.93	30.44

Appendix E

P2P Market Simulation - Results for All Cases

E.1 P2P Market Simulation Price, Energy and Hour Heat Maps

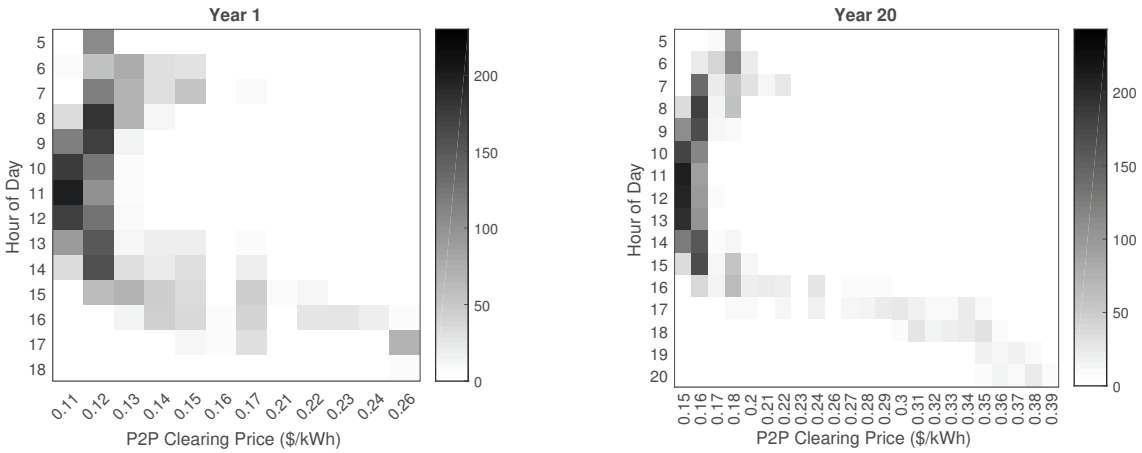

Figure E.1: Heat map of P2P clearing prices for each hour of the day in Year 1 and Year 20 (P2P simulation case A)

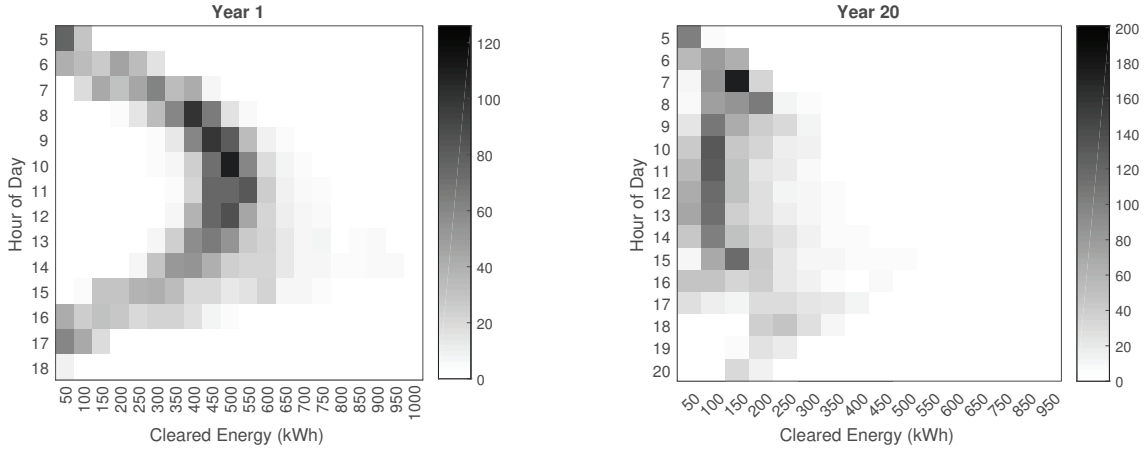

Figure E.2: Heat map of P2P cleared energy for each hour of the day in Year 1 and Year 20 (P2P simulation case A)

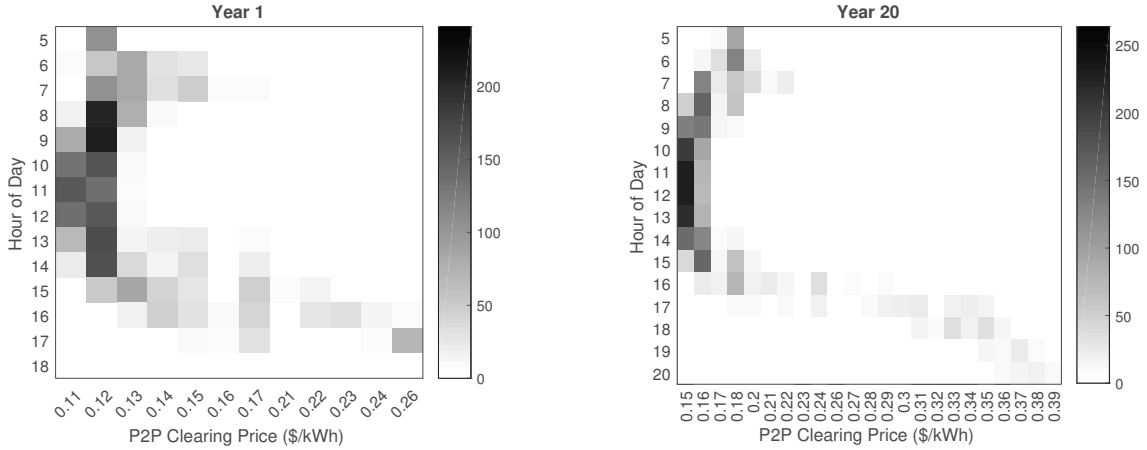

Figure E.3: Heat map of P2P clearing prices for each hour of the day in Year 1 and Year 20 (P2P simulation case B)

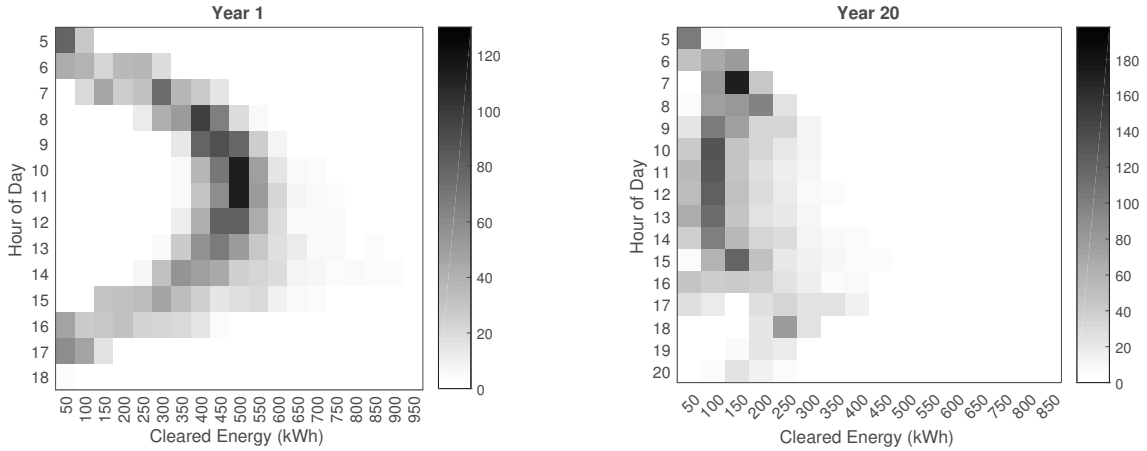

Figure E.4: Heat map of P2P cleared energy for each hour of the day in Year 1 and Year 20 (P2P simulation case B)

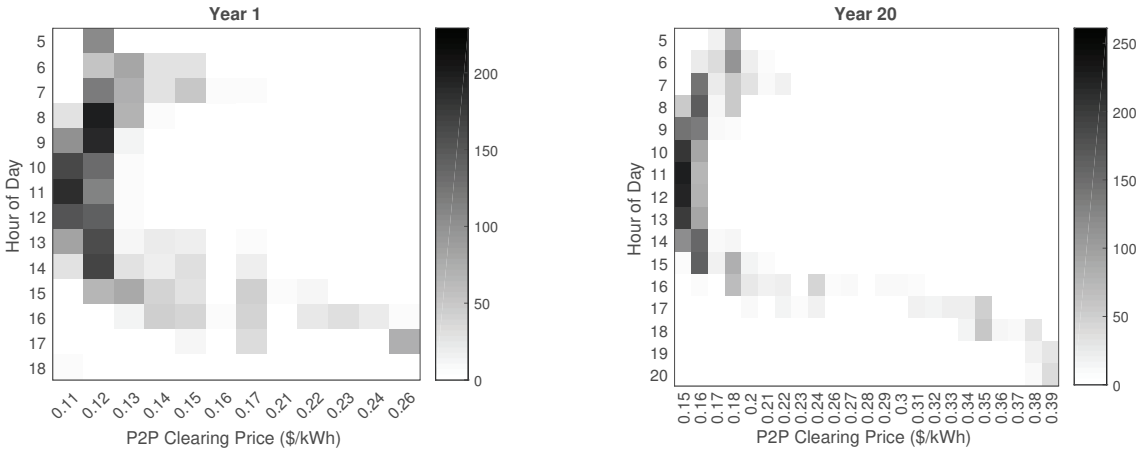

Figure E.5: Heat map of P2P clearing prices for each hour of the day in Year 1 and Year 20 (P2P simulation case C)

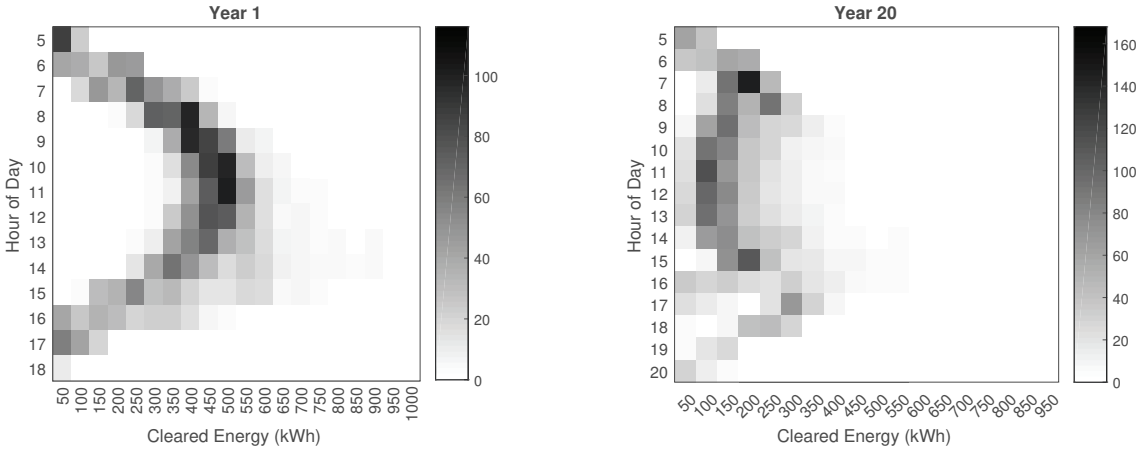

Figure E.6: Heat map of P2P cleared energy for each hour of the day in Year 1 and Year 20 (P2P simulation case C)

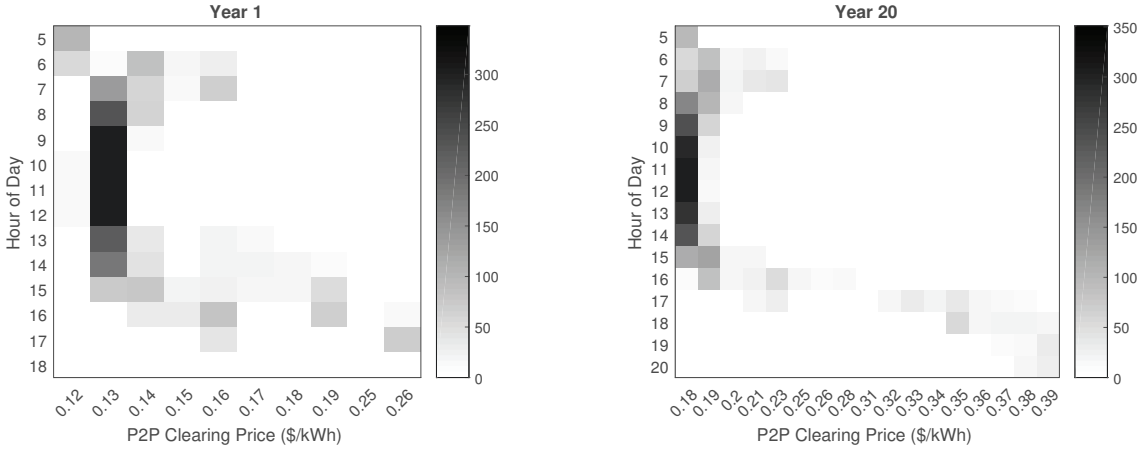

Figure E.7: Heat map of P2P clearing prices for each hour of the day in Year 1 and Year 20 (P2P simulation case D)

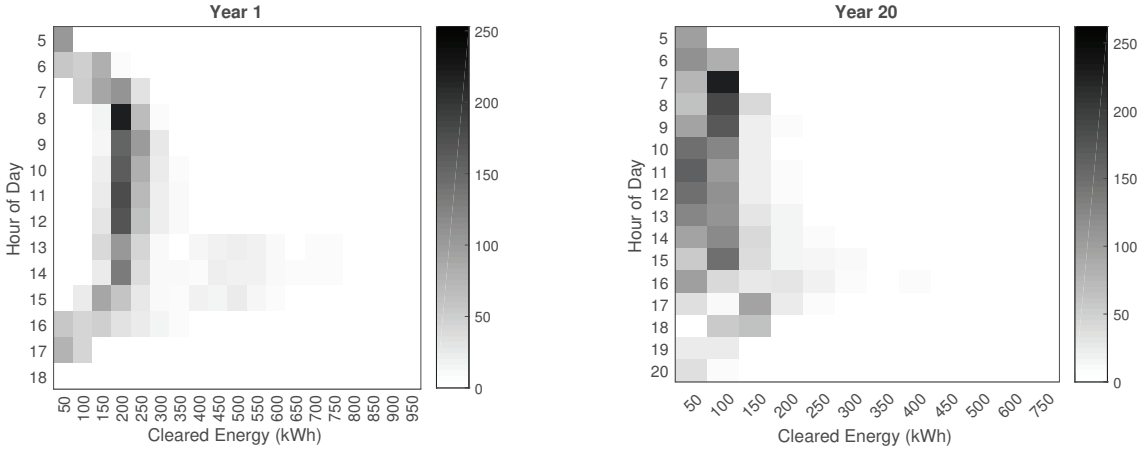

Figure E.8: Heat map of P2P cleared energy for each hour of the day in Year 1 and Year 20 (P2P simulation case D)

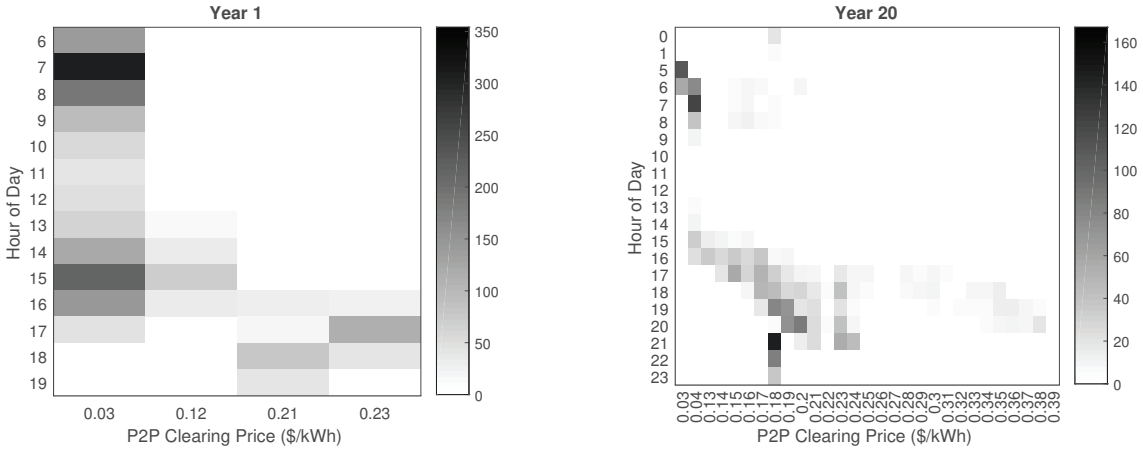

Figure E.9: Heat map of P2P clearing prices for each hour of the day in Year 1 and Year 20 (P2P simulation case E)

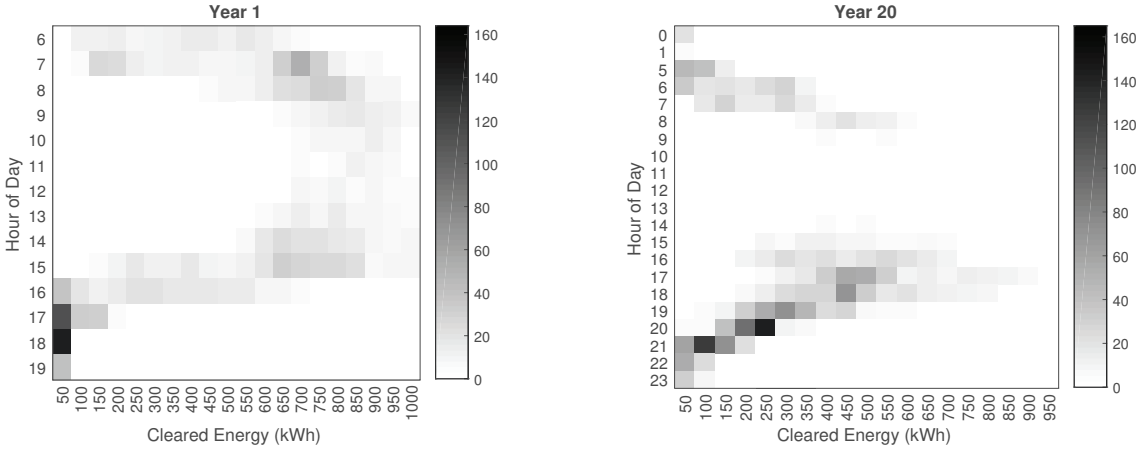

Figure E.10: Heat map of P2P cleared energy for each hour of the day in Year 1 and Year 20 (P2P simulation case E)

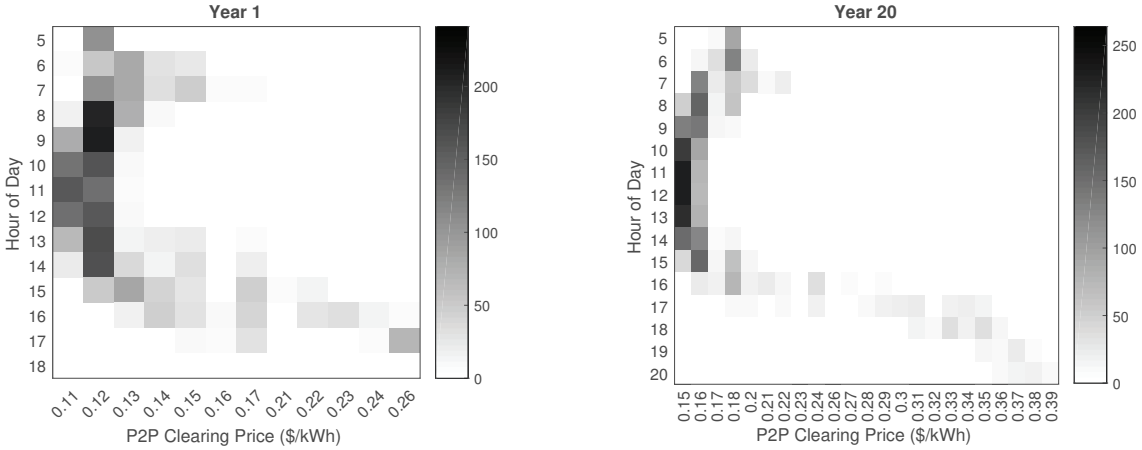

Figure E.11: Heat map of P2P clearing prices for each hour of the day in Year 1 and Year 20 (P2P simulation case F)

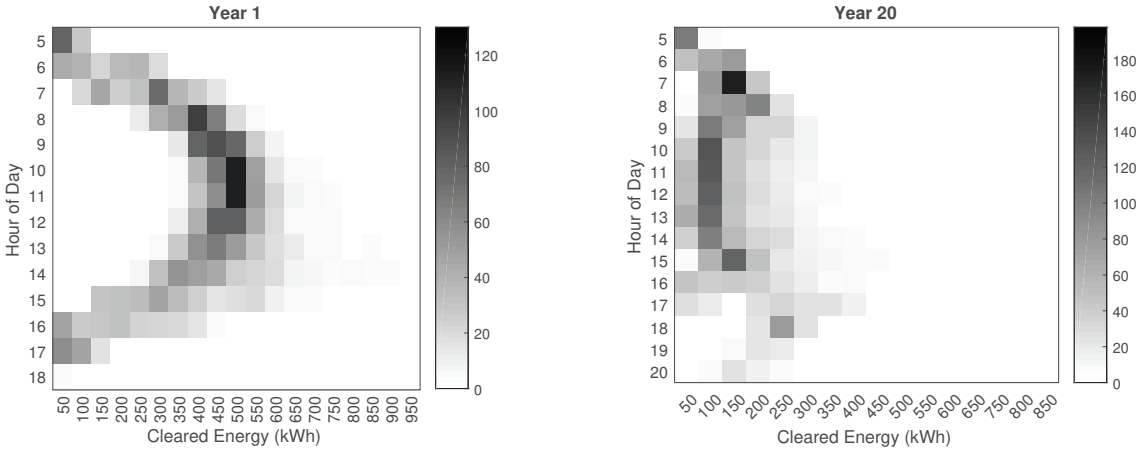

Figure E.12: Heat map of P2P cleared energy for each hour of the day in Year 1 and Year 20 (P2P simulation case F)

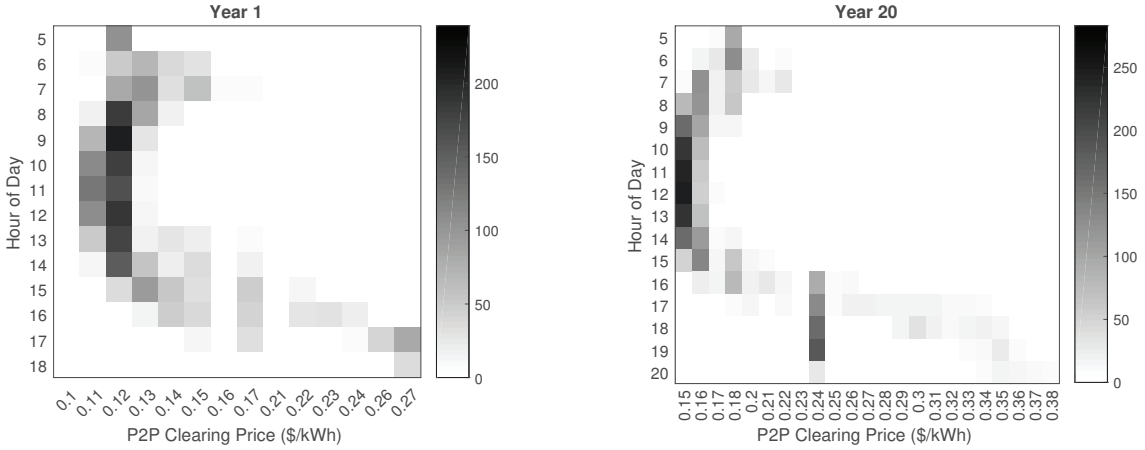

Figure E.13: Heat map of P2P clearing prices for each hour of the day in Year 1 and Year 20 (P2P simulation case G)

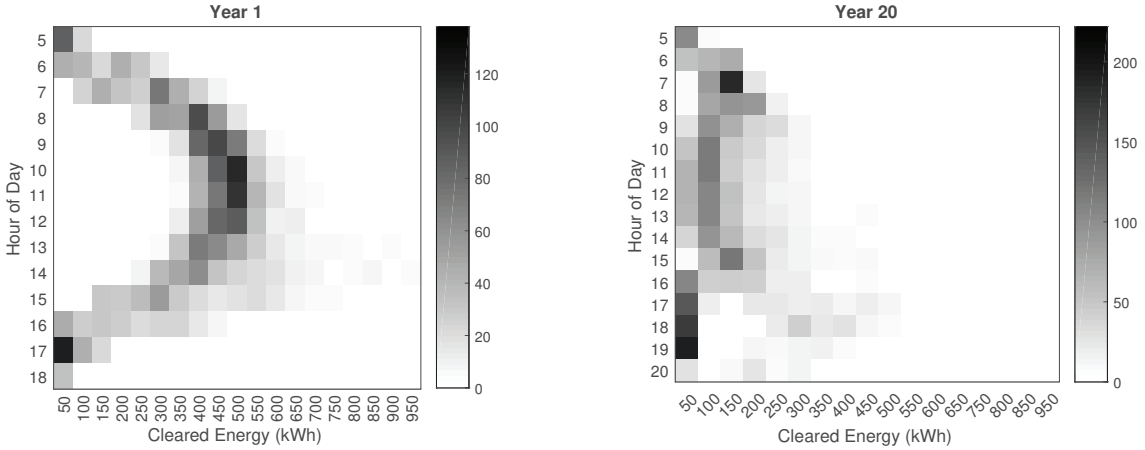

Figure E.14: Heat map of P2P cleared energy for each hour of the day in Year 1 and Year 20 (P2P simulation case G)

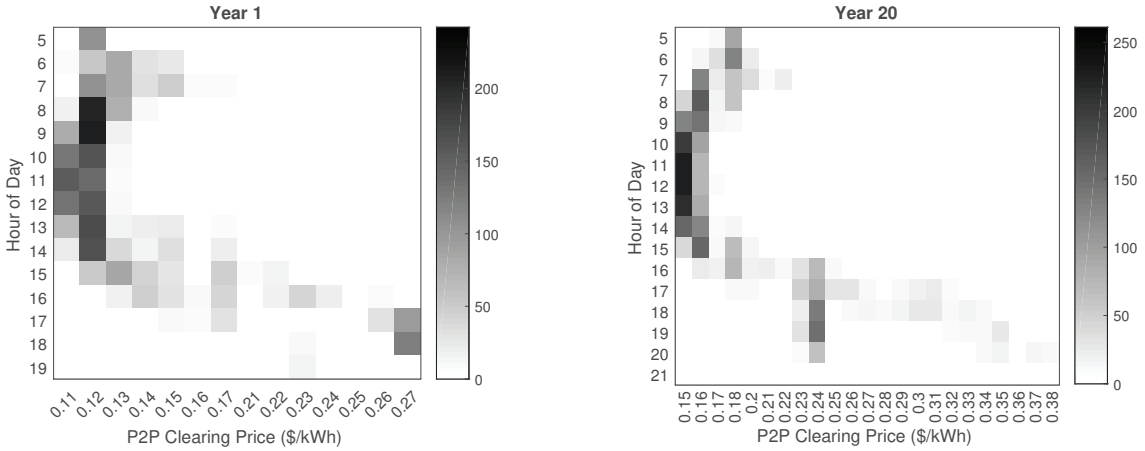

Figure E.15: Heat map of P2P clearing prices for each hour of the day in Year 1 and Year 20 (P2P simulation case H)

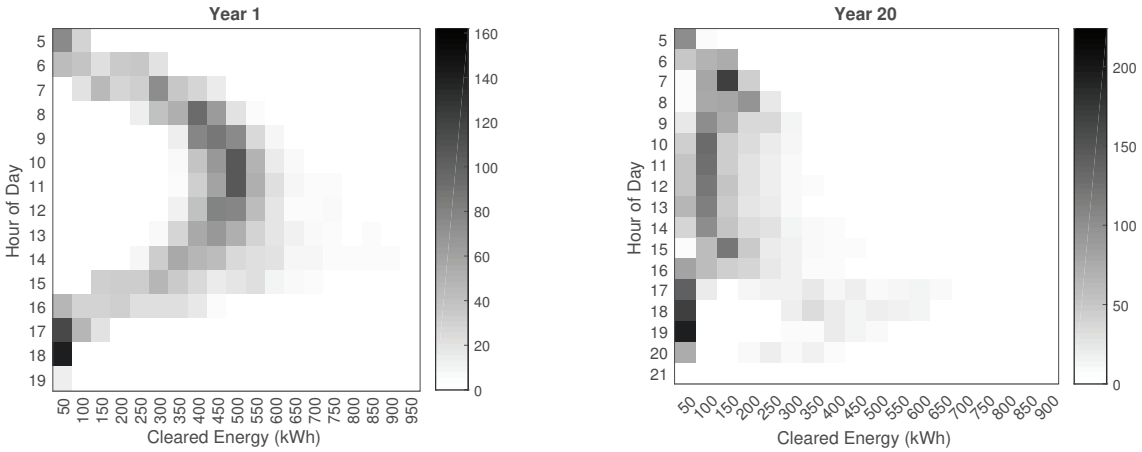

Figure E.16: Heat map of P2P cleared energy for each hour of the day in Year 1 and Year 20 (P2P simulation case H)

E.2 Optimised DER Average Energy Flow

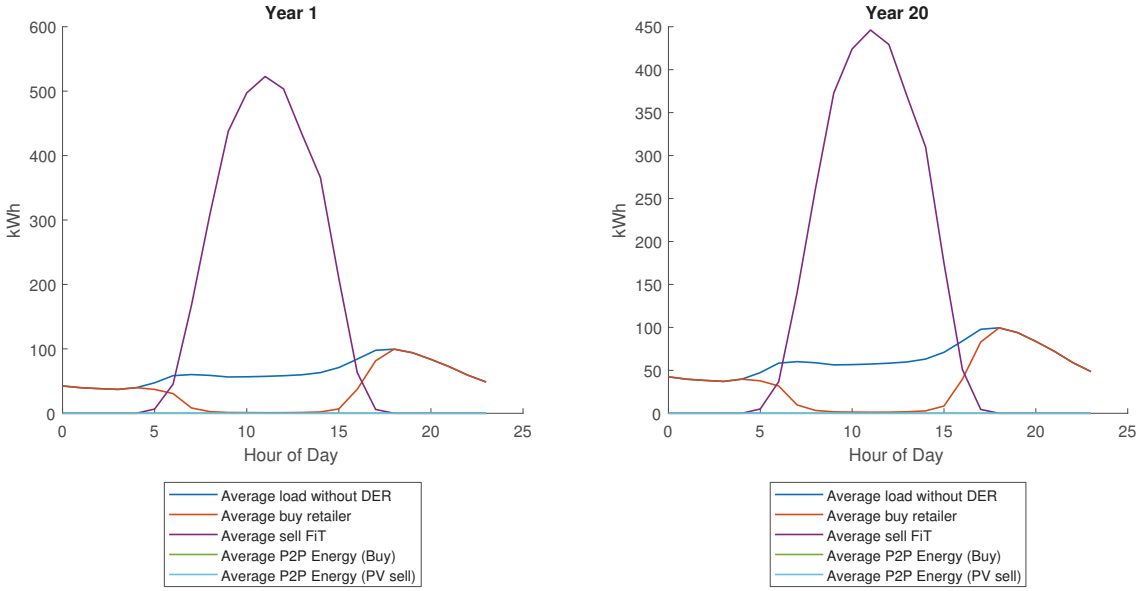

Figure E.17: Average energy purchases and sales across 100 test customers in Year 1 and Year 20 (Scenario 0)

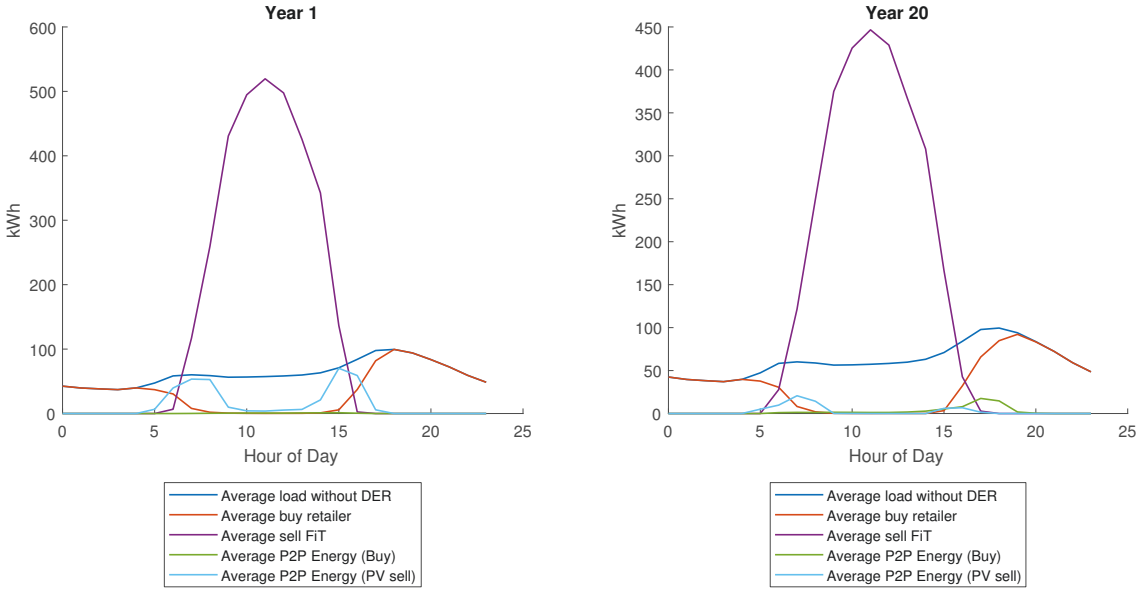

Figure E.18: Average energy purchases and sales across 100 test customers in Year 1 and Year 20 (Scenario 1a)

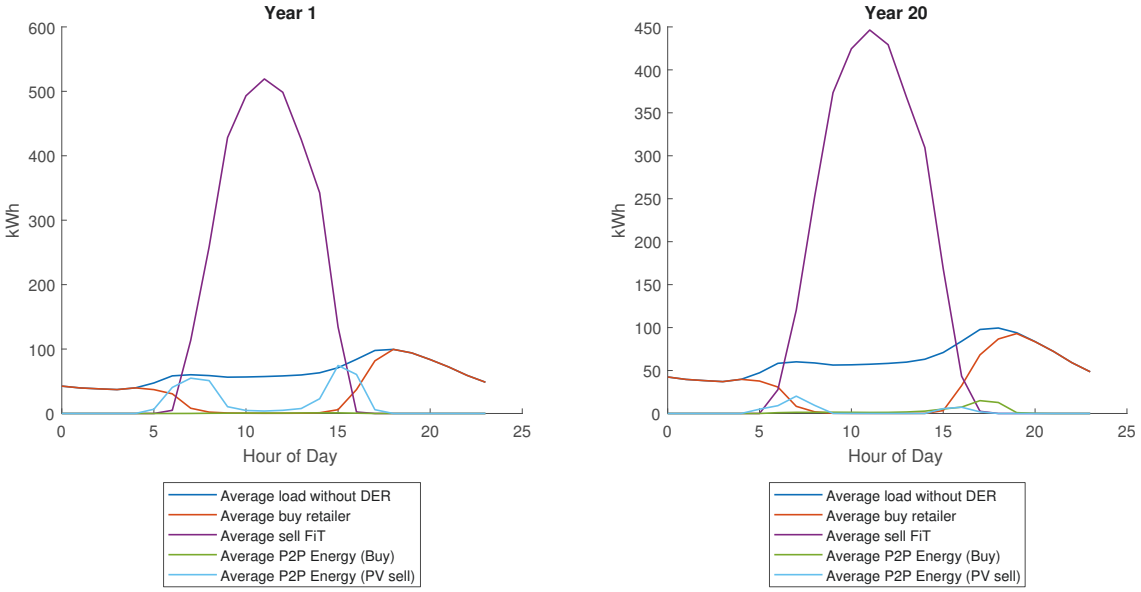

Figure E.19: Average energy purchases and sales across 100 test customers in Year 1 and Year 20 (Scenario 1b)

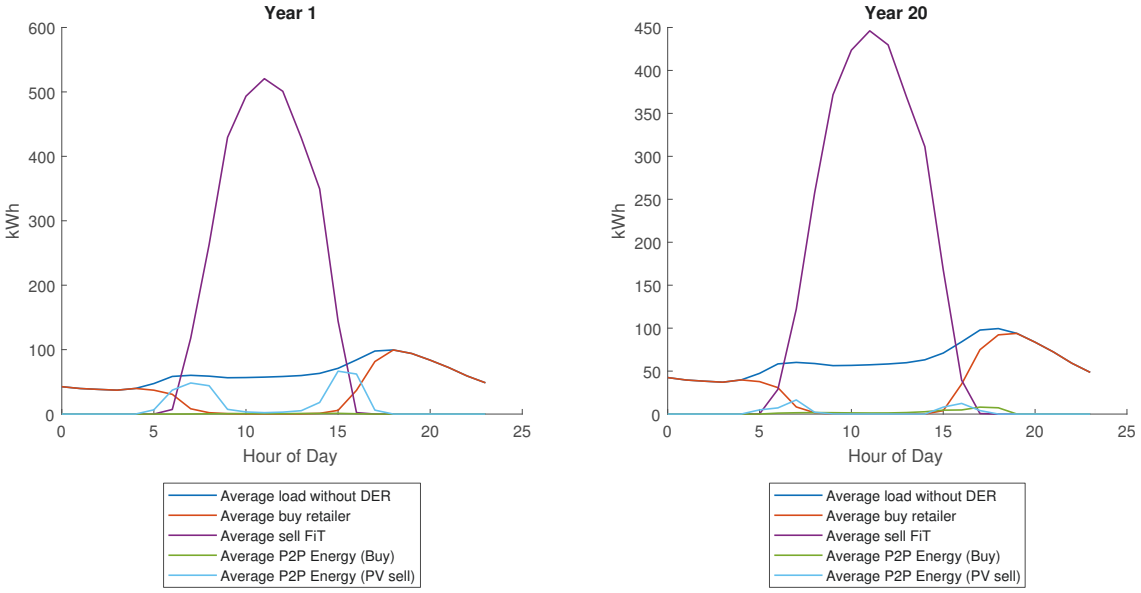

Figure E.20: Average energy purchases and sales across 100 test customers in Year 1 and Year 20 (Scenario 1c)

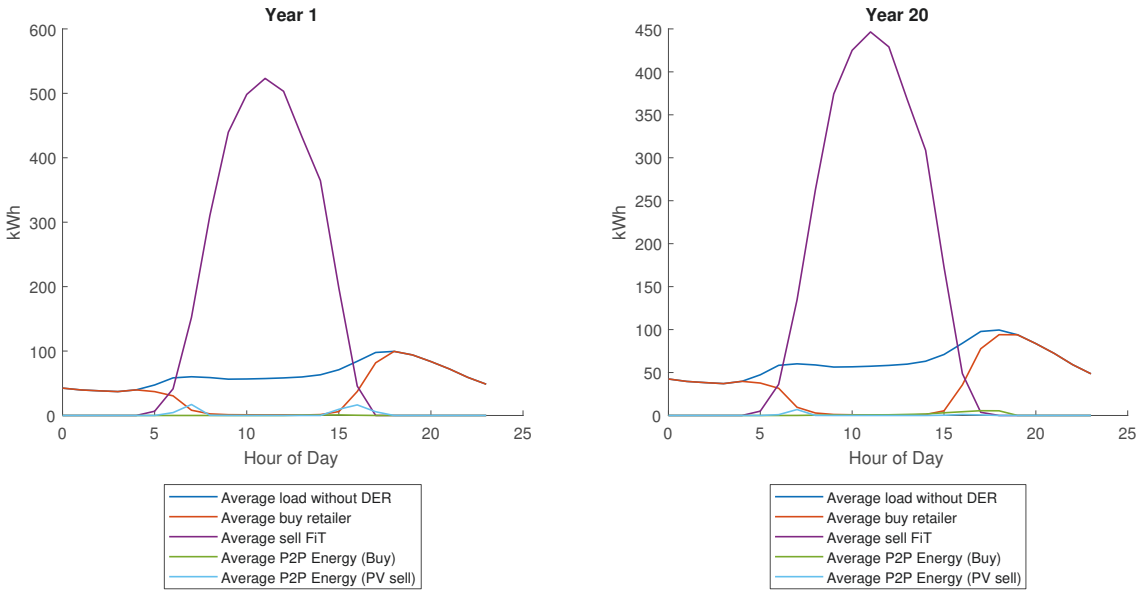

Figure E.21: Average energy purchases and sales across 100 test customers in Year 1 and Year 20 (Scenario 2)

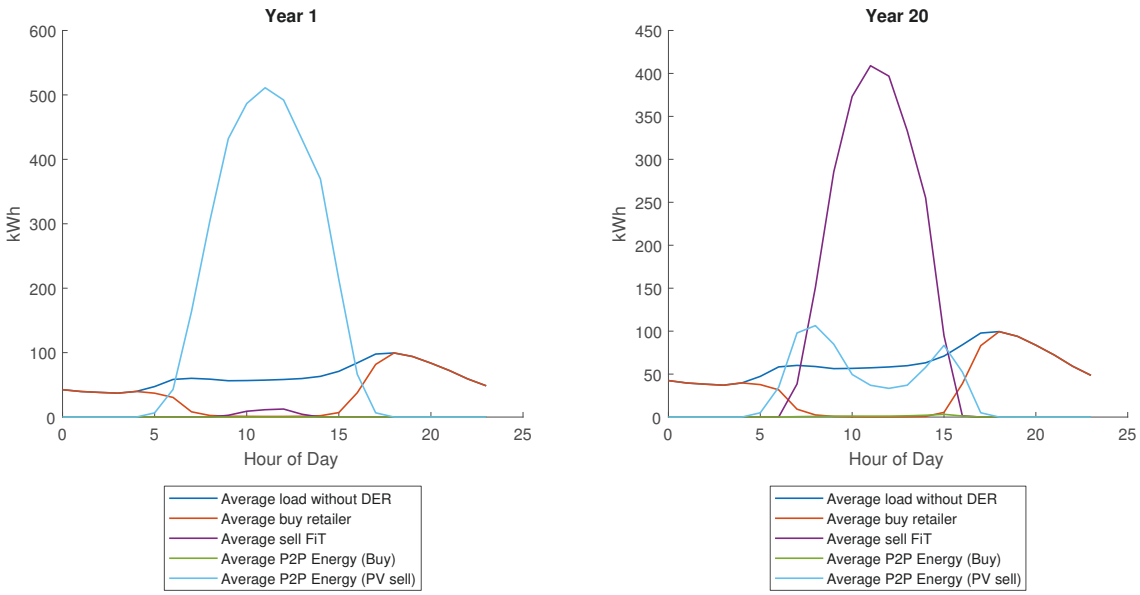

Figure E.22: Average energy purchases and sales across 100 test customers in Year 1 and Year 20 (Scenario 3)

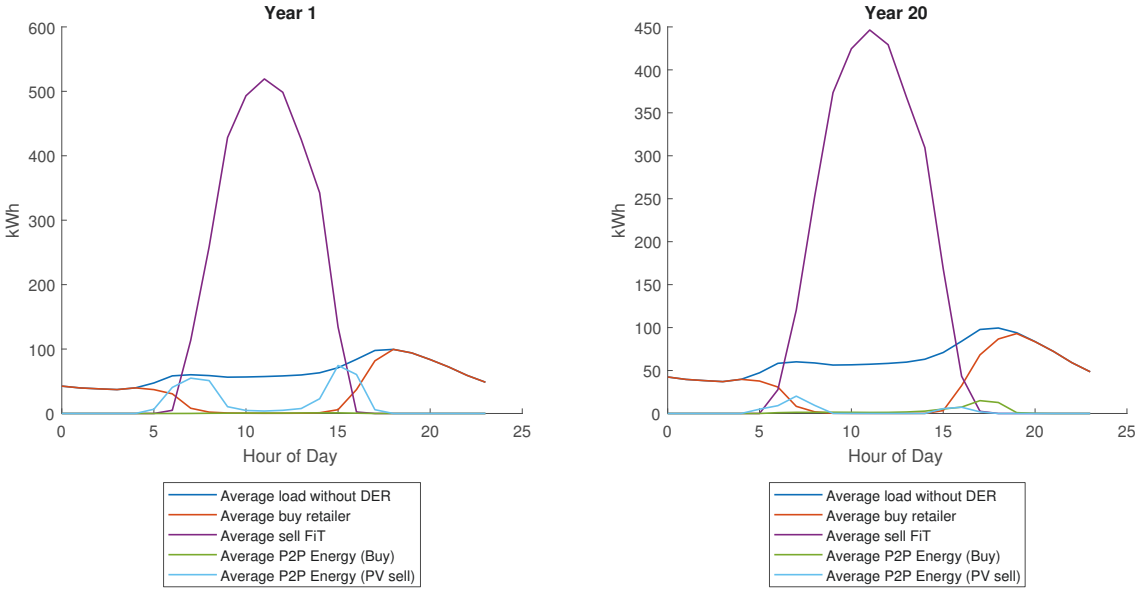

Figure E.23: Average energy purchases and sales across 100 test customers in Year 1 and Year 20 (Scenario 6)

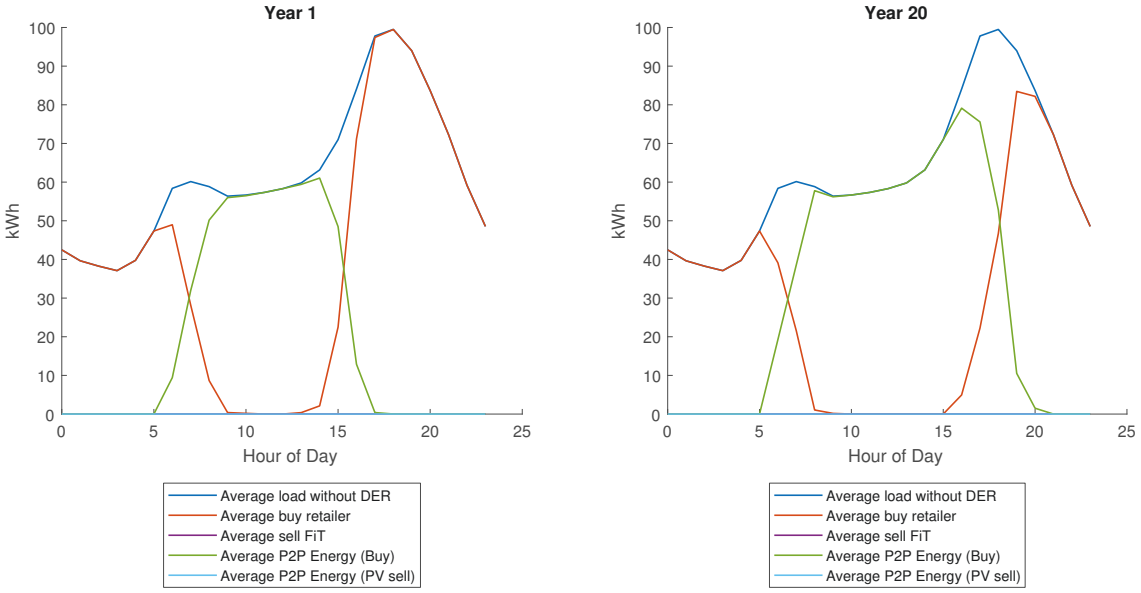

Figure E.24: Average energy purchases and sales across 100 test customers in Year 1 and Year 20 (Scenario 7a)

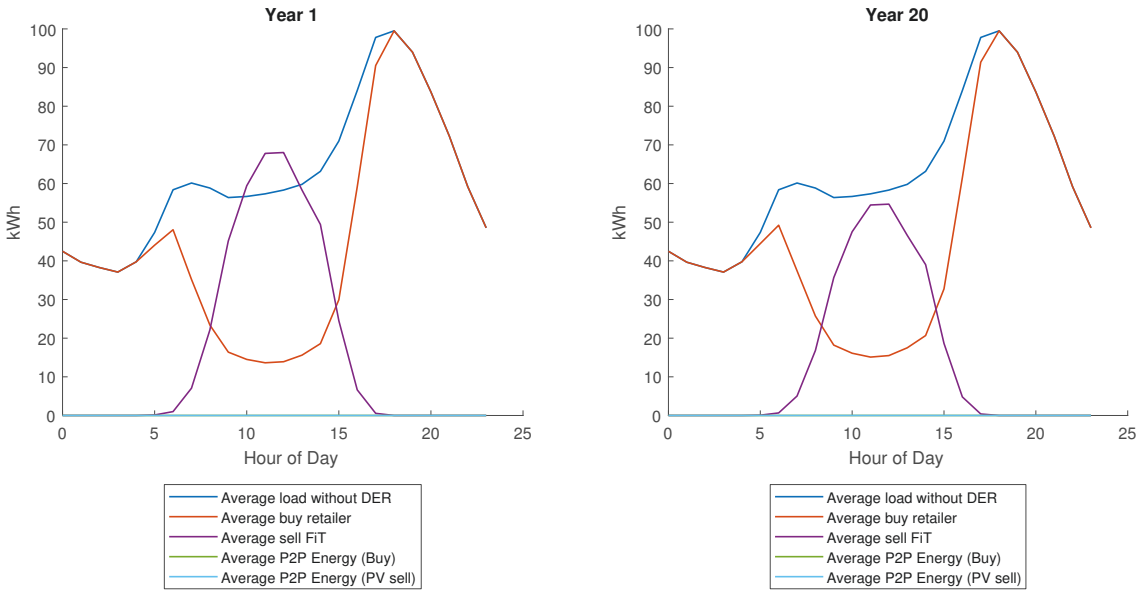

Figure E.25: Average energy purchases and sales across 100 test customers in Year 1 and Year 20 (Scenario 7b)

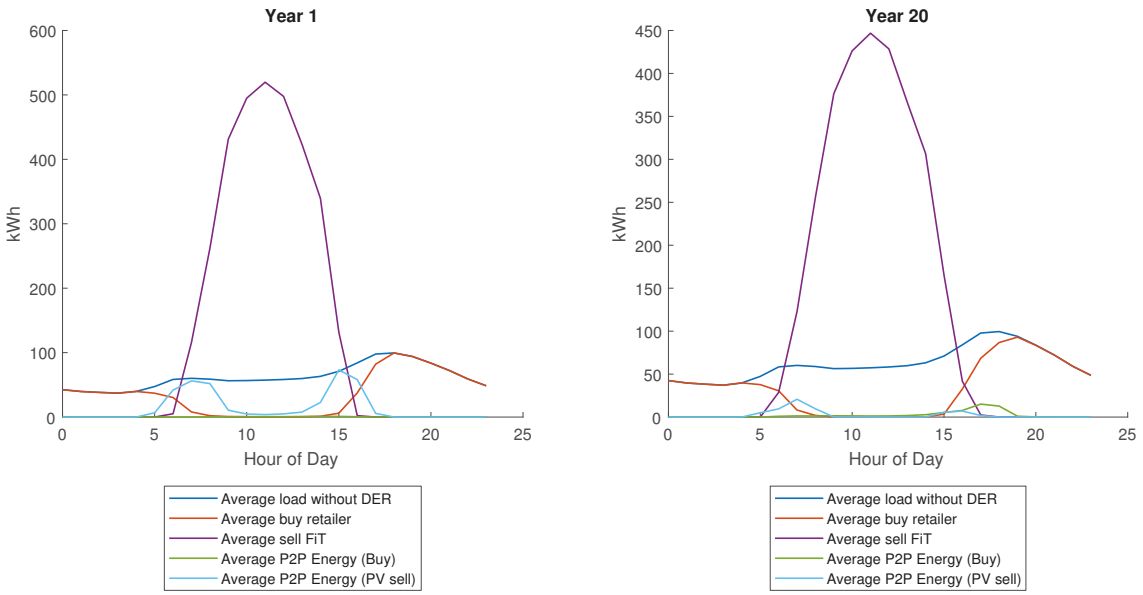

Figure E.26: Average energy purchases and sales across 100 test customers in Year 1 and Year 20 (Scenario 8)

Bibliography

[1] M. Norris, R. Cliff, R. Sharp, S. Koci, and H. Gardner, "Smart Grid, Smart City: Shaping Australia's energy future executive report," Arup, Report, July 2014.

[2] International Energy Agency, "Technology roadmap: Energy storage," Report, 2014. [Online]. Available: http://www.iea.org/publications/freepublications/publication/technology-roadmap-solar-photovoltaic-energy---2014-edition.html

[3] P. W. Parfomak, "Energy storage for power grids and electric transportation: A technology assessment," in *Energy Storage Technologies for Power Grids and Electric Transportation*, ser. Energy Policies, Politics and Prices, R. M. Burns and R. M. Ford, Eds. New York: Nova Science Publishers, 2012, ch. 1, pp. 1–127.

[4] Office of Energy Efficiency and Renewable Energy - Vehicle Technologies Office, "Fiscal year 2013 annual progress report for energy storage R&D," U.S. Department of Energy, Report DOE/EE-1038, February 2014.

[5] Y. Nishi, "Past, present and future of lithium-ion batteries: Can new technologies open up new horizons?" in *Lithium-Ion Batteries: Advances and Applications*, G. Pistoia, Ed. Amsterdam: Elsevier, 2014, ch. 2.

[6] P. S. Fox-Penner, *Smart Power: Climate Change, the Smart Grid, and the Future of Electric Utilities*. Washington, DC: Island Press, 2010.

[7] T. Sousa *et al.*, "Peer-to-peer and community-based markets: A comprehensive review," *Renewable and Sustainable Energy Reviews*, vol. 104, pp. 367–378, 2019.

[8] J. Ruotsalainen, J. Karjalainen, M. Child, and S. Heinonen, "Culture, values, lifestyles, and power in energy futures: A critical peer-to-peer vision for renewable energy," *Energy Research & Social Science*, vol. 34, pp. 231–239, 2017.

[9] X. Feng, J. Stoupis, S. Mohagheghi, and M. Larsson, "Introduction to smart grid applications," in *Smart Grid: Applications, Communications, and Security*, L. T. Berger and K. Iniewski, Eds. Hoboken, N.J.: Wiley, 2012, ch. 1, p. 464.

[10] P. Palensky and D. Dietrich, "Demand side management: Demand response, intelligent energy systems, and smart loads," *IEEE Transactions on Industrial Informatics*, vol. 7, no. 3, pp. 381–388, 2011.

[11] M. Tasdighi, H. Ghasemi, and A. Rahimi-Kian, "Residential microgrid scheduling based on smart meters data and temperature dependent thermal load modeling," *IEEE Transactions on Smart Grid*, vol. 5, no. 1, pp. 349–357, 2014.

[12] O. Tan, D. Gunduz, and H. V. Poor, "Increasing smart meter privacy through energy harvesting and storage devices," *Selected Areas in Communications, IEEE Journal on*, vol. 31, no. 7, pp. 1331–1341, 2013.

[13] M. Norris, R. Cliff, R. Sharp, S. Koci, and H. Gardner, "Smart Grid, Smart City: Shaping Australia's energy future national cost benefit assessment," Arup, Report, Jul. 2014.

[14] Victorian Government. (2015, 28 March) Smart meters: End of rollout. [Online]. Available: http://www.smartmeters.vic.gov.au/about-smart-meters/end-of-rollout

[15] Council of European Energy Regulators, "Status review of regulatory aspects of smart metering - including an assessment of roll-out as of 1 January 2013," Report C13-RMF-54-05, 12 September 2013.

[16] M. Gonzalez, "Smart grid investment grows with widespread smart meter installations," Worldwatch Institute, Report, 22 May 2014.

[17] Department of Energy and Climate Change, "Smart meters, Great Britain, quarterly report to end December 2014," Government of the United Kingdom,, Report, 19 March 2015.

[18] Office of Electricity Delivery and Energy Reliability, "Smart grid investment grant program progress report II," U.S. Department of Energy,, Report, October 2013.

[19] Deloitte, "Advanced metering infrastructure cost benefit analysis final report," Victorian Department of Treasury and Finance, Report, 2 August 2011.

[20] A. Faruqui, R. Hledik, and J. Tsoukalis, "The power of dynamic pricing," *The Electricity Journal*, vol. 22, no. 3, pp. 42–56, 2009.

[21] L. McIntosh, E. Langham, J. Rutovitz, and A. Atherton, "Methodology for calculating a local network credit," Institute for Sustainable Futures, Report, August 2016.

[22] PG&E. (2015) Demand bidding program (DBP). [Online]. Available: http://www.pge.com/en/mybusiness/save/energymanagement/dbp/index.page

[23] A. H. Mohsenian-Rad and A. Leon-Garcia, "Optimal residential load control with price prediction in real-time electricity pricing environments," *IEEE Transactions on Smart Grid*, vol. 1, no. 2, pp. 120–133, 2010.

[24] S. Borenstein, M. Jaske, and A. Rosenfeld, "Dynamic pricing, advanced metering, and demand response in electricity markets," University of California Energy Institute - Center for the Study of Energy Markets, Report, October 2002.

[25] N. Hatziargyriou, H. Asano, R. Iravani, and C. Marnay, "Microgrids," *Power and Energy Magazine, IEEE*, vol. 5, no. 4, pp. 78–94, 2007.

[26] X. Hu and K. Tseng, "Integration of multiple modularized distributed energy resource devices into AC grid of buildings: Issue of active power circulation," *IEEE Transactions on Industrial Electronics*, vol. 61, no. 11, pp. 6118–6127, 2014.

[27] T. Wood and L. Carter, "Fair pricing for power," Grattan Institute,, Report 2014-8, July 2014.

[28] J. Moshövel *et al.*, "Analysis of the maximal possible grid relief from PV-peak-power impacts by using storage systems for increased self-consumption," *Applied Energy*, vol. 137, pp. 567–575, 2015.

[29] T. Wood, D. Blowers, and C. Chisholm, "Sundown, sunrise: How Australia can finally get solar power right," Grattan Institute,, Report 2015-2, May 2015.

[30] A. Zelenka, R. Perez, R. Seals, and D. Renné, "Effective accuracy of satellite-derived hourly irradiances," *Theoretical and Applied Climatology*, vol. 62, no. 3-4, pp. 199–207, 1999.

[31] M. Paulescu, E. Paulescu, P. Gravila, and V. Badescu, *Weather Modeling and Forecasting of PV Systems Operation*, ser. Green energy and technology. London; New York: Springer, 2013.

[32] ETH Zurich. (2017, 2017) Global Energy Balance Archive. [Online]. Available: http://www.geba.ethz.ch/

[33] World Meteorological Organization. (2017) World Radiation Data Centre. [Online]. Available: http://wrdc.mgo.rssi.ru/

[34] M. Wild *et al.*, "The global energy balance from a surface perspective," *Climate Dynamics*, vol. 40, no. 11, pp. 3107–3134, 2013.

[35] J. Remund *et al.*, "Meteonorm global meteorological database handbook part I: Software, version 7.2," Meteotest, Report, March 2017.

[36] C. Vernay, S. Pitaval, and P. Blanc, "Review of satellite-based surface solar irradiation databases for the engineering, the financing and the operating of photovoltaic systems," *Energy Procedia*, vol. 57, pp. 1383–1391, 2014.

[37] H. Gilgen, M. Wild, and A. Ohmura, "Means and trends of shortwave irradiance at the surface estimated from Global Energy Balance Archive data," *Journal of Climate*, vol. 11, no. 8, pp. 2042–2061, 1998.

[38] J. Remund *et al.*, "Meteonorm global meteorological database handbook part II: Theory, version 7.2," Meteotest, Report, March 2017.

[39] R. J. Aguiar, M. Collares-Pereira, and J. P. Conde, "Simple procedure for generating sequences of daily radiation values using a library of Markov transition matrices," *Solar Energy*, vol. 40, no. 3, pp. 269–279, 1988.

[40] R. Aguiar and M. Collares-Pereira, "TAG: A time-dependent, autoregressive, Gaussian model for generating synthetic hourly radiation," *Solar Energy*, vol. 49, no. 3, pp. 167–174, 1992.

[41] National Renewable Energy Laboratory. (2017) About the National Solar Radiation Database. [Online]. Available: https://nsrdb.nrel.gov/about

[42] ——. (2017) Weather data. [Online]. Available: https://energyplus.net/weather

[43] Alfred Wegener Institute. (2017) World Radiation Monitoring Center - Baseline Surface Radiation Network. [Online]. Available: http://bsrn.awi.de/

[44] Australian Government Bureau of Meteorology. (2012, 26 August) One minute solar data. [Online]. Available: http://www.bom.gov.au/climate/data/oneminsolar/about-IDCJAC0022.shtml

[45] Solargis s.r.o., "Solargis solar resource database: Description and accuracy," Report, 2016. [Online]. Available: http://solargis.com/assets/doc/Solargis-database-description-and-accuracy.pdf

[46] Vaisala, "Vaisala 3TIER services global solar dataset - Methodology and validation," Report B211641EN-A, 2017.

[47] P. Ineichen, "Five satellite products deriving beam and global irradiance validation on data from 23 ground stations," University of Geneva, Report, 2011.

[48] MINES ParisTech/Transvalor. (2017, July 2017) SoDa: Web services. [Online]. Available: http://www.soda-pro.com/web-services#top

[49] C. Rigollier, M. Lefèvre, and L. Wald, "The method Heliosat-2 for deriving shortwave solar radiation from satellite images," *Solar Energy*, vol. 77, no. 2, pp. 159–169, 2004.

[50] MINES ParisTech/Transvalor. (2016, October 2016) Heliosat-2. [Online]. Available: http://www.soda-pro.com/help/helioclim/heliosat-2

[51] National Aeronautics and Space Administration. (2017) Surface meteorology and Solar Energy. [Online]. Available: https://eosweb.larc.nasa.gov/sse/

[52] R. Perez *et al.*, "A new operational model for satellite-derived irradiances: Description and validation," *Solar Energy*, vol. 73, no. 5, pp. 307–317, 2002.

[53] ——, "Satellite-to-irradiance modeling - A new version of the SUNY model," in *2015 IEEE 42nd Photovoltaic Specialist Conference (PVSC)*, 14-19 June 2015 2015, Conference Proceedings, pp. 1–7.

[54] European Commission Joint Research Centre. (2018, 10 May 2017) PVGIS users manual. [Online]. Available: http://re.jrc.ec.europa.eu/pvg_static/en/manual.html

[55] Australian Government Bureau of Meteorology. (2013, 13 December) Climate data online. [Online]. Available: http://www.bom.gov.au/climate/data/

[56] ——, "Gridded hourly solar global horizontal irradiance metadata," 2016. [Online]. Available: http://www.bom.gov.au/climate/data-services/docs/Metadata_IDCJAD0026_gridded_hourly_GHI.pdf

[57] G. T. Weymouth and J. F. Le Marshall, "Estimation of daily surface solar exposure using GMS-5 stretched-VISSR observations: the system and basic results." *Australian Meteorology Magazine*, vol. 50, no. 4, pp. 263–278, 2001.

[58] B. Ridley, J. Boland, and P. Lauret, "Modelling of diffuse solar fraction with multiple predictors," *Renewable Energy*, vol. 35, no. 2, pp. 478–483, 2010.

[59] C. Blanksby, D. Bennett, and S. Langford, "Improvement to an existing satellite data set in support of an Australia solar atlas," *Solar Energy*, vol. 98, pp. 111–124, 2013.

[60] R. J. Davy, J. R. Huang, and A. Troccoli, "Improving the accuracy of hourly satellite-derived solar irradiance by combining with dynamically downscaled estimates using generalised additive models," *Solar Energy*, vol. 135, pp. 854–863, 2016.

[61] Australian Renewable Energy Agency, "Integrated solar radiation data sources over Australia - Final report: Project results and lessons learnt," Report, August 2015.

[62] Australian Government Bureau of Meteorology. (2016, 27 June) Australian hourly solar irradiance gridded data. [Online]. Available: http://www.bom.gov.au/climate/how/newproducts/IDCJAD0111.shtml

[63] Australian Renewable Energy Agency, "Australian Renewable Energy Mapping Infrastructure," 8 March 2017 2017. [Online]. Available: https://nationalmap.gov.au/renewables/

[64] A. Hammer, "Documentation - EnMetSOL: Satellite data - Available regions at Oldenburg University," University of Oldenburg, Report, 14 March 2016.

[65] T. Huld, R. Müller, and A. Gambardella, "A new solar radiation database for estimating PV performance in Europe and Africa," *Solar Energy*, vol. 86, no. 6, pp. 1803–1815, 2012.

[66] Satel-light. (2017) The European of daylight and solar radiation. [Online]. Available: http://www.satellight.com/indexgA.htm

[67] C. Hoyer-Klick, M. Lefèvre, A. Oumbe, M. Schroedter Homscheidt, and L. Wald, "User's guide to the SoDa and SOLEMI services," Report, 2010.

[68] R. Meyer *et al.*, "SOLEMI: A new satellite-based service for high-resolution and precision solar radiation data for Europe, Africa and Asia," in *ISES Solar World Congress*, June 2003, Conference Proceedings.

[69] Clean Power Research. (2017, 2017) SolarAnywhere. [Online]. Available: https://www.solaranywhere.com/

[70] Australian Government Bureau of Meteorology, "Gridded hourly solar direct normal irradiance metadata," 2016. [Online]. Available: http://www.bom.gov.au/climate/data-services/docs/Metadata_IDCJAD0027_gridded_hourly_DNI.pdf

[71] J. Stackhouse, P.W. *et al.*, "Surface meteorology and Solar Energy (SSE) release 6.0 methodology version 3.2.0," NASA, Report, 2 June 2016.

[72] A. Hammer *et al.*, "Direct normal irradiance for CSP based on satellite images of Meteosat Second Generation," in *SolarPACES*, Berlin, 2009, Conference Proceedings.

[73] J. Trentmann and U. Pfeifroth, "Algorithm theoretical baseline document meteosat solar surface radiation and effective cloud albedo climate data records - Heliosat," EUMETSAT Satellite Applications Facility on Climate Monitoring, Report SAF/CM/DWD/ATBD/METEOSAT/HEL 2.2, 11 January 2017.

[74] J. Trentmann, U. Pfeifroth, and S. Kothe, "Product user manual meteosat solar surface irradiance and effective cloud albedo climate data records SARAH 2," EUMETSAT Satellite Applications Facility on Climate Monitoring, Report SAF/CM/DWD/PUM/METEOSAT/HEL 2.1, 11 January 2017.

[75] National Aeronautics and Space Administration. (2018) MODIS - Moderate Resolution Imaging Spectroradiometer. [Online]. Available: https://modis.gsfc.nasa.gov/about/

[76] ECMWF. (2018) Copernicus atmosphere monitoring system. [Online]. Available: https://atmosphere.copernicus.eu/

[77] National Aeronautics and Space Administration. (2018) Global Modelling and Assimilation Office - Reanalysis. [Online]. Available: https://gmao.gsfc.nasa.gov/reanalysis/MERRA/

[78] M. Lefèvre, "Joint report on interpolation scheme "Meteosat" and database "Climatology I (Meteosat)"," Report, 2002.

[79] C. A. Gueymard, "A globally calibrated aerosol optical depth gridded dataset for improved solar irradiance predictions," in *EGU General Assembly*, vol. 14, Vienna, Austria, 2012, Conference Proceedings, p. 1.

[80] M. Sengupta *et al.*, "A physics-based GOES satellite product for use in NREL's National Solar Radiation Database: Preprint," NREL, Report NREL/CP-5D00-62237, 2014.

[81] National Aeronautics and Space Administration. (2018) MISR - Multi-angle Imaging SpectroRadiometer. [Online]. Available: https://www-misr.jpl.nasa.gov/

[82] ——. (2018, 11 January 2018) AERONET - Aerosol Robotic Network. [Online]. Available: https://aeronet.gsfc.nasa.gov/

[83] J. Remund, L. Wald, M. Lefèvre, T. Ranchin, and H. Page, John, "Worldwide linke turbidity information," in *ISES Solar World Congress 2003*. Göteborg, Sweden: International Solar Energy Society (ISES), 16-19 June 2003, Conference Proceedings, p. 13 p.

[84] H. G. Beyer, C. Costanzo, and D. Heinemann, "Modifications of the Heliosat procedure for irradiance estimates from satellite images," *Solar Energy*, vol. 56, no. 3, pp. 207–212, 1996.

[85] D. Dumortier, "The satellight model of turbidity variations in Europe," Ecole Nationale des Travaux Publics de l'Etat, Report, September 1998.

[86] National Oceanic and Atmospheric Administration. Global forecast system (GFS). [Online]. Available: https://www.ncdc.noaa.gov/data-access/model-data/model-datasets/global-forcast-system-gfs

[87] A. Hammer, "Anwendungspezifische solarstrahlungsinformationen aus Meteosat-Daten," PhD thesis, 2000.

[88] A. Hammer *et al.*, "Solar energy assessment using remote sensing technologies," *Remote Sensing of Environment*, vol. 86, no. 3, pp. 423–432, 2003.

[89] D. Cano *et al.*, "A method for the determination of the global solar radiation from meteorological satellite data," *Solar Energy*, vol. 37, no. 1, pp. 31–39, 1986.

[90] D. P. Dee *et al.*, "The ERA-interim reanalysis: Configuration and performance of the data assimilation system," *Quarterly Journal of the Royal Meteorological Society*, vol. 137, no. 656, pp. 553–597, 2011.

[91] R. Perez, P. Ineichen, E. Maxwell, R. Seals, and A. Zelenka, "Dynamic global-to-direct irradiance conversion models," *ASHRAE Transactions*, vol. 98, no. 1, pp. 354–369, 1992.

[92] C. A. Gueymard, "REST2: High-performance solar radiation model for cloudless-sky irradiance, illuminance, and photosynthetically active radiation - Validation with a benchmark dataset," *Solar Energy*, vol. 82, no. 3, pp. 272–285, 2008.

[93] C. Rigollier, O. Bauer, and L. Wald, "On the clear sky model of the ESRA - European Solar Radiation Atlas - With respect to the Heliosat method," *Solar Energy*, vol. 68, no. 1, pp. 33–48, 2000.

[94] R. Perez, P. Ineichen, E. Maxwell, R. Seals, and A. Zelenka, "Dynamic models for hourly global-to-direct irradiance conversion," in *Proceedings of ISES World Congress*, Denver, Colorado, 1991, Conference Proceedings.

[95] E. Maxwell, "A quasi-physical model for converting hourly global to direct normal insolation," Solar Energy Research Institute, Report SERI/TR-215-3087, August 1987.

[96] R. W. Mueller *et al.*, "Rethinking satellite-based solar irradiance modelling: The SOLIS clear-sky module," *Remote Sensing of Environment*, vol. 91, no. 2, pp. 160–174, 2004.

[97] Z. Qu, B. Gschwind, M. Lefevre, and L. Wald, "Improving HelioClim-3 estimates of surface solar irradiance using the McClear clear-sky model and recent advances in atmosphere composition," *Atmos. Meas. Tech.*, vol. 7, no. 11, pp. 3927–3933, 2014, aMT.

[98] M. Lefèvre *et al.*, "McClear: A new model estimating downwelling solar radiation at ground level in clear-sky conditions," *Atmos. Meas. Tech.*, vol. 6, no. 9, pp. 2403–2418, 2013, aMT.

[99] M. Geiger, L. Diabaté, L. Ménard, and L. Wald, "A web service for controlling the quality of measurements of global solar irradiation," *Solar Energy*, vol. 73, no. 6, pp. 475–480, 2002.

[100] J. Page, "Algorithms for the Satellight programme," Report, June 1996.

[101] D. Dumortier, "Mesure, analyse et modélisation du gisement lumineux. Application à l'évaluation des performances de l'éclairage naturel des bâtiments." PhD thesis, 1995.

[102] A. Skartveit, J. A. Olseth, and M. E. Tuft, "An hourly diffuse fraction model with correction for variability and surface albedo," *Solar Energy*, vol. 63, no. 3, pp. 173–183, 1998.

[103] P. Ineichen, "A broadband simplified version of the Solis clear sky model," *Solar Energy*, vol. 82, no. 8, pp. 758–762, 2008.

[104] ——, "Comparison and validation of three global-to-beam irradiance models against ground measurements," *Solar Energy*, vol. 82, no. 6, pp. 501–512, 2008.

[105] A. Kemper, "Bestimmung der diffusstrahlung unter wolken aus daten des satelliten MSG," Diploma thesis, 2007.

[106] M. Fontoynont *et al.*, "SatelLight: A WWW server which provides high quality daylight and solar radiation data for Western and Central Europe," in *9th Conference on Satellite Meteorology and Oceanography*, vol. EUM-P-22. Paris, France: American Meteorological Society Ed., Boston, Massachusetts, USA, 25 May 1998, Conference Proceedings, pp. 434–437.

[107] E. Lorenz, "Improved diffuse radiation model, MSG. Report for the EC-project PVSAT-2: Intelligent performance check of PV system operation based on satellite data," University of Oldenburg, Report, 2007.

[108] R. E. Bird and R. L. Hulstrom, "Review, evaluation, and improvement of direct irradiance models," *Journal of Solar Energy Engineering*, vol. 103, no. 3, pp. 182–192, 1981, 10.1115/1.3266239.

[109] M. Iqbal, *An Introduction to Solar Radiation*. Toronto: Academic Press, 1983.

[110] R. W. Mueller, C. Matsoukas, A. Gratzki, H. D. Behr, and R. Hollmann, "The CM-SAF operational scheme for the satellite based retrieval of solar surface irradiance - A LUT based eigenvector hybrid approach," *Remote Sensing of Environment*, vol. 113, no. 5, pp. 1012–1024, 2009.

[111] R. Mueller, T. Behrendt, A. Hammer, and A. Kemper, "A new algorithm for the satellite-based retrieval of solar surface irradiance in spectral bands," *Remote Sensing*, vol. 4, pp. 622–647, 2012.

[112] J. K. Copper and A. G. Bruce, "Comparison of annual global horizontal irradiation maps for Australia," in *Asia-Pacific Solar Research Conference*, Sydney, 4-6 December 2018, Conference Proceedings.

[113] B. Urschel. (2016, 19 Jul. 2005) The analemma. [Online]. Available: http://www.analemma.com/pages/framespage.html

[114] J. Spencer, "Fourier series representation of the position of the sun," *Search*, vol. 2 (5), no. 172, 1971.

[115] J. A. Duffie and W. A. Beckman, *Solar Engineering of Thermal Processes*. Hoboken, N.J.: Wiley, 2013, vol. 4th.

[116] J. Pickard and J. Spencer, "Fourier paper," 3 February 1998. [Online]. Available: https://www.mail-archive.com/sundial@uni-koeln.de/msg01050.html

[117] National Oceanic and Atmospheric Administration. (2016) Solar calculation details. [Online]. Available: http://www.esrl.noaa.gov/gmd/grad/solcalc/calcdetails.html

[118] N. A. Engerer and F. P. Mills, "Validating nine clear sky radiation models in Australia," *Solar Energy*, vol. 120, pp. 9–24, 2015.

[119] P. Ineichen, "Comparison of eight clear sky broadband models against 16 independent data banks," *Solar Energy*, vol. 80, no. 4, pp. 468–478, 2006.

[120] F. Kasten, "Parametriesirung der globalstahlung durch bedeckungsgrad und trubungsfaktor," *Annal. Meteorol. Neue Folge*, vol. 20, pp. 49–50, 1984.

[121] J. Copper, "Measurement and verification of solar irradiance and residential building simulation models for Australian climates," PhD thesis, 2012.

[122] C. A. Gueymard, "Clear-sky irradiance predictions for solar resource mapping and large-scale applications: Improved validation methodology and detailed performance analysis of 18 broadband radiative models," *Solar Energy*, vol. 86, no. 8, pp. 2145–2169, 2012.

[123] V. Badescu *et al.*, "Accuracy analysis for fifty-four clear-sky solar radiation models using routine hourly global irradiance measurements in romania," *Renewable Energy*, vol. 55, pp. 85–103, 2013.

[124] C. Long and Y. Shi, "The QCRad value added product: Surface radiation measurement quality control testing, including climatology configurable limits," DOE Office of Science Atmospheric Radiation Measurement (ARM) Program (United States), Report DOE/SC-ARM/TR-074, 2006.

[125] F. Kasten, "The linke turbidity factor based on improved values of the integral Rayleigh optical thickness," *Solar Energy*, vol. 56, no. 3, pp. 239–244, 1996.

[126] N. A. Engerer and F. P. Mills, "KPV: A clear-sky index for photovoltaics," *Solar Energy*, vol. 105, pp. 679–693, 2014.

[127] J. K. Copper and A. B. Sproul, "Comparative study of mathematical models in estimating solar irradiance for Australia," *Renewable Energy*, vol. 43, pp. 130–139, 2012.

[128] Q. Zhang, J. Huang, and S. Lang, "Development of typical year weather data for Chinese locations," *ASHRAE transactions*, vol. 108, p. 1063, 2002.

[129] D. Seo, J. Huang, and M. Krarti, "Development of models for hourly solar radiation prediction," *ASHRAE Transactions*, vol. 114, no. 1, 2008.

[130] D. Seo and M. Krarti, "Hourly solar radiation model suitable for worldwide typical weather file generation," *Journal of Solar Energy Engineering*, vol. 133, no. 4, pp. 041 002–041 002–8, 2011, 10.1115/1.4003883.

[131] A. M. Noorian, I. Moradi, and G. A. Kamali, "Evaluation of 12 models to estimate hourly diffuse irradiation on inclined surfaces," *Renewable Energy*, vol. 33, no. 6, pp. 1406–1412, 2008.

[132] J. L. Torres, M. De Blas, A. García, and A. de Francisco, "Comparative study of various models in estimating hourly diffuse solar irradiance," *Renewable Energy*, vol. 35, no. 6, pp. 1325–1332, 2010.

[133] C. Bertrand, G. Vanderveken, and M. Journée, "Evaluation of decomposition models of various complexity to estimate the direct solar irradiance over Belgium," *Renewable Energy*, vol. 74, pp. 618–626, 2015.

[134] C. A. Gueymard and J. A. Ruiz-Arias, "Extensive worldwide validation and climate sensitivity analysis of direct irradiance predictions from 1-min global irradiance," *Solar Energy*, vol. 128, pp. 1–30, 2016.

[135] G. Abal, D. Aicardi, R. Alonso Suárez, and A. Laguarda, "Performance of empirical models for diffuse fraction in Uruguay," *Solar Energy*, vol. 141, pp. 166–181, 2017.

[136] D. G. Erbs, S. A. Klein, and J. A. Duffie, "Estimation of the diffuse radiation fraction for hourly, daily and monthly-average global radiation," *Solar Energy*, vol. 28, no. 4, pp. 293–302, 1982.

[137] D. T. Reindl, W. A. Beckman, and J. A. Duffie, "Evaluation of hourly tilted surface radiation models," *Solar Energy*, vol. 45, no. 1, pp. 9–17, 1990.

[138] J. Boland, J. Huang, and B. Ridley, "Decomposing global solar radiation into its direct and diffuse components," *Renewable and Sustainable Energy Reviews*, vol. 28, pp. 749–756, 2013.

[139] J. Boland, L. Scott, and M. Luther, "Modelling the diffuse fraction of global solar radiation on a horizontal surface," *Environmetrics*, vol. 12, no. 2, pp. 103–116, 2001.

[140] J. Orgill and K. Hollands, "Correlation equation for hourly diffuse radiation on a horizontal surface," *Solar Energy*, vol. 19, no. 4, pp. 357–359, 1977.

[141] J. Boland, B. Ridley, and B. Brown, "Models of diffuse solar radiation," *Renewable Energy*, vol. 33, no. 4, pp. 575–584, 2008.

[142] M. Collares-Pereira and A. Rabl, "The average distribution of solar radiation-correlations between diffuse and hemispherical and between daily and hourly insolation values," *Solar Energy*, vol. 22, no. 2, pp. 155–164, 1979.

[143] B. Y. H. Liu and R. C. Jordan, "The interrelationship and characteristic distribution of direct, diffuse and total solar radiation," *Solar Energy*, vol. 4, no. 3, pp. 1–19, 1960.

[144] W. Köppen, "Band I, Teil C, Das geographische system der klimate," in *Handbuch der klimatologie*, R. Geiger and W. Köppen, Eds. Gebrüder Borntraeger, 1936, pp. 1–44.

[145] F. Rubel, K. Brugger, K. Haslinger, and I. Auer, "The climate of the European Alps: Shift of very high resolution Köppen-Geiger climate zones 1800-2100," *Meteorologische Zeitschrif*, vol. 16, no. 2, pp. 115–125, 2017.

[146] M. Kottek, J. Grieser, C. Beck, B. Rudolf, and F. Rubel, "World map of the Köppen-Geiger climate classification updated," *Meteorologische Zeitschrif*, vol. 15, no. 3, pp. 259–263, 2006.

[147] H. Stern, G. de Hoedt, and J. Ernst, "Objective classification of Australian climates," *Australian Meterological Magazine*, vol. 49, pp. 87–96, 2000.

[148] M. Peel, B. Finlayson, and T. McMahon, "Updated world map of the Köppen-Geiger climate classification," *Hydrology and Earth System Sciences*, vol. 11, pp. 1633–1644, 2007.

[149] R. Crosbie *et al.*, "Changes in Köppen-Geiger climate types under a future climate for Australia: Hydrological implications," *Hydrology and Earth System Sciences*, vol. 16, pp. 3341–3349, 2012.

[150] Australian Government Bureau of Meteorology. (2016, November) Climate classification maps. [Online]. Available: http://www.bom.gov.au/jsp/ncc/climate_averages/climate-classifications/index.jsp

[151] Climate Change and Infectious Diseases Group. (2018) World map of the Köppen-Geiger climate classification. [Online]. Available: http://koeppen-geiger.vu-wien.ac.at/present.htm

[152] M. Journée and C. Bertrand, "Quality control of solar radiation data within the RMIB solar measurements network," *Solar Energy*, vol. 85, no. 1, pp. 72–86, 2011.

[153] L. F. L. Lemos *et al.*, "Assessment of solar radiation components in Brazil using the BRL model," *Renewable Energy*, vol. 108, pp. 569–580, 2017.

[154] S. Younes, R. Claywell, and T. Muneer, "Quality control of solar radiation data: Present status and proposed new approaches," *Energy*, vol. 30, no. 9, pp. 1533–1549, 2005.

[155] S. Pashiardis and S. A. Kalogirou, "Quality control of solar shortwave and terrestrial long-wave radiation for surface radiation measurements at two sites in Cyprus," *Renewable Energy*, vol. 96, pp. 1015–1033, 2016.

[156] World Meteorological Organization, "Guide to the global observing system," Report WMO-488, 2007.

[157] J. D. Rhodes, C. R. Upshaw, W. J. Cole, C. L. Holcomb, and M. E. Webber, "A multi-objective assessment of the effect of solar PV array orientation and tilt on energy production and system economics," *Solar Energy*, vol. 108, no. 0, pp. 28–40, 2014.

[158] B. Y. H. Liu and R. C. Jordan, "The long-term average performance of flat-plate solar-energy collectors: With design data for the U.S., its outlying possessions and Canada," *Solar Energy*, vol. 7, no. 2, pp. 53–74, 1963.

[159] R. Perez, P. Ineichen, R. Seals, J. Michalsky, and R. Stewart, "Modeling daylight availability and irradiance components from direct and global irradiance," *Solar Energy*, vol. 44, no. 5, pp. 271–289, 1990.

[160] S. A. Khalil and A. M. Shaffie, "A comparative study of total, direct and diffuse solar irradiance by using different models on horizontal and inclined surfaces for Cairo, Egypt," *Renewable and Sustainable Energy Reviews*, vol. 27, pp. 853–863, 2013.

[161] R. Wattan and S. Janjai, "An investigation of the performance of 14 models for estimating hourly diffuse irradiation on inclined surfaces at tropical sites," *Renewable Energy*, vol. 93, pp. 667–674, 2016.

[162] K. Yong Sheng *et al.*, "Optimal orientation and tilt angle for maximizing in-plane solar irradiation for PV applications in Singapore," *Photovoltaics, IEEE Journal of*, vol. 4, no. 2, pp. 647–653, 2014.

[163] C. Gueymard, "An anisotropic solar irradiance model for tilted surfaces and its comparison with selected engineering algorithms," *Solar Energy*, vol. 38, no. 5, pp. 367–386, 1987. [Online]. Available: http://www.sciencedirect.com/science/article/pii/0038092X87900090

[164] T. Muneer, "Solar radiation model for Europe," *Building Services Engineering Research and Technology*, vol. 11, no. 4, pp. 153–163, 1990.

[165] C. A. Gueymard, "Direct and indirect uncertainties in the prediction of tilted irradiance for solar engineering applications," *Solar Energy*, vol. 83, no. 3, pp. 432–444, 2009.

[166] J. E. Hay, "Calculation of monthly mean solar radiation for horizontal and inclined surfaces," *Solar Energy*, vol. 23, no. 4, pp. 301–307, 1979.

[167] A. Skartveit and J. Asle Olseth, "Modelling slope irradiance at high latitudes," *Solar Energy*, vol. 36, no. 4, pp. 333–344, 1986.

[168] M. David, P. Lauret, and J. Boland, "Evaluating tilted plane models for solar radiation using comprehensive testing procedures, at a southern hemisphere location," *Renewable Energy*, vol. 51, pp. 124–131, 2013.

[169] R. Perez, R. Seals, P. Ineichen, R. Stewart, and D. Menicucci, "A new simplified version of the perez diffuse irradiance model for tilted surfaces," *Solar Energy*, vol. 39, no. 3, pp. 221–231, 1987.

[170] J. Freeman, J. Whitmore, L. Kaffine, N. Blair, and A. P. Dobos, "System Advisor Model: Flat plate photovoltaic performance modeling validation report," National Renewable Energy Laboratory, Report NREL/TP-6A20-60204, Dec. 2013.

[171] PVsyst SA. (2019) Transposition model. [Online]. Available: http://files.pvsyst.com/help/meteo_transposition.htm

[172] P. Ineichen, "Global irradiance on tilted and oriented planes: model validations," Institute for Environmental Sciences, University of Geneva, Report, 2011.

[173] Folsom Labs. (2019) Helioscope: Mathematical formulation. [Online]. Available: https://www.helioscope.com/documentation/mathematical-formulation

[174] HOMER Energy. (2016, 30 Oct 2015) 10488 - How HOMER calculates the radiation incident on the PV array. [Online]. Available: http://usersupport.homerenergy.com/customer/en/portal/articles/2186872-10488---how-homer-calculates-the-radiation-incident-on-the-pv-arr-

[175] Sandia Corporation. (2016) PV performance modeling collaborative: An industry and national laboratory collaborative to improve photovoltaic performance modeling. [Online]. Available: https://pvpmc.sandia.gov/

[176] Y.-P. Chang, "Optimal the tilt angles for photovoltaic modules using PSO method with nonlinear time-varying evolution," *Energy*, vol. 35, no. 5, pp. 1954–1963, 2010.

[177] E. D. Mehleri, P. L. Zervas, H. Sarimveis, J. A. Palyvos, and N. C. Markatos, "Determination of the optimal tilt angle and orientation for solar photovoltaic arrays," *Renewable Energy*, vol. 35, no. 11, pp. 2468–2475, 2010.

[178] J. E. Hay and J. A. Davies, "Calculations of the solar radiation incident on an inclined surface," in *First Canadian Solar Radiation Data Workshop*, J. E. Hay and T. Won, Eds. Canada: Canadian Atmospheric Environment Service, 1980, Conference Proceedings, pp. 59–72.

[179] R. C. Temps and K. L. Coulson, "Solar radiation incident upon slopes of different orientations," *Solar Energy*, vol. 19, no. 2, pp. 179–184, 1977.

[180] T. M. Klucher, "Evaluation of models to predict insolation on tilted surfaces," *Solar Energy*, vol. 23, no. 2, pp. 111–114, 1979.

[181] R. Perez, R. Stewart, C. Arbogast, R. Seals, and J. Scott, "An anisotropic hourly diffuse radiation model for sloping surfaces: Description, performance validation, site dependency evaluation," *Solar Energy*, vol. 36, no. 6, pp. 481–497, 1986.

[182] B. Espinar *et al.*, "Analysis of different comparison parameters applied to solar radiation data from satellite and german radiometric stations," *Solar Energy*, vol. 83, no. 1, pp. 118–125, 2009.

[183] C. A. Gueymard, "A review of validation methodologies and statistical performance indicators for modeled solar radiation data: Towards a better bankability of solar projects," *Renewable and Sustainable Energy Reviews*, vol. 39, pp. 1024–1034, 2014.

[184] Fraunhofer ISE, "Current and future cost of photovoltaics: Long-term scenarios for market development, system prices and LCOE of utility-scale PV systems," Agora Energiewende, Report 059/01-S-2015/EN, February 2015.

[185] Australian Government Clean Energy Regulator. (2019, 17 May) Historical postcode data for small-scale installations. [Online]. Available: http://www.cleanenergyregulator.gov.au/RET/Forms-and-resources/Postcode-data-for-small-scale-installations/historical-postcode-data-for-small-scale-installations

[186] Renewable Energy Policy Network for the 21st Century (REN21), "Renewables 2014 global status report," Report, 2014.

[187] International Renewable Energy Agency. (2018) Country rankings. [Online]. Available: https://www.irena.org/Statistics/View-Data-by-Topic/Capacity-and-Generation/Country-Rankings

[188] J. L. Gray, "The physics of the solar cell," in *Handbook of Photovoltaic Science and Engineering*, A. Luque and S. S. Hegedus, Eds. John Wiley & Sons, Ltd, 2005, ch. 3, pp. 61–112.

[189] R. A. Messenger and J. Ventre, *Photovoltaic Systems Engineering*. Boca Raton, FL: CRC Press/Taylor & Francis, 2010, vol. 3.

[190] J. M. Olson, D. J. Friedman, and S. Kurtz, "High-efficiency III-V multijunction solar cells," in *Handbook of Photovoltaic Science and Engineering*, A. Luque and S. S. Hegedus, Eds. John Wiley & Sons, Ltd, 2005, ch. 9, pp. 359–411.

[191] Fraunhofer ISE, "Photovoltaics report (2014) updated: 28 July 2014," Report, 2014.

[192] A. Gharakhani Siraki and P. Pillay, "Study of optimum tilt angles for solar panels in different latitudes for urban applications," *Solar Energy*, vol. 86, no. 6, pp. 1920–1928, 2012.

[193] A. Colli and W. J. Zaaiman, "Maximum-power-based PV performance validation method: Application to single-axis tracking and fixed-tilt c-Si systems in the Italian alpine region," *Photovoltaics, IEEE Journal of*, vol. 2, no. 4, pp. 555–563, 2012.

[194] J. Kern and I. Harris, "On the optimum tilt of a solar collector," *Solar Energy*, vol. 17, no. 2, pp. 97–102, 1975.

[195] Australian Government Clean Energy Regulator, "Postcode data for small-scale installations," 2016. [Online]. Available: http://www.cleanenergyregulator.gov.au/DocumentAssets/Pages/Postcode-data-for-small-scale-installations.aspx

[196] ——. (2015, 2 June) Financial incentives. [Online]. Available: http://www.cleanenergyregulator.gov.au/RET/How-to-participate-in-the-Renewable-Energy-Target/Financial-incentives

[197] Australian Government Climate Change Authority, "Renewable Energy Target review," Report, December 2014.

[198] Independent Pricing and Regulatory Tribunal, "Solar feed-in tariffs in 2016-17," Report, June 2016.

[199] ——, "Solar feed-in tariff benchmark 2019-20," Report, April 2019.

[200] A. K. Yadav and S. S. Chandel, "Tilt angle optimization to maximize incident solar radiation: A review," *Renewable and Sustainable Energy Reviews*, vol. 23, pp. 503–513, 2013.

[201] T. Khatib, I. A. Ibrahim, and A. Mohamed, "A review on sizing methodologies of photovoltaic array and storage battery in a standalone photovoltaic system," *Energy Conversion and Management*, vol. 120, pp. 430–448, 2016.

[202] J. Widen, E. Wackelgard, and P. D. Lund, "Options for improving the load matching capability of distributed photovoltaics: Methodology and application to high-latitude data," *Solar Energy*, vol. 83, no. 11, pp. 1953–1966, 2009.

[203] T. Beck, H. Kondziella, G. Huard, and T. Bruckner, "Assessing the influence of the temporal resolution of electrical load and PV generation profiles on self-consumption and sizing of PV-battery systems," *Applied Energy*, vol. 173, pp. 331–342, 2016.

[204] G. Merei, C. Berger, and D. U. Sauer, "Optimization of an off-grid hybrid PV-wind-diesel system with different battery technologies using genetic algorithm," *Solar Energy*, vol. 97, pp. 460–473, 2013.

[205] A. González, J.-R. Riba, A. Rius, and R. Puig, "Optimal sizing of a hybrid grid-connected photovoltaic and wind power system," *Applied Energy*, vol. 154, pp. 752–762, 2015.

[206] C. Koo, T. Hong, M. Lee, and J. Kim, "An integrated multi-objective optimization model for determining the optimal solution in implementing the rooftop photovoltaic system," *Renewable and Sustainable Energy Reviews*, vol. 57, pp. 822–837, 2016.

[207] B. Zhao *et al.*, "Optimal sizing, operating strategy and operational experience of a stand-alone microgrid on Dongfushan Island," *Applied Energy*, vol. 113, pp. 1656–1666, 2014.

[208] A. Khare and S. Rangnekar, "A review of particle swarm optimization and its applications in solar photovoltaic system," *Applied Soft Computing*, vol. 13, no. 5, pp. 2997–3006, 2013.

[209] A. K. Bansal, R. A. Gupta, and R. Kumar, "Optimization of hybrid PV/wind energy system using Meta Particle Swarm Optimization (MPSO)," in *India International Conference on Power Electronics 2010 (IICPE2010)*, 28-30 January 2011, Conference Proceedings, pp. 1–7.

[210] Y. S. Zhao, J. Zhan, Y. Zhang, D. P. Wang, and B. G. Zou, "The optimal capacity configuration of an independent wind/PV hybrid power supply system based on improved PSO algorithm," in *Advances in Power System Control, Operation and Management (APSCOM 2009), 8th International Conference on*, 8-11 Nov. 2009 2009, Conference Proceedings, pp. 1–7.

[211] M. Bashir and J. Sadeh, "Size optimization of new hybrid stand-alone renewable energy system considering a reliability index," in *Environment and Electrical Engineering (EEEIC), 2012 11th International Conference on*, 18-25 May 2012, Conference Proceedings, pp. 989–994.

[212] X. Han, H. Zhang, X. Yu, and L. Wang, "Economic evaluation of grid-connected microgrid system with photovoltaic and energy storage under different investment and financing models," *Applied Energy*, vol. 184, pp. 103–118, 2016.

[213] J. Chen and H. E. Garcia, "Economic optimization of operations for hybrid energy systems under variable markets," *Applied Energy*, vol. 177, pp. 11–24, 2016.

[214] G. Merei, J. Moshövel, D. Magnor, and D. U. Sauer, "Optimization of self-consumption and techno-economic analysis of PV-battery systems in commercial applications," *Applied Energy*, vol. 168, pp. 171–178, 2016.

[215] G. Mulder *et al.*, "The dimensioning of PV-battery systems depending on the incentive and selling price conditions," *Applied Energy*, vol. 111, pp. 1126–1135, 2013.

[216] B. Del Fabbro, A. Valentincic, and A. F. Gubina, "An adequate required rate of return for grid-connected PV systems," *Solar Energy*, vol. 132, pp. 73–83, 2016.

[217] G. G. Pillai, G. A. Putrus, T. Georgitsioti, and N. M. Pearsall, "Near-term economic benefits from grid-connected residential PV (photovoltaic) systems," *Energy*, vol. 68, pp. 832–843, 2014.

[218] R. Bakhshi and J. Sadeh, "A comprehensive economic analysis method for selecting the PV array structure in grid-connected photovoltaic systems," *Renewable Energy*, vol. 94, pp. 524–536, 2016.

[219] B. P. Numbi and S. J. Malinga, "Optimal energy cost and economic analysis of a residential grid-interactive solar PV system- case of eThekwini municipality in South Africa," *Applied Energy*, vol. 186, Part 1, pp. 28–45, 2017.

[220] Reserve Bank of Australia. (2016) Inflation target. [Online]. Available: http://www.rba.gov.au/inflation/

[221] S. A. Y. Lin, "The modified internal rate of return and investment criterion," *The Engineering Economist*, vol. 21, no. 4, pp. 237–247, 1976.

[222] W. Johnston and R. Egan, "National survey report of PV power applications in Australia 2015," Australian PV Institute, Report, June 2016.

[223] Australian Bureau of Statistics. (2016, 26 October) 6401.0 - Consumer Price Index, Australia, Sep 2016. [Online]. Available: http://www.abs.gov.au/ausstats/abs@.nsf/mf/6401.0

[224] Australian Government Clean Energy Regulator. (2016) Small generation unit STC calculator. [Online]. Available: https://www.rec-registry.gov.au/rec-registry/app/calculators/sgu-stc-calculator

[225] J. Sun, C.-H. Lai, and X.-J. Wu, *Particle Swarm Optimisation: Classical and Quantum Perspectives*. Boca Raton, Fla.: CRC Press, 2012.

[226] J. Kennedy and R. Eberhart, "Particle swarm optimization," in *Neural Networks, 1995. Proceedings., IEEE International Conference on*, vol. 4, Nov/Dec 1995 1995, Conference Proceedings, pp. 1942–1948.

[227] J. Sun, J. Liu, and W. Xu, "Using quantum-behaved particle swarm optimization algorithm to solve non-linear programming problems," *International Journal of Computer Mathematics*, vol. 84, no. 2, pp. 261–272, 2007.

[228] K. E. Parsopoulos and M. N. Vrahatis, "Unified particle swarm optimization for solving constrained engineering optimization problems," in *Advances in Natural Computation: First International Conference, ICNC 2005, Changsha, China, August 27-29, 2005, Proceedings, Part III*, L. Wang, K. Chen, and Y. S. Ong, Eds. Berlin, Heidelberg: Springer-Verlag, 2005, pp. 582–591.

[229] S. Chowdhury, W. Tong, A. Messac, and J. Zhang, "A mixed-discrete particle swarm optimization algorithm with explicit diversity-preservation," *Structural and Multidisciplinary Optimization*, vol. 47, no. 3, pp. 367–388, 2013.

[230] Australian Government Department of Industry, Innovation and Science, "Smart-Grid Smart-City customer trial data," 2016. [Online]. Available: https://data.gov.au/dataset/smart-grid-smart-city-customer-trial-data

[231] J. K. Copper, A. B. Sproul, and S. Jarnason, "Photovoltaic (PV) performance modelling in the absence of onsite measured plane of array irradiance (POA) and module temperature," *Renewable Energy*, vol. 86, pp. 760–769, 2016.

[232] Z. Ren, G. Grozev, and A. Higgins, "Modelling impact of PV battery systems on energy consumption and bill savings of Australian houses under alternative tariff structures," *Renewable Energy*, vol. 89, pp. 317–330, 2016.

[233] D. Parra and M. K. Patel, "Effect of tariffs on the performance and economic benefits of PV-coupled battery systems," *Applied Energy*, vol. 164, pp. 175–187, 2016.

[234] D. Chung, C. Davidson, R. Fu, K. Ardani, and R. Margolis, "U.S. photovoltaic price and cost breakdowns: Q1 2015 benchmarks for residential, commercial, and utility-scale systems," National Renewable Energy Laboratory, Report NREL/TP-6A20-64746, September 2015.

[235] T. Brinsmead, P. Graham, J. Hayward, E. Ratnam, and L. Reedman, "Future energy storage trends: An assessment of the economic viability, potential uptake and impacts of electrical energy storage on the NEM 2015-2035," CSIRO, Report EP155039, September 2015.

[236] "Projections of uptake of small-scale systems," Jacobs, Report, 6 June 2016.

[237] S. Jun, F. Bin, and X. Wenbo, "Particle swarm optimization with particles having quantum behavior," in *Proceedings of the 2004 Congress on Evolutionary Computation (IEEE Cat. No.04TH8753)*, vol. 1, 19-23 June 2004, Conference Proceedings, pp. 325–331 Vol.1.

[238] J. Sun, W. Fang, X. Wu, Z. Xie, and W. Xu, "QoS multicast routing using a quantum-behaved particle swarm optimization algorithm," *Engineering Applications of Artificial Intelligence*, vol. 24, no. 1, pp. 123–131, 2011.

[239] S. Jun, X. Wenbo, and F. Bin, "A global search strategy of quantum-behaved particle swarm optimization," in *IEEE Conference on Cybernetics and Intelligent Systems*, vol. 1, 1-3 December 2004, Conference Proceedings, pp. 111–116.

[240] J. Liu, J. Sun, and W. Xu, "Quantum-behaved particle swarm optimization for integer programming," in *Lecture Notes in Computer Science (including subseries Lecture Notes in Artificial Intelligence and Lecture Notes in Bioinformatics)*, 2006, vol. 4233 LNCS - II, pp. 1042–1050.

[241] D. Reicosky, L. Winkelman, J. Baker, and D. Baker, "Accuracy of hourly air temperatures calculated from daily minima and maxima," *Agricultural and Forest Meteorology*, vol. 46, no. 3, pp. 193–209, 1989.

[242] C. T. de Wit, *Simulation of Assimilation, Respiration, and Transpiration of Crops*. Wageningen: Pudoc, 1978.

[243] G. Hoogenboom and M. G. Huck, "Rootsimu v4.0," *Agronomy and soils departmental series-Auburn University, Alabama Agricultural Experiment Station (USA)*, 1986.

[244] Tesla Motors, "Powerwall 2 DC datasheet," 2016.

[245] Enphase, "Enphase AC battery datasheet," 2016.

[246] Tesla Motors. (2016) Powerwall 2. [Online]. Available: https://www.tesla.com/en_AU/powerwall

[247] Solar Quotes. (2016, December) Solar battery storage comparison table. [Online]. Available: https://www.solarquotes.com.au/battery-storage/comparison-table/

[248] ——. (2019, 25 July) Solar battery storage comparison table. [Online]. Available: https://www.solarquotes.com.au/battery-storage/comparison-table

[249] TransGrid, "iDemand: A technical guide to Transgrid's Western Sydney electricity demand management system," 2015.

[250] W. De Soto, S. A. Klein, and W. A. Beckman, "Improvement and validation of a model for photovoltaic array performance," *Solar Energy*, vol. 80, no. 1, pp. 78–88, 2006.

[251] J. J. Liang, A. K. Qin, P. N. Suganthan, and S. Baskar, "Comprehensive learning particle swarm optimizer for global optimization of multimodal functions," *IEEE Transactions on Evolutionary Computation*, vol. 10, no. 3, pp. 281–295, 2006.

[252] H. Long and X. Zhang, "Quantum-behaved particle swarm optimization based on comprehensive learning," in *Advances in Electronic Commerce, Web Application and Communication: Volume 2*, D. Jin and S. Lin, Eds. Berlin, Heidelberg: Springer-Verlag, 2012, pp. 15–20.

[253] L. Diestelmeier, "Changing power: Shifting the role of electricity consumers with blockchain technology - policy implications for EU electricity law," *Energy Policy*, vol. 128, pp. 189–196, 2019.

[254] Power Ledger, "White paper," Report, 2018.

[255] A. Roy, A. Bruce, and I. MacGill, "The potential value of peer-to-peer energy trading in the Australian National Electricity Market," in *Asia-Pacific Solar Research Conference*, 2016, Conference Proceedings.

[256] Australian Energy Market Commission, "Rule determination, National Electricity Amendment(distribution network pricing arrangements) Rule 2014," Report, 27 November 2014.

[257] J. Rutovitz, E. Langham, S. Teske, A. Atherton, and L. McIntosh, "Virtual trials of local network charges and local electricity trading: Summary report," Institute of Sustainable Futures, Report, May 2016.

[258] J. Rutovitz, E. Langham, and J. Downes, "A level playing field for local energy," Institute for Sustainable Futures, Report, November 2014.

[259] LO3 Energy. (2018) Innovations. [Online]. Available: https://lo3energy.com/innovations/

[260] M. R. Alam, M. St-Hilaire, and T. Kunz, "Peer-to-peer energy trading among smart homes," *Applied Energy*, vol. 238, pp. 1434–1443, 2019.

[261] J. M. Zepter, A. Lüth, P. Crespo del Granado, and R. Egging, "Prosumer integration in wholesale electricity markets: Synergies of peer-to-peer trade and residential storage," *Energy and Buildings*, vol. 184, pp. 163–176, 2019.

[262] A. Lüth, J. M. Zepter, P. Crespo del Granado, and R. Egging, "Local electricity market designs for peer-to-peer trading: The role of battery flexibility," *Applied Energy*, vol. 229, pp. 1233–1243, 2018.

[263] M. R. Alam, M. St-Hilaire, and T. Kunz, "An optimal P2P energy trading model for smart homes in the smart grid," *Energy Efficiency*, vol. 10, no. 6, pp. 1475–1493, 2017.

[264] M. Andoni *et al.*, "Blockchain technology in the energy sector: A systematic review of challenges and opportunities," *Renewable and Sustainable Energy Reviews*, vol. 100, pp. 143–174, 2019.

[265] AGL, "Peer-to-peer distributed ledger technology assessment," Report, October 2017.

[266] J. Besnainou. (2018, 17 January) From the Brooklyn Microgrid to EXERGY - A conversation with Lawrence Orsini, CEO of LO3 energy. Cleantech Group. [Online]. Available: https://www.cleantech.com/from-the-brooklyn-microgrid-to-exergy-a-conversation-with-lawrence-orsini-ceo-of-lo3-energy/

[267] W. Tushar *et al.*, "Energy storage sharing in smart grid: A modified auction-based approach," *IEEE Transactions on Smart Grid*, vol. 7, no. 3, pp. 1462–1475, 2016.

[268] C. Zhang, J. Wu, Y. Zhou, M. Cheng, and C. Long, "Peer-to-peer energy trading in a microgrid," *Applied Energy*, vol. 220, pp. 1–12, 2018.

[269] S. Nguyen, W. Peng, P. Sokolowski, D. Alahakoon, and X. Yu, "Optimizing rooftop photovoltaic distributed generation with battery storage for peer-to-peer energy trading," *Applied Energy*, vol. 228, pp. 2567–2580, 2018.

[270] N. Liu *et al.*, "Energy-sharing model with price-based demand response for microgrids of peer-to-peer prosumers," *IEEE Transactions on Power Systems*, vol. 32, no. 5, pp. 3569–3583, 2017.

[271] E. Münsing, J. Mather, and S. Moura, "Blockchains for decentralized optimization of energy resources in microgrid networks," in *2017 IEEE Conference on Control Technology and Applications (CCTA)*, 27-30 August 2017, Conference Proceedings, pp. 2164–2171.

[272] Y. Zhou, J. Wu, and C. Long, "Evaluation of peer-to-peer energy sharing mechanisms based on a multiagent simulation framework," *Applied Energy*, vol. 222, pp. 993–1022, 2018.

[273] C. Long *et al.*, "Peer-to-peer energy trading in a community microgrid," in *2017 IEEE Power & Energy Society General Meeting*, 16-20 July 2017, Conference Proceedings, pp. 1–5.

[274] C. Long, J. Wu, Y. Zhou, and N. Jenkins, "Peer-to-peer energy sharing through a two-stage aggregated battery control in a community microgrid," *Applied Energy*, vol. 226, pp. 261–276, 2018.

[275] C. Long, J. Wu, C. Zhang, M. Cheng, and A. Al-Wakeel, "Feasibility of peer-to-peer energy trading in low voltage electrical distribution networks," *Energy Procedia*, vol. 105, pp. 2227–2232, 2017.

[276] T. Morstyn, A. Teytelboym, and M. D. Mcculloch, "Bilateral contract networks for peer-to-peer energy trading," *IEEE Transactions on Smart Grid*, vol. 10, no. 2, pp. 2026–2035, 2019.

[277] Energy Networks Association, "Electricity network tariff reform handbook," Report, May 2016.

[278] R. Passey, N. Haghdadi, A. Bruce, and I. MacGill, "Designing more cost reflective electricity network tariffs with demand charges," *Energy Policy*, vol. 109, pp. 642–649, 2017.

[279] S. Oliva H, "Assessing the growth of residential PV exports with energy efficiency and the opportunity for local generation network credits," *Renewable Energy*, vol. 121, pp. 451–459, 2018.

[280] Australian Energy Market Commission, "Final rule determination, National Electricity Amendment (local generation network credits) Rule 2016," Report, 8 December 2016.

[281] J. Kang *et al.*, "Enabling localized peer-to-peer electricity trading among plug-in hybrid electric vehicles using consortium blockchains," *IEEE Transactions on Industrial Informatics*, vol. 13, no. 6, pp. 3154–3164, 2017.

[282] W. Tushar *et al.*, "Transforming energy networks via peer-to-peer energy trading: The potential of game-theoretic approaches," *IEEE Signal Processing Magazine*, vol. 35, no. 4, pp. 90–111, 2018.

[283] C. Zhang, J. Wu, C. Long, and M. Cheng, "Review of existing peer-to-peer energy trading projects," *Energy Procedia*, vol. 105, pp. 2563–2568, 2017.

[284] Open Utility, "A glimpse into the future of Britain's energy economy," Report, 2016.

[285] Vandebron. (2019) About us. [Online]. Available: https://vandebron.nl/over-ons

[286] Tennet Holding B.V. (2019, 29 January) TenneT: Continuing with blockchain after successful pilots. [Online]. Available: https://www.tennet.eu/news/detail/tennet-continuing-with-blockchain-after-successful-pilots/

[287] Brooklyn Microgrid. (2019) Brooklyn Microgrid 101. [Online]. Available: https://www.brooklyn.energy/bmg-101

[288] Sonnen. (2019) What is the sonnenCommunity? [Online]. Available: https://sonnengroup.com/sonnencommunity/

[289] Australian Renewable Energy Agency. (2018) Latrobe Valley microgrid feasibility study. [Online]. Available: https://arena.gov.au/projects/latrobe-valley-microgrid-feasibility-study/

[290] Greensync, "Creating the grid of tomorrow, today - A deX white paper," Report, 2018.

[291] Australian Renewable Energy Agency. (2017) Simply Energy Virtual Power Plant (VPP). [Online]. Available: https://arena.gov.au/projects/simply-energy-virtual-power-plant-vpp/

[292] Government of Western Australia. (2018, 5 December) New trial enables customers to buy and sell solar energy. [Online]. Available: https://www.mediastatements.wa.gov.au/Pages/McGowan/2018/12/New-trial-enables-customers-to-buy-and-sell-solar-energy.aspx

[293] Power Ledger. (2017, 16 November) Australian Government awards grant to $8 million project in the City of Fremantle using the Power Ledger platform. [Online]. Available: https://medium.com/power-ledger/australian-government-awards-grant-to-8-million-project-in-the-city-of-fremantle-using-the-power-2dbadfad50ae

[294] ——. (2018) Projects. [Online]. Available: https://www.powerledger.io/#projects

[295] Australian Energy Market Commission, "Rule determination, National Electricity Amendment (expanding competition in metering and related services) Rule 2015," Report, 26 November 2015.

[296] Australian Energy Regulator. (2019) Determinations & access arrangements. [Online]. Available: https://www.aer.gov.au/networks-pipelines/determinations-access-arrangements

[297] Ausgrid, "Revised regulatory proposal 1 July 2019 to 30 June 2024," Report, January 2019.

[298] ——, "Revised proposal attachment 10.01 tariff structure statement," Report, January 2019.

[299] ——, "Revised proposal attachment 10.10 indicative pricing schedule distribution use of system charges," Report, January 2019.

[300] ——, "Revised proposal attachment 10.11 indicative pricing schedule transmission use of system charges," Report, January 2019.

[301] ——, "Revised proposal attachment 10.13 indicative pricing schedule climate change fund charges," Report, January 2019.

[302] Solar Choice. (2019, 11 February) Residential solar PV price index - February 2019. [Online]. Available: https://www.solarchoice.net.au/blog/51210/blog/residential-solar-pv-price-index-february-2019

[303] R. Brakels. (2018, 10 October) Tesla raises Powerwall 2 price - just in time for Australian battery subsidies. [Online]. Available: https://www.solarquotes.com.au/blog/tesla-powerwall-2-price-rise/

[304] Tesla Motors. (2019) Powerwall. [Online]. Available: https://www.tesla.com/en_AU/powerwall

[305] R. Brakels. (2019, 23 July) Good news! Tesla drops price of Powerwall 2 by $650 - Less than one-quarter previous price hike. [Online]. Available: https://www.solarquotes.com.au/blog/tesla-powerwall-price-drop/

[306] J. A. Rice, *Mathematical Statistics and Data Analysis*, ser. Duxbury advanced series. Belmont, CA: Thomson/Brooks/Cole, 2007.